

# **EFFECT OF TEMPERATURE AND DEFORMATION ON THE THERMO-MECHANICAL PROPERTIES OF THERMOSET EPOXIES**

by

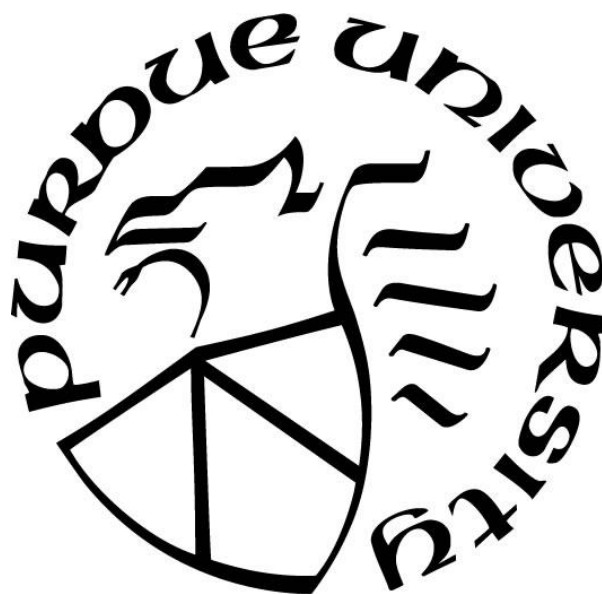
**Yelin Ni**

**A Dissertation**

*Submitted to the Faculty of Purdue University*

*In Partial Fulfillment of the Requirements for the degree of*

**Doctor of Philosophy**



Davidson School of Chemical Engineering

West Lafayette, Indiana

May 2020

**THE PURDUE UNIVERSITY GRADUATE SCHOOL**  
**STATEMENT OF COMMITTEE APPROVAL**

**Dr. James M. Caruthers, Chair**

Davidson School of Chemical Engineering

**Dr. Bryan W. Boudouris**

Davison School of Chemical Engineering,  
Department of Chemistry

**Dr. You-Yeon Won**

Davidson School of Chemical Engineering

**Dr. R. Byron Pipes**

School of Aeronautics and Astronautics,  
School of Materials Engineering,  
Davidson School of Chemical Engineering

**Approved by:**

Dr. John Morgan

Head of Graduate Program

*To my parents and friends*

## **ACKNOWLEDGMENTS**

I would like to thank my advisor Dr. James Caruthers for his support and guidance during my studies. The door to Prof. Caruthers' office was always open whenever I ran into a problem about my research. His advices and ideas expanded my scientific knowledge and steered me the right direction. I would also like to thank Dr. Bryan Boudouris, Dr. You-Yeon Won and Dr. Byron Pipes for their helpful suggestions and for serving on my committee.

I would like to thank Dr. Grigori Medvedev for day-to-day conversations on research questions, for explaining things until I understand and for sharing insights on many research topics. I would like to acknowledge Dr. JungSuk Kim for GPC trace, Daniel Wilcox for dielectric spectroscopic measurements, Hosup Song for stress relaxation results, Dr. Yury Zvinevich, Dr. Jeffrey Switzer and Dr. Silei Xiong for helping with setting up lab equipment, and Nick Humphrey for machining specimens and molds.

I would like to thank my friends and family especially my parents for their continual support throughout my life. Special thanks to my close friends Dr. Xinrui Xu and Dr. Yunlan Zhang for always listening and giving me positive answers, and my feline friend Momoko for companion and comforting. Finally I would like to thank Hwa-Ching for his love and support.

## TABLE OF CONTENTS

LIST OF TABLES .....	8
LIST OF FIGURES .....	9
ABSTRACT.....	17
1. INTRODUCTION .....	19
1.1 References.....	24
2. RETHINKING THE ANALYSIS OF THE LINEAR VISCOELASTIC BEHAVIOR OF AN EPOXY POLYMER NEAR AND ABOVE THE GLASS TRANSITION .....	26
2.1 Introduction.....	27
2.2 Experimental .....	29
2.2.1 Dynamic Mechanical Experiments.....	29
2.2.2 Stress Relaxation Experiments .....	31
2.2.3 Dielectric Experiments .....	31
2.3 Experimental Results .....	32
2.3.1 New Methodology for Analyzing Linear Viscoelastic Response.....	41
2.3.2 Spectral Analysis of the Epon1009-MDA Epoxy System.....	48
2.4 Discussion .....	52
2.5 References.....	58
3. LINEAR VISCOELASTIC RELAXATION IN THE $\alpha$ AND $\alpha+$ REGIONS OF LINEAR POLYMERS, CROSSLINKED POLYMERS AND SMALL MOLECULES ...	64
3.1 Introduction.....	65
3.2 Experimental .....	69
3.3 Results.....	73
3.3.1 Linear Relaxation Behavior of EPON1009F-MDA .....	73
3.3.2 Linear Relaxation Behavior of Phenoxy.....	77
3.3.3 Linear Relaxation Behavior of EPON825-MDA .....	80
3.3.4 Linear Viscoelastic Behavior of a Series of DGEBA Resins Cured with DDS 84	
3.4 Discussion .....	90
3.5 References.....	102

4. EFFECT OF DEFORMATION HISTORY ON STRESS-STRAIN BEHAVIORS OF GLASSY POLYMERS FROM A MOBILITY PERSPECTIVE .....	107
4.1 Signatures of Stress-Strain Behaviors Explained by Mobility Change .....	109
4.2 Constitutive Models Describing Mobility .....	110
4.2.1 Maxwell Model.....	111
4.2.2 Nonlinear, “Material Clock” Models.....	112
“Stress Clock” Models .....	113
“Strain Clock” Models .....	115
4.2.3 “Internal Variable History Clock” Models .....	116
Effect of Strain Rate .....	118
Effect of Physical Aging .....	119
4.3 Internal Variable History Clock Model Predictions for Multi-Step Stress-Strain Behaviors .....	121
4.3.1 Two-Step Switch of Strain Rate Behaviors .....	122
4.3.2 Three-Step Loading-Unloading-Reloading Behaviors .....	124
4.3.3 Four-Step Loading-Unloading-Creep-Reloading Behaviors .....	126
Effect of Creep Duration at a Low Creep Stress .....	127
Effect of Creep Duration at a High Creep Stress .....	128
Effect of Creep Stress.....	130
4.4 Experimental .....	132
4.4.1 Machining of Dogbone Specimen .....	132
4.4.2 Experimental Settings .....	133
4.4.3 Temperature Measurement .....	136
4.4.4 Strain Measurement .....	137
4.4.5 Run-to-Run Deviation of Bar and Dogbone-Shaped Specimens .....	139
4.5 Results.....	141
4.5.1 Effect of Physical Aging with No Deformation .....	141
4.5.2 Effect of Creep Duration at a Small Creep Stress .....	143
4.5.3 Effect of Creep Duration at a Large Creep Stress .....	145

4.5.4	Effect of Creep Stress .....	146
4.5.5	Summary.....	148
4.6	Reference .....	150
5.	CONCLUSION.....	153
APPENDIX A. DIELECTRIC ANALYSIS FOR EPON 1009F-MDA.....		155
APPENDIX B. EQUATION (2-5) FITTING PARAMETERS FOR ALL ISOTHERMS		157
APPENDIX C. MOLECULAR WEIGHT DISTRIBUTION FOR EPON RESINS .....		158
APPENDIX D. VISCOELASTIC RELAXATION DATA.....		162
APPENDIX E. OTHER MECHANICAL DATASETS OF GLASS-FORMING MATERIALS INVESTIGATED.....		186

## LIST OF TABLES

Table 3.1. Characteristics of DGEBA resins. ....	72
Table 3.2. $T_{ref}$ used to construct master curves in Figure 3.13A through Figure 3.19A, $T_g$ and WLF parameters for the series of DGEBA resins cured with DDS.....	89
Table 4.1. Features of a single-step nonlinear stress-strain behavior of a glassy polymer. ....	109
Table 4.2. Plasticity-based constitutive models for polymers in glassy state .....	114
Table 4.3. “Strain clock” constitutive models for polymers in glassy state .....	116
Table 4.4. “Internal variable history clock” constitutive models for polymers in glassy state .....	116
Table 4.5. Features of multi-step stress-strain behaviors of glassy polymers .....	121
Table 4.6 Run-to-run variation of actual strain rate and yield stress for all specimens.....	140
Table 4.7 Actual strain rate and unscaled yield stress for each test included in Figure 4.26.....	142
Table 4.8 Actual strain rate and unscaled yield stress for each test included in Figure 4.27.....	144
Table 4.9 Actual strain rate and unscaled yield stress for each test included in Figure 4.28.....	146
Table 4.10 Actual strain rate and unscaled yield stress for each test included in Figure 4.29 and Figure 4.30 .....	147



## LIST OF FIGURES

Figure 1.1. Schematic relaxation spectrum of a glassy material near $T_g$ .	20
Figure 1.2. Generalized Maxwell model.....	21
Figure 2.1. Linear viscoelastic storage (A and C) and loss (B and D) shear moduli isotherms vs frequency for Epon1009 epoxy resin cured with MDA at the following temperatures: 180°C – red diamonds, 160°C – orange diamonds, 140°C – cyan diamonds, 130°C – blue diamonds, 125°C – magenta diamonds, 120°C – red pluses, 115°C – orange pluses, 112.5°C – green pluses, 110°C – cyan pluses, 107.5°C – blue pluses, 105°C – magenta pluses, 102.5°C – red circles, 100°C – orange circles, 97.5°C – green circles, 95°C – cyan circles, 92.5°C – blue circles, 90°C – magenta circles.	33
Figure 2.2. The Epon1009-MDA epoxy storage and loss master curves from time-temperature superposition of the isothermal data shown in Figure 2.1, using the $\log a_T$ shift function shown in Figure 2.3. Symbols have same meaning as in Figure 2.1. Panels A and B display the approximate master curves from the high temperature isotherms of Figure 2.1A and B; panels C and D display the approximate master curves from the lower temperature isotherms of Figure 2.1C and D; panels E and F are expanded views of C and D, respectively.....	34
Figure 2.3. Temperature dependence of the time-temperature shift function for approximate superposition of (i) the dynamic $G'$ and $G''$ isotherms shown in Figure 2.2A-B (blue circles) and Figure 2.2C-D (magenta circles) and (ii) the $G(t)$ stress relaxation isotherms shown in Figure 2.5 (magenta diamonds). The dashed line indicates $T_g$ .	37
Figure 2.4. Linear viscoelastic stress relaxation modulus isotherms for Epon1009 epoxy resin cured with MDA. Symbols indicating temperature have the same meaning as in Figure 2.1.....	37
Figure 2.5. Stress relaxation modulus master curve for Epon1009 epoxy resin cured with MDA using the isotherms shown in Figure 2.4 with the $\log a_T$ shift data shown in Figure 2.3. Symbols have same meaning as in Figure 2.4.	38
Figure 2.6. Linear viscoelastic storage (A) and loss (B and C) shear moduli isotherms vs frequency for Epon1009 epoxy resin cured with MDA; symbols indicate the dynamic experiment at the following temperatures: 180°C – red diamonds, 160°C – orange diamonds, 140°C – cyan diamonds, 130°C – blue diamonds, 125°C – magenta diamonds, 120°C – red pluses, 115°C – orange pluses, 112.5°C – green pluses, 110°C – cyan pluses, 107.5°C – blue pluses, 105°C – magenta pluses, 102.5°C – red circles, 100°C – orange circles, 97.5°C – green circles, 95°C – cyan circles, 92.5°C – blue circles, 90°C – magenta circles. The thick solid lines indicate the transformed stress relaxation data, where the colors correspond to the same temperatures used in the dynamic data.. Black lines are fits using the model described in the text.	40
Figure 2.7. Schematic of the spectral components at two temperatures, where the temperature $T_B$ of panel B is lower than the temperature $T_A$ in panel A. See text for further description.....	45

Figure 2.8. Density of relaxation processes vs relaxation time for Epon1009-MDA for various temperatures: 130°C – blue, 120°C – red, 110°C – cyan, 100°C – orange, and 90°C – magenta.49

Figure 2.9. Relaxation map for 1009 MDA epoxy system: (A)  $\alpha$ -region, every 3,000<sup>th</sup> process is shown i.e. the leftmost process is process No.50, the next process to the right is process No.3050, the subsequent processes are incremented by 3000, where the rightmost process is process No.87,050; (B)  $\alpha$ + region, every 300<sup>th</sup> process is shown i.e. the leftmost process is process No.50, next process to the right is process No.350, etc. the rightmost process is process No.3050. In (A) vertical dashed line indicates  $T_g$  at 374.5 K (101.5°C); in (B)  $T_g$  corresponds to the right edge of the box.....51

Figure 2.10. Storage dielectric susceptibility isotherms vs frequency for Epon1009 epoxy resin cured with MDA at the following temperatures: 180°C – red diamonds, 160°C – orange diamonds, 150°C – green diamonds, 140°C – cyan diamonds, 130°C – blue diamonds, 125°C – magenta diamonds, 120°C – red pluses.....55

Figure 3.1. Molecular structures of DGEBA materials and di-amine crosslinkers. ....69

Figure 3.2. Attempted superposition of  $G'$  storage and  $G''$  loss isotherms for EPON1009F-MDA epoxy. Temperatures: 112.5°C – green, 115°C – orange, 120°C – red. ....74

Figure 3.3. EPON1009F-MDA  $G'$  (A) and  $G''$  (B) master curves via frequency-temperature superposition of the isotherms from Ref. [10] with a reference temperature  $T_{ref} = 130^\circ\text{C}$  and the  $\log a_T$  shift factor shown in Figure 3.4A (pluses). Symbols indicate isotherms: 130°C – blue, 140°C – cyan, 160°C – orange, 180°C – red diamonds. Solid line is fit using the component of the relaxation spectrum in Figure 3.3B marked as  $\alpha$ +. ....74

Figure 3.4. (A) Shift factors for the  $\alpha$ -component (circles) and the  $\alpha$ +-component (pluses) of the relaxation spectrum required to effect the fit to the  $G'$  and  $G''$  data shown in Figure 3.5; lines are guide to the eye. (B)  $\alpha$ - and  $\alpha$ +-components of the relaxation spectrum at two temperatures: 107.5°C – blue and 120°C – red;  $\alpha$ -component is shown in lighter color for better visibility. Dashed line indicates region where determination of the  $\alpha$ -component becomes uncertain. ....76

Figure 3.5. EPON1009F-MDA storage (A) and loss (B) isotherms for the temperatures: 100°C – orange circles, 102.5°C – red circles, 105°C – magenta pluses, 107.5°C – blue pluses, 110°C – cyan pluses, 112.5°C – green pluses, 115°C – orange pluses, 120°C – red pluses, 125°C – magenta diamonds, 130°C – blue diamonds. Lines are fit using the additive combination of the  $\alpha$ - and  $\alpha$ +-components of the relaxation spectrum shown in Figure 3.4B with the temperature shifts shown in Figure 3.4A. ....77

Figure 3.6. The linear viscoelastic shear storage (A) and (C) and loss (B) and (D) moduli for phenoxy at the glass transition ( $T_g = 98^\circ\text{C}$ ) and above (A) and (B) and in the flow region, i.e. above 160°C, (C) and (D). Isotherms in (A) and (B) are at: 95°C (O), 100°C (X), 105°C (O), 110°C (X), 120°C (O), and 140°C (X). Isotherms in (C) and (D) are at: 160°C (+), 180°C ( $\Delta$ ), 200°C (+), 220°C ( $\Delta$ ), 240°C (+), and 260°C ( $\Delta$ ) Lines are fits using the relaxation spectrum shown Figure 3.8B. ....78

Figure 3.7. Phenoxy  $G'$  (A) and  $G''$  (B) master curves via frequency-temperature superposition of the isotherms shown in Figure 3.5 with a reference temperature  $T_{\text{ref}} = 105^\circ\text{C}$  and the  $\log a_T$  shift factor shown in Figure 3.8A. Colors/symbols have same meaning as in Figure 3.6. Solid lines are the predictions using the relaxation spectrum shown in Figure 3.8B. ....79

Figure 3.8. (A) The  $\log a_T$  shift factor for phenoxy required to effect approximate frequency-temperature superposition resulting in the  $G'$  and  $G''$  master curves shown in Figure 3.7. The black line is a WLF fit with  $C_1 = 6.14$  and  $C_2 = 29.26^\circ\text{C}$  and the red line is a WLF fit with  $C_1 = 9.49$  and  $C_2 = 66.73^\circ\text{C}$ . (B) The  $\log H$  phenoxy relaxation spectrum determined from the linear viscoelastic  $G'$  and  $G''$  data. ....80

Figure 3.9. Dynamic shear responses for EPON 825-MDA near and above glass transition temperature ( $T_g = 183^\circ\text{C}$ ). Storage and loss isotherms are shown for the following temperatures:  $185^\circ\text{C}$  ( $\Delta$ ),  $190^\circ\text{C}$  ( $\Delta$ ),  $195^\circ\text{C}$  ( $\Delta$ ),  $200^\circ\text{C}$  ( $\Delta$ ),  $205^\circ\text{C}$  ( $\Delta$ ),  $210^\circ\text{C}$  ( $\Delta$ ) and  $220^\circ\text{C}$  ( $\Delta$ ) from top to bottom respectively. Lines are the predictions using the relaxation spectrum shown in Figure 3.11B. ....81

Figure 3.10. Temperature dependence of equilibrium moduli  $G_e$  as determined from the  $G'$  values at the lowest frequency of 0.01Hz. The solid line is the prediction from rubber elasticity with  $G_e = 4.38 \times 10^{-5} T$ . ....82

Figure 3.11. EPON825-MDA  $G'$  (A) and  $G''$  (B) master curves via frequency-temperature superposition of the isotherms shown in Figure 3.9C and D with a reference temperature  $T_{\text{ref}} = 190^\circ\text{C}$  and the  $\log a_T$  shift factor shown in Figure 3.12A. Symbols have same meaning as in Figure 3.9. The solid lines are the predictions using the relaxation spectrum shown in Figure 3.12B....83

Figure 3.12. (A) The  $\log a_T$  shift factor for EPON825-MDA required to effect approximate frequency-temperature superposition resulting in the  $G'$  and  $G''$  master curves shown in Figure 3.11. The solid line is a WLF fit with  $C_1 = 11.18$  and  $C_2 = 59.12^\circ\text{C}$ . (B) The  $\log H$  EPON825-MDA relaxation spectrum determined from the linear viscoelastic  $G'$  and  $G''$  data. ....84

Figure 3.13. (A)  $G'$  and  $G''$  master curves for EPON828-DDS. Isotherms before shift are given in Figure A.4. Symbols indicate the isotherms temperature:  $G'$ :  $222^\circ\text{C}$  ( $\circ$ ),  $225^\circ\text{C}$  ( $\circ$ ),  $228^\circ\text{C}$  ( $+$ ),  $233^\circ\text{C}$  ( $+$ ),  $238^\circ\text{C}$  ( $+$ ),  $248^\circ\text{C}$  ( $+$ );  $G''$ :  $222^\circ\text{C}$  ( $\times$ ),  $225^\circ\text{C}$  ( $\times$ ),  $228^\circ\text{C}$  ( $\Delta$ ),  $233^\circ\text{C}$  ( $\Delta$ ),  $238^\circ\text{C}$  ( $\Delta$ ),  $248^\circ\text{C}$  ( $\Delta$ ),  $257^\circ\text{C}$  ( $\Delta$ ),  $267^\circ\text{C}$  ( $\Delta$ ). Solid line is fit using Equation (3.1) with the relaxation spectrum shown in panel (B). ....85

Figure 3.14. (A)  $G'$  and  $G''$  master curves for EPON834-DDS. Isotherms before shift are given in Figure A.5. Symbols indicate the isotherms temperature:  $G'$ :  $181^\circ\text{C}$  ( $\circ$ ),  $184^\circ\text{C}$  ( $\circ$ ),  $187^\circ\text{C}$  ( $\circ$ ),  $191^\circ\text{C}$  ( $\circ$ ),  $196^\circ\text{C}$  ( $\circ$ ),  $201^\circ\text{C}$  ( $+$ ),  $206^\circ\text{C}$  ( $+$ ),  $211^\circ\text{C}$  ( $+$ );  $G''$ :  $181^\circ\text{C}$  ( $\times$ ),  $184^\circ\text{C}$  ( $\times$ ),  $187^\circ\text{C}$  ( $\times$ ),  $191^\circ\text{C}$  ( $\times$ ),  $196^\circ\text{C}$  ( $\times$ ),  $201^\circ\text{C}$  ( $\Delta$ ),  $206^\circ\text{C}$  ( $\Delta$ ),  $211^\circ\text{C}$  ( $\Delta$ ),  $221^\circ\text{C}$  ( $\Delta$ ),  $231^\circ\text{C}$  ( $\Delta$ ),  $241^\circ\text{C}$  ( $\Delta$ ). Solid line is fit using Equation (3.1) with the relaxation spectrum shown in panel (B). .....86

Figure 3.15. (A)  $G'$  and  $G''$  master curves for EPON1001F-DDS. Isotherms before shift are given in Figure A.6. Symbols indicate the isotherms temperature:  $G'$ :  $140^\circ\text{C}$  ( $\circ$ ),  $143^\circ\text{C}$  ( $\circ$ ),  $146^\circ\text{C}$  ( $\circ$ ),  $149^\circ\text{C}$  ( $\circ$ ),  $152^\circ\text{C}$  ( $+$ ),  $155^\circ\text{C}$  ( $+$ ),  $158^\circ\text{C}$  ( $+$ ),  $163^\circ\text{C}$  ( $+$ ),  $168^\circ\text{C}$  ( $+$ ),  $173^\circ\text{C}$  ( $+$ );  $G''$ :

140°C (×), 143°C (×), 146°C (×), 149°C (×), 152°C (△), 155°C (△), 158°C (△), 163°C (△), 168°C (△), 173°C (△), 178°C (△), 188°C (□), 198°C (□). Solid line is fit using Equation (3.1) with the relaxation spectrum shown in panel (B). .....86

Figure 3.16. (A)  $G'$  and  $G''$  master curves for EPON1002F-DDS. Isotherms before shift are given in Figure A.7. Symbols indicate the isotherms temperature:  $G'$ : 130°C (○), 132.5°C (○), 136°C (○), 139°C (○), 141°C (+), 147°C (+), 152°C (+), 157°C (+), 167°C (+);  $G''$ : 130°C (×), 132.5°C (×), 136°C (×), 139°C (×), 141°C (△), 147°C (△), 152°C (△), 157°C (△), 167°C (△), 177°C (△), 187°C (△). Solid line is fit using Equation (3.1) with the relaxation spectrum shown in panel (B). .....87

Figure 3.17. (A)  $G'$  and  $G''$  master curves for EPON1004F-DDS. Isotherms before shift are given in Figure A.8. Symbols indicate the isotherms temperature:  $G'$ : 120°C (○), 125°C (○), 130°C (○), 135°C (○), 140°C (+), 145°C (+), 155°C (+);  $G''$ : 120°C (×), 125°C (×), 130°C (×), 135°C (×), 140°C (△), 145°C (△), 155°C (△). Solid line is fit using Equation (3.1) with the relaxation spectrum shown in panel (B). .....87

Figure 3.18. (A)  $G'$  and  $G''$  master curves for EPON1007F-DDS. Isotherms before shift are given in Figure A.9. Symbols indicate the isotherms temperature:  $G'$ : 115°C (○), 120.5°C (○), 125.5°C (○), 130.5°C (+), 135.5°C (+), 145.5°C (+), 155°C (+);  $G''$ : 115°C (×), 120.5°C (×), 125.5°C (×), 130.5°C (△), 135.5°C (△), 145.5°C (△), 155°C (△). Solid line is fit using Equation (3.1) with the relaxation spectrum shown in panel (B). .....88

Figure 3.19. (A)  $G'$  and  $G''$  master curves for EPON1009F-DDS. Isotherms before shift are given in Figure A.10. Symbols indicate the isotherms temperature:  $G'$ : 103°C (○), 108°C (○), 113°C (○), 118°C (○), 123°C (○), 128°C (+), 133°C (+), 138°C (+);  $G''$ : 103°C (×), 108°C (×), 113°C (×), 118°C (×), 123°C (×), 128°C (△), 133°C (△), 138°C (△). Solid line is fit using Equation (3.1) with the relaxation spectrum shown in panel (B). .....88

Figure 3.20.  $\log a_T$  vs temperature for the DDS series. The values  $T_{ref}$  are given in Table 4.2. Materials are indicated as follows: EPON828-DDS – red, EPON834-DDS – orange, EPON1001F-DDS – green, EPON1002F-DDS – cyan, EPON1004F-DDS – blue, EPON1007F-DDS – magenta, EPON1009F-DDS – grey. ....89

Figure 3.21. Storage (A) and loss (B) dielectric susceptibility for DGEBA monomer at 288 K; data are from Casalini et al.[40] Line is fit using the relaxation spectrum shown in Figure 3.22.....92

Figure 3.22. Relaxation times spectrum for DGEBA monomer at 288 K – red and the  $\alpha$ -process for the EPON1009F-MDA – blue. The spectrum for DGEBA monomer (obtained from the analysis of the dielectric relaxation data of Casalini et al[40]) has been shifted vertically by 9.3 decades. ....92

Figure 3.23. (A)  $\log a_T$  vs temperature for DGEBA based systems: DGEBA monomer – blue squares, phenoxy – red plusses, EPON 1009F-MDA ( $\alpha$ +) – dark green plusses, EPON 1009F-MDA ( $\alpha$ ) – green plusses, EPON 825-MDA – black plusses, EPON 828-DDS – red circles, EPON 834-DDS – orange circles, EPON 1001F-DDS – green circles, EPON 1002F-DDS – cyan circles, EPON 1004F-DDS – blue circles, EPON 1007F-DDS – magenta circles, EPON 1009F-DDS –

black circles, DGEBA-DEA (Adolf et al[45]) – blue diamonds.  $T_{ref}$  is given in Table 4.2. (B) Materials for which only WLF parameters are available: DGEBA-DDM – solid green, DGEBA-25%DDM/75%AN – dashed green, DGEBA-HMDA – solid red, DGEBA-25%HMDA/75%HA – dashed red, DGEBA-IPD – solid black, DGEBA-30%IPD/70%TMCA – dashed black, Gerard et al[25]); EPON1001F-MA/DDS – solid blue (Plazek and Choy[32]). DGEBA monomer – blue squares and EPON 834-DDS – orange circles are shown for reference. ....94

Figure 3.24. Relaxation times spectra for DGEBA-MDA systems: DGEBA monomer – blue solid line, phenoxy – red dotted line; EPON 1009F-MDA ( $\alpha$ ) – dark green solid line; EPON 1009F-MDA ( $\alpha$ +) – light green solid line; EPON 825-MDA – black dotted line. ....96

Figure 3.25. Relaxation times spectra for DGEBA based polymers: phenoxy – red dotted line, EPON 825-MDA – black dotted line; solid lines: EPON 828-DDS – solid red line; EPON 834-DDS – solid orange line; EPON 1001F-DDS – solid green line; EPON 1002F-DDS – solid cyan line; EPON 1004F-DDS – solid blue line; EPON 1007F-DDS – solid magenta line; and EPON 1009F-DDS – solid grey line. ....97

Figure 3.26. Relaxation times spectra for: phenoxy – red dotted line; EPON 825-MDA – black dotted line; PS-3Armed – solid red line; PBd1 – solid orange line; PBd2 – solid green line; PPO – solid cyan line; DPPI-G5 – solid blue line; and PMMA-EGDMA – solid magenta line. ....98

Figure 3.27. Relaxation times spectra for: EPON 825-MDA – black dotted line; solid lines: DGEBA monomer – blue, EPON 1009F-MDA ( $\alpha$ ) – dark green, OS – red, OIB – cyan, O $\alpha$ MS – magenta. ....99

Figure 3.28. Relaxation times spectra for: EPON 1009F-MDA ( $\alpha$ ) – dark green, DGEBA monomer – blue, m-Toluidine1 – red, m-Toluidine2 – cyan, SB – orange. ....100

Figure 4.1. Predicted stress-strain behavior by Maxwell model (black line) compared to experimental data (blue line) obtained for a crosslinked DGEBA material at  $T_g - 16^\circ\text{C}$ . ....112

Figure 4.2. Predicted stress-strain behavior by a one-dimensional stress clock model (black line) compared to experimental data (blue line) obtained for a crosslinked DGEBA material at  $T_g - 16^\circ\text{C}$ . ....113

Figure 4.3. Predicted stress-strain behavior by a one-dimensional strain clock model (black line) compared to experimental data (blue line) obtained for a crosslinked DGEBA material at  $T_g - 16^\circ\text{C}$ . ....115

Figure 4.4. Left: Predicted stress-strain behavior by a one-dimensional internal variable history clock model (black line) compared to experimental data (blue line) obtained for a crosslinked DGEBA material at  $T_g - 16^\circ\text{C}$ . Right: Evolution of the internal variable S mobility with larger strain. The dashed line in both panels indicates the strain at yield. ....117

Figure 4.5. Left: Predicted stress-strain behavior by a one-dimensional internal variable history clock model at the following strain rates:  $1.1 \times 10^{-4}/\text{s}$  (black),  $5.5 \times 10^{-4}/\text{s}$  (brown),  $1.1 \times 10^{-3}/\text{s}$  (red). Right: Corresponding internal variable S mobility change with strain at the same strain rates. .119

Figure 4.6. Solution to Equation (4.6) which indicates how internal variable S mobility decreases with longer aging time. ....	120
Figure 4.7. Left: Predicted stress-strain behavior by a one-dimensional internal variable history clock model for quenched (black) and 30-min aged (red dashed) materials. Right: Corresponding internal variable S mobility change with strain. ....	120
Figure 4.8. Left: Stress-strain behavior of PMMA at $T_g - 15.8\text{ }^\circ\text{C}$ at a slow strain rate ( $8.3 \times 10^{-6}/\text{s}$ ) jumping to a fast strain rate ( $8.3 \times 10^{-4}/\text{s}$ ). Right: Stress-strain behaviors during a fast-to-slow strain rate switch experiment. [32] .....	122
Figure 4.9. Left: Predicted stress-strain behaviors by a one-dimensional internal variable history clock model for slow-to-fast (Upperleft) and fast-to-slow (Lowerleft) strain rate switch experiment. Right: Corresponding internal variable S mobility change with strain.....	123
Figure 4.10. Stress-strain behaviors of polycarbonate at $T_g - 123\text{ }^\circ\text{C}$ during 2 cycles of loading at $10^{-3}/\text{s}$ . [26] .....	124
Figure 4.11. Left: Predicted stress-strain behaviors for loading-unloading-reloading experiment. Right: Corresponding internal variable S mobility change with strain.....	125
Figure 4.12. Left: Predicted stress-strain behaviors for loading-unloading-reloading experiment with different unloading rates as follows: $10^{-3}/\text{s}$ (blue), $10^{-4}/\text{s}$ (cyan), $10^{-5}/\text{s}$ (magenta). Right: Corresponding internal variable S mobility change with strain.....	125
Figure 4.13. Stress-strain behaviors of a tBA-co-XLS polymer at $T_g - 16\text{ }^\circ\text{C}$ during 2 cycles of loading with different intermediate aging times. The polymer is tert-butyl acrylate (tBA), poly(ethylene glycol) dimethacrylate (PEGDMA) and di(ethylene glycol) dimethacrylate (DEGDMA) random copolymer network, with 10 wt% PEGDMA-DEGDMA (XLS) crosslink density. [33] .....	126
Figure 4.14. Stress-strain behaviors of polycarbonate at $T_g - 123\text{ }^\circ\text{C}$ during a 4-step loading-unloading-creep-reloading experiment where the creep stress is 1.2 MPa.....	127
Figure 4.15. Left: Predicted loading-unloading-creep-reloading stress-strain behaviors where the creep stress is 0.15 MPa. Right: Corresponding S mobility change with strain. ....	128
Figure 4.16. Stress-strain behaviors of polycarbonate at $T_g - 123\text{ }^\circ\text{C}$ during a 4-step loading-unloading-creep-reloading experiment where the creep stress is 59 MPa.....	129
Figure 4.17. Left: Predicted loading-unloading-creep-reloading stress-strain behaviors where the creep stress is 51.28 MPa. Right: Corresponding S mobility change with strain. ....	130
Figure 4.18. Stress-strain behaviors of polycarbonate at $T_g - 123\text{ }^\circ\text{C}$ during a 4-step loading-unloading-creep-reloading experiment where the creep stresses are 1.2, 42 and 59 MPa. ....	130
Figure 4.19. Left: Predicted loading-unloading-creep-reloading stress-strain behaviors where the creep stress is varied: 0.15 MPa (black), 30.31 MPa (dark green), 40.25 MPa (cyan), 46.73 MPa (magenta), and 51.28 MPa (grey). Right: Corresponding S mobility change with strain. ....	131
Figure 4.20. Machining of a stack of dogbone specimens.....	133

Figure 4.21. Instrument setup for the 4-step experiment consisting: (A) 1kN load cell, (B) crosshead that moves up and down with the upper grip, (C) thermal chamber, and (D) camera to track dots on the specimen for strain measurement. ....	134
Figure 4.22. Thermal history and mechanical inputs for each cycle of 5-step tensile test. During the test, temperature is kept at 85 °C ( $T_g - 13$ °C) while the mechanical stimuli at each step are illustrated as solid lines: (i) loading at 1 mm/min crosshead extension, (ii) unloading at -1 mm/min, (iii) creep at a constant force, (iv) reloading at 1 mm/min, and (v) unloading at -1 mm/min. Mechanical responses are schematically plotted as dotted lines. Residual extension after each test is removed by annealing the specimen at 140 °C ( $T_g + 38$ °C). ....	135
Figure 4.23. Temperature gradient inside the thermal chamber near grips and specimen. ....	136
Figure 4.24. Strain obtained by camera tracking five white dots located on the upper half of a strip EPON 1009f-MDA specimen during uniaxial tension at 85 °C ( $T_g - 17$ °C) at a constant overhead speed of 1 mm/min. The red line represents the strain defined by two dots nearest upper grip, while the cyan line is by two dots in the center part. The black line represents average strain of two segments in the middle as plotted in orange and green lines. ....	137
Figure 4.25. Stress-Strain behaviors of EPON 1009f-MDA strip bar and dogbone-shape specimens at 85 °C ( $T_g - 17$ °C) during uniaxial tension. Two repeats for each specimen are plotted. Crosshead speed input for all test is 1 mm/min, corresponding to a nominal strain rate of $1.67 \times 10^{-4}$ /s. Actual strain rates are given in Table 4.6. Black cross symbols indicate the maximum stress (yield stress $\sigma_Y$ ) during initial loading. ....	139
Figure 4.26. Scaled stress-strain behaviors of EPON 1009f-MDA bar specimen #1 at 85 °C ( $T_g - 17$ °C) during loading-unloading tensile tests. Before the test, specimen was aged inside Instron thermal chamber at 85 °C ( $T_g - 17$ °C) for a certain amount of time as labeled in figure. Thermal history for each test cycle is plotted in Figure 4.22. ....	142
Figure 4.27. Scaled stress-strain behaviors of EPON 1009f-MDA dogbone specimens at 85 °C ( $T_g - 17$ °C) during 4-step tensile experiments following the protocol in Figure 4.22. The creep time in step (iii) is given in figure legend. The creep force is 5N, corresponding to a nominal creep stress of 0.4 MPa. ....	143
Figure 4.28. Scaled stress-strain (left) and stress-time (right) behaviors of EPON 1009f-MDA dogbone specimens at 85 °C ( $T_g - 17$ °C) during 4-step tensile experiments following the protocol in Figure 4.22. The creep time in step (iii) is given in figure legend. The creep force is 180N, corresponding to a nominal creep stress of 15 MPa. ....	145
Figure 4.29. Scaled stress-strain behaviors of EPON 1009f-MDA dogbone specimens at 85 °C ( $T_g - 17$ °C) during 4-step tensile experiments following the protocol in Figure 4.22. The creep force in step (iii) is given in figure legend. The creep time is 8 min. ....	147
Figure 4.30. Scaled stress-strain behaviors of EPON 1009f-MDA dogbone specimens at 85 °C ( $T_g - 17$ °C) during 4-step tensile experiments following the protocol in Figure 4.22. The creep force in step (iii) is given in figure legend. The creep time is 3 min. ....	148

Figure 4.31. Stress overshoot during a second loading after creep or aging step compared across different datasets. Materials are all in glassy state but tested at different temperatures. ....149



## ABSTRACT

Linear viscoelastic behaviors for diglycidyl ether of bisphenol-A epoxy (DGEBA) resins cured with 4,4'-methylenedianiline (MDA) have been studied. For a particular DGEBA/MDA material with a glass transition temperature ( $T_g$ ) of 102 °C, dynamic shear moduli were measured from  $10^{-2}$  to  $10^{1.7}$  Hz for 41 temperatures between -150 °C and 180 °C. Because DGEBA/MDA epoxies are thermorheologically complex, construction of master curves via time-temperature superposition is not applicable. Stress relaxation experiments were performed from 90 °C to 112.5 °C using the same specimen. A combination of Fourier transformed transient data and dynamic data extended the frequency window of an isotherm to 6 orders of magnitude. A new methodology was developed for determining the relaxation spectrum, where the spectral density changes under the constraint that all spectral components have the same strength. This new method accommodates thermorheological complexity. The analysis was performed throughout the entire temperature range, including sub- $T_g$  low-temperature glassy state (i.e.,  $\gamma$  region), sub- $T_g$  "excess wing" (i.e.,  $\beta$  region), glass-to-rubber transition zone (i.e.,  $\alpha$  region), and above- $T_g$  plateau and terminal zones. In sub- $T_g$   $\gamma$  and  $\beta$  regions, dielectric relaxation data were analyzed using the same method.

Spectral analysis was applied to a variety of glassy-forming materials, including linear polymers, crosslinked polymers, oligomers and small molecules, with a focus on the relaxation processes in glass-to-rubber transition region (i.e., near and above  $\alpha$  region). Spectra were constructed from (i) experimental data of a series of linear and crosslinked DGEBA polymers with different crosslink densities, and (ii) digitized literature data consisting storage and loss isotherms near and above  $T_g$ . A second relaxation process was found at higher temperatures and longer relaxation times than the main  $\alpha$  peak, which is designated as the " $\alpha^+$ " process, where the molecular mechanism of  $\alpha^+$  is unknown. For molecular glass formers no  $\alpha^+$  process is observed. For other materials the  $\alpha^+$  process is present as a shoulder on  $\alpha$  peak.

In addition to temperature, deformation also affects mobility, where in the absence of deformation the mobility will decrease as the materials evolves towards the equilibrium state in a process called “physical aging”. Two major ideas how mobility is affected by deformation: rejuvenation and accelerated aging. In accelerated aging, the molecular mobility is decreased after deformation. In rejuvenation, the mobility will increase. To discriminate these two models, a set of 4-step non-linear tensile experiments were performed on a crosslinked DGEBA polymer at  $T_g - 16\text{ }^{\circ}\text{C}$ . The effect of deformation history was evaluated by comparing the mobility before and after the large deformation, where the mobility was quantified as the magnitude of stress overshoot on a stress-strain curve during reloading in the 4-step experiment. The experimental results at  $T_g - 16\text{ }^{\circ}\text{C}$  are predominantly due to aging effect but the aging is not accelerated by the presence of deformation history.

# 1. INTRODUCTION

Polymers are critical engineering materials widely used in a variety of applications ranging from electronics packaging to airplane composites. Despite the industrial significance, a fundamental understanding of the glassy state remains one of the outstanding problems in condensed matter physics.

Glassy state refers to amorphous solid state, while glass transition is the term to describe the process that an equilibrium liquid cools down at a sufficiently fast rate preventing crystallization and reaches the glassy state. The temperature at which glass transition happens is the glass transition temperature,  $T_g$ . Thermoplastic polymers are typically used below the material's  $T_g$ , where they are stiff in the glassy state. They are manufactured above  $T_g$  in the form of melt that more readily flows. During the glass transition, their mechanical properties (e.g., modulus) change by three orders of magnitude. Other material properties such as heat capacity  $c_p$ , dielectric permittivity  $\epsilon$ , magnetic susceptibility  $\chi$ , also change sharply during glass transition. Although detected in different ways, these material properties are all correlated and governed by the same underlying physical mechanism.

The key concept that relates all signature behaviors of glasses is “molecular mobility”, which refers to the rate at which the material is capable of relaxing or responding to external stimulus. The glassy state is a non-equilibrium state that exhibits physical aging where molecular mobility constantly decreases. The mobility depends on temperature and deformation histories. The glassy state can be entered/exited isotropically via cooling/heating or pressurizing/depressurizing.[1] Glassy state can also be exited by applying large anisotropic deformation, where mobility of the material increases dramatically with deformation.[2, 3] The emphasis of this dissertation is to study how mobility is affected by temperature and deformation history.

Experimentally, molecular mobility can be directly detected by photobleaching of a dye molecule[2-6], and/or spectroscopic methods such as dielectric relaxation[7, 8], nuclear magnetic resonance [9], light scattering[10, 11]. These techniques use a molecular-size probe to measure the property changes with frequency to identify relaxation processes.

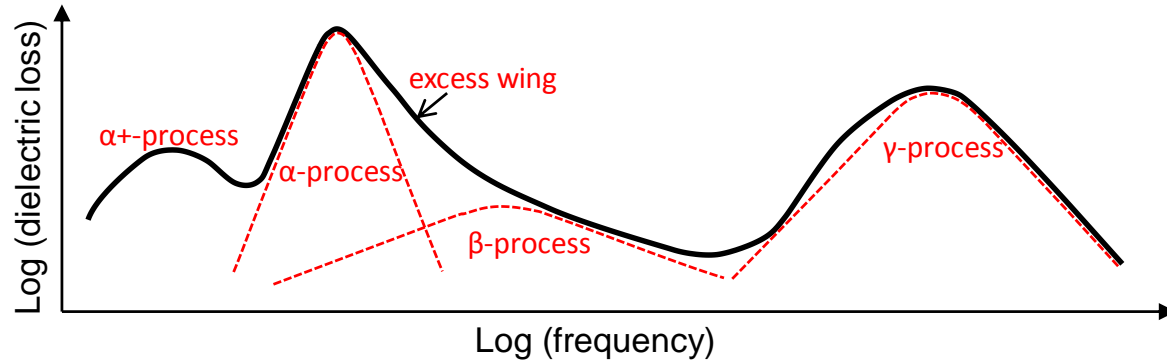


Figure 1.1. Schematic relaxation spectrum of a glassy material near  $T_g$ .

A typical dielectric loss relaxation spectrum is shown in Figure 1.1, where relaxation processes manifest as peaks, shoulders, and plateaus. The highest peak is called “ $\alpha$  relaxation” and is associated with glass transition mechanism. The processes at lower frequencies than  $\alpha$  peak are “ $\alpha+$  relaxations” which will be discussed in Chapter 3. Next to the main  $\alpha$  peak at higher frequencies is a shoulder designated as “ $\beta$  relaxation” or the “excess wing” that manifests as a slowly decaying, broad peak. At higher frequencies there are  $\gamma$  relaxations, where the molecular mechanisms of these peaks are not fully understood.[12] Each relaxation process is characterized by its peak location on frequency axis, or  $\log\tau$ . Since the same relaxation process can show up at different temperatures with different  $\log\tau$ , the temperature dependence of  $\log\tau$  mobility is studied based on a sequence of frequency scans at isothermal conditions.

The second type of experiments are on a macroscopic level and are indirectly probing molecular mobility, such as enthalpy relaxation [13], volume relaxation [14-16], stress relaxation [17], dynamic mechanical analysis[18], all within linear viscoelastic region where the input is a small perturbation that does not change the current state of mobility. These methods also measure the time- or frequency-dependent properties under isothermal conditions. A practical way of extracting loga mobility has been predominantly used in literature, where isotherms were shifted along time or frequency axis to partially overlap with other isotherms and stitched into “master curves”. This method is called “time-temperature superposition”, which is only applicable when the material is thermorheologically simple. For polymers above their  $T_g$ , thermorheological simplicity is a good assumption since molecular motions above  $T_g$  can be explained by the same

underlying physics, i.e., the “spring-and-bead” Rouse model. In the above- $T_g$  region, different relaxation processes are associated to different modes of Rouse solution to the same equation, therefore different processes have the same temperature dependence and the bulk behaviors are time-temperature invariant. However, near and below  $T_g$  polymers are thermorheologically complex which precludes the traditional superposition method. A new method that does not require superposition to probe the temperature dependence of mobility will be demonstrated in Chapter 2 with a dynamic mechanical dataset. This new method will use each pair of storage and loss shear and dielectric isotherms to determine relaxation spectrum based on the generalized Maxwell model.

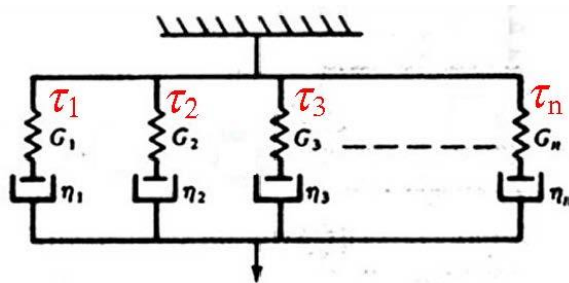


Figure 1.2. Generalized Maxwell model.

An analogy of the generalized Maxwell model is illustrated in Figure 1.2, where  $n$  Maxwell elements are connected in parallel to describe relaxation behaviors in linear viscoelastic regions for a given temperature.[19] Each Maxwell element is characterized by a relaxation time  $\tau_i$  assuming the relaxation behaviors have a distribution over the entire time range. If the relaxation time  $\tau_i$  is uniformly spaced over the entire time range, contribution of each Maxwell element to the entire relaxation process is demonstrated as a relaxation spectrum. The uniform spacing assumption of relaxation time axis is also revisited in the new method as described in Chapter 2, where the temperature dependence of  $\log \tau$  mobility is extracted from the new spectrum. Using the spectrum method, a variety of glass-forming materials will be investigated in Chapter 3, where materials of different chemical structures are compared with a focus on mobility change in glass-to-rubber transition region. The dataset consists of all types of glass-forming materials with the knowledge that glass transition is a fundamental signature that should be explained by the same underlying mechanism for polymeric and molecular glasses.

A third type of experiments uses non-linear stimuli to investigate how mobility is affected by external conditions, i.e., temperature, deformation and thermal and deformational histories. Constitutive models have been proposed to describe the temperature and deformation dependences reflected in various thermo-mechanical experiments. A list of experimental signatures that should be addressed by constitutive models includes but is not limited to:

- Pressure-volume-temperature (PVT) behavior studied in dilatometer where specific volume of a glass-forming material depends on both temperature and pressure. Practically,  $T_g$ , coefficient of thermal expansion, and bulk modulus increase with higher formation pressure.
- Nonlinear volume relaxation which measures the change of specific volume in response to a sudden jump in temperature. More interestingly, if there are multiple steps of temperature change, the response will also be dependent on the thermal history in addition to the current temperature.
- Nonlinear enthalpy relaxation where enthalpy or heat capacity response is measured after a change in temperature. Again, thermal history is a key factor that will affect current enthalpy behaviors. For example, an overshoot of heat capacity in DSC temperature scan will increase with more sub- $T_g$  annealing time or slower cooling rate, while an undershoot has also been observed for a hyper-quenched glass (i.e., cooled into glassy state at  $10^6$  °C/s).
- Nonlinear stress relaxation where the stress changes with time after a sudden change of strain.
- Nonlinear stress-strain behaviors during a constant strain rate experiment, where many discriminative signatures can be observed, such as post-yield softening, and are affected by thermal and deformation histories. A complete analysis of stress-strain behaviors using mobility-based models will be given in Chapter 4.
- Nonlinear creep experiment, where stress is constant and strain behaviors are analyzed, with a focus on the tertiary creep where the strain rate accelerates and is correlated to the post-yield softening region on a stress-strain curve.

Evaluation of constitutive models will require datasets that encompass a wide range of nonlinear behaviors. Specifically, a critical set of experiments has been proposed to test two contradictory ideas in literature as to whether mobility will increase or decrease after removal of a large deformation compared to the initial state.

The “rejuvenation” assumption says a large deformation pulse will cause an increase in mobility and a reverse of the physical aging process, i.e., the material is more like a freshly quenched glass after being deformed.[20] The rejuvenation idea was first experimentally demonstrated by Struik when he performed cyclic creep experiment on PVC at  $T_g - 60\text{ }^\circ\text{C}$ .[21] The specimen was imposed to a large-stress (29.45 MPa) creep pulse in between 6 cycles of small-stress (2.95 MPa) probing creeps. The compliance (indicator of mobility) right after the large-stress pulse significantly increases and then gradually decrease in the subsequent cyclic probing creeps. The effect of the large deformation is an increase of mobility although the material is experiencing aging where mobility decreases. Large deformation has a counter effect to aging as if the material is rejuvenated.

On the other hand, a completely opposite assumption “accelerated aging” has also been proposed and also experimentally proved that external deformation can accelerate the aging process. Sternstein used three PMMA specimens to show the effect of deformation.[22] One specimen was slowly cooled from  $T_g + 20\text{ }^\circ\text{C}$  to  $T_g - 90\text{ }^\circ\text{C}$  and has the lowest mobility. A second specimen was quenched to  $T_g - 90\text{ }^\circ\text{C}$  possessing a high mobility. The second specimen experienced 900 min of aging at  $T_g - 90\text{ }^\circ\text{C}$  before four cycles of stress relaxation at 0.5% strain. The mobility is decreasing in each cycle and approaching the mobility of the slowly cooled specimen. The total time of mechanical experiment is 6000 min. The third specimen was also quenched along with the second specimen, but aged at  $T_g - 90\text{ }^\circ\text{C}$  for 9000 min before being deformed to 0.5%. It has been found that the mobility of the third specimen after 9000 min of aging is similar to the second specimen after 900 min of aging. The conclusion is that, (i) 9000 min vs. 900 min physical aging at  $T_g - 90\text{ }^\circ\text{C}$  has no measurable difference, and (ii) stress relaxation at 0.5% strain is more effective than solely time to push the glassy material towards an equilibrium state. In this case, the exposure to mechanical stimuli (such as the 0.5% strain deformation) accelerated the physical aging process and supported the “accelerated aging” assumption.

Whether the effect of deformation history is “rejuvenation” or “accelerated aging” actually depends on the current mobility and the magnitude of deformation.[23] Experiments consisting multiple steps of deformation are necessary to differentiate the conditions at which aging will be accelerated or decelerated.[24] In Chapter 4, a set of multi-step experiments will be described where the effect of a creep deformation history will be examined by comparing the stress-strain behaviors before and after this creep step.

## 1.1 References

1. Colucci, D.M., et al., *Isochoric and isobaric glass formation: Similarities and differences*. Journal of Polymer Science Part B: Polymer Physics, 1997. **35**(10): p. 1561-1573.
2. Bending, B., et al., *Measurement of segmental mobility during constant strain rate deformation of a poly (methyl methacrylate) glass*. Macromolecules, 2014. **47**(2): p. 800-806.
3. Lee, H.-N., et al., *Deformation-induced mobility in polymer glasses during multistep creep experiments and simulations*. Macromolecules, 2009. **42**(12): p. 4328-4336.
4. Lee, H.-N., et al., *Direct measurement of molecular mobility in actively deformed polymer glasses*. Science, 2009. **323**(5911): p. 231-234.
5. Bending, B. and M. Ediger, *Comparison of mechanical and molecular measures of mobility during constant strain rate deformation of a PMMA glass*. Journal of Polymer Science Part B: Polymer Physics, 2016. **54**(19): p. 1957-1967.
6. Lee, H.-N., et al., *Dye reorientation as a probe of stress-induced mobility in polymer glasses*. The Journal of chemical physics, 2008. **128**(13): p. 134902.
7. Stickel, F., E.W. Fischer, and R. Richert, *Dynamics of glass-forming liquids. I. Temperature-derivative analysis of dielectric relaxation data*. The Journal of chemical physics, 1995. **102**(15): p. 6251-6257.
8. Schneider, U., et al., *Dielectric and far-infrared spectroscopy of glycerol*. Journal of non-crystalline solids, 1998. **235**: p. 173-179.
9. Kruk, D., A. Herrmann, and E. Rössler, *Field-cycling NMR relaxometry of viscous liquids and polymers*. Progress in nuclear magnetic resonance spectroscopy, 2012. **63**: p. 33-64.
10. Du, W., et al., *Light-scattering study of the liquid-glass transition in propylene carbonate*. Physical Review E, 1994. **49**(3): p. 2192.
11. Sokolov, A., et al., *Comparison of Raman-and neutron-scattering data for glass-forming systems*. Physical Review B, 1995. **52**(14): p. R9815.
12. Angell, C.A., et al., *Relaxation in glassforming liquids and amorphous solids*. Journal of applied physics, 2000. **88**(6): p. 3113-3157.



13. Hodge, I.M., *Enthalpy relaxation and recovery in amorphous materials*. Journal of Non-Crystalline Solids, 1994. **169**(3): p. 211-266.
14. Kovacs, A.J., et al., *Isobaric volume and enthalpy recovery of glasses. II. A transparent multiparameter theory*. Journal of Polymer Science: Polymer Physics Edition, 1979. **17**(7): p. 1097-1162.
15. Kovacs, A.J., *Transition vitreuse dans les polymères amorphes. Etude phénoménologique*, in *Fortschritte der hochpolymeren-forschung*. 1964, Springer. p. 394-507.
16. Bero, C.A. and D.J. Plazek, *Volume-dependent rate processes in an epoxy resin*. Journal of Polymer Science Part B: Polymer Physics, 1991. **29**(1): p. 39-47.
17. Colucci, D., P. O'Connell, and G. McKenna, *Stress relaxation experiments in polycarbonate: a comparison of volume changes for two commercial grades*. Polymer Engineering & Science, 1997. **37**(9): p. 1469-1474.
18. Kovacs, A., R.A. Stratton, and J.D. Ferry, *Dynamic mechanical properties of polyvinyl acetate in shear in the glass transition temperature range*. The Journal of Physical Chemistry, 1963. **67**(1): p. 152-161.
19. Ferry, J.D., *Viscoelastic properties of polymers*. 1980: John Wiley & Sons.
20. Struik, L., *The mechanical enhancement of physical aging*. Polymer, 1980. **21**(8): p. 962-967.
21. Struik, L.C.E., *Physical aging in amorphous polymers and other materials*. 1977.
22. FA, M., C. FC, and S. SS, *Mechanically Enhanced Aging of Glassy Polymers*. 1976.
23. McKenna, G.B., *Mechanical rejuvenation in polymer glasses: fact or fallacy?* Journal of Physics: Condensed Matter, 2003. **15**(11): p. S737.
24. Dreistadt, C., et al., *Experimental study of the polycarbonate behaviour during complex loadings and comparison with the Boyce, Parks and Argon model predictions*. Materials & Design, 2009. **30**(8): p. 3126-3140.

## 2. RETHINKING THE ANALYSIS OF THE LINEAR VISCOELASTIC BEHAVIOR OF AN EPOXY POLYMER NEAR AND ABOVE THE GLASS TRANSITION

This chapter contains publication in press. It is reproduced from *Macromolecules*, 2020, DOI: 10.1021/acs.macromol.9b02634; Copyright © 2020, American Chemical Society. In this paper, I synthesized EPON 1009F-MDA specimen and performed Dynamic Mechanical Analysis. Hosup Song performed stress relaxation experiment. Daniel A. Wilcox performed dielectric experiments. Grigori A. Medvedev performed the non-uniformly spaced relaxation spectrum method.

Relaxation processes in polymers are characterized by the relaxation spectra that is determined from linear viscoelastic master curves constructed via time-temperature superposition. However, if the linear viscoelastic isotherms have sufficient time/frequency width, thermo-rheological complexity emerges, which precludes construction of a master curve and thus determination of the relaxation spectra via traditional methods. In this communication we propose a different approach for analyzing linear viscoelastic relaxation data. The linear viscoelastic behavior was evaluated for a diglycidyl ether of bisphenol-A epoxy cured with 4,4'-methylenedianiline with a glass transition temperature ( $T_g$ ) of 101.5°C. The dynamic storage and loss moduli were measured from  $10^{-2}$  to  $10^{1.7}$  Hz for 19 temperatures between 90°C and 180°C. The experimental window was extended using stress relaxation experiments for up to 8h at the same temperatures between 90°C and 112.5°C where the dynamic experiments were performed. The stress relaxation data were converted to the dynamic response, where the composite dynamic response now extends over nearly six logarithmic decades. The  $G'$  and  $G''$  response for this single-phase polymer is thermo-rheologically complex, thus precluding construction of master curves via time-temperature superposition. The traditional method of determining relaxation spectra implicitly assumes a constant spectral density, where the spectral strength is a function of the relaxation time. An alternative approach is to assume that individual spectral contributions have a constant height where the spectral density changes. This alternative approach is in better agreement with the physics of dielectric relaxation and readily accounts for thermo-rheological complexity. A methodology for determining the spectral density from the individual isotherms has been developed and applied to the epoxy dynamic data. A relaxation map of how the individual

relaxation times change with temperature was developed. The implications for using this new methodology for the analysis of the linear viscoelastic properties of polymers are discussed.

## 2.1 Introduction

The analyses of linear viscoelastic data is a key method employed in polymer science to probe the dynamics of the relaxation processes. Specifically, dynamic or transient data are collected over a convenient experimental window that extends between two to four logarithmic decades; subsequently, the isotherms are typically shifted along the  $\log(\text{time})$  or  $\log(\text{frequency})$  axis using time-temperature superposition<sup>1</sup> to construct a master curve (at least for single phase polymers where a single relaxation mechanism is expected). The implicit assumption of time-temperature superposition is that all relaxation processes are identically affected by temperature, (i.e., the material is thermo-rheologically simple). In fact, the process of using time-temperature superposition to construct master curves with extremely wide time (or frequency) ranges is a well-established procedure that is described in almost every polymer science and engineering textbook. However, there is evidence that linear viscoelastic isotherms do not exactly superpose,<sup>2-12</sup> although the mismatch between neighboring isotherms is often small – in part because the experimental window that is available in mechanical experiments is limited. Therefore, there is a critical need to evaluate the appropriateness of this oft-implemented method in many practical polymer science methodology.

Dielectric relaxation experiments probe a much wider experimental window – up to eight logarithmic decades or more using broadband dielectric methods. The dielectric data show significant lack of superposition,<sup>13-16</sup> (i.e., the response is clearly thermo-rheologically complex even for single phase polymers). The typical method of analysis involves fitting the data to the sum of two or more empirical functions like Kohlrausch-Williams-Watts (KWW), Cole-Cole, or Havriliak-Negami.<sup>17-20</sup> In these situations, the presence of multiple relaxation processes is not unreasonable; thus, the need to use multiple relaxation functions is not in itself a problem. However, when multiple isotherms are fit with these functions, the parameters in the individual relaxation function change with temperature, often in a complicated, non-monotonic manner. The need for multiple empirical relaxation functions each with multiple parameters that change with

temperature demonstrates that this fitting approach is just a parameterization of the data. Moreover, empirical fitting does not provide insights that are translatable across different polymer chemistries, which limits the molecular-level picture painted by these types of parameterization strategies.

The transient and dynamic relaxation behaviors (both linear viscoelastic and dielectric) are also analyzed in terms of relaxation spectra, where if the experimental data are thermo-rheologically complex the shape of the spectra change with temperature. Implicit in this traditional method of analysis is the assumption of constant spectral density (or, equivalently, constant spectral spacing for a discrete spectral representation). This implies that with change in temperature a given spectral contribution will change both its location on the time/frequency axis and its strength. However, the change in spectral strength with temperature is problematic, especially for the dielectric response. Specifically, the relaxation time associated with a given molecular dipole will obviously change with temperature, but temperature will only have a minor effect on the strength of a dipole that is controlled primarily by partial charge separation.<sup>21</sup> Thus, the significant change in spectral intensity that is required when one fits the typical data is *aphysical*. To the extent that via linear response theory<sup>22</sup> both dielectric relaxation and linear viscoelastic mechanical relaxation probe the underlying molecular dynamics of the polymer, the aforementioned difficulties with the traditional analysis of the dielectric response will also be present in the analysis of the linear viscoelastic response.

The objective of this effort is two-fold. First, we develop a new method for analyzing thermo-rheologically complex data that does not make the assumption of constant spectral density with the consequence that the spectral strength undergoes significant changes with temperature. Second, this method is applied to a typical crosslinked epoxy resin. Linear viscoelastic dynamic mechanical and stress relaxation data of the epoxy system are measured from just below the glass transition temperature ( $T_g$ ) to  $T_g+78.5^\circ\text{C}$ , which is the temperature where oxidative degradation begins to affect the mechanical response for this material. Thus, this paper probes the alpha response associated with the glass transition as well as network relaxation processes that occur at longer times and higher temperatures.

The material to be examined in this communication is a typical diepoxide resin cured with a diamine. There is a large literature on the linear viscoelastic behavior of epoxy resins, where for the majority of this literature a dynamic property like the in-phase or out-of-phase shear modulus at one frequency is measured as a function of temperature. Because these data are at only one frequency, they do not directly probe the viscoelastic relaxation process; thus, we will not attempt to review this aspect of the literature. There have been several studies of the viscoelastic and dielectric response of epoxy resin based systems.<sup>5, 23-25</sup> Plazek and coworkers studied the effect of crosslink density of diglycidyl ether of bisphenol A (DGEBA) in creep and creep recovery, where they observed the increase in the intensity of the relaxation process as times longer than the main alpha transition with decreasing crosslink density.<sup>26-27</sup>

The chapter will be organized as follows: (i) the experimental methods and material preparation will be described in the next section, (ii) next the dynamic mechanical behavior of the epoxy resin will be reported, (iii) subsequently the new analysis method for a thermo-rheologically complex material will be developed and applied to the data from the epoxy resin and (iv) finally the implications of the new methodology for analyzing the linear viscoelastic response of polymers will be discussed.

## **2.2 Experimental**

### **2.2.1 Dynamic Mechanical Experiments**

Epoxy test specimens were prepared from a diglycidyl ether of bisphenol-A (DGEBA) with an epoxide equivalent of 2786 g/mole (EPON Resin 1009F, Hexion Inc.) that was cured with a stoichiometric amount of 4,4'-methylenedianiline, MDA, (Sigma-Aldrich). Sheets of the Epon1009F-MDA were made by the following procedure: First, degassed Epon1009F resin was mixed with MDA at 200°C using a mechanical stirrer. The mixture was then transferred into a preheated 4 in × 4 in metal mold. The material in the mold was cured in Carver Model 3889 heat press at 150°C for 0.5 h under 1250 lbs pressure. Finally, the material was post-cured in the mold at 130°C for 10 h at an applied pressure of 1250 psi. Using a Q2000 DSC (TA Instruments) at a heating rate of 10°C·min<sup>-1</sup> the T<sub>g</sub> of the cured Epon1009F-MDA material was determined to be

101.5±1°C When comparing different sheets of the Epon1009F-MDA system, variations in  $T_g$  of ±1.5°C were observed due to variation in the synthesis and/or manufacturing process. Epon1009F-MDA sheets with a uniform thickness of 4 mm were cut into 12 mm wide strips using a surface grinder with a diamond cutoff wheel. The dimensions of the test rectangular specimen used in the dynamic mechanical experiments were 40 mm × 11.74 mm × 4.06 mm, where the final length of the test specimen was measured as the distance between instrument grips.

Test specimens for the dynamic mechanical experiments were annealed at 160°C for 8 h in a vacuum oven at 30 torr in order to remove residual moisture. The specimens were then quenched to room temperature from 160°C. After cooling to room temperature, all of the specimens were stored in an airtight bag filled with a desiccant at room temperature until mounted in the rheometer.

The dynamic mechanical response was determined using an ARES-G2 rheometer (TA Instruments) from  $10^{-2}$  Hz to  $10^{+1.7}$  Hz (inertial effects dominate the response at higher frequencies; thus, measurements at frequencies greater than  $10^{+1.7}$  Hz were not used) with five frequencies per logarithmic decade. The specimen was mounted in the rheometer at room temperature (i.e., 78°C below  $T_g$ ) and then cooled to −150°C for the first frequency scan experiment. Then the temperature was increased in discrete steps until it reached 180°C. The specimen was annealed for 15 to 90 minutes at each temperature prior to beginning the dynamic measurements to eliminate any transient relaxation. The annealing time was adjusted so that  $\tan\delta$  response at 1 Hz, which was continuously monitored during annealing, became constant. After annealing at a given temperature, a frequency sweep was applied starting at the lowest frequency of  $10^{-2}$  Hz and continuing to the highest frequency of  $10^{+2}$  Hz. For the lowest frequencies of  $10^{-2}$  to 2 Hz 10 cycles were used to determine the storage and loss moduli, and for frequencies higher than 2 Hz 15 to 250 cycles were used. The temperature was then increased to the next test temperature and the procedure was repeated as described above, including the annealing and the frequency scan steps. Strain magnitudes of 0.01% to 1% were applied depending on the temperature. Linearity was assured by observing that the same moduli responses were obtained during a second frequency sweep with twice the strain. At temperatures above room temperature, the thermal chamber was continually purged with dry nitrogen gas in order (i) to avoid moisture intake and (ii) to prevent oxidative degradation especially at temperatures above 120°C.

### 2.2.2 Stress Relaxation Experiments

At selected temperatures from 90°C to 112.5°C stress relaxation experiment were performed for up to 8 h in the ARES-G2 rheometer using a torsion bar specimen with the same dimensions as in the dynamic test. Since it was impractical to reproduce the entire thermal history of the dynamic experiment from –150°C prior to each of the stress relaxation experiments, the stress relaxation specimen was placed in the rheometer grips at room temperature, heated to 90°C and then annealed at that temperature for 3 h. The applied strain in the stress relaxation experiments was adjusted from 0.0125% at 90°C to 3% at 112.5°C to maximize the stress signal, but where the response still remained in the linear regime.

### 2.2.3 Dielectric Experiments

A sheet of Epon1009-MDA with a uniform thickness of 1.83 mm was prepared following the procedure described above. The sheet was annealed at 130°C for 1.5 h in a vacuum oven at 80 Torr to remove residual moisture, and thereafter stored in an airtight bag filled with desiccant. This sheet was transferred to a thermal evaporator where a uniform 60 nm layer of gold was deposited on both sides of the sheet. Then the gold-coated sheet was (i) placed on a metal block heated to 130°C (i.e.  $T_g + 28^\circ\text{C}$ ) on a laboratory press; (ii) a 30 mm diameter circular die that was also heated to 130°C was placed on the specimen; and (iii) the die was pushed through the gold coated Epon1009-MDA specimen using a small hydraulic press. The gold coated sample was then annealed once more at 130°C for 1.5 h in a vacuum oven at 80 Torr before being returned to storage under a moisture-free atmosphere.

The gold-coated circular specimens were loaded into a Concept 40 Novocontrol dielectric spectrometer. The sample in the Novocontrol spectrometer was kept under a nitrogen blanket to ensure that there was no moisture absorption. The dielectric measurements started at –150 °C and carried out in discrete temperature steps until 180°C. The dielectric response for the temperatures from  $T_g$  and above (which is the focus of this paper) were compromised by the presence of parasitic losses like conduction and electrode polarization, where it was not possible to obtain robust determination of the underlying dynamic dielectric material response (see SI for additional details). This is unfortunate, because broadband dielectric measurement would significantly extend the

frequency range from that available mechanically. The origin of the extraneous dielectric loss mechanisms is unknown, where it could be from very small amounts of ionic impurities in the resin, interactions between the epoxy resin and the electrode or just an inherent feature of the particular epoxy resin chemistry being studied.

### 2.3 Experimental Results

The linear viscoelastic  $G'$  and  $G''$  data for the 1009-MDA system are shown in Figure 2.1 for frequencies from  $10^{-2}$  to  $10^{+1.7}$  Hz. The high temperature data from 120°C to 180°C are shown in the Figure 2.1A-B and the low temperature data from 90°C to 120°C are shown separately in Figure 2.1C-D. The DSC  $T_g$  for this material is 101.5°C. The data in Figure 2.1A-B and Figure 2.1C-D were shifted along the log frequency axis to effect the best superposition possible, where the 120°C isotherms were chosen as reference; however, exact superposition was not possible for all isotherms. If full superposition was not possible the isotherms were shifted so that the data had maximum overlap.

The resulting master curves constructed using 120°C to 180°C isotherms are shown in Figure 2.2A-B and master curve constructed using the lower temperature 90°C to 120°C isotherms are shown in Figure 2.2C-D. Figure 2.2E-F is an expanded view of the upper right corner of Figure 2.2C-D. The associated  $\log a_T$  shift function is shown in Figure 2.3, where the reference temperature is 120°C.



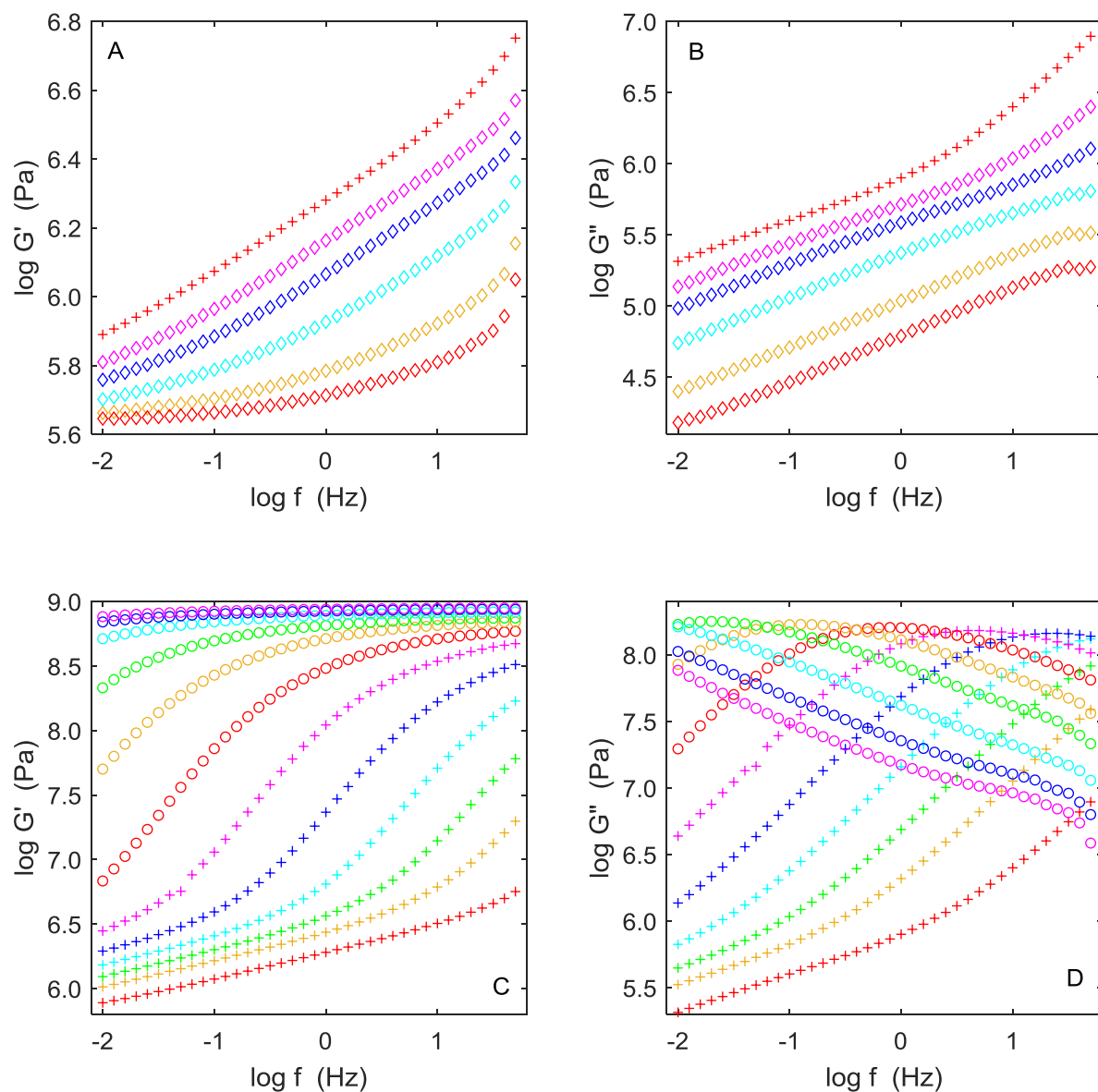


Figure 2.1. Linear viscoelastic storage (A and C) and loss (B and D) shear moduli isotherms vs frequency for Epon1009 epoxy resin cured with MDA at the following temperatures: 180°C – red diamonds, 160°C – orange diamonds, 140°C – cyan diamonds, 130°C – blue diamonds, 125°C – magenta diamonds, 120°C – red pluses, 115°C – orange pluses, 112.5°C – green pluses, 110°C – cyan pluses, 107.5°C – blue pluses, 105°C – magenta pluses, 102.5°C – red circles, 100°C – orange circles, 97.5°C – green circles, 95°C – cyan circles, 92.5°C – blue circles, 90°C – magenta circles.

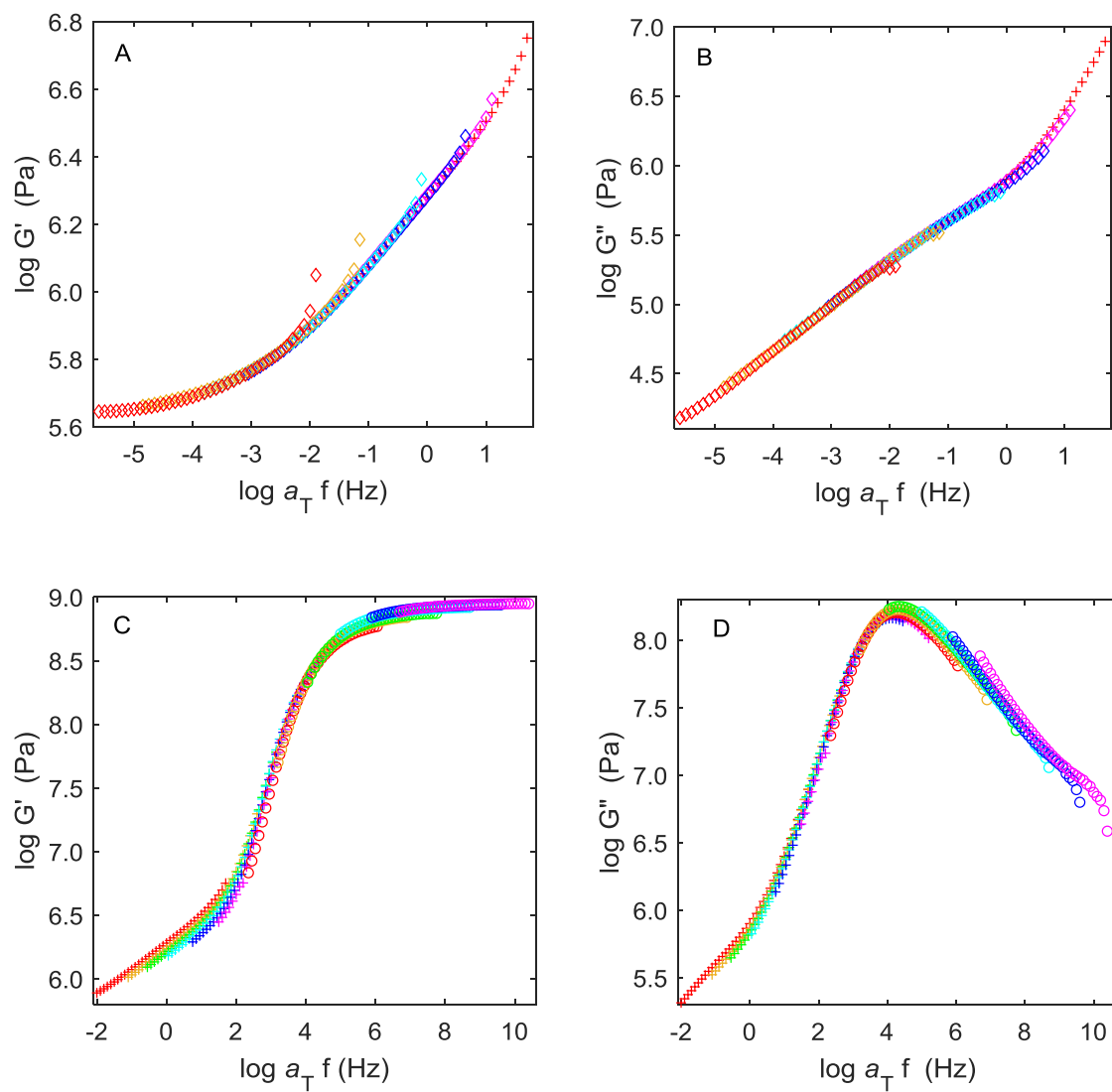
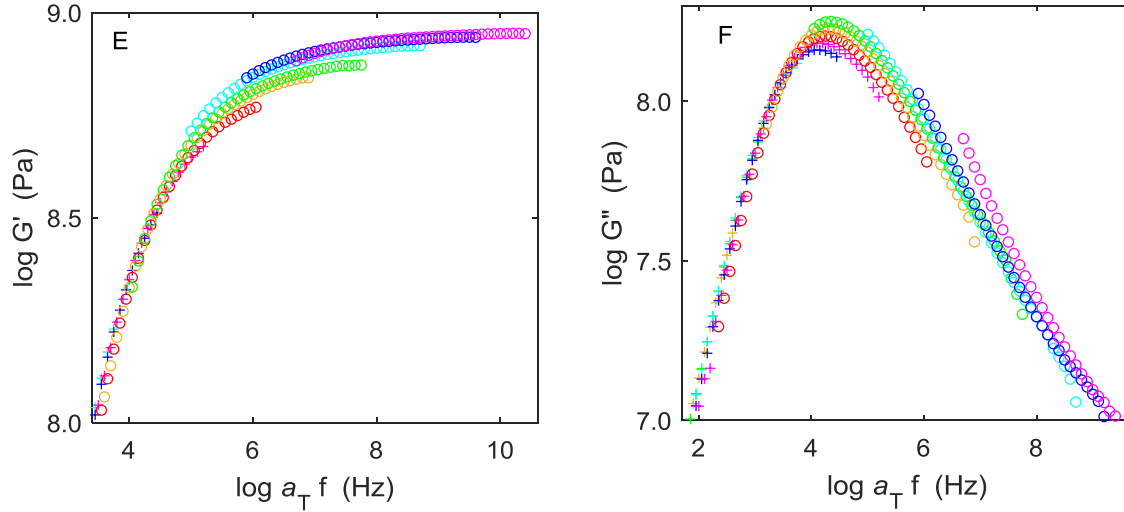


Figure 2.2. The Epon1009-MDA epoxy storage and loss master curves from time-temperature superposition of the isothermal data shown in Figure 2.1, using the  $\log a_T$  shift function shown in Figure 2.3. Symbols have same meaning as in Figure 2.1. Panels A and B display the approximate master curves from the high temperature isotherms of Figure 2.1A and B; panels C and D display the approximate master curves from the lower temperature isotherms of Figure 2.1C and D; panels E and F are expanded views of C and D, respectively.

Figure 2.2 continued



Examining the approximate master curves in Figure 2.2 it is clear that this epoxy material is thermo-rheologically complex, especially in the vicinity of the glass transition temperature. First, in Figure 2.2A and B the low frequency relaxation process appears to be nearly thermo-rheologically simple as the superposition of the storage and loss isotherms is apparently successful for the temperatures above 130°C (i.e.,  $T_g + 28.5^\circ\text{C}$ ), which we designate as the  $\alpha^+$ -process. However, even for the  $\alpha^+$ -process there is not a perfect superposition. One could perhaps ascribe this discrepancies to experimental problems; however, as shown in Figure 2.2A the shifted 180°C  $G'$  data (red diamonds) curvature is inconsistent with the master curve for all frequencies – similar curvature is also present in the other isotherms although not as readily apparent as for 180°C isotherm. Second, the high frequency  $\alpha$ -process associated with the glass transition shown in Figure 2.2C-D exhibits lack of superposition at both low frequencies, i.e. for  $\log(a_T f)$  values from  $-2$  to  $2$ , and at higher frequencies, i.e. for  $\log(a_T f)$  values from  $4$  to  $10$ . This lack of superposition is clearly shown in Figure 2.2E-F, where the significant change in the peak maximum precludes any superposition.

Sometimes practitioners in the field apply arbitrary vertical shifts in addition to the horizontal shifts along the  $\log f$  axis. However, there is no justification for this procedure other than a desire to preserve time-temperature superposition with its implicit assumption that all relaxation

processes are affected equally by temperature. However, there is no physical reason for applying a vertical shift in the glass transition region.

In Figure 2.3 the  $\log a_T$  shift function is shown for the approximate superposition of the dynamic data shown in Figure 2.2. There is a change in the slope in the  $\log a_T$  vs  $1/T$  plot in the vicinity of 120°C indicating a transition from the  $\alpha^+$ -dominated response (shown as blue circles) to the  $\alpha$ -dominated response (shown as magenta circles).

In order to extend the time scale of the viscoelastic response, linear stress relaxation experiments were performed at the same temperatures at which the dynamic data were collected. The stress relaxation isotherms are shown in Figure 2.4. Time-temperature superposition was attempted (Figure 2.5), where overlap between neighboring isotherms was maximized for the intermediate times. There is systematic lack of superposition of the long time tails for all isotherms. The lack of superposition decreases (but is still present) at higher temperatures. This observation is consistent with the dynamic data where superposition was better, but not perfect, at higher temperatures where the  $\alpha^+$ -process is the dominant relaxation mechanism. The  $\log a_T$  shifts for the stress relaxation data are shown in Figure 2.3. The temperature dependence of  $\log a_T$  shift for the stress relaxation data is compared to that determined from the dynamic experiments, where there is an agreement within the uncertainty of the superposition procedures. The overall lack of time-temperature superposition of the  $G(t)$  isotherms is consistent with the lack of superposition of the  $G'$  and  $G''$  isotherms.

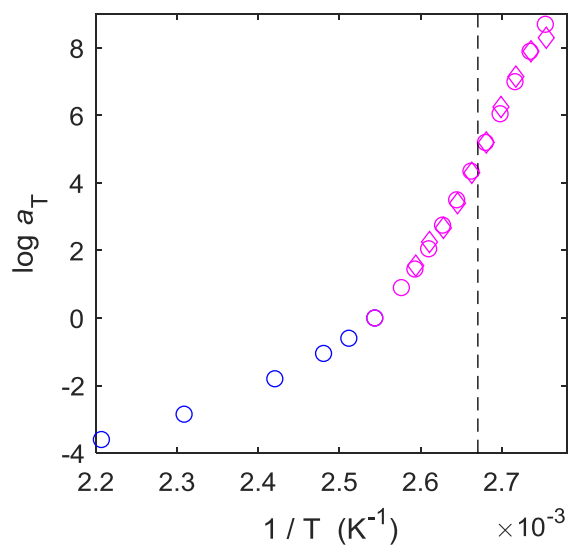


Figure 2.3. Temperature dependence of the time-temperature shift function for approximate superposition of (i) the dynamic  $G'$  and  $G''$  isotherms shown in Figure 2.2A-B (blue circles) and Figure 2.2C-D (magenta circles) and (ii) the  $G(t)$  stress relaxation isotherms shown in Figure 2.5 (magenta diamonds). The dashed line indicates  $T_g$ .

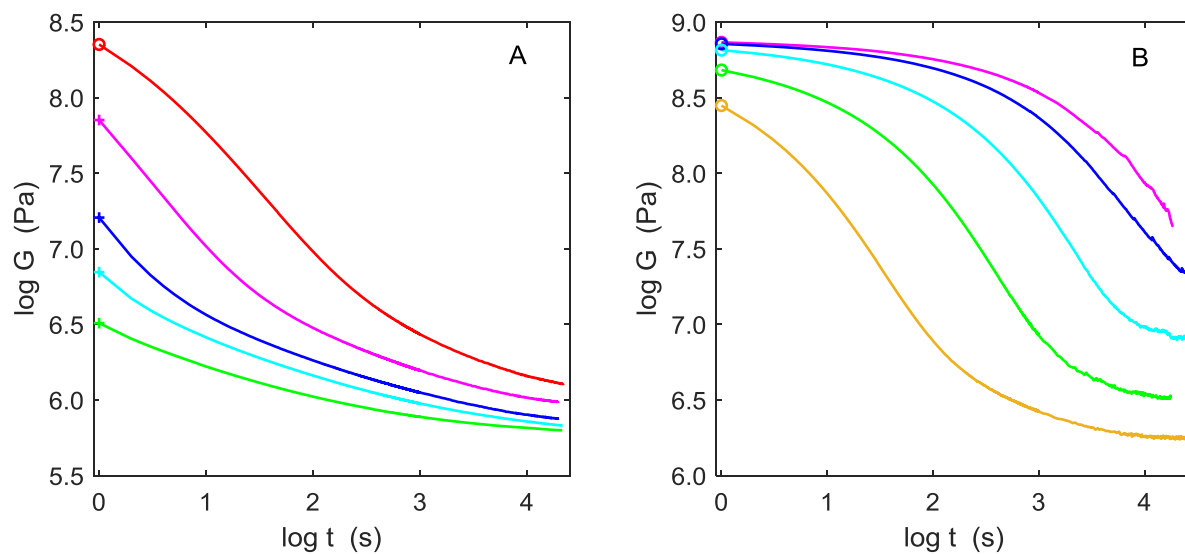


Figure 2.4. Linear viscoelastic stress relaxation modulus isotherms for Epon1009 epoxy resin cured with MDA. Symbols indicating temperature have the same meaning as in Figure 2.1.

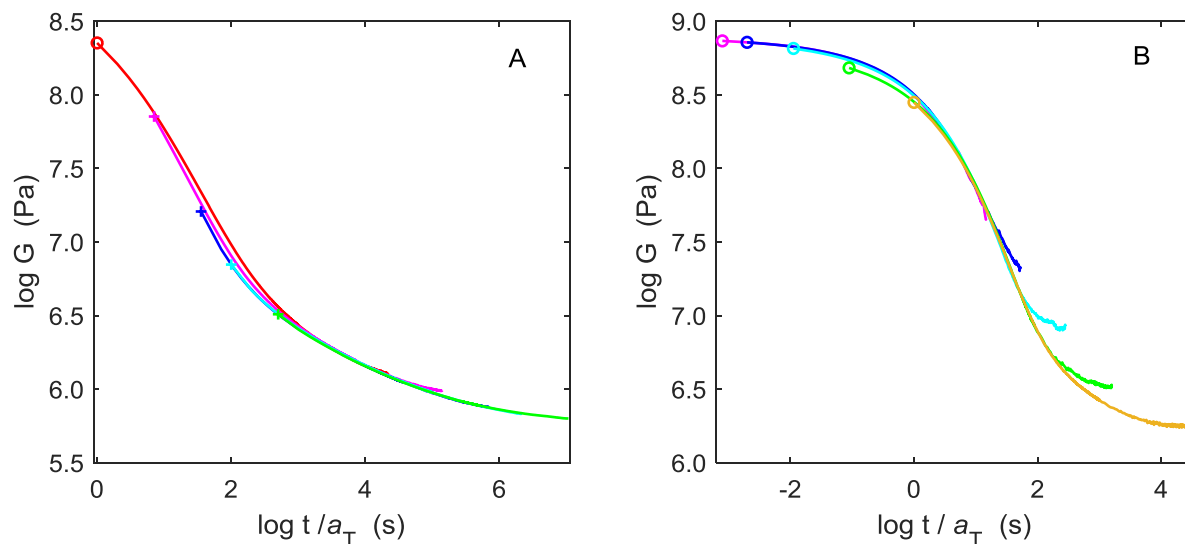


Figure 2.5. Stress relaxation modulus master curve for Epon1009 epoxy resin cured with MDA using the isotherms shown in Figure 2.4 with the  $\log a_T$  shift data shown in Figure 2.3. Symbols have same meaning as in Figure 2.4.

The primary objective of performing the linear viscoelastic stress relaxation experiments at exactly the same temperatures as the dynamic viscoelastic is to extend the accessible experimental window. Specifically, stress relaxation was performed for up to 8 h (i.e., nearly 30,000 s) which would correspond to a frequency of approximately  $10^{-4.46}$  Hz, thereby extending the dynamic data range by almost two and a half logarithmic decades without any time-temperature shifting procedure. However, a note is in order. Unfortunately, it is not possible to avoid specimen-to-specimen variation arising due to variation in the curing process. As a result, the data shown in Figure 2.4A (and hence in Figure 2.5A) and the data shown in Figure 2.4B (and hence in Figure 2.5B) are for two different specimens, where the difference in  $T_g$  was approximately  $2^\circ\text{C}$ . When shifted horizontally along the  $\log(t)$  axis by 0.9 the isotherms from these the dynamic and stress relaxation data sets agree well.

The stress relaxation data were converted into dynamic data using the following procedure. First, an individual isotherm was fit with the Prony series. Then each exponential term in the Prony series was converted analytically to the equivalent storage and loss response using the standard formulae.<sup>1</sup> This two-step procedures was found to be preferable, as compared to direct numerical

Fourier transform of the raw data as the effects of the finite of the experimental window and noise in the data are reduced. However, even this procedure inevitably produces spurious results at higher frequencies. This is because, although application of a step strain on our apparatus is executed within 1s, the Prony series fitting of the shape of the measured stress response involves components with the characteristic times at least an order-of-magnitude shorter. The magnitudes of these short-time components with the relaxation times of the order of seconds are highly sensitive to the details of the fitting procedure and impact the transformed  $G'$  and  $G''$  responses at higher frequencies. The following methodology was employed to alleviate this uncertainty. In the course of fitting a  $G(t)$  isotherm to the Prony series the regularization parameter and the range and the spacing of the relaxation times were widely varied. Only the portions of the  $G'(\omega)$  and  $G''(\omega)$  curves converted from the Prony series that were unaffected by such variations were retained.

The procedure above was applied to each isotherm where the resulting transformed stress relaxation data are shown in Figure 2.6. There is excellent agreement between the dynamic data and the transformed transient data for most of the isotherms. As expected, the place where there is a small discrepancy at 102.5°C and 105.0°C – isotherms in the  $T_g$  region where thermal history is most important. Specifically, the procedure for the dynamic measurements was, after completing a frequency scan at a given temperature, to (i) increase the temperature by 10°C (or 5°C or 2.5°C), (ii) allow the specimen to equilibrate/anneal for 90 min and (iii) begin the frequency scan from the lowest frequency, where the first frequencies take on the order of 10 min to complete, but all frequencies for 1 Hz to  $10^{1.7}$  Hz only take a few seconds to complete. This thermal history is more than adequate at temperatures well below  $T_g$  where physical aging is slow on the experimental timescale and at temperatures well above  $T_g$  where the specimen equilibrates quickly. However, in the  $T_g$  region details of the thermal history become important, where it was not practical to attempt to mimic the history of the dynamic experiment that started at -150°C. Also, there is an almost imperceptible discrepancy in the  $G''$  response at 112.5°C for which we have no explanation at this point. In summary, the combination of the dynamic and stress relaxation data provides a much better picture of the linear viscoelastic response of the Epon1009-MDA polymer than is afforded by either method in isolation.

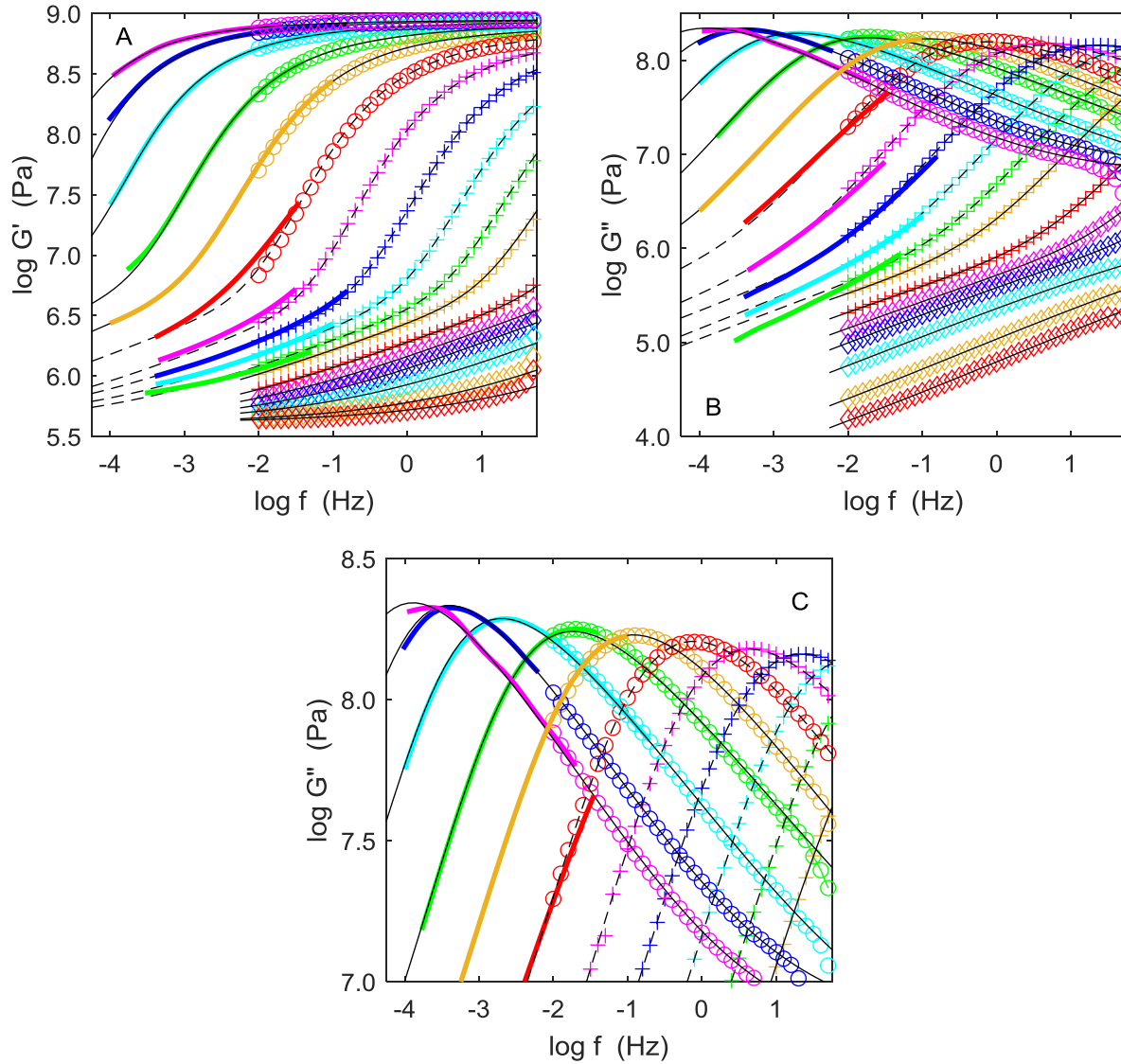


Figure 2.6. Linear viscoelastic storage (A) and loss (B and C) shear moduli isotherms vs frequency for Epon1009 epoxy resin cured with MDA; symbols indicate the dynamic experiment at the following temperatures: 180°C – red diamonds, 160°C – orange diamonds, 140°C – cyan diamonds, 130°C – blue diamonds, 125°C – magenta diamonds, 120°C – red pluses, 115°C – orange pluses, 112.5°C – green pluses, 110°C – cyan pluses, 107.5°C – blue pluses, 105°C – magenta pluses, 102.5°C – red circles, 100°C – orange circles, 97.5°C – green circles, 95°C – cyan circles, 92.5°C – blue circles, 90°C – magenta circles. The thick solid lines indicate the transformed stress relaxation data, where the colors correspond to the same temperatures used in the dynamic data.. Black lines are fits using the model described in the text.



### 2.3.1 New Methodology for Analyzing Linear Viscoelastic Response

The  $G'(\omega)$  and  $G''(\omega)$  isotherms that were extended to lower frequencies by the Fourier transform of the  $G(t)$  stress relaxation response comprise the full complement of the linear viscoelastic data. The key point at hand is how to use this data to glean information regarding the underlying relaxation processes.

One possibility, commonly applied, is to assume that the experimentally observed response is due to the linear combination of a small number of relaxation processes, where each of the individual processes is non-Debye with a specific functional form (, e.g., KWW,<sup>19, 28</sup> Havriliak-Negami,<sup>18</sup> and Cole-Davidson).<sup>29</sup> Each isotherm is then fit with the sum of these empirical functions. If a sufficient number of functions is chosen it is possible to fit the experimental data, but the difficulty is that the temperature dependencies of parameters in the individual functions are not weak and sometimes not even monotonic.<sup>30-39</sup> Thus, unless there is some fundamental reason that an underlying molecular process must have a particular form (and there is no commonly agreed upon reasons for using any particular functional form), this approach is akin to curve fitting.

Another common approach for analyzing viscoelastic data is to determine the relaxation spectrum  $H(\log \tau)$  defined by the following<sup>1</sup>

$$\begin{aligned} G'(\omega) &= G_e + \int_{-\infty}^{\infty} H(\log \tau) \frac{\omega^2 \tau_i^2}{1 + \omega^2 \tau_i^2} d(\log \tau) \\ G''(\omega) &= \int_{-\infty}^{\infty} H(\log \tau) \frac{\omega \tau_i}{1 + \omega^2 \tau_i^2} d(\log \tau) \end{aligned} \quad (2.1)$$

Or, equivalently, in the discrete spectral form by

$$\begin{aligned} G'(\omega) &= G_e + \sum_{i=1}^n G_i \frac{\omega^2 \tau_i^2}{1 + \omega^2 \tau_i^2} \\ G''(\omega) &= \sum_{i=1}^n G_i \frac{\omega \tau_i}{1 + \omega^2 \tau_i^2} \end{aligned} \quad (2.2)$$

where the strength of each process is  $G_i$ . The continuous version is a Fredholm integral of the first kind, which is known to be ill-posed, i.e. small fluctuations in the data can cause large fluctuations in the associated spectrum. The discrete version given in Equation (2.2), although not formally ill-posed, nevertheless exhibits similar numerical instabilities. In order to address this difficulty various regularization methods<sup>40-45</sup> have been developed to enable robust determination of  $\{G_i\}$  for each isotherm. The original data has now been mapped to the set of  $\{G_i\}$ ; however, there is a serious issue with this approach. A typical spectral inversion of linear viscoelastic data or dielectric relaxation data results in spectral intensity that has a range of several orders-of-magnitude; for example, the  $\{G_i\}$  spectrum for the data shown in Figure 2.6 will be similar to the  $G''(\omega)$  data and thus will have intensity differences of three orders-of-magnitude. In case of the dielectric experiment, a given  $G_i$  is now  $\varepsilon_i$ , where  $\varepsilon_i$  is the dipole moment that results from a specific molecular polarizability. It follows that to have two  $\varepsilon_i$ 's with the respective values differing by three orders-of-magnitude would require either: (i) enormous differences in the local charge or (ii) the size of the molecular units that are undergoing reorientation differ by orders-of-magnitude. The presence of large charges or large scale alignment of dipoles surely would have been observed experimentally, where their experimental absence eliminates this interpretation of the dielectric relaxation response. Although dielectric relaxation data for the Epon1009-MDA system reported in this paper cannot be analyzed quantitatively due to the confounding effects of conduction and electrode polarization (see Appendix for details), the dielectric response does qualitatively exhibit order-of-magnitude changes. And, there are literature reports on the dielectric studies for DGEBA epoxy resins<sup>46</sup> that show order-of-magnitude changes in the dielectric response. Thus, the traditional method of determining a relaxation spectrum is problematic even for a single isotherm.

Implicit in the continuous representation is a constant spectral density (or equivalently in the discrete representation a uniform spectral spacing on the  $\log \tau$  axis). An alternative perspective would be to have uniform spectral strength, but where the spectral density changes. When the  $G''(\omega)$  (or the associated  $\varepsilon''$  dielectric response) is large, the spectral density is also large and when  $\varepsilon''(\omega)$  is small the spectral density is also small. Thus, there is no need to invoke the *aphysical*

large dipole assumption described in the previous paragraph to rationalize the large changes in the magnitude of the associated dielectric spectrum, just that there are significant differences in the number of dipoles with nearly identical relaxation times. Also, individual spectral components are not required to have exactly the same temperature dependence, which then will result in the thermo-rheologically complex response observed experimentally. The challenge is to now develop a method for determining the spectral density from the  $G'(\omega)$  and  $G''(\omega)$  isotherms.

In the traditional approach, the spacing of  $\log \tau_i$  is set first (and is usually uniform on the  $\log \tau$  axis) and then the  $G_i$  magnitudes are optimized to fit the experimental data, i.e., the  $G'(\omega)$  and  $G''(\omega)$  isotherms. Unlike in the traditional approach we will fix the value of the spectral strength so that  $G_i = \bar{G}$  for all  $i$  and then let  $\{\log \tau_i\}$  be the unknowns over which the optimization is carried out. Does this approach have a physical basis? We believe so. In fact virtually all molecular mechanisms proposed to date, for example the Rouse model for a linear polymer chain<sup>47</sup> and the ideal Gaussian network model for a polymer network,<sup>48-49</sup> predict the discrete relaxation spectra, where the spectral strength of all individual processes is constant.

Now we turn to practical implementation of the new approach. It is immediately realized that, in order to account for the three order-of-magnitude change in the  $G''(\omega)$  data, it requires at least a thousand individual spectral components, because the three order-of-magnitude intensity change in  $G''(\omega)$  is due to just the bunching together of a thousand or more spectral components in the region near the  $G''(\omega)$  maximum. Standard optimization methods are completely unfeasible when there are a thousand or more unknowns. A different approach is needed.

Unlike in the previous method where the  $\log \tau_i$  values were evenly spaced along the time axis from  $-\infty$  to  $+\infty$ , it is expected that there will be minimum and maximum  $\log \tau$  for each isotherm as dictated by the data. Suppose the set of  $\{\log \tau_i(T_A)\}$  has been determined at a temperature  $T_A$  which is the highest experimental temperature as illustrated in Figure 2.7A. The set of processes (all of which have a spectral strength, i.e. height, of unity) is located within the experimental window that is indicated with dashed lines. The process with the longest relaxation time is assigned the index

1. At the next experimental temperature,  $T_B$  ( $T_B < T_A$ ), all processes will shift, each with its individual shift factor. It seems reasonable to assume that:

- with decrease in temperature all process can only become slower i.e. move from left to right along the relaxation time axis
- any process existing at a higher temperature cannot disappear; however, the processes may exit the experimental window on the right
- new processes may enter the experimental window on the left (this is illustrated in Figure 2.7B, where three new processes colored in red are shown)

Once a process leaves the experimental window, its exact location cannot be established from the experimental data, because the fit is no longer sensitive to it. This is illustrated in Figure 2.7B, where both 1 and 1' locations are equally possible, because they have no effect on the data in the experimental window. However, the continued existence of these long-time process will still manifest in the measured  $G'(\omega)$  storage component of the modulus. The two equations corresponding to Equation (2.2) are:

$$\begin{aligned} G'(\omega) &= G_e + \bar{G} \sum_{i=1}^n \frac{\omega^2 \tau_i^2}{1 + \omega^2 \tau_i^2} \\ G''(\omega) &= \bar{G} \sum_{i=1}^n \frac{\omega \tau_i}{1 + \omega^2 \tau_i^2} \end{aligned} \quad (2.3)$$

where  $\bar{G}$  is the constant intensity for all spectral components. Now consider an isotherm where the  $\tau_1$  process has just moved out of the experimental window. If the lowest experimental frequency is  $\omega_{\min}$ , then for the  $\tau_1$  relaxation time that has just moved outside the experimental window one has  $\omega_{\min} \tau_1 \gg 1$ . Thus, the storage and loss moduli when the  $\tau_1$  process has just moved out of the experimental window are

$$\begin{aligned} G'(\omega \gg \omega_{\min}) &= G_e + \bar{G} + \bar{G} \sum_{i=2}^n \frac{\omega^2 \tau_i^2}{1 + \omega^2 \tau_i^2} \\ G''(\omega \gg \omega_{\min}) &= \bar{G} \sum_{i=2}^n \frac{\omega \tau_i}{1 + \omega^2 \tau_i^2} \end{aligned} \quad (2.4)$$

For the  $G'$  response the  $\bar{G}$  outside the summation is the contribution from the  $\tau_1$  process, where the lower index on the summation is now 2. If equilibrium modulus is zero (as in the case of thermoplastics) or has been independently measured so that the quantity  $G'(\omega \ll \omega_{\min}) - G_e$  can be accurately evaluated, then the presence of extra  $\bar{G}$  contribution as seen in Equation (2.4) may be perceived in the  $G'$  data. In contrast, the  $\bar{G}$  from the  $\tau_1$  process does not contribute to the  $G''$  data that is seen in the experimental window.

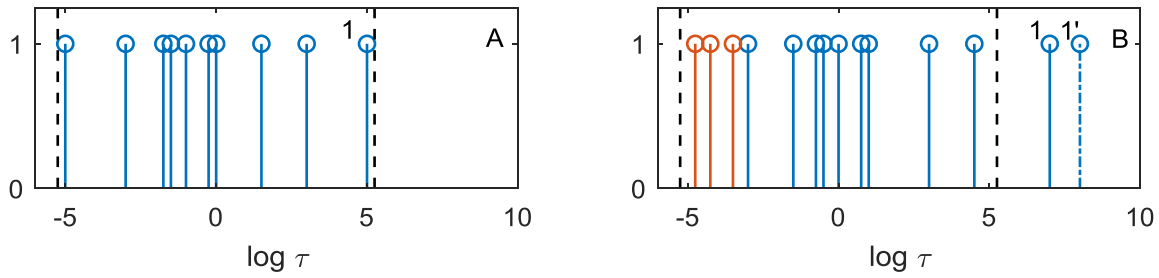


Figure 2.7. Schematic of the spectral components at two temperatures, where the temperature  $T_B$  of panel B is lower than the temperature  $T_A$  in panel A. See text for further description.

Straightforward nonlinear optimization over potentially thousands of  $\tau_i$ s to fit Equation (2.3) to a given isotherm is not possible. To make the problem manageable, a smooth function for the density of processes  $\rho(\log \tau)$  will be used so that the optimization can be performed using a smaller number of parameters of this function. Ideally the function  $\rho(\log \tau)$  would come from a physics based model; however, at present such a physics based model does not exist. Consequently, the function  $\rho(\log \tau)$  is purely phenomenological. For a given isotherm the functional form of phenomenological  $\rho(\log \tau)$  is irrelevant as long as the fit is achieved. Although we have no formal proof, but upon experimenting with several vastly different functions including polynomials we found that the resulting set of  $\{\log \tau_i\}$  determined is essentially the same provided the target experimental data are sufficiently smooth. Moreover, different isotherms do not have to be fit using the same functional form of  $\rho(\log \tau)$ , since no meaning is assigned to a specific functional form.

Based upon our experience, we found that the following form of the density function yielded a consistently good fit for the entire experimental temperature range:

$$\rho(x) = \bar{\rho} \frac{\left[ (1-A) \tanh(k_\alpha (x-x_\alpha)) + 1 + A \right] \left[ (1-B) \tanh(-k_s (x-x_s)) + 1 + B \right]}{4 \left[ 1 + \exp(k_{nt} (x-x_{nt})) \right]} \quad (2.5)$$

where  $x = \log \tau$  and  $\bar{\rho}, A, B, k_\alpha, x_\alpha, k_s, x_s, k_{nt}, x_{nt}$  are the parameters that must be optimized for each isotherm. The optimization procedure will now be described.

The first question is what the value of  $\bar{G}$  should be. Clearly  $\bar{G}$  has no lower bound. Specifically, suppose for a given value of  $\bar{G}$  a set of  $\{\log \tau_i\}$  is found that fits the data via Equation (2.3). Then by replacing each  $\log \tau_i$  with a pair located at  $\log \tau_i - \delta$  and  $\log \tau_i + \delta$  (where  $\delta$  is infinitesimally small) and setting the spectral strength value to  $\bar{G}/2$  the fit is preserved – by this procedure a solution for arbitrarily small  $\bar{G}$  can always be obtained. On the other hand, the upper bound on  $\bar{G}$  is set by the data. Specifically, if the separation between adjacent processes (i.e. between  $\log \tau_i$  and  $\log \tau_{i+1}$ ) is sufficiently large these processes will appear as separate peaks on the loss isotherm. Because the distance between processes is related to the  $\bar{G}$  magnitude, then the smoothness of the experimental curve puts an upper bound on  $\bar{G}$ . If the relaxation behavior is due to discrete, physically real, Debye processes, then the true value of  $\bar{G}$  (or  $\bar{\epsilon}$  in case of the dielectric relaxation) would be set from the experimental data by resolving individual relaxation process; however, this will require significant improvement of existing experimental techniques.

We are now ready to describe the recipe for determining the discrete relaxation spectrum from  $G'(\omega)$  and  $G''(\omega)$  isotherms, which is as follows:

1. Select the highest temperature isotherm and make an initial guess for the parameters in empirical function for  $\rho(\log \tau)$  given in Equation (2.5) (or an alternative empirical function). This requires some skill in the initial choice of the parameters in the empirical function.

2. Choose the longest relaxation time resolvable from the data, i.e.  $x_1 = \log \tau_{\max}$ . A good choice for  $\log \tau_{\max}$  is  $-\log \omega_{\min} + 1.5$ , i.e. 1.5 logarithmic decades beyond the minimum frequency of the data – a relaxation process with a given  $\tau$  can influence the viscoelastic response about 1.5 logarithmic decades on either side of its value. One can check if the choice of  $x_1$  is good, by increasing  $x_1$  and seeing that it has no effect on the fitting of the  $G'(\omega)$  and  $G''(\omega)$  data.
3. The subsequent spectral components (in the descending order) can now be determined sequentially from the relaxation function; specifically,

$$x_1 - x_2 = \frac{1}{\rho(x_1)}; \quad x_2 - x_3 = \frac{1}{\rho(x_2)}; \quad x_3 - x_4 = \frac{1}{\rho(x_3)}; \quad \text{etc.}$$

where  $x_i = \log \tau_i$ . The last spectral component is when it stops making any contribution to the isothermal response, where a good criterion is  $x_{\text{final}} = -\log \omega_{\max} - 1.5$ .  $\omega_{\max}$  is the maximum frequency in the  $G'(\omega)$  and  $G''(\omega)$  data.

4. Now that all of the relaxation times have been determined, the predicted  $G'(\omega)$  and  $G''(\omega)$  response is evaluated using Equation (2.3). The RMS error between the experimental data and the predictions is calculated using  $\{x_i = \log \tau_i\}$ , where the error depends upon the choice of the parameters in the empirical fitting function. Thus, steps 1 through 4 constitute the evaluation or RMS error for a given choice of parameters in the  $\rho(\log \tau)$  fitting function, which can be used in a standard optimization program. Thus, from optimization of the  $\rho(\log \tau)$  fitting function to the  $G'(\omega)$  and  $G''(\omega)$  one has the set  $\{x_i = \log \tau_i\}$  that describe the data for that isotherm.

Once  $\rho(\log \tau)$  has been optimized for the highest temperature isotherm, one moves down to the next highest temperature and determines the  $\{x_i = \log \tau_i\}$  at that temperature. This process is continued at sequentially lower temperatures until all isotherms have been analyzed. A reasonable initial estimate of  $\rho(\log \tau)$  for a specific isotherm would use the same parameters in Equation (2.5)

as were used at the previous temperature, but then change  $x_\alpha$ ,  $x_s$  and  $x_{nt}$  by  $\Delta$  which is the shift of the  $\log \omega$  axis needed for approximate superposition of the neighboring isotherms, i.e.  $x_\alpha \rightarrow x_\alpha + \Delta$ , etc.

The process above is straightforward, readily implemented in a user friendly software, where optimization of an isotherm typically takes only a few minutes on a desktop PC.

Each isotherm as it is being optimized must be examined to make sure that (i) the  $\{x_i = \log \tau_i\}$  set accurately describe the data for each isotherm and (ii) the initial guess for that isotherm produces reasonable results, where sometimes that initial guess has to be improved by hand. Also, a function like Equation (2.5) is general, but for some isotherms certain parts of the function do not contribute to  $G'(\omega)$  and  $G''(\omega)$  data, e.g. at high temperatures the factor containing  $A$ ,  $k_\alpha$ , and  $x_\alpha$  is irrelevant and at low temperatures the factor containing  $k_{nt}$  and  $x_{nt}$  does not contribute in a meaningful way. Thus, for these isotherms the optimization only occurs over the remaining parameters. Again, the form of the  $\rho(\log \tau)$  fitting function is arbitrary as long as the resulting  $\{x_i = \log \tau_i\}$  describes the data within the accuracy of the data. As with any nonlinear optimization problem the initial guess is all-important, where there is need for intelligent human control to ensure that the computer does not produce foolish answers. However, the answer does not depend upon the particular form of  $\rho(x)$  as long as it enables accurate fitting of the  $G'(\omega)$  and  $G''(\omega)$  isotherms.

### 2.3.2 Spectral Analysis of the Epon1009-MDA Epoxy System

The new analysis of determining the spectral density versus the spectral height has been applied to the Epon1009-MDA data shown in Figure 2.6. The values of the fitting parameters used in the  $\rho(\log \tau)$  fitting function given in Equation (2.5) are provided in the SI for all isotherms, where a constant spectral strength of  $\bar{G} = 10^4$  Pa was used. The spectral density required to fit the extended dynamic data is shown in Figure 2.8 for selected temperatures from 90°C to 120°C where  $\rho(\log \tau)$  for intermediate temperatures lie in between those that are shown. Three regions in the spectra are apparent: (i) the longer relaxation time processes, e.g.  $\log \tau > 0$  on the cyan curve, associated with



the beginning of the Rouse and/or network relaxation processes. Remarkably, the  $\log \rho$  vs  $\log \tau$  dependence in this long time region is nearly linear with the slope close to  $-1/3$ . We propose to call this region the  $\alpha+$  region; (ii) the next region is that associated with the glass transition and is characterized by sharp increase in density of the relaxation processes manifesting as a “peak” on the loss curves in Figure 2.6B. This  $\alpha$ -proper relaxation process spans approximately two orders-of-magnitude on the relaxation time axis, i.e. from -2 to 0 on the cyan curve; and, (iii) finally, at relaxation times shorter than maximum spectral density the glass transition’s “excess wing” is observed. On the left hand side of the excess wing, i.e. for the shortest relaxation times on the magenta curve in Figure 2.8, the density of processes becomes nearly constant. The shape of the spectral density is similar at all temperatures, but there are differences both in the height of the  $\alpha$ -proper peak and in the peak width indicative of the lack of time-temperature superposition of the dynamic mechanical properties shown in Figure 2.2.

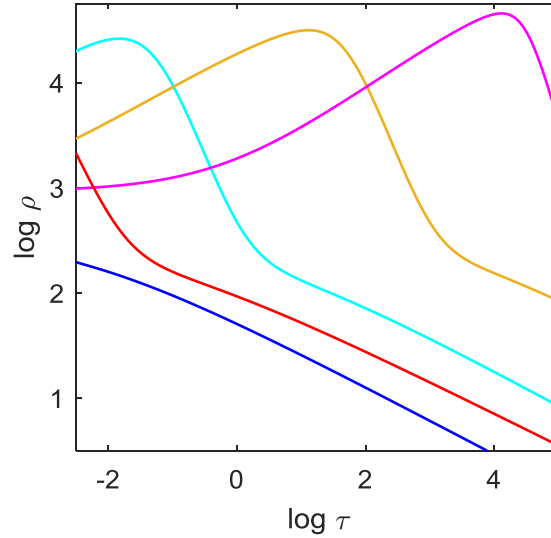


Figure 2.8. Density of relaxation processes vs relaxation time for Epon1009-MDA for various temperatures: 130°C – blue, 120°C – red, 110°C – cyan, 100°C – orange, and 90°C – magenta.

The temperature dependence of each of the relaxation times is obtained using the procedure described in the previous section. For  $\bar{G}=10^4$  Pa approximately 90,000 processes are required to fit the data in Figure 2.6. Although this may appear as an extremely large number of processes it

is consistent with the range of the  $G'(\omega)$  and  $G''(\omega)$  data. Specifically, when the magnitude of the storage and loss data change by three orders-of-magnitude, there must be a thousand or more relaxation processes at the peak maximum than at the minimum; and, at the peak minimum one does not see a response consistent with an individual Debye process but rather a smooth response that involves several relaxation processes. Thus, of order  $10^5$  relaxation processes is what would be expected from the experimental data. A key feature of the algorithm described in the previous section is that these processes can be robustly determined.

A map of the relaxation times for Epon1009F-MDA is shown in Figure 2.9. Each line corresponds to a given process, where  $\tau_i$  is the relaxation time of the  $i$ -th process at the temperature indicated and the leftmost line corresponds to the 50<sup>th</sup> process. Processes 1 through 49 are from the low frequency data at the highest temperature (see Step 2 in the algorithm in the previous section); thus, these are progressively more difficult to extract as temperature is lowered and hence have the greatest uncertainty. Consequently, we have chosen to not include the first 49 relaxation processes in the relaxation map. At any temperature, the vertical line corresponds to the distribution of the discrete relaxation times and results in the density of relaxation processes shown in Figure 2.8. Important features of the relaxation map are.

1. The range of  $\log \tau_i$  is 7.5 logarithmic decades which is wider than the 6.0 logarithmic decades width of the experimental data. This occurs because processes with relaxation times that are within a decade shorter/longer than the slowest/fastest frequency in the experimental window still contribute to the experimentally measured data.
2. The lines are not parallel, which would be required if the material was thermo-rheologically simple.
3. The lines are much sparser in upper left and low right corner of Figure 2.9 as compared to the center where the lines are tightly bunched. The tightly bunched lines in the center correspond to the maximum in the  $\alpha$ -peak.

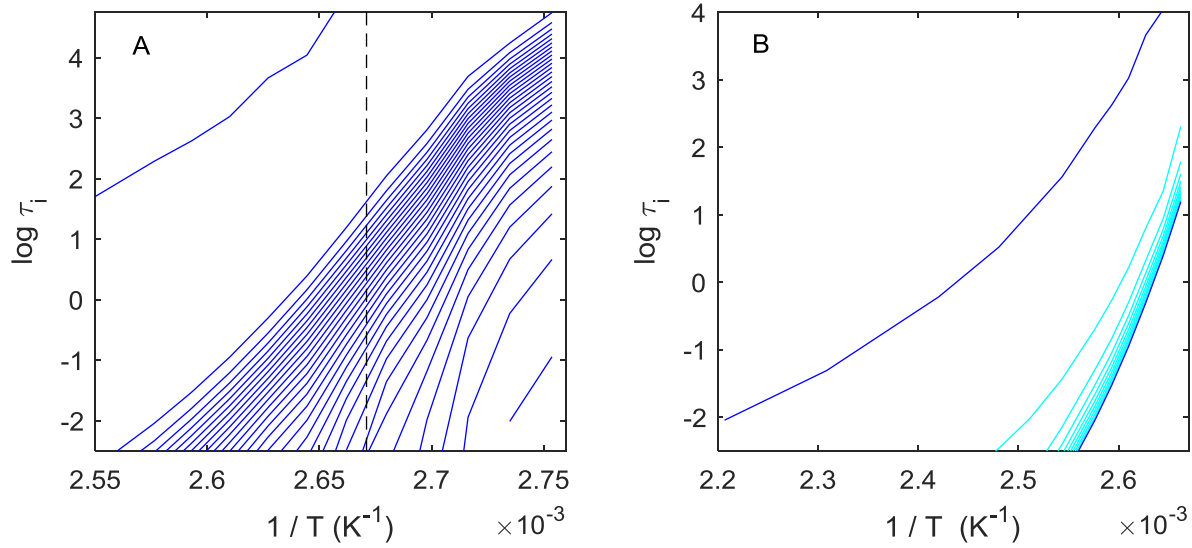


Figure 2.9. Relaxation map for 1009 MDA epoxy system: (A)  $\alpha$ -region, every 3,000<sup>th</sup> process is shown i.e. the leftmost process is process No.50, the next process to the right is process No.3050, the subsequent processes are incremented by 3000, where the rightmost process is process No.87,050; (B)  $\alpha+$  region, every 300<sup>th</sup> process is shown i.e. the leftmost process is process No.50, next process to the right is process No.350, etc. the rightmost process is process No.3050. In (A) vertical dashed line indicates  $T_g$  at 374.5 K (101.5°C); in (B)  $T_g$  corresponds to the right edge of the box.

4. To a first approximation the tightly bunched lines that correspond to the  $\alpha$ -peak are somewhat parallel, especially if one neglects relaxation processes that are not near the maximum density in the relaxation map. This is the reason why time-temperature superposition may appear to work if the frequency range is not 6 logarithmic decades as for the Epon1009-MDA data shown in Figure 2.6, but the 4 logarithmic decades or less that is often reported in the literature.
5. The spacing in the upper left hand corner in Figure 2.9A is sparse and highly non-uniform (this is even more apparent in Figure 2.9B). This is consistent with the decay in the perceived intensity of the  $\alpha+$ -process as seen at high temperatures and low frequencies in Figure 2.6 and at long times in Figure 2.8.

6. At temperature below  $T_g$  the temperature dependence of the relaxation processes becomes concave downward as compared to processes that are concave upward at higher temperatures. The concave downward curvature at temperatures below  $T_g$  is consistent with the transition from WLF-like behavior in  $\log a_T$  above  $T_g$  to a more Arrhenian behavior below  $T_g$ .<sup>50-52</sup>

The relaxation map in Figure 2.9 and the spectral density in Figure 2.8 are the only results that can be rationally and robustly determined from the combined dynamic and transient linear viscoelastic data shown in Figure 2.6.

## 2.4 Discussion

The linear viscoelastic behavior in shear over more than six logarithmic decades in frequency has been determined for a series of temperatures from just below  $T_g$  to well above  $T_g$  for a DGEBA diepoxide cured with MDA – a typical epoxy resin system. The more than six order-of-magnitude range of the relaxation response, that is significantly larger than that usually reported (typically four orders-of-magnitude or less) for linear viscoelastic measurements, is the result of combining the dynamic and stress relaxation measurements obtained at the same temperature. Specifically, the stress relaxation data were converted to the low frequency dynamic response via standard interconversion formulae and then combined with the measured  $G'(\omega)$  and  $G''(\omega)$  data. These results were obtained with a standard rheometer that has both dynamic and transient capabilities with modern temperature control so that the temperature of the dynamic and transient experiments is the same within  $\pm 0.1\text{K}$ . Thus, this wide frequency range of linear viscoelastic data can be readily achieved by using a modern rheometer, enabling a much better picture of the viscoelastic behavior of polymers and other time dependent materials.

The key features from examining the isotherms of linear viscoelastic storage,  $G'$ , and loss,  $G''$ , moduli (see Figure 2.6) are: (i) there are at least two distinct relaxation processes and (ii) the isotherms are thermo-rheologically complex. The main relaxation process is the  $\alpha$ -process associated with the glass transition, and there is a second relaxation process at higher temperatures that we designate as the  $\alpha+$ -process. The name  $\alpha+$  was chosen because the process in question is

located at relaxation times longer than  $\alpha$ , where its molecular origin is not well-established – perhaps it is associated with the Rouse modes or some network relaxation modes. For the isotherms at high temperatures where the  $\alpha$ -process dominates, time-temperature superposition appears to almost work, although careful examination of the tails of the  $G'(\omega)$  and  $G''(\omega)$  isotherms indicate a small, but systematic, lack of superposition (see Figure 2.2A and B). As expected, the lack of superposition becomes pronounced for isotherms in the transition region between the  $\alpha$  and  $\alpha$ + processes. Examining the main  $\alpha$ -process, the lack of superposition of both  $G'(\omega)$  and  $G''(\omega)$  isotherms in Figure 2.2E and F is readily apparent. A similar lack of superposition is also observed in the linear viscoelastic stress relaxation isotherms (see Figure 2.5). The application of vertical shifting in addition to the horizontal  $\log a_T$  shifting would decrease the lack of superposition, but there is no physical justification for such a vertical shift (which would not be systematic) and it would still not result in full superposition of all the isotherms.

It is clear that this particular DGEBA-MDA epoxy system is thermo-rheologically complex. Because there are at least two relaxation mechanisms it is not surprising that there is a lack of superposition in the intermediate region where both relaxation processes are operative. However, thermo-rheological complexity is present, but weak, in the  $\alpha$ + region and it is clearly present in the  $\alpha$  region itself. The DGEBA-MDA system is single phase so the thermo-rheological complexity is not due to multi-phase effects. The thermo-rheological complexity appears to be an integral feature of the  $\alpha$  and  $\alpha$ + processes if the frequency/time range of the experimental window is wide enough. We posit that thermo-rheological complexity is not the exception, but the norm, for glass forming materials if the viscoelastic data have a sufficiently wide range. Thermo-rheological complexity is a standard feature of dielectric data, where broadband dielectric data over eight orders-of-magnitude are typical.<sup>21, 53</sup> Not including blends and multiphase polymers where thermo-rheological complexity is expected,<sup>54-56</sup> thermo-rheological complexity has also been observed in mechanical experiments on single phase polymers.<sup>2-12</sup> Thus, thermo-rheological complexity reported in this paper is not due to some unusual feature of the DGEBA-MDA epoxy resin, but a common feature of the transition region in glass forming materials.

Thermo-rheological complexity precludes the application of the traditional approach of constructing master curves and determining the relaxation spectrum from the master curves.<sup>1</sup> Moreover, there are serious problems with the traditional interpretation of the linear frequency/time response in terms of a relaxation spectrum that implicitly assumes a constant spectral density for a continuous representation (or equivalently constant spacing in a discrete spectrum). The inherent difficulties in the traditional approach are most clearly apparent with respect to dielectric relaxation. First, the dielectric strength depends upon charge (or partial charge) separation of molecular dipoles, where it is inconceivable that there are 3 to 4 order-of-magnitude differences in the dipole strength that are required to fit the 3 to 4 order-of-magnitude difference between the smallest and the largest values of  $\varepsilon''(\omega)$  observed in the dielectric spectra<sup>57-58</sup> ( $\varepsilon''(\omega)$  has a similar changes in magnitude as observed in the  $G''(\omega)$  data shown in Figure 2.1). Second, the strength of a dipole is a very weak function of temperature and, thus, cannot account for the temperature dependence of the peak height in  $\varepsilon''(\omega)$  response that would be similar to that seen in the  $G''(\omega)$  isotherms shown in Figure 2.1. Although the current study has not reported on the dielectric behavior due to parasitic conduction and electrode polarization effects (see Appendix), similar dielectric effects are reported for many glass forming materials,<sup>11, 30, 32, 36, 59-66</sup> which are also present for this DGEBA-MDA epoxy resins for temperature below  $T_g$  that will be reported in a future publication.

A common approach to analyzing linear viscoelastic and especially dielectric relaxation data is the use of empirical functions (KWW, Havriliak-Negami, etc.), where each function is associated with the presumed fundamental process such as  $\alpha$ -,  $\beta$ -,  $\gamma$ -process, etc., which are in turn thought to be related to specific molecular motions. Apparent thermo-rheological complexity of the data does not present a problem since different processes and hence the corresponding functions are expected to have different temperature dependencies. Changes in the peak height in  $\varepsilon''(\omega)$  response with temperature for a given process (e.g.  $\alpha$ -peak) can be accommodated by employing temperature dependent shape parameters.<sup>15, 20</sup> The observation that in many cases such dependencies turn out to be non-systematic<sup>30-36, 38, 67</sup> is perhaps troubling but not enough to rule out the entire approach. However, the empirical functions approach has another problem that is underappreciated. Consider the storage dielectric susceptibility  $\varepsilon'(\omega)$  isotherms for the Epon1009F-MDA epoxy shown in

Figure 2.10. Note that for each isotherm the frequency range has been truncated to exclude the electrode polarization effect (whereas the measurements were carried out for the range from  $10^{-2}$  Hz to  $10^{+6.9}$  Hz). Also the isotherms for temperatures below  $120^{\circ}\text{C}$  are not shown because the identification of the portion of the response due to electrode polarization could not be done robustly.

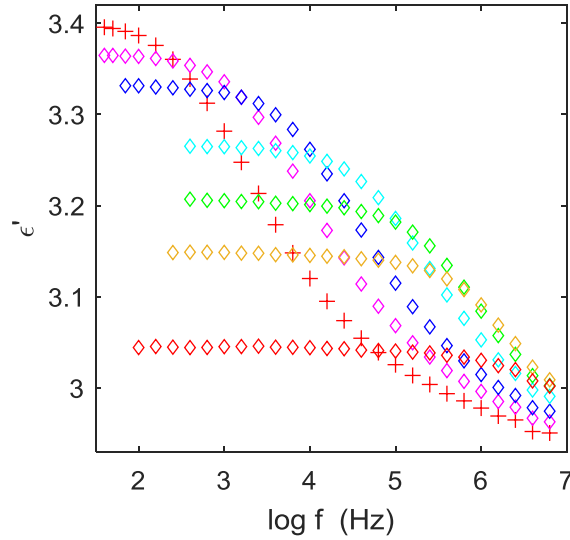


Figure 2.10. Storage dielectric susceptibility isotherms vs frequency for Epon1009 epoxy resin cured with MDA at the following temperatures:  $180^{\circ}\text{C}$  – red diamonds,  $160^{\circ}\text{C}$  – orange diamonds,  $150^{\circ}\text{C}$  – green diamonds,  $140^{\circ}\text{C}$  – cyan diamonds,  $130^{\circ}\text{C}$  – blue diamonds,  $125^{\circ}\text{C}$  – magenta diamonds,  $120^{\circ}\text{C}$  – red pluses.

The behavior shown in Figure 2.10 will look familiar to any of dielectric spectroscopy of molecular and/or polymeric glass forming materials.<sup>30, 36, 46, 57, 66-74</sup> Specifically, it is seen that the static susceptibility i.e.  $\varepsilon_0 = \varepsilon'(\omega \rightarrow 0)$ , which is easily identified as the flat portion of the response, increases with decreasing temperature. As discussed in more details in the Appendix, such an increase in  $\varepsilon_0$  can only occur if the area under the relaxation spectrum (or the total strength of the dielectric signal) increases. When using the empirical functions approach to describe the relaxation data the area under one or more of these functions has to be made a function of temperature. This manifests as the temperature dependence of parameters  $\Delta\varepsilon_{\alpha}(T)$ ,  $\Delta\varepsilon_{\beta}(T)$ , etc. as reported in the literature for many materials.<sup>31, 35, 37, 39, 51, 62, 67, 75-77</sup> This is dissatisfying for the same reason mentioned in the previous paragraph – a strength of a dipole is a very weak function of temperature

and, thus, cannot account for the temperature dependence of the peak area; especially since, as observed for most materials studied this dependence is strong above  $T_g$  but disappears below  $T_g$ , which would not be expected if it was a consistent temperature trend. A new approach for analyzing linear viscoelastic relaxation without the implicit assumption of constant spectral density is needed.

A new analysis methodology has been developed where the spectral strength is assumed to be constant, and the spectral density is adjusted to describe the data. This new approach can quantitatively describe the relaxation data, where the spectral density for the Epon1009-MDA system is shown in Figure 2.8. The spectral density changes by 3 orders-of-magnitude consistent with the similar change in the magnitude of the  $G'(\omega)$  and  $G''(\omega)$  data shown in Figure 2.6; however, there is no difficulty in having changes of this magnitude in the spectral density – there are just more processes with similar relaxation times. Also, there is no difficulty in accommodating thermo-rheological complexity, since different spectral contributions can have different temperature dependencies effecting changes in spectral density that in turn affect how the height of the  $G''(\omega)$  peak changes with temperature – all without changing the strength of any particular dipole. Finally, the increase in static dielectric susceptibility with decrease in temperature is due to the emergence of new processes at the short relaxation time end of the spectrum. Note that this is different from processes moving into the experimental window – the latter already exist and hence contribute to  $\varepsilon_0$  [but not to  $\varepsilon''(\omega)$ ,  $G'(\omega)$  and  $G''(\omega)$ ].

The spectral density analysis methodology is more robust than the traditional determination of the relaxation spectra. Specifically, the relationship between the relaxation spectrum and the experimental data as shown in Equation (2.1) is a Fredholm integral of the first kind that is ill-conditioned and requires regularization methods for solution.<sup>40-41</sup> The reason for the ill-conditioned behavior is that there is no inherent limitation on the spectral strength, which allows for large fluctuations between neighboring spectral contributions so that large positive and *apophysical* negative terms in the spectrum that effectively cancel each other. Once the spectral strength is set to a constant value, this particular source of instability disappears. Although we have no formal proof, the analysis method described in the previous section for determining the spectral



density is robust – not needing any special smoothing method, e.g. regularization, to generate over 90,000 spectral components. It is perhaps significant that the physically motivated constraint in the new method that the spectral intensity is constant appears to lead to a more robust solution methodology.

In the current analysis we have assumed that there was a single strength for all relaxation processes, which is consistent with Rouse<sup>47</sup> and network<sup>48-49</sup> relaxation models. There is no reason why there could not be several different processes, e.g. multiple molecular dipoles of different strengths. However, one would not expect the dipoles to have widely different strengths; thus, the spectral density should remain the dominate cause of the order-of-magnitude change in the dielectric/viscoelastic data. There would need to be some physically motivated justification for different spectral strengths, where without such justification parsimony requires the simplest assumption of constant spectral strength.

The relaxation map shown in Figure 2.9 for the Epon1009-MDA epoxy system is the full description of the relaxation behavior. A master curve like that shown in Figure 2.2 and Figure 2.5 may perhaps appear to be more useful, but it is unjustified. Unfortunately in much of the linear viscoelastic literature (i) the data is of a more limited frequency/time range so that lack of superposition is not readily apparent, (ii) points at the ends of the frequency/time range are often eliminated just because they do not superpose, (iii) physically unjustified vertical shifts are applied to improve superposition, and (iv) symbols are sometimes made large to obscure lack of superposition – these are the undisclosed methods that are often used in the analysis of viscoelastic data. Moreover, except in special cases (e.g., Rouse relaxation of polymers at temperatures well above the  $\alpha$ -process) there is no physical justification for why all relaxation processes should have the same temperature dependence as required by time-temperature superposition. In our opinion, time-temperature superposition must be regarded as a special case, where in general it should be used with extreme caution. In particular, the extension of the  $\log(\text{frequency})$  or  $\log(\text{time})$  axis by many orders-of-magnitude should be regarded with skepticism unless there is a clear mechanistic reason why all relevant relaxation processes should have the same temperature dependence.

The only thing that can be said with confidence concerns the relaxation response inside the frequency/temperature window that is experimentally accessible, i.e. the relaxation map shown in Figure 2.9. The key challenge is to now determine a fundamental model for the shape of the relaxation map, where the availability of such a model (e.g. like the Rouse or reptation models for the terminal relaxation of chain molecules) would potentially enable extension of the log(frequency) or log(time) scale. In order to begin developing such a model it will be useful to obtain extended relaxation data like that shown in Figure 2.6 for a variety of polymers and small molecules with systematic changes in the molecular architecture – data that will lead to the spectral density shown in Figure 2.8 and the relaxation map shown in Figure 2.9 for the various systems. Perhaps by examining how changes in molecular architecture affect the relaxation map (much like the relaxation spectra reported in Ferry's<sup>1</sup> seminal monograph on viscoelastic behavior polymers) a better understanding of the relaxation response in the glass transition region of polymers will begin to emerge.

## 2.5 References

1. Ferry, J. D., *Viscoelastic Properties of Polymers*. 3<sup>rd</sup> ed.; John Wiley and Sons: New York, 1980; p 641.
2. Plazek, D. J., Temperature Dependence of the Viscoelastic Behavior of Polystyrene. *J. Phys. Chem.* **1965**, 69 (10), 3480-3487.
3. Plazek, D. J., Magnetic Bearing Torsional Creep Apparatus. *J. Polym. Sci. Polym. Phys.* **1968**, 6 (3), 621-638.
4. Cavaille, J. Y.; Jourdan, C.; Perez, J.; Monnerie, L.; Johari, J. P., Time-Temperature Superposition and Dynamic Mechanical Behavior of Atactic Polystyrene. *J. Polym. Sci. Pol. Phys.* **1987**, 25 (6), 1235-1251.
5. Mikolajczak, G.; Cavaille, J. Y.; Perez, J., Dynamic mechanical behaviour and its dependence on preparation method of structural epoxide resin. *Polymer* **1987**, 28 (12), 2023-2031.
6. Alegria, A.; Macho, E.; Colmenero, J., Dynamic Mechanical Study of Four Amorphous Polymers around and above the Glass Transition. Breakdown of the Time-Temperature Superposition Principle in the Frame of the Coupling Model. *Macromolecules* **1991**, 24 (18), 5196-5202.
7. Zorn, R.; McKenna, G. B.; Willner, L.; Richter, D., Rheological Investigation of Polybutadienes Having Different Microstructures over a Large Temperature Range. *Macromolecules* **1995**, 28 (25), 8552-8562.

8. Plazek, D. J.; Chay, I. C.; Ngai, K. L.; Roland, C. M., Viscoelastic properties of polymers. 4. Thermorheological complexity of the softening dispersion in polyisobutylene. *Macromolecules* **1995**, 28 (19), 6432-6436.
9. Inoue, T.; Onogi, T.; Yao, M.-L.; Osaki, K., Viscoelasticity of low molecular weight polystyrene. Separation of rubbery and glassy components. *J. Polym. Sci. Pol. Phys.* **1999**, 37 (4), 389-397.
10. Robertson, C. G.; Rademacher, C. M., Coupling Model Interpretation of Thermorheological Complexity in Polybutadienes with Varied Microstructure. *Macromolecules* **2004**, 37 (26), 10009-10017.
11. Ding, Y.; Sokolov, A. P., Breakdown of Time–Temperature Superposition Principle and Universality of Chain Dynamics in Polymers. *Macromolecules* **2006**, 39 (9), 3322-3326.
12. Wu, X.; Zhou, X.; Liu, C.; Zhu, Z., Slow dynamics of the  $\alpha$  and  $\alpha'$  relaxation processes in poly(methyl methacrylate) through the glass transition studied by mechanical spectroscopy. *J. Appl. Phys.* **2009**, 106 (1), 013527.
13. Kudlik, A.; Benkhof, S.; Blochowicz, T.; Tschirwitz, C.; Rossler, E. A., The dielectric response of simple organic glass formers. *J. Mol. Struct.* **1999**, 479, 201-2018.
14. Hofmann, A.; Kremer, F.; Fischer, E. W.; Schonhals, A., The Scaling of the  $\alpha$ - and  $\beta$ -Relaxation in Low Molecular Weight and Polymeric Glassforming Systems. In *Disorder Effects on Relaxational Processes*, Richert, R.; Blumen, A., Eds. Springer: Berlin Heidelberg New York, 1994; pp 309-331.
15. Kremer, F.; Schonhals, A., The Scaling of the Dynamics of Glasses and Supercooled Liquids. In *Broadband Dielectric Spectroscopy*, Kremer, F.; Schonhals, A., Eds. Springer-Verlag: Berlin, Heidelberg, 2003; pp 99-131.
16. Lunkenheimer, P.; Loidl, A., Glassy Dynamics Beyond the  $\alpha$ -Relaxation. In *Broadband Dielectric Spectroscopy*, Kremer, F.; Schonhals, A., Eds. Springer-Verlag: Berlin, Heidelberg, 2003; pp 131-165.
17. Cole, K. S.; Cole, R. H., Dispersion and Absorption in Dielectrics I. Alternating Current Characteristics. *J. Chem. Phys.* **1941**, 9 (4), 341-351.
18. Havriliak, S.; Negami, S., A complex plane representation of dielectric and mechanical relaxation processes in some polymers. *Polymer* **1967**, 8, 161-210.
19. Williams, G.; Watts, D. C., Non-symmetrical dielectric relaxation behaviour arising from a simple empirical decay function. *Trans. Faraday Society* **1970**, 66, 80-85.
20. Schonhals, A.; Kremer, F., Analysis of Dielectric Spectra. In *Broadband Dielectric Spectroscopy*, Kremer, F.; Schonhals, A., Eds. Springer-Verlag: Berlin, Heidelberg, 2003; pp 57-97.
21. Richert, R., Supercooled Liquids and Glasses by Dielectric Relaxation Spectroscopy. In *Adv. Chem. Phys.*, Rice, S. A.; Dinner, A. R., Eds. John Wiley and Sons: New York, 2015; Vol. 156, pp 101-193.

22. Kubo, R., Statistical-Mechanical Theory of Irreversible Processes. I. General Theory and Simple Applications to Magnetic and Conduction Problems. *J. Phys. Soc. Jpn.* **1957**, *12* (6), 570-586.
23. Hassan, M. K.; Tucker, S. J.; Abukmail, A.; Wiggins, J. S.; Mauritz, K. A., Polymer chain dynamics in epoxy based composites as investigated by broadband dielectric spectroscopy. *Arabian Journal of Chemistry* **2016**, *9* (2), 305-315.
24. Lairez, D.; Emery, J. R.; Durand, D.; Pethrick, R. A., Dielectric study of epoxy vitrification: does a percolation model apply? *Macromolecules* **1992**, *25* (26), 7208-7210.
25. Andjelić, S.; Mijović, J., Dynamics of Carbonyl-Modified-Epoxy/Amine Networks by FTIR and Dielectric Relaxation Spectroscopy. *Macromolecules* **1998**, *31* (24), 8463-8473.
26. Plazek, D. J.; Choy, I. C., The physical properties of bisphenol-a-based epoxy resins during and after curing. II. Creep behavior above and below the glass transition temperature. *J. Polym. Sci. Pol. Phys.* **1989**, *27* (2), 307-324.
27. Plazek, D. J.; Chay, I.-C., The evolution of the viscoelastic retardation spectrum during the development of an epoxy resin network. *J. Polym. Sci. Pol. Phys.* **1991**, *29* (1), 17-29.
28. Kohlrausch, R., Theorie des elektrischen Rückstandes in der Leidener Flasche. *Annalen der Physik* **1854**, *167* (2), 179-214.
29. Davidson, D. W.; Cole, R. H., Dielectric Relaxation in Glycerol, Propylene Glycol, and n-Propanol. *J. Chem. Phys.* **1951**, *19* (12), 1484-1490.
30. Alegría, A.; Guerrica-Echevarría, E.; Tellería, I.; Colmenero, J., Non-Debye dielectric relaxation around the liquid-glass transition of a glass-forming polymer. *Phys. Rev. B* **1993**, *47* (22), 14857-14865.
31. Garwe, F.; Schonhals, A.; Lockwenz, H.; Beiner, M.; Schroter, K.; Donth, E., Influence of Cooperative  $\alpha$  Dynamics on Local  $\beta$  Relaxation during the Development of the Dynamic Glass Transition in Poly(n-alkyl methacrylate)s. *Macromolecules* **1996**, *29* (1), 247-253.
32. Bergman, R.; Alvarez, F.; Alegria, A.; Colmenero, J., The merging of the dielectric  $\alpha$ - and  $\beta$ -relaxations in poly-(methyl methacrylate). *J. Chem. Phys.* **1998**, *109* (17), 7546-7555.
33. Dionísio, M.; Fernandes, A. C.; Mano, J. F.; Correia, N. T.; Sousa, R. C., Relaxation Studies in PEO/PMMA Blends. *Macromolecules* **2000**, *33* (3), 1002-1011.
34. Qi, F.; Goresy, T. E.; Bohmer, R.; Doss, A.; Diezemann, G.; Hinze, G.; Sillescu, H.; Blochowicz, T.; Gainaru, C.; Rossler, E. A.; Zimmermann, H., Nuclear magnetic resonance and dielectric spectroscopy of a simple supercooled liquid: 2-methyl tetrahydrofuran. *J. Chem. Phys.* **2003**, *118* (16), 7431-7438.
35. Minoguchi, A.; Kitai, K.; Nozaki, R., Difference and similarity of dielectric relaxation processes among polyols. *Phys Rev E* **2003**, *68*, 031501.
36. Tyagi, M.; Alegria, A.; Colmenero, J., Heterogeneous dynamics of poly(vinyl acetate) far above  $T_g$ : A combined study by dielectric spectroscopy and quasielastic neutron scattering. *J. Chem. Phys.* **2005**, *122* (24), 244909.

37. Power, G.; Vij, J. K.; Johari, G. P., Orientation polarization from faster motions in the ultraviscous and glassy diethyl phthalate and its entropy. *J. Chem. Phys.* **2006**, *124*, 044513.
38. Zhao, J.; McKenna, G. B., Response to “Comment on ‘Temperature divergence of the dynamics of a poly(vinyl acetate) glass: Dielectric vs. mechanical behaviors’” [J. Chem. Phys. *139*, 137101 (2013)]. *J. Chem. Phys.* **2013**, *139* (13), 137102.
39. Svajdlenkova, H.; Ruff, A.; Lunkenheimer, P.; Loidl, A.; Bartos, J., Primary  $\alpha$  and secondary  $\beta$  relaxation dynamics of meta-toluidine in the liquid state investigated by broadband dielectric spectroscopy. *J. Chem. Phys.* **2017**, *147*, 084506.
40. Tikhonov, A. N.; Arsenin, V. Y., *On the solution of ill-posed problems*. Wiley: New York, 1977; p 258.
41. Honerkamp, J.; Weese, J., Tikhonovs regularization method for ill-posed problems. *Continuum Mech. Thermodyn.* **1990**, *2* (1), 17-30.
42. Schäfer, H.; Sternin, E.; Stannarius, R.; Arndt, M.; Kremer, F., Novel Approach to the Analysis of Broadband Dielectric Spectra. *Phys. Rev. Lett.* **1996**, *76* (12), 2177-2180.
43. Tuncer, E.; Macdonald, J. R., Comparison of methods for estimating continuous distributions of relaxation times. *J. Appl. Phys.* **2006**, *99* (7), 074106.
44. Zasetsky, A. Y.; Buchner, R., Quasi-linear least squares and computer code for numerical evaluation of relaxation time distribution from broadband dielectric spectra. *J. Phys.-Condens. Mat.* **2010**, *23* (2), 025903.
45. Domínguez-Espinosa, G.; Ginestar, D.; Sanchis, M. J.; Díaz-Calleja, R.; Riande, E., Retardation time spectra computed from complex compliance functions. *J. Chem. Phys.* **2008**, *129* (10), 104513.
46. Pisignano, D.; Capaccioli, S.; Casalini, R.; Lucchesi, M.; Rolla, P. A.; Justl, A.; Rössler, E., Study of the relaxation behaviour of a tri-epoxy compound in the supercooled and glassy state by broadband dielectric spectroscopy. *J. Phys.-Condens. Mat.* **2001**, *13* (20), 4405-4419.
47. Rouse Jr., P. E., A Theory of the Linear Viscoelastic Properties of Dilute Solutions of Coiling Polymers. *The Journal of Chemical Physics* **1953**, *21* (7), 1272-1280.
48. Gurtovenko, A. A.; Gotlib, Y. Y., Intra- and Interchain Relaxation Processes in Meshlike Polymer Networks. *Macromolecules* **1998**, *31* (17), 5756-5770.
49. Gurtovenko, A. A.; Gotlib, Y. Y., Viscoelastic Dynamic Properties of Meshlike Polymer Networks: Contributions of Intra- and Interchain Relaxation Processes. *Macromolecules* **2000**, *33* (17), 6578-6587.
50. Casalini, R.; Roland, C. M., Aging of the Secondary Relaxation to Probe Structural Relaxation in the Glassy State. *Phys. Rev. Lett.* **2009**, *102* (3), 035701.
51. Capaccioli, S.; Prevosto, D.; Lucchesi, M.; Rolla, P. A.; Casalini, R.; Ngai, K. L., Identifying the genuine Johari–Goldstein  $\beta$ -relaxation by cooling, compressing, and aging small molecular glass-formers. *J. Non-Cryst. Solids* **2005**, *351* (33), 2643-2651.

52. Dhinojwala, A.; Wong, G. K.; Torkelson, J. M., Rotational reorientation dynamics of dispersed 1 in polystyrene:  $\alpha$ -relaxation dynamics probed by second harmonic generation and dielectric relaxation. *J. Chem. Phys.* **1994**, *100* (8), 6046-6054.
53. Kremer, F.; Schonhals, A., Broadband Dielectric Measurement Techniques ( $10^{-6}$  Hz to  $10^{12}$  Hz). In *Broadband Dielectric Spectroscopy*, Kremer, F.; Schonhals, A., Eds. Springer-Verlag: Berlin, Heidelberg, 2003; pp 35-56.
54. Zetsche, A.; Kremer, F.; Jung, W.; Schulze, H., Dielectric study on the miscibility of binary polymer blends. *Polymer* **1990**, *31* (10), 1883-1887.
55. Ezquerro, T. A.; Majszczyk, J.; Baltà-Calleja, F. J.; López-Cabarcos, E.; Gardner, K. H.; Hsiao, B. S., Molecular dynamics of the  $\alpha$  relaxation during crystallization of a glassy polymer: A real-time dielectric spectroscopy study. *Phys. Rev. B* **1994**, *50* (9), 6023-6031.
56. Urakawa, O.; Ujii, T.; Adachi, K., Dynamic heterogeneity in a miscible poly(vinyl acetate)/poly(ethylene oxide) blend. *J. Non-Cryst. Solids* **2006**, *352*, 5042-5049.
57. Schneider, U.; Lunkenheimer, P.; Brand, R.; Loidl, A., Dielectric and far-infrared spectroscopy of glycerol. *J. Non-Cryst. Solids* **1998**, *235-237*, 173-179.
58. Brand, R.; Lunkenheimer, P.; Schneider, U.; Loidl, A., Excess wing in the dielectric loss of glass-forming ethanol: A relaxation process. *Phys. Rev. B* **2000**, *62* (13), 8878-8883.
59. Hintermeyer, J.; Herrmann, A.; Kahlau, R.; Goiceanu, C.; Rossler, E. A., Molecular Weight Dependence of Glassy Dynamics in Linear Polymers Revisited. *Macromolecules* **2008**, *41* (23), 9335-9344.
60. Delbreilh, L.; Dargent, E.; Grenet, J.; Saiter, J.-M.; Bernes, A.; Lacabanne, C., Study of poly(bisphenol A carbonate) relaxation kinetics at the glass transition temperature. *Eur. Polym. J.* **2007**, *43* (1), 249-254.
61. Lorthioir, C.; Alegria, A.; Colmenero, J.; Deloche, B., Heterogeneity of the Segmental Dynamics of Poly(dimethylsiloxane) in a Diblock Lamellar Mesophase: Dielectric Relaxation Investigations. *Macromolecules* **2004**, *37* (20), 7808-7817.
62. Casalini, R.; Snow, A. W.; Roland, C. M., Temperature Dependence of the Johari–Goldstein Relaxation in Poly(methyl methacrylate) and Poly(thiomethyl methacrylate). *Macromolecules* **2013**, *46* (1), 330-334.
63. Bartos, J.; Sausa, O.; Schwartz, G. A.; Alegria, A.; Alberdi, J. M.; Arbe, A.; Kristiak, J.; Colmenero, J., Positron annihilation and relaxation dynamics from dielectric spectroscopy and nuclear magnetic resonance: Cis–trans-1,4-poly(butadiene). *J. Chem. Phys.* **2011**, *134* (16), 164507.
64. Bogoslovov, R. B.; Hogan, T. E.; Roland, C. M., Clarifying the Molecular Weight Dependence of the Segmental Dynamics of Polybutadiene. *Macromolecules* **2010**, *43* (6), 2904-2909.
65. Elfadl, A. A.; Kahlau, R.; Herrmann, A.; Novikov, V. N.; Rossler, E. A., From Rouse to Fully Established Entanglement Dynamics: A Study of Polyisoprene by Dielectric Spectroscopy. *Macromolecules* **2010**, *43* (7), 3340-3351.

66. Mijovic, J.; Sun, M.; Han, Y., Normal and Segmental Mode Dynamics of End-Functionalized Poly(propylene oxide) by Dielectric Relaxation Spectroscopy and Dynamic Mechanical Spectroscopy. *Macromolecules* **2002**, *35* (16), 6417-6425.
67. Casalini, R.; Fioretto, D.; Livi, A.; Lucchesi, M.; Rolla, P. A., Influence of the glass transition on the secondary relaxation of an epoxy resin. *Phys. Rev. B* **1997**, *56* (6), 3016-3021.
68. Schneider, U.; Lunkenheimer, P.; Brand, R.; Loidl, A., Broadband dielectric spectroscopy on glass-forming propylene carbonate. *Phys Rev E* **1999**, *59* (6), 6924-6936.
69. Dixon, P. K.; Wu, L.; Nagel, S. R., Scaling in the Relaxation of Supercooled Liquids. *Phys. Rev. Lett.* **1990**, *65* (9), 1108-1111.
70. Nakanishi, M.; Nozaki, R., Systematic study of the glass transition in polyhydric alcohols. *Phys Rev E* **2011**, *83* (5), 051503.
71. Fukao, K.; Uno, S.; Miyamoto, Y.; Hoshino, A.; Miyaji, H., Dynamics of  $\alpha$  and  $\beta$  processes in thin polymer films: Poly (vinyl acetate) and poly(methyl methacrylate). *Phys Rev E* **2001**, *64* (5), 051807.
72. Psarras, G. C.; Soto Beobide, A.; Voyiatzis, G. A.; Karahaliou, P. K.; Georga, S. N.; Krontiras, C. A.; Sotiropoulos, J., Dielectric and Conductivity Processes in Poly(ethylene terephthalate) and Poly(ethylene naphthalate) Homopolymers and Copolymers. *J. Polym. Sci. Pol. Phys.* **2006**, *44* (21), 3078-3092.
73. Tyagi, M.; Alegría, A.; Colmenero, J., Broadband dielectric study of oligomer of poly(vinyl acetate): A detailed comparison of dynamics with its polymer analog. *Phys Rev E* **2007**, *75* (6), 061805.
74. Mashimoto, S.; Nozaki, R.; Yagihara, S.; Takeishi, S., Dielectric relaxation of poly(vinyl acetate). *J. Chem. Phys.* **1982**, *77* (12), 6259-6262.
75. Fitz, B. D.; Mijovic, J., Segmental Dynamics in Poly(methylphenylsiloxane) Networks by Dielectric Relaxation Spectroscopy. *Macromolecules* **1999**, *32* (10), 3518-3527.
76. Kirst, K. U.; Kremer, F.; Pakula, T.; Hollingshurst, J., Molecular dynamics of cyclic and linear poly(dimethylsiloxanes). *Colloid. Polym. Sci.* **1994**, *272* (11), 1420-1429.
77. Power, G.; Johari, G. P.; Vij, J. K., Relaxation strength of localized motions in D-sorbitol and mimicry of glass-softening thermodynamics. *J. Chem. Phys.* **2003**, *119* (1), 435-442.

### 3. LINEAR VISCOELASTIC RELAXATION IN THE $\alpha$ AND $\alpha+$ REGIONS OF LINEAR POLYMERS, CROSSLINKED POLYMERS AND SMALL MOLECULES

This chapter contains submitted manuscript to Polymers. In this chapter, I synthesized EPON 1009F-MDA, phenoxy and EPON 825-MDA specimen, performed Dynamic Mechanical Analysis (MDA), and analyzed dynamic mechanical data of phenoxy, EPON 825-MDA and digitized literature data using spectrum method. David B. Curliss synthesized a series of EPON resins cured with DDS and performed DMA experiments. Grigori A. Medvedev analyzed EPON 1009F-MDA and EPON 828 resin.

The dynamic linear viscoelastic behavior in the region above  $T_g$  was studied for a series of diglycidyl ether of bisphenol-A (DGEBA) based epoxy resins cured with methylenedianiline (MDA) and diphenyl diamino sulfone (DDS) as well as phenoxy resin, which is a linear DGEBA-based polymer. Master curves were constructed from the frequency dependent storage and loss isotherms. The relaxation spectra were determined, where two different relaxation processes were seen: the  $\alpha$ -process that precedes formation of the glass and a  $\alpha+$ -process that occurs at longer relaxation times and higher temperatures. The relaxation spectrum was also determined from reported dielectric relaxation data for the DGEBA monomer (Casalini et al. Phys. Rev. B, 1997). For the tighter amine cured DGEBA systems a single broad relaxation peak was observed vs a loose DGEBA network and phenoxy thermoplastic that exhibited both an  $\alpha$ -process that is narrower than the tighter DGEBA networks and a shoulder at longer relaxation times that is identified as an  $\alpha+$ -process. The molecular origin of the  $\alpha+$ -process is uncertain, but could be the beginning of the Rouse modes, a network relaxation processes or some other long time processes. The DGEBA monomer exhibited a relaxation spectrum with a very abrupt end at relaxation times that are just a little bit larger than the relaxation time at the peak of the  $\alpha$ -process. The transition between the tighter networks with the broad  $\alpha$  relaxation process and the phenoxy and looser networks occurs over a very narrow molecular weight range. Relaxation data for other polymer, oligomer and small molecule systems exhibit similar dependence of the relaxation spectrum upon molecular structure. For the series of DGEBA materials the temperature dependence of  $\log a_T$  exhibits two branches when adjusted for  $T_g$ : the tight DGEBA networks all exhibit the steep  $\log a_T$



temperature dependence vs the DGEBA monomer, phenoxy and looser DGEBA networks, including networks with defects from the presence of monoamines, exhibiting the less steep  $\log a_T$  temperature dependence. Relaxation spectrum for moderately crosslinked EPON1009F-MDA system consists of  $\alpha$  and  $\alpha+$  components with different temperature dependencies; intriguingly, temperature dependence of  $\log a_T$  for the main  $\alpha$ -process follows the steep branch vs the  $\alpha+$ -process following the less steep branch.

### 3.1 Introduction

Key features of amorphous polymers and other glass forming materials in the glass-to-rubber transition region above  $T_g$  are (i) the super-Arrhenian temperature dependence of the mobility and (ii) the relaxation spectrum with the main process, typically designated as the  $\alpha$ -relaxation process, having a wedge-like shape. There has been considerable effort in developing an understanding of the super-Arrhenian temperature dependence of the mobility, where a variety of models have been proposed including free volume,[1-3] excess/configurational entropy,[4] excess/configuration internal energy,[5, 6] density scaling,[7] etc. There has been much less work done on developing a fundamental understanding of the shape of the relaxation spectrum for the  $\alpha$ -process. There have been studies where the  $\alpha$ -relaxation spectrum has been measured using various experimental techniques (see discussion below). However, there is no agreed upon fundamental model of the spectral shape, even though there have been several attempts at molecular models.[8, 9] The  $\alpha$ -relaxation spectrum is asymmetric on  $\log$  (time) scale with a peak at long times followed at shorter times (i.e., on the left-hand side of the spectrum) by the so-called excess wing that decays in an approximately linear fashion with respect to the logarithm of the relaxation time. One of the key questions regarding the relaxation spectrum is the shape of long relaxation time slope of the  $\alpha$ -peak (i.e., on the right-hand side of the spectrum). Specifically, whether the decrease with increasing relaxation time is rapid or gradual – a feature that has important implications in the development of any model for describing the  $\alpha$ -relaxation. Critically, the emergence of additional relaxation processes at long times that we here designate as the alpha-plus,  $\alpha+$ , processes can confound observation of long relaxation time region of the  $\alpha$ -spectrum. These longer time processes may include the beginning of the Rouse modes for linear polymers or network relaxation processes for crosslinked polymers; however, since the origin of these longer time processes is not

established, we use the designation  $\alpha+$  without any specific assignment of molecular mechanism. The objective of this paper is to critically examine the relaxation spectra in the  $\alpha$  and  $\alpha+$  region by (i) measuring the linear viscoelastic relaxation behavior for a series of epoxide resins of differing crosslink density including a thermoplastic with the same repeat unit and (ii) assessing the literature for other polymeric and molecular glass formers where the relaxation data has been reported.

The relaxation behavior of glass forming materials in the transition zone has been studied by several experimental techniques, including linear viscoelastic measurements, broadband dielectric spectroscopy, photon correlation spectroscopy, and field-cycling NMR relaxometry. In each of these techniques the final result is frequency dependent in-phase/storage and out-of-phase/loss susceptibilities. These storage and loss susceptibilities are obtained for several temperatures in the transition zone and then analyzed to extract the relaxation spectrum. The preferred method of analysis involves frequency-temperature superposition as a first step, and when superposition does not hold (i.e. the material is thermo-rheologically complex) alternative analysis procedures that are beyond the scope of this paper are required.[10] Although straightforward in principle, this program has been carried out fully only for a small number of molecular and polymeric glass formers, because experiments in the transition zone (where the storage susceptibility changes by orders-of-magnitude over a relatively narrow temperature range) are challenging. For linear viscoelastic measurements the parallel plate or cone-and-plate setup performs well at higher temperatures, but it becomes progressively more difficult to prevent slippage as the temperature is lowered toward  $T_g$ , and the frequency range of mechanical experiments is limited to less than 100Hz due to inertia effects. Broadband dielectric spectroscopy has the largest frequency range; however, for many materials, especially polymers, the effects of conduction and electrode polarization[11] conspire to obscure the intrinsic relaxation response at lower frequencies. The photon correlation spectroscopy technique does not suffer from the same shortcoming as the dielectric spectroscopy, e.g. the study of n-propanol where the  $\alpha$ -process was seen vs spurious processes seen in dielectric spectroscopy.[12] However, analysis of the photon correlation spectroscopy data involves conversion of the measured intensity autocorrelation function  $g_2(t)$  into the orientation autocorrelation function  $g_1(t)$  using an empirical equation, where it is the function  $g_1(t)$  that is analyzed to obtain the generalized susceptibility. Field-cycling NMR relaxometry is a

versatile technique for analysis of both molecular and polymeric glass formers;[13] however, it also involves analysis steps that rely on model assumptions.[14] In summary, linear viscoelastic experiments provide the most direct information on the susceptibility (i.e. viscoelastic shear moduli in this case) without the parasitic processes that often obscure dielectric relaxation, but are challenging to carry out in the transition zone. From this perspective the *crosslinked* polymer systems represent a ‘sweet spot’, since for these materials the torsion bar setup works well both in the vicinity of  $T_g$  and at higher temperatures vs parallel plates required for molecular glass formers and uncrosslinked polymers.

Using the combination of the methods described in the previous paragraph with an emphasis on field-cycling NMR, Rossler and coworkers studied the relaxation spectra in the  $\alpha$  and  $\alpha+$  regions for several polymer systems, including polybutadiene (PBd), polyisoprene (PI), polystyrene (PS), polydimethylsiloxane (PDMS), and poly(propylene glycol) (PPG) where the molecular weight was systematically varied from monomer to high molecular weight linear polymers.[15-17] The effect of molecular architecture was explored using dendrimers of PPG vs linear PPG.[13] They observed that segmental dynamics associated with the  $\alpha$ -process are universal, while longer relaxation time  $\alpha+$  processes are material dependent. Polymers can exhibit a range of relaxation behaviors – from Rouse-like to entanglement dominated, depending upon the molecular weight. For molecular glass formers the storage and loss susceptibilities at low frequencies exhibit the asymptotic behavior  $\chi' \sim \omega^2$  and  $\chi'' \sim \omega$ , respectively, that corresponds to the longest relaxation time Debye process. In contrast, polymeric systems exhibit a broad shoulder in the loss isotherms described by a power law, i.e.  $\chi'' \sim \omega^n$ , where the exponent  $n$  passes through several regimes typically between 0.5 (the Rouse value[18]) and 0.9. Terminal relaxation with  $\chi' \sim \omega^2$  and  $\chi'' \sim \omega$  is still obtained at sufficiently low frequencies. The studies described above provide important insight into the relaxation processes present in the long time region of the  $\alpha$ -process; however, a similar analysis has not been performed for linear viscoelastic relaxation behavior of crosslinked polymeric systems, which will be a focus of this paper.

The determination of the linear viscoelastic behavior above  $T_g$  typically employs a well-developed methodology to probe the relaxation processes in polymers. Specifically, the material response is

assumed to be thermo-rheologically simple, where the temperature dependence of the  $\log a_T$  shift function is usually described using the empirical VFT[19-21](or the equivalent WLF[22]) equation. However, thermo-rheological simplicity may not be a good assumption even for single-phase polymers, but only an approximation resulting from the relatively narrow window of accessible frequencies or times available in linear viscoelastic experiments. In a recent paper,[10] the relaxation behavior of the  $\alpha$ -process, including the excess wing and the  $\alpha^+$  region was investigated for a diglycidyl ether of bisphenol-A di-epoxide (DGEBA) cured with methylene dianiline (MDA). Dynamic shear  $G'$  and  $G''$  data were combined with transient  $G(t)$  data to construct numerous isotherms that spanned nearly six orders-of-magnitude to provide the most extensive set of linear viscoelastic data for any glass forming material. The linear viscoelastic response was thermo-rheologically complex even though the DGEBA-MDA epoxy network is a single-phase material. The material possessed two distinct relaxation regions: (i) an  $\alpha$ -process that exhibits a maximum in the  $G''$  response with an excess wing that decays as the relaxation time decreases and (ii) an  $\alpha^+$ -process at longer times that appears as a distinct shoulder on the long-time side of the main  $\alpha$ -peak. Although both the  $\alpha^-$  and  $\alpha^+$ -processes are individually thermo-rheologically complex, to a zero order approximation each process can be treated as thermo-rheologically simple, but with different super-Arrhenian temperature dependencies.

Most studies of the viscoelastic behavior of polymers are just a temperature scan of a viscoelastic property like the storage or loss modulus as a function of temperature at a single frequency, which does not fully probe the relaxation behavior. Proper measurement of the linear viscoelastic response requires measurement of the time or frequency dependence at various temperatures, which is the focus of this work. The frequency/time dependent linear relaxation behavior above  $T_g$  has been studied for numerous linear polymers.[23] Studies of the linear viscoelastic response for network polymers are more limited, but do include epoxy resins,[24-26] crosslinked polyesters,[27] PMMA,[28] poly(2-ethoxyethyl methacrylate),[29] and polyurethane.[30] Of particular interest are two studies by Plazek and Choy[31, 32] where they measured the linear viscoelastic recoverable compliance for a series of cured DGEBA epoxies that included both on- and off-stoichiometric materials. In these studies, they observed the emergence of a shoulder in the retardation spectrum on the long-time side of the  $\alpha$ -peak that they attributed to an entanglement

network. However, the epoxy resins have a molecular weight between crosslinks that is well below the entanglement molecular weight; thus, it is difficult to see how this second relaxation shoulder can be a result of entanglements. In the Discussion section we will provide more extensive analysis of literature data on the linear viscoelastic relaxation behavior of linear and network polymers as well as oligomers and small molecule glass formers.

The paper is organized as follows: First the experimental methods will be provided. Then the linear viscoelastic relaxation data for the series of DGEBA will be presented in the Results section, followed by the Discussion section which will provide a comparative analysis of the relaxation spectra for both the DGEBA series studied in this paper and other polymeric and molecular glass forming systems that have been reported in the literature. More detailed analysis of the relaxation behavior of the DGEBA-DDS series of materials studied here and of the literature data is provided in the Appendix D.

### 3.2 Experimental

A series of linear and crosslinked diglycidal ether bisphenol-A (DGEBA) polymers will be studied. The crosslinked polymers were synthesized using diepoxide DGEBA resins with differing molecular weight as shown in Figure 3.1, that were cured with 4,4'-methylenedianiline (MDA) or 4,4'-diaminodiphenyl sulfone (DDS). A high molecule linear DGEBA thermoplastic is phenoxy, where the terminal group in the phenoxy is hydroxyl group. The protocols for making specimens for each of these resin systems will now be described.

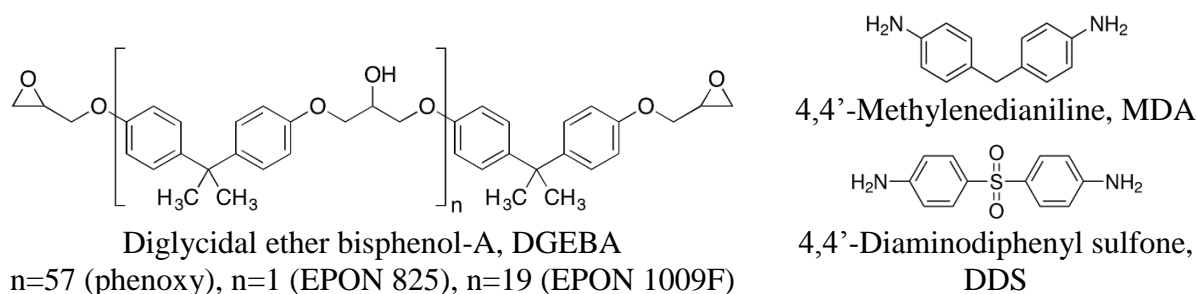


Figure 3.1. Molecular structures of DGEBA materials and di-amine crosslinkers.

The phenoxy PKHJ thermoplastic (Gabriel Phenoxies, Inc.) has a  $M_n = 16$  kg/mol and  $M_w = 57$  kg/mol as quoted by the manufacturer. Phenoxy sheets were made as follows: pellets were degassed and compressed into a sheet using a two-roll mill where the rolls were heated at 160 °C to reduce the number of bubbles, transferred into a 6 in  $\times$  4 in metal mold, and a 2mm-thick phenoxy sheet was made by compression molding under 1250 psi in a heat press at 130 °C. Circular specimens of 8mm and 25mm diameters were cut from the sheet for mechanical testing in an ARES-G2 rheometer using parallel plate geometry. Strip specimens used in the torsion bar experiments were made using a surface grinder with a diamond cut-off wheel. The circular specimens used in the parallel plate experiments were made as follows: the phenoxy sheet was placed on a flat metal support that was heated to 130 °C, and then a sharp circular die was pushed through the heated material using a hand hydraulic press. All test specimens were then heated in the vacuum oven at 110 °C for 30 mins to remove any residual moisture that may have been absorbed in the specimen manufacturing process. The  $T_g$  of specimen was 98 °C determined in a 10 °C/min heating ramp with a Q2000 DSC (TA Instruments).

EPON825 (Hexion Inc.) DEGBA diepoxide resin has an epoxy equivalent of 171 g/mol as determined by titration.[33] The EPON825 was cured with a stoichiometric amount of 4,4'-methylenedianiline, MDA, (Sigma-Aldrich) to make EPON825-MDA test specimens. The procedure for making the EPON825-MDA specimens is as follows: (1) MDA pellets were ground into powder; (2) powdered MDA was added into EPON 825 liquid resin via continuous magnetic stirring, where the mixing was complete after 5 min at 100 °C which is the melting point of MDA; (3) the pre-cure mixture was placed in a vacuum oven at -80 kPa at 40 °C for 15 minutes to remove gas entrapped during mixing; (4) the mixture was poured into a mold that was a pair of glass plates separated by a Teflon-encapsulated O-ring spacer, where the inner surfaces of glass plates were pretreated with a 1,1-difluoroethane powder mold release (MR™311 Dry Film Release Agent Aerosol, Sprayon Products); and, (5) the mixture in the mold was cured at 120 °C for 30 mins, then 160 °C for 1.5 hrs and finally post-cured at 200 °C for 10 hrs.

EPON1009F (Hexion, Inc.) DEGBA resin has an epoxide equivalent 2737 g/mol as determined by titration.[33] The EPON1009F diepoxide resin was cured with a stoichiometric amount of 4,4'-methylenedianiline, MDA, (Sigma-Aldrich) to make EPON1009F-MDA test specimens. Because

EPON1009F has a much higher viscosity than EPON825, the test sheets required a different manufacturing procedure that has been described elsewhere.[10]

The EPON series of DEGBA resins are commercial products. The molecular weight distribution of the EPON resins were determined via GPC analysis using the follow procedure: (i) the resin was dissolved in THF to produce a 5 mg/ml solution; (ii) the solution was equilibrated at room temperature for 4 hrs to ensure complete dissolution; (iii) the resulting solution was passed through a 0.20  $\mu\text{m}$  filter to remove any particulate matter; (iv) GPC analysis was performed using a Viscotek GPCmax VE 2001. The samples were injected into the 200  $\mu\text{L}$  injection loop and passed through Viscotek T2000 and T2500 6  $\mu\text{m}$  Org GPC/SEC columns in series inside of a 35  $^{\circ}\text{C}$  oven with a flow rate of 1.0 ml/min. Both the differential RI detector and a capillary viscometer were employed. Refractive index increment ( $dn/dc$ ) of EPON1009F was determined to be 0.203 ml/g from the RI peak. The molecular weights dependence of the GPC elution volume was determined using polystyrene standards with molecular weights from 890 g/mol to 47,300 g/mol, which were then corrected to account for the difference between polystyrene and the DGEBA using a procedure described in the SI. The GPC traces of the various resins are shown in the SI, including the  $\bar{M}_n$  and  $\bar{M}_w$  for each of the EPON resins. The EPON828 resin is primarily the monomer with a very small amount of dimer and trimer, and EPON825 is a purified version of the EPON828 resin where most of the dimers and trimers have been removed. The rest of the EPON series of resins are mixtures of DGEBA diepoxides with a broad distribution of molecular weights. It is important to measure the molecular weight distribution of non-monomeric epoxy resins to be aware of possible compositional variations even if the epoxide equivalent of different resin batches are the same.

EPON828 through EPON1009F purchased from Shell were cured with a stoichiometric amount of 4,4'-diaminodiphenyl sulfone, DDS.[34] The epoxide equivalent molecular weights were determined via titration and are given in Table 1. The EPON828-DDS through EPON1002F-DDS sheets were manufactured in the same manner to the EPON825-MDA sheets. The EPON1004F-DDS through EPON1009F-DDS have a high viscosity in liquid state. Thus, these sheets for these resin systems were manufactured in a similar manner to EPON825-MDA with changes in three steps: (i) in step (2) the mixture was quenched and ground into a powder before being transferred

into the mold; (ii) in step (4) a metal compression mold was used; and, (iii) in step (5) the mixture was cured at 200 °C for 10 hrs under a pressure of 1.5 to 2 ksi and then post-cured at 200 °C for 10 hrs under 0.1 to 0.2 ksi.

Table 3.1. Characteristics of DGEBA resins.

<b>DGEBA</b>	<b>EEW (g/mol)</b>	<b>Crosslinker</b>	<b>T<sub>g</sub> (°C)</b>
EPON825	171	MDA	185
EPON828	189	DDS	204
EPON834	245	DDS	171
EPON1001F	536	DDS	127
EPON1002F	678	DDS	119
EPON1004F	842	DDS	102
EPON1007F	1862	DDS	97
EPON1009F	3050	DDS	95
EPON1009F	2737	MDA	102

Sheets were cut into rectangular specimens using a surface grinder with a diamond cut-off blade (for MDA-cured samples), or with a high speed water cooled abrasive saw (for DDS-cured samples). Test specimens were annealed at 200 °C under 80 torr for 2 hours to remove any residual moisture. All specimens were stored in an airtight bag filled with desiccants until mounted onto the rheometer. T<sub>g</sub> of the various cured resins listed in 1 were determined using (i) DSC at a 10 °C/min heating rate for MDA-cured specimens, and (ii) dilatometer for DDS-cured specimens.

For the phenoxy and MDA cured specimens an ARES G2 Rheometer (TA Instruments) was used to determine the linear viscoelastic dynamic response. Torsion bar geometry was used for the EPON825-MDA and EPON1009F-MDA specimens and the parallel plate geometry was used for the phenoxy material. Test temperatures ranged from T<sub>g</sub> to the highest possible temperature before specimen began to discolor on the surface, indicating the start of degradation. Specimens were allowed to equilibrate for 15 mins at each temperature before beginning the frequency scan from 0.01 Hz to 50 Hz. Strains increased from 0.01% (near T<sub>g</sub>) to 1% (at T<sub>g</sub>+20 °C and above). The specimen was continuously bathed in nitrogen gas to prevent moisture absorption and reduce oxidation.



The dynamic mechanical response in torsion for the DDS cured specimens was measured on a Rheometrics RMS-800/RDS-II spectrometer with a 2kg normal and torsional force load cell, using a bar specimen. Isotherms were obtained at frequencies from 0.1 to 100 rad/s from  $-150^{\circ}\text{C}$  to  $T_g+50^{\circ}\text{C}$ . In order to remain in the linear viscoelastic region yet have the maximum signal, the strain was 0.1% below  $T_g$ , 0.3 and 0.5% strain near and above  $T_g$ .

### 3.3 Results

The effect of crosslink density on the linear viscoelastic relaxation spectrum has been determined for a chemically homologous series of two DGEBA-based epoxy network polymers, one cured with MDA and second cured with DDS, and the associated uncrosslinked phenoxy thermoplastic. For the MDA cured epoxy networks EPON1009F diepoxide with an average eighteen DGEBA repeat unit (although as shown in the Appendix EPON1009F has a broad distribution of molecular weights) is compared with a network made with EPON825 that has only one DGEBA repeat unit (with an very small amount of trimer). For the DDS cured system a set of 7 diepoxide networks will be reported from the EPON828 material, which has slightly more dimer/trimer content than the monomer EPON825, to the EPON1009F with its larger molecular weight.

#### 3.3.1 Linear Relaxation Behavior of EPON1009F-MDA

The linear viscoelastic  $G'$  and  $G''$  storage and loss shear moduli isotherms of EPON1009F-MDA in the temperature range from  $100^{\circ}\text{C}$  (i.e.  $T_g - 1.5^{\circ}\text{C}$ ) to  $180^{\circ}\text{C}$  have been reported elsewhere,[10] where it was found that the frequency-temperature superposition procedure for this material fails. Specifically, lack of superposition is apparent in case of the  $112.5^{\circ}\text{C}$ ,  $115^{\circ}\text{C}$  and  $120^{\circ}\text{C}$  isotherms as shown in Figure 3.2. It was also reported [10] that the isotherms for the temperatures from  $130^{\circ}\text{C}$  to  $180^{\circ}\text{C}$  can be shifted along the frequency axis to achieve superposition, where the corresponding master curves are shown in Figure 3.3. The highest frequency data points are adversely affected by inertia effects. Also the highest temperature isotherm, i.e.  $180^{\circ}\text{C}$ , begins to exhibit inconsistent behavior at the lowest frequencies, which we attribute to difficulty of maintaining the desired shear kinematic field for the bar specimen when the modulus becomes too low.

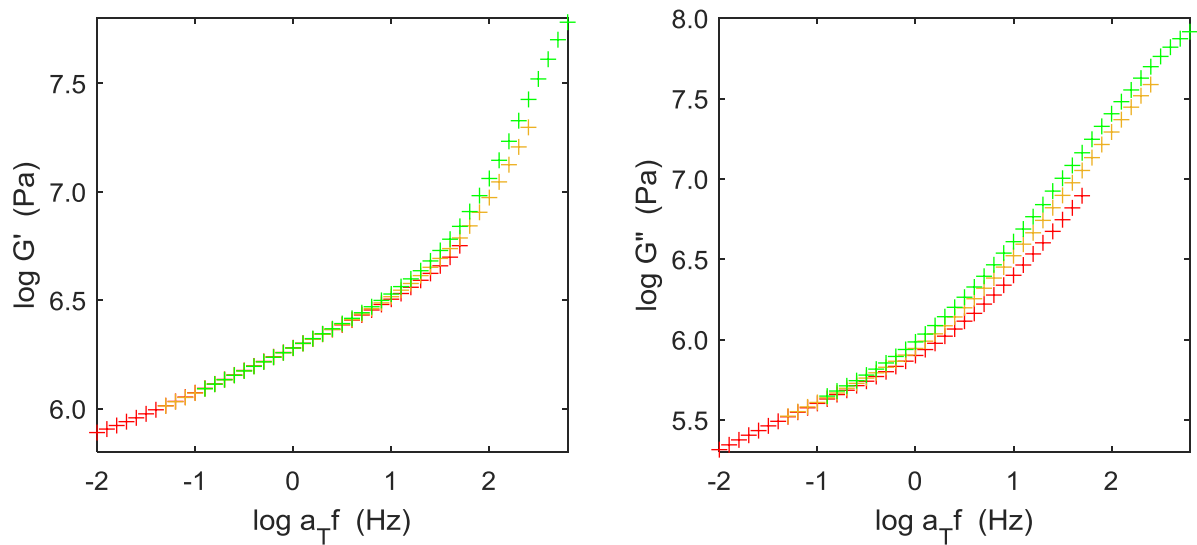


Figure 3.2. Attempted superposition of  $G'$  storage and  $G''$  loss isotherms for EPON1009F-MDA epoxy. Temperatures: 112.5°C – green, 115°C – orange, 120°C – red.

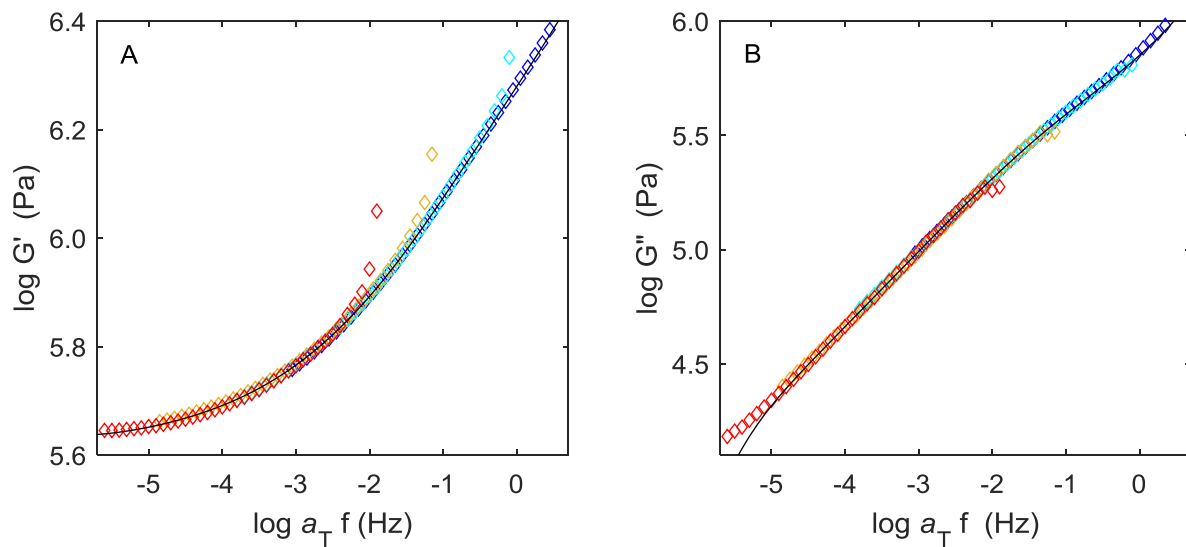


Figure 3.3. EPON1009F-MDA  $G'$  (A) and  $G''$  (B) master curves via frequency-temperature superposition of the isotherms from Ref. [10] with a reference temperature  $T_{\text{ref}} = 130^\circ\text{C}$  and the  $\log a_T$  shift factor shown in Figure 3.4A (pluses). Symbols indicate isotherms: 130°C – blue, 140°C – cyan, 160°C – orange, 180°C – red diamonds. Solid line is fit using the component of the relaxation spectrum in Figure 3.3B marked as  $\alpha^+$ .

The standard spectral representation[23] used to fit the storage and loss master curves is

$$\begin{aligned} G' &= G_{\infty} + \int_{-\infty}^{\infty} H(\log \tau) \frac{f^2 \tau^2}{1 + f^2 \tau^2} d \log \tau \\ G'' &= \int_{-\infty}^{\infty} H(\log \tau) \frac{f \tau}{1 + f^2 \tau^2} d \log \tau \end{aligned} \quad (3.1)$$

In principle, failure of the overall superposition procedure requires a more sophisticated analysis for obtaining the relaxation spectrum, for example along the lines outlined in Ref. [10]. However, it is sufficient for the purpose of this paper (and for the limited temperature range above  $T_g$  of interest here) to assume that the relaxation spectrum consists of at least two components, each with its own temperature dependence. In other words, the Equation (3.1) is replaced with an additive ansatz

$$\begin{aligned} G' &= G_{\infty} + \int_{-\infty}^{\infty} H^{\alpha+}(\log \tau) \frac{f^2 \tau^2}{1 + f^2 \tau^2} d \log \tau + \int_{-\infty}^{\infty} H^{\alpha}(\log \tau) \frac{f^2 \tau^2}{1 + f^2 \tau^2} d \log \tau \\ G'' &= \int_{-\infty}^{\infty} H^{\alpha+}(\log \tau) \frac{f \tau}{1 + f^2 \tau^2} d \log \tau + \int_{-\infty}^{\infty} H^{\alpha}(\log \tau) \frac{f \tau}{1 + f^2 \tau^2} d \log \tau \end{aligned} \quad (3.2)$$

The two spectral components, denoted as the  $\alpha^{+}$ - and  $\alpha$ -processes, are shown in Figure 3.3B, where their temperature dependencies are shown in Figure 3.4A. The fits to  $G'$  and  $G''$  isotherms for the temperature range from 100°C to 130°C using Equation (3.2) with the  $\alpha$ - and  $\alpha^{+}$ -components shifted separately using the shift factors in Figure 3.4A are shown in Figure 3.5. The  $\alpha$  spectrum has well defined peak; in contrast, the  $\alpha^{+}$  spectrum abruptly ends at lower relaxation times. The latter behavior is not unusual, for example the relaxation spectrum for the Rouse model has a minimum relaxation time (and, at shorter relaxation times, has a shape that is similar to that of the  $\alpha^{+}$  process in Figure 3.4B). The reason for thermo-rheologically complex response of the EPON1009F-MDA system is apparent from Figure 3.4A as the temperature shift factors for  $\alpha$ - and  $\alpha^{+}$ -components are different. This is also observed in Figure 3.4B, where at lower temperature of 107.5°C the  $\alpha$ -curve crosses the  $\alpha^{+}$ -curve and at higher temperature of 120°C the  $\alpha$ -curve lies underneath the  $\alpha^{+}$ -curve.

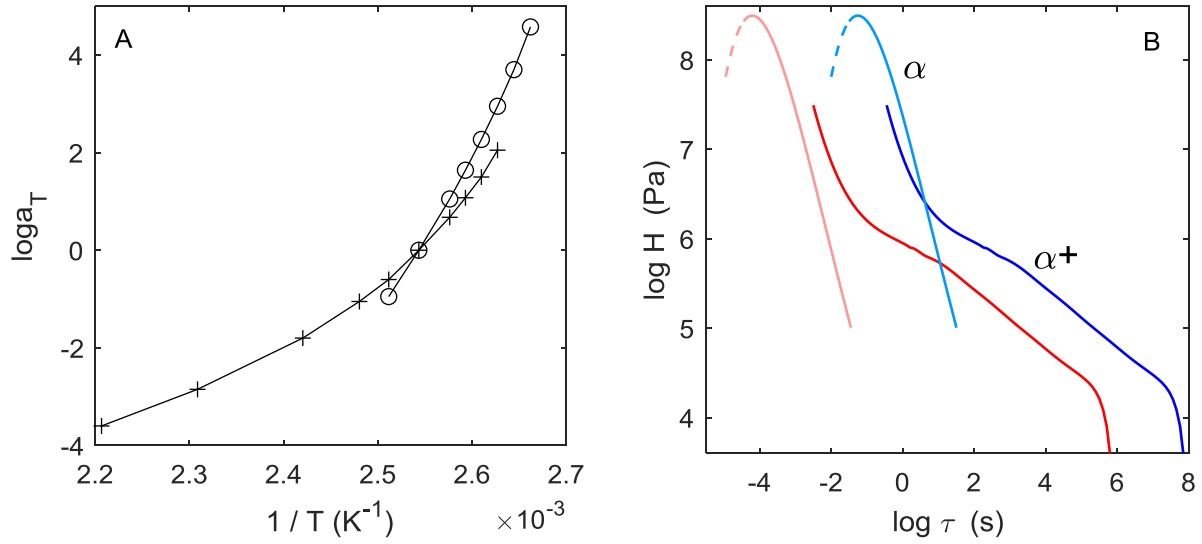


Figure 3.4. (A) Shift factors for the  $\alpha$ -component (circles) and the  $\alpha^+$ -component (plusses) of the relaxation spectrum required to effect the fit to the  $G'$  and  $G''$  data shown in Figure 3.5; lines are guide to the eye. (B)  $\alpha$ - and  $\alpha^+$ -components of the relaxation spectrum at two temperatures: 107.5°C – blue and 120°C – red;  $\alpha$ -component is shown in lighter color for better visibility. Dashed line indicates region where determination of the  $\alpha$ -component becomes uncertain.

Note that the shape of the  $\alpha$ -component of the relaxation spectrum is not fully determined, where on the shorter time side additional processes move into the experimental window. These processes belong to what is typically designated as the ‘excess wing’ of the  $\alpha$ -relaxation process and determination of excess wing is beyond the scope of this communication. As shown in Figure 3.5, the excess wing processes begin to play more prominent role for the 105 °C and lower isotherms, whereas the  $\alpha$ -process proper is responsible for smaller and smaller portion of the viscoelastic response. Specifically for the lowest temperature isotherms in Figure 3.5 at 100°C, i.e. the orange circles, only the lower frequency portion of the response is due to  $\alpha$ -process. If the excess wing is assumed to be a process independent from the main  $\alpha$ -process, it will have a still different temperature dependence than either  $\alpha$ - or  $\alpha^+$ -process.[35] The uncertainty in the shape of the  $\alpha$ -peak proper is emphasized in Figure 3.4B by drawing the left-hand-side of the peak as dashed line, which indicates that only the shape of the longer relaxation times side of the  $\alpha$ -peak is robustly determined. It is the right-hand-side of  $\alpha$ -peak that is the focus of this communication, where the dashed line convention indicating the uncertainty in the left-hand-side of the  $\alpha$ -peak will be used

when other materials are analyzed. Finally, how robustly is the maximum of the  $\alpha$ -peak determined? The answer depends on the data for a particular material. In the case of EPON1009F-MDA the shape of the top portion of the  $\alpha$ -peak is dictated by fitting the storage and loss isotherms at 110°C (cyan plusses in Figure 3.5). Analysis shows that neither height nor location of the  $\alpha$ -peak can be changed by more than 5% without visibly affecting the quality of fit in Figure 3.5.

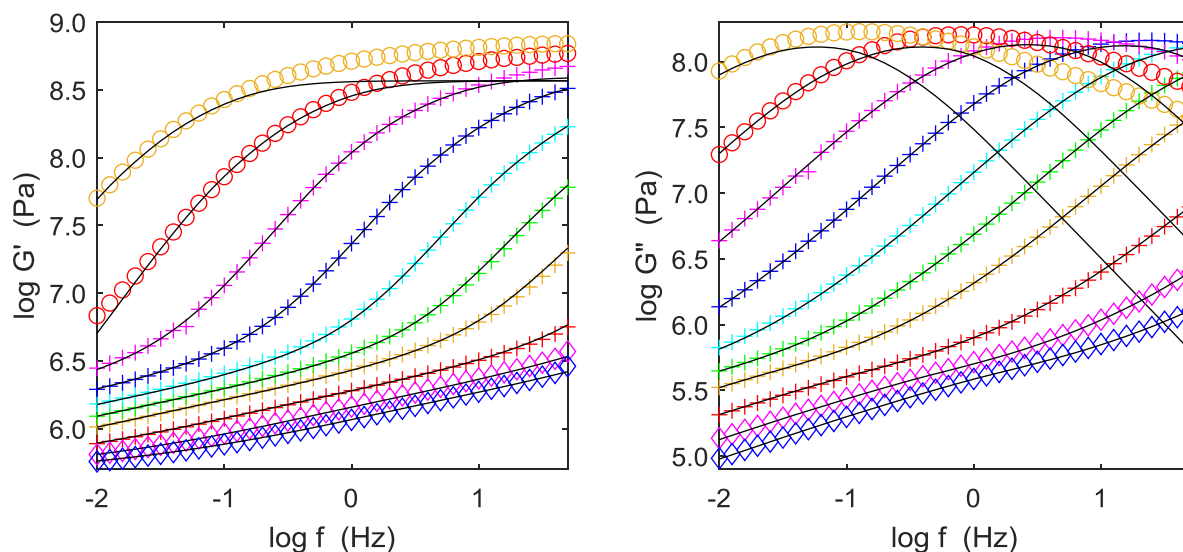


Figure 3.5. EPON1009F-MDA storage (A) and loss (B) isotherms for the temperatures: 100°C – orange circles, 102.5°C – red circles, 105°C – magenta plusses, 107.5°C – blue plusses, 110°C – cyan plusses, 112.5°C – green plusses, 115°C – orange plusses, 120°C – red plusses, 125°C – magenta diamonds, 130°C – blue diamonds. Lines are fit using the additive combination of the  $\alpha$ - and  $\alpha^+$ -components of the relaxation spectrum shown in Figure 3.4B with the temperature shifts shown in Figure 3.4A.

### 3.3.2 Linear Relaxation Behavior of Phenoxy

The frequency-dependent, linear viscoelastic  $G'$  and  $G''$  moduli for phenoxy were measured over 3.5 orders of magnitude in frequency and are shown in Figure 3.6 for isotherms from 95 °C ( $T_g - 3$  °C) to 260 °C ( $T_g + 162$  °C). The isotherms show the typical features for a thermoplastic material of high molecular weight. The glass transition was observed in the 95 °C to 110 °C isotherms, where  $G'$  drops by 3 orders of magnitude. Data above 10 Hz at 95 °C and 100 °C are suspect due to potential slippage at the surface of the parallel plates and were not used in the subsequent determination of the relaxation spectrum. Examining the 120 °C isotherm, the entanglement

plateau is observed. For isotherms at 220 °C and above, the terminal relaxation is observed at frequencies below 0.1 Hz, where the slopes  $d \log G' / d \log f$  and  $d \log G'' / d \log f$  approach 2 and 1, respectively, as predicted by Rouse theory for terminal relaxation.[36]

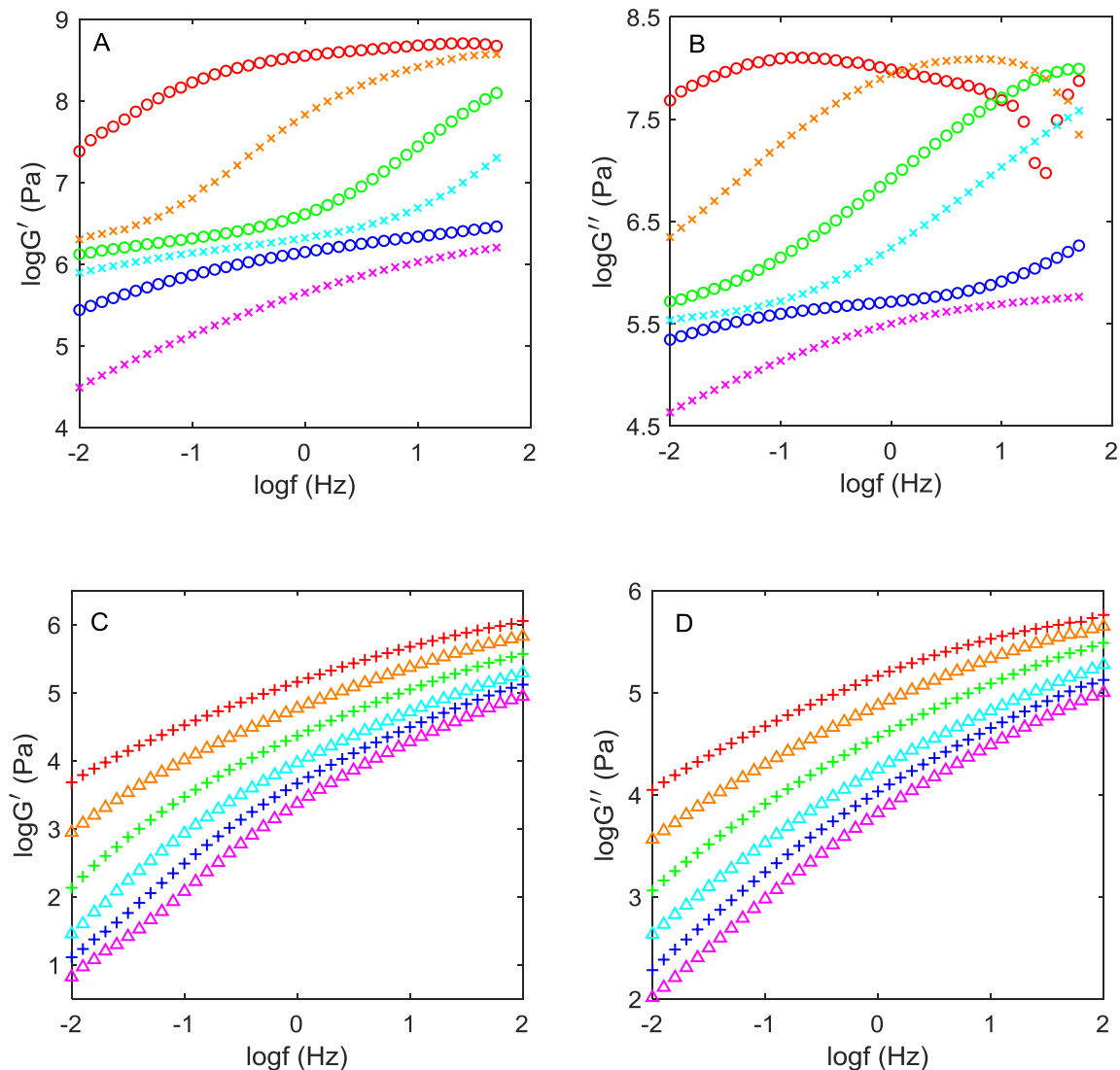


Figure 3.6. The linear viscoelastic shear storage (A) and (C) and loss (B) and (D) moduli for phenoxy at the glass transition ( $T_g = 98^\circ\text{C}$ ) and above (A) and (B) and in the flow region, i.e. above  $160^\circ\text{C}$ , (C) and (D). Isotherms in (A) and (B) are at:  $95^\circ\text{C}$  ( $\circ$ ),  $100^\circ\text{C}$  ( $\times$ ),  $105^\circ\text{C}$  ( $\circ$ ),  $110^\circ\text{C}$  ( $\times$ ),  $120^\circ\text{C}$  ( $\circ$ ), and  $140^\circ\text{C}$  ( $\times$ ). Isotherms in (C) and (D) are at:  $160^\circ\text{C}$  ( $+$ ),  $180^\circ\text{C}$  ( $\triangle$ ),  $200^\circ\text{C}$  ( $+$ ),  $220^\circ\text{C}$  ( $\triangle$ ),  $240^\circ\text{C}$  ( $+$ ), and  $260^\circ\text{C}$  ( $\triangle$ ). Lines are fits using the relaxation spectrum shown Figure 3.8B.

Time-temperature superposition was used to construct the  $G'$  and  $G''$  master curves shown in Figure 3.7 with a reference temperature of 105 °C, where the  $\log a_T$  shift function is shown in Figure 3.8A. Approximate superposition was observed over the entire frequency range of 11 logarithmic decades for both the  $G'$  and  $G''$  isotherms from 100 °C to 260 °C with the exception of the  $G''$  isotherm at 120 °C as seen in Figure 3.7B. The lack of superposition for 120 °C isotherm may be an experimental error or an indication two relaxation processes each having a different temperature dependence, as was the case for the EPON1009F-MDA system described in the previous section. The difference between the phenoxy and the EPON1009F-MDA data is that in the latter the lack of superposition was observed for all isotherms at temperatures less than 120 °C (see Figure 3.2). In contrast, for the phenoxy superposition is lost for the  $G''$  isotherm at 120 °C as shown in Figure 3.7B, but the superposition appears to work at lower temperatures (see Figure 3.7). It is important to note that the claim of approximate superposition for the phenoxy (with the exception of the 120 °C  $G''$  isotherm) is limited to the region between  $\alpha$ - and  $\alpha$ + processes, where no claim is made concerning superposition of the dynamic linear viscoelastic data in the excess wing, the glass transition or sub- $T_g$  relaxation regions.

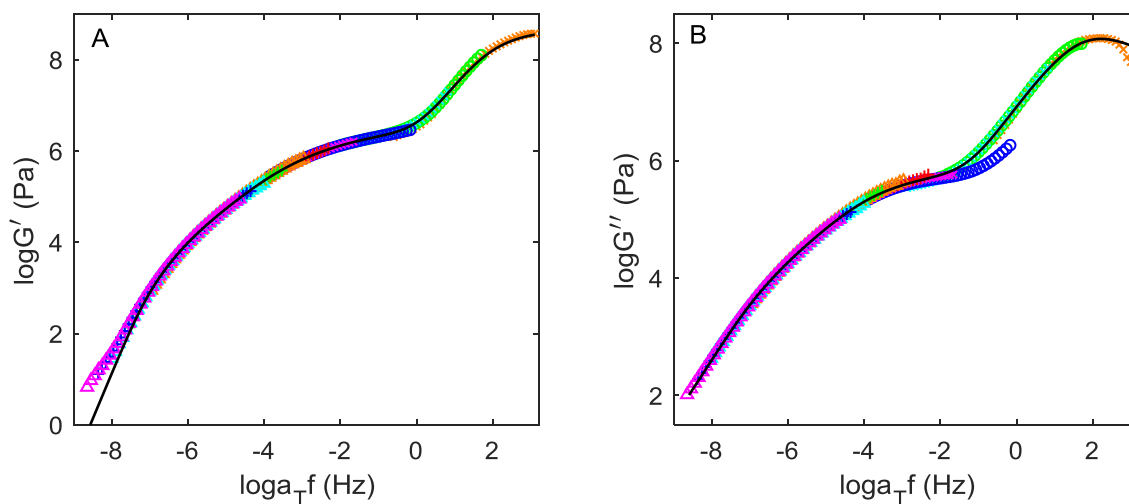


Figure 3.7. Phenoxy  $G'$  (A) and  $G''$  (B) master curves via frequency-temperature superposition of the isotherms shown in Figure 3.5 with a reference temperature  $T_{\text{ref}} = 105$  °C and the  $\log a_T$  shift factor shown in Figure 3.8A. Colors/symbols have same meaning as in Figure 3.6. Solid lines are the predictions using the relaxation spectrum shown in Figure 3.8B.

The temperature dependence of the  $\log a_T$  is shown in Figure 3.8A. The shift factor from 95 °C to 160 °C was fit the WLF equation using  $C_1 = 6.14$  and  $C_2 = 29.26$  °C, where it does an excellent job of fitting the  $\log a_T$  values. However, at temperatures above 160 °C the shift factors are not described by the same WLF function, where the new WLF constants are  $C_1 = 9.49$  and  $C_2 = 66.73$  °C. Determination of the spectrum implicitly assumes  $G'$  and  $G''$  master curves over the full frequency range. Using Equation (3.1), the relaxation time spectrum for phenoxy is obtained, where the predictions of  $G'$  and  $G''$  response are shown as lines in Figure 3.7 and the spectrum is shown in Figure 3.8B.

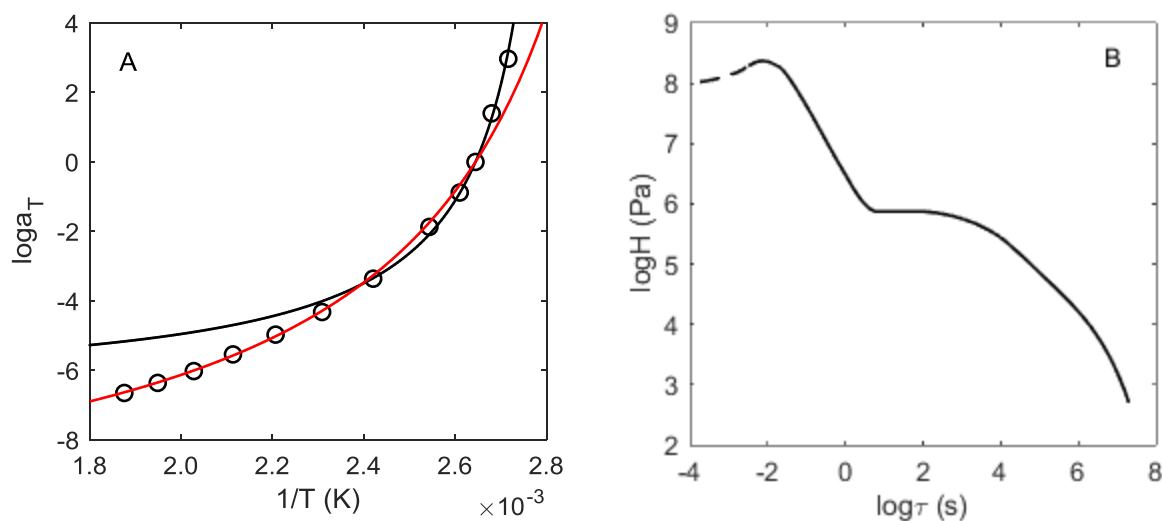


Figure 3.8. (A) The  $\log a_T$  shift factor for phenoxy required to effect approximate frequency-temperature superposition resulting in the  $G'$  and  $G''$  master curves shown in Figure 3.7. The black line is a WLF fit with  $C_1 = 6.14$  and  $C_2 = 29.26$  °C and the red line is a WLF fit with  $C_1 = 9.49$  and  $C_2 = 66.73$  °C. (B) The  $\log H$  phenoxy relaxation spectrum determined from the linear viscoelastic  $G'$  and  $G''$  data.

### 3.3.3 Linear Relaxation Behavior of EPON825-MDA

The linear viscoelastic  $G'$  and  $G''$  storage and loss moduli of EPON825-MDA are shown in Figure 3.9 for temperatures from 185 °C ( $T_g + 2$  °C) to 220 °C ( $T_g + 37$  °C). The glass transition is observed in the 185 °C to 200 °C isotherms, where above 220 °C the specimen exhibits thermal degradation during the course of frequency scan. Isotherms for lower temperatures will be reported elsewhere.



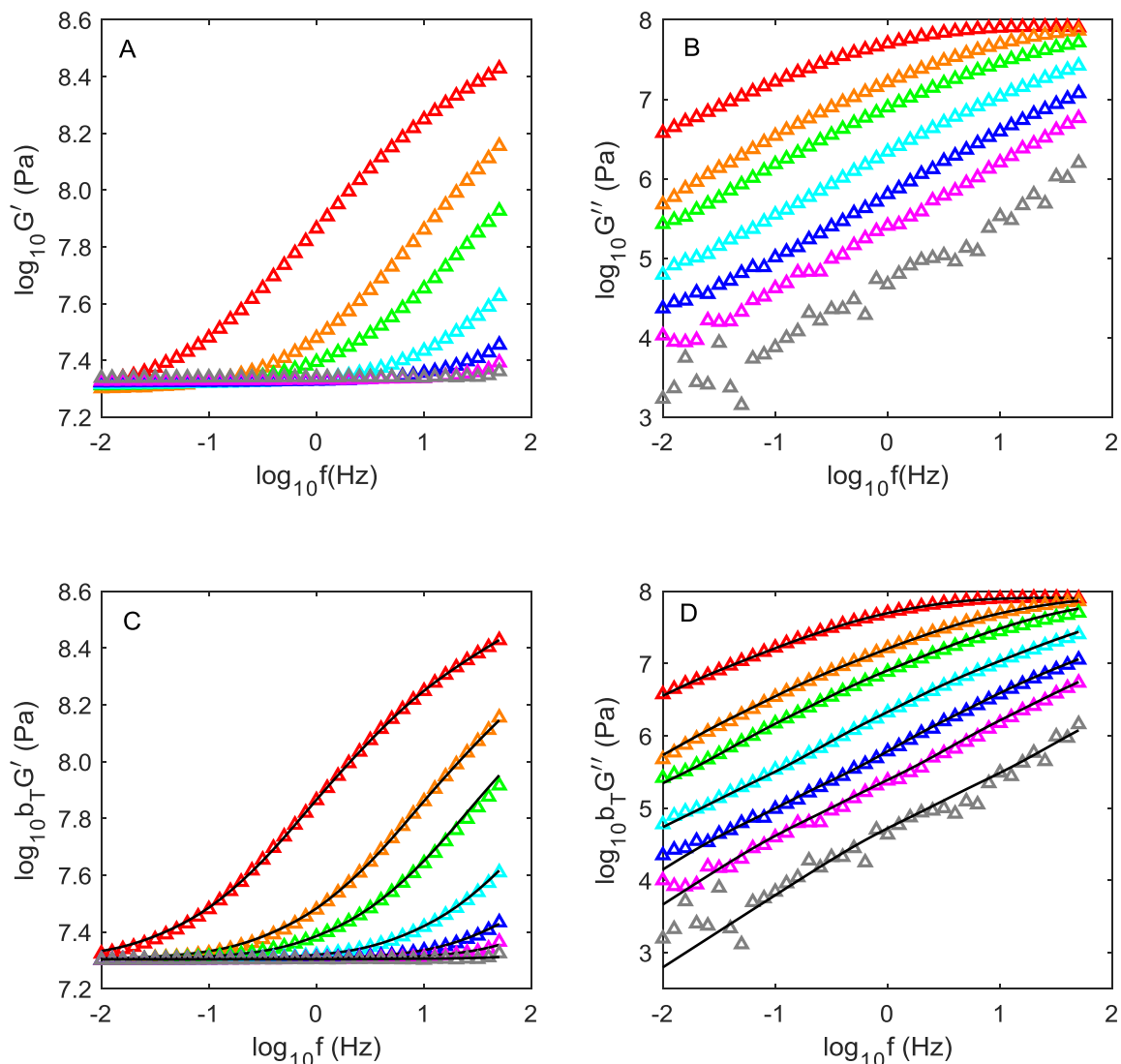


Figure 3.9. Dynamic shear responses for EPON 825-MDA near and above glass transition temperature ( $T_g = 183^\circ\text{C}$ ). Storage and loss isotherms are shown for the following temperatures:  $185^\circ\text{C}$  ( $\triangle$ ),  $190^\circ\text{C}$  ( $\triangle$ ),  $195^\circ\text{C}$  ( $\triangle$ ),  $200^\circ\text{C}$  ( $\triangle$ ),  $205^\circ\text{C}$  ( $\triangle$ ),  $210^\circ\text{C}$  ( $\triangle$ ) and  $220^\circ\text{C}$  ( $\triangle$ ) from top to bottom respectively. Lines are the predictions using the relaxation spectrum shown in Figure 3.11B.

At  $220^\circ\text{C}$   $G'$  isotherm is flat for all frequencies and  $G''$  response exhibits noticeable scatter due to the extremely small values of  $\tan\delta$  of less than  $10^{-3}$  that occur for this nearly elastic response; nevertheless, the  $220^\circ\text{C}$  isothermal response is repeatable. There is a systematic change in the elastic modulus in Figure 3.9A, where the temperature dependence of the equilibrium elastic

modulus  $G_e$  determined from the  $G'$  value at 0.01Hz is shown in Figure 3.10. The solid line in Figure 3.10 is the linear line with zero intercept at  $T=0$  K that would be expected from rubber elasticity.[37] The discrepancy at 458 K (185 °C) is not unexpected, since some relaxation is still present at 0.01 Hz. There is a difference between the data at higher temperatures and what would be expected from rubber elasticity; specifically, the molecular weight between crosslinks ( $M_c$ ) is 226 g/mol calculated from the slope of Figure 3.10 and is higher than the experimentally determined  $M_c$  of 342 g/mol, although the single DGEBA repeat unit between crosslinks may not have sufficient degrees of freedom to satisfy the statistical requirements of a Gaussian chain. In Figure 3.9C the effect of the elasticity has been accounted for using a  $b_T = G_e(T) / G_e(T_{ref})$  vertical shift, which is equivalent to the traditional  $b_T = \rho T / \rho_{ref} T_{ref}$  that is employed for a material that exhibits rubber elasticity with  $G_e \sim T$ .

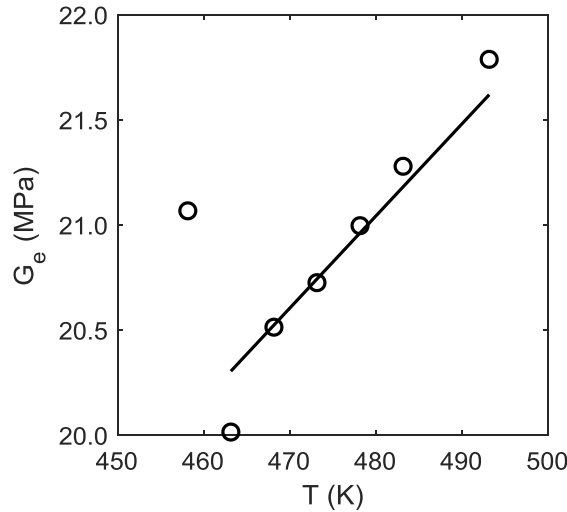


Figure 3.10. Temperature dependence of equilibrium moduli  $G_e$  as determined from the  $G'$  values at the lowest frequency of 0.01Hz. The solid line is the prediction from rubber elasticity with  $G_e = 4.38 \times 10^{-5} T$ .

Using the isotherms in Figure 3.9C and D master curves were constructed as shown in Figure 3.11, where superposition of both the  $G'$  and  $G''$  isotherms was achieved, i.e. in contrast to the EPON1009F-MDA system the tightly crosslinked EPON825-MDA material was thermo-rheologically simple above  $T_g$ . The  $\log a_T$  shift function for EPON825-MDA is shown in Figure

3.12A, where it is well described by the WLF equation. The relaxation spectrum was determined from the data in Figure 3.11 using the Equation (3.1). The EPON825-MDA relaxation spectrum shows a single  $\alpha$ -process that is in contrast to the EPON1009F-MDA and phenoxy relaxation spectra shown in Figure 3.4B and Figure 3.8B, respectively, where in both EPON1009F-MDA and phenoxy materials there is relatively more narrow  $\alpha$ -process accompanied at long times by a distinct broad  $\alpha$ +-process.

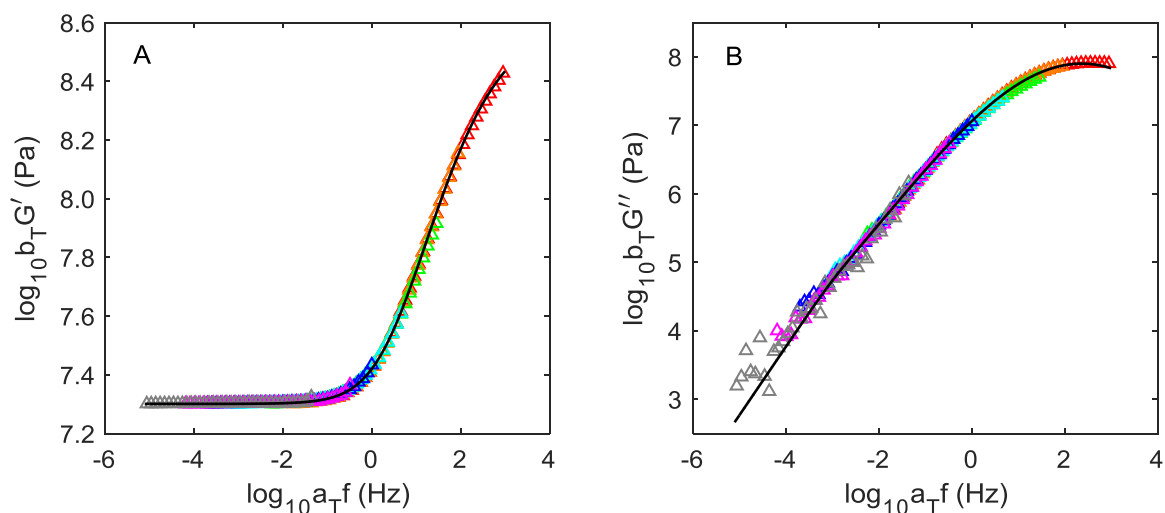


Figure 3.11. EPON825-MDA  $G'$  (A) and  $G''$  (B) master curves via frequency-temperature superposition of the isotherms shown in Figure 3.9C and D with a reference temperature  $T_{\text{ref}} = 190^\circ\text{C}$  and the  $\log a_T$  shift factor shown in Figure 3.12A. Symbols have same meaning as in Figure 3.9. The solid lines are the predictions using the relaxation spectrum shown in Figure 3.12B.

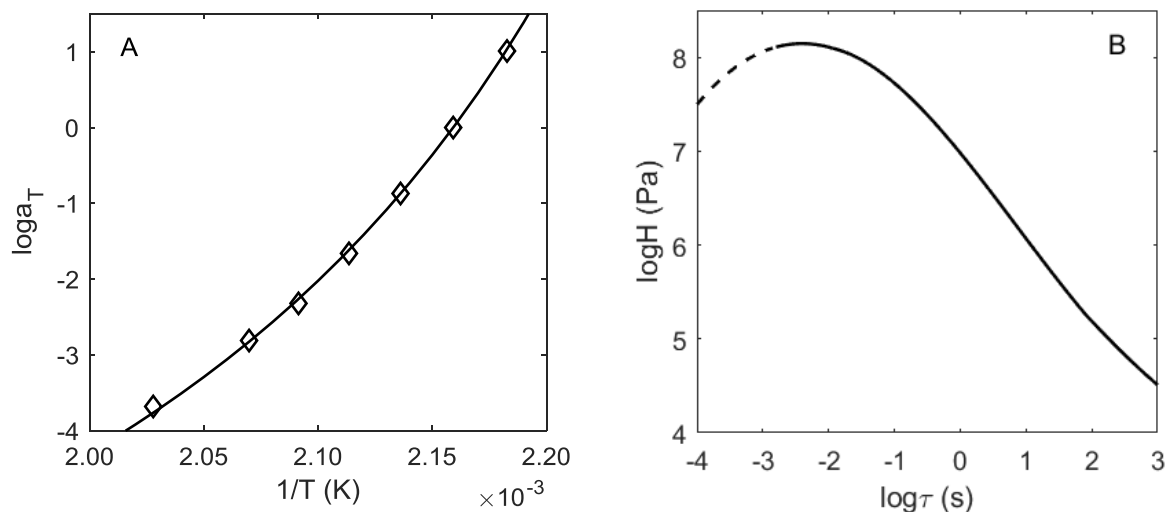


Figure 3.12. (A) The  $\log a_T$  shift factor for EPON825-MDA required to effect approximate frequency-temperature superposition resulting in the  $G'$  and  $G''$  master curves shown in Figure 3.11. The solid line is a WLF fit with  $C_1 = 11.18$  and  $C_2 = 59.12$  °C. (B) The  $\log H$  EPON825-MDA relaxation spectrum determined from the linear viscoelastic  $G'$  and  $G''$  data.

### 3.3.4 Linear Viscoelastic Behavior of a Series of DGEBA Resins Cured with DDS

The linear viscoelastic  $G'$  and  $G''$  behavior at temperatures from  $T_g$  to well-above  $T_g$  have been measured for a series of DGEBA epoxy resins cured with DDS in the frequency interval from 0.01 Hz to 50 Hz. The isotherms are given in AppendixD1 and the resulting master curves are given in Figure 3.13A through Figure 3.19A, where the associated  $\log a_T$  shift factors are given in Figure 3.20 (and where the choice of  $T_{ref}$  is explained below). Good superposition of both the  $G'$  and  $G''$  isotherms was observed. However, data for the DDS systems were collected on the Rheometrics RMS-800/RDS-II spectrometer that did not have similar accuracy or as tight temperature control as the ARES G2 Rheometer used to measure  $G'$  and  $G''$  for the phenoxy, EPON825-MDA and EPON1009F-MDA materials. The temperature dependence of  $\log a_T$  for all of the DGEBA-DDS systems was fit with the WLF equation with the parameters given in Table 4.2. The WLF equation describes the data well for all the materials, unlike for phenoxy shown in Figure 3.8A, where the high temperature  $\log a_T$  data deviates from the WLF prediction; however, the phenoxy data extends 160 °C above  $T_g$  vs approximately only 60 °C above  $T_g$  for the DGEBA-DDS systems. The choice of the  $T_{ref}$  isotherm for a given material is arbitrary; however, to compare across

materials the  $T_{\text{ref}}$  has to be consistent, where choosing  $T_{\text{ref}}$  at a fixed distance from  $T_g$  would be one possibility. Unfortunately, as seen in Table 4.2,  $T_g$  value depends on the experiment in which it is determined, for example dilatometry vs DSC, dilatometric or DSC  $T_g$ 's are not available for all DGEBA-DDS systems studied here. An alternative is the temperature  $T_\alpha$  defined as the temperature at which the loss modulus  $G''$  passes through a maximum during a temperature scan at the frequency of 1rad/s, where the  $T_\alpha$  values are given in Table 4.2. The reference temperature is chosen as  $T_{\text{ref}}=T_\alpha +10^\circ\text{C}$  for each material. Using this definition of  $T_{\text{ref}}$ , the  $\log a_T$  vs temperature behavior is plotted in Figure 3.20 for all of the DGEBA-DDS systems. Except for scatter at higher temperatures (where the superposition of isotherms is most uncertain), the  $\log a_T$  vs temperature dependence is similar for all DGEBA-DDS systems.

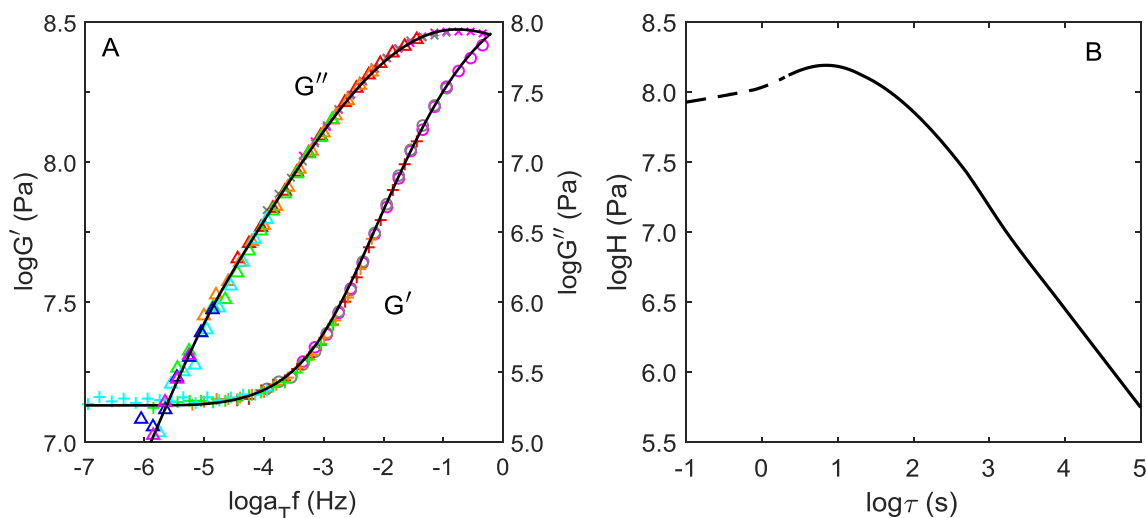


Figure 3.13. (A)  $G'$  and  $G''$  master curves for EPON828-DDS. Isotherms before shift are given in Figure A.4. Symbols indicate the isotherms temperature:  $G'$ : 222°C (○), 225°C (○), 228°C (+), 233°C (+), 238°C (+), 248°C (+);  $G''$ : 222°C (×), 225°C (×), 228°C (△), 233°C (△), 238°C (△), 248°C (△), 257°C (△), 267°C (△). Solid line is fit using Equation (3.1) with the relaxation spectrum shown in panel (B).

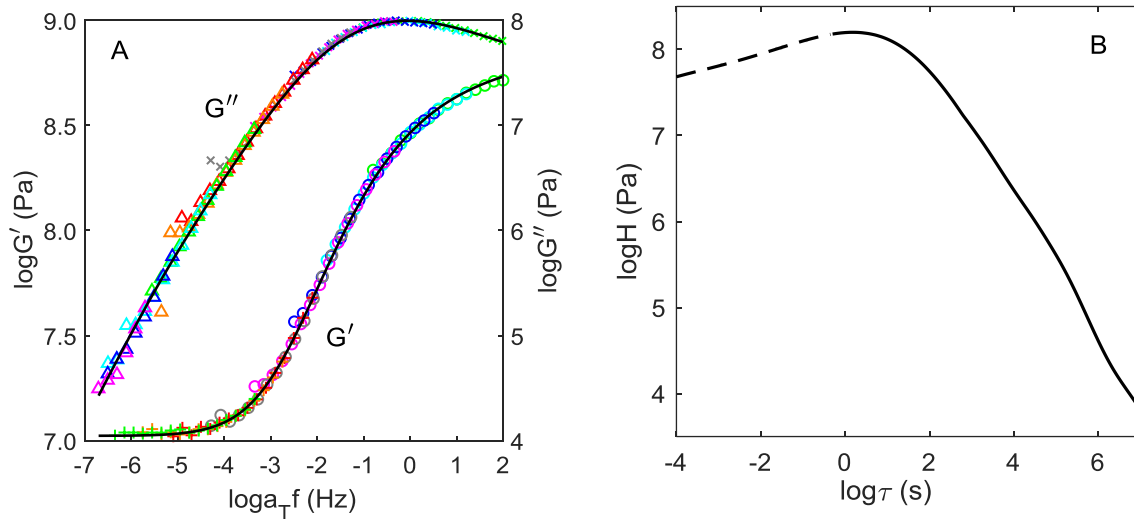


Figure 3.14. (A)  $G'$  and  $G''$  master curves for EPON834-DDS. Isotherms before shift are given in Figure A.5. Symbols indicate the isotherms temperature:  $G'$ : 181°C (○), 184°C (○), 187°C (○), 191°C (○), 196°C (○), 201°C (+), 206°C (+), 211°C (+);  $G''$ : 181°C (×), 184°C (×), 187°C (×), 191°C (×), 196°C (×), 201°C (△), 206°C (△), 211°C (△), 221°C (△), 231°C (△), 241°C (△). Solid line is fit using Equation (3.1) with the relaxation spectrum shown in panel (B).

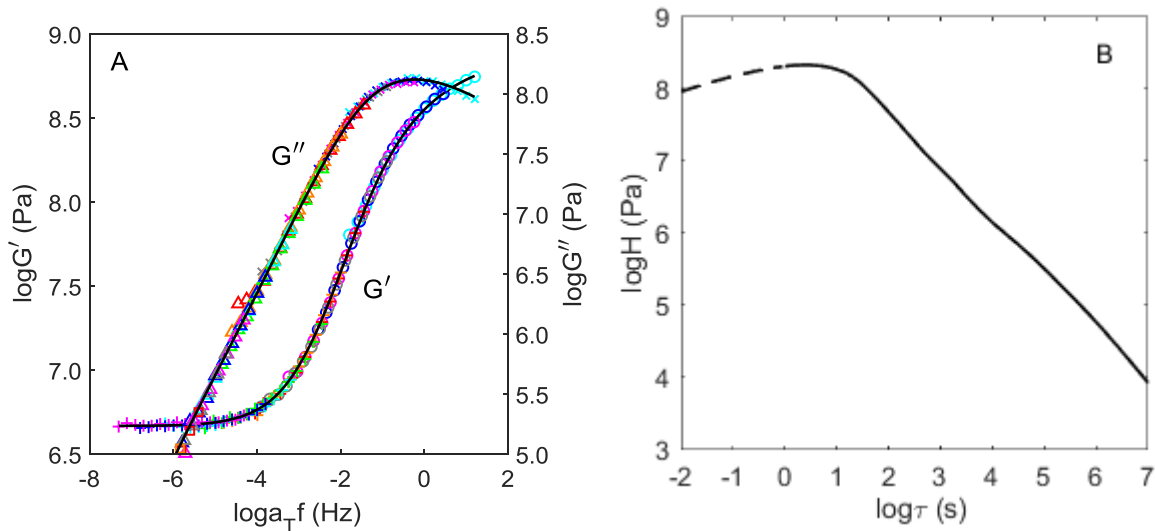


Figure 3.15. (A)  $G'$  and  $G''$  master curves for EPON1001F-DDS. Isotherms before shift are given in Figure A.6. Symbols indicate the isotherms temperature:  $G'$ : 140°C (○), 143°C (○), 146°C (○), 149°C (○), 152°C (+), 155°C (+), 158°C (+), 163°C (+), 168°C (+), 173°C (+);  $G''$ : 140°C (×), 143°C (×), 146°C (×), 149°C (×), 152°C (△), 155°C (△), 158°C (△), 163°C (△), 168°C (△), 173°C (△), 178°C (△), 188°C (□), 198°C (□). Solid line is fit using Equation (3.1) with the relaxation spectrum shown in panel (B).

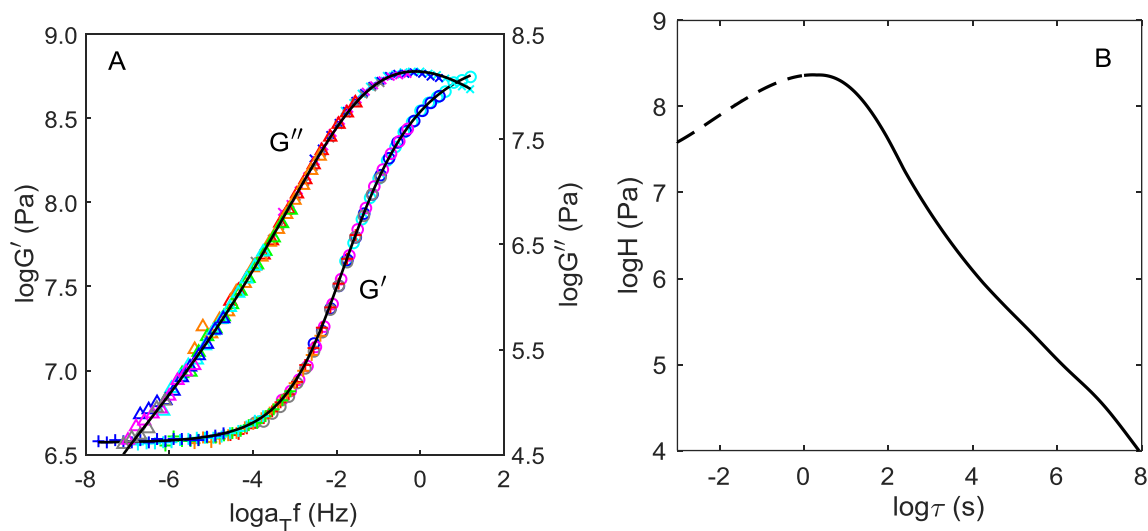


Figure 3.16. (A)  $G'$  and  $G''$  master curves for EPON1002F-DDS. Isotherms before shift are given in Figure A.7. Symbols indicate the isotherms temperature:  $G'$ : 130°C (○), 132.5°C (○), 136°C (○), 139°C (○), 141°C (+), 147°C (+), 152°C (+), 157°C (+), 167°C (+);  $G''$ : 130°C (×), 132.5°C (×), 136°C (×), 139°C (×), 141°C (△), 147°C (△), 152°C (△), 157°C (△), 167°C (△), 177°C (△), 187°C (△). Solid line is fit using Equation (3.1) with the relaxation spectrum shown in panel (B).

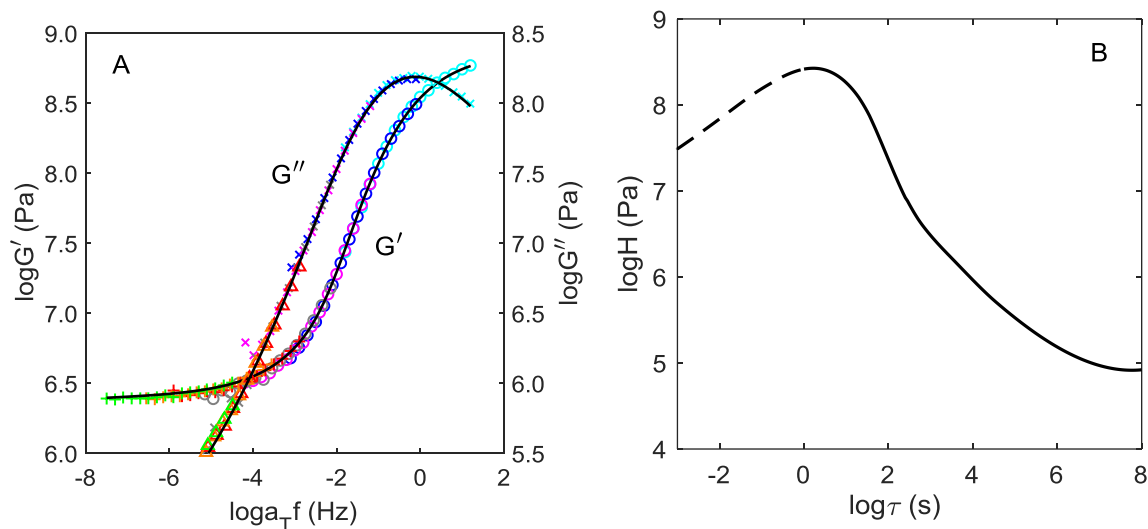


Figure 3.17. (A)  $G'$  and  $G''$  master curves for EPON1004F-DDS. Isotherms before shift are given in Figure A.8. Symbols indicate the isotherms temperature:  $G'$ : 120°C (○), 125°C (○), 130°C (○), 135°C (○), 140°C (+), 145°C (+), 155°C (+);  $G''$ : 120°C (×), 125°C (×), 130°C (×), 135°C (×), 140°C (△), 145°C (△), 155°C (△). Solid line is fit using Equation (3.1) with the relaxation spectrum shown in panel (B).

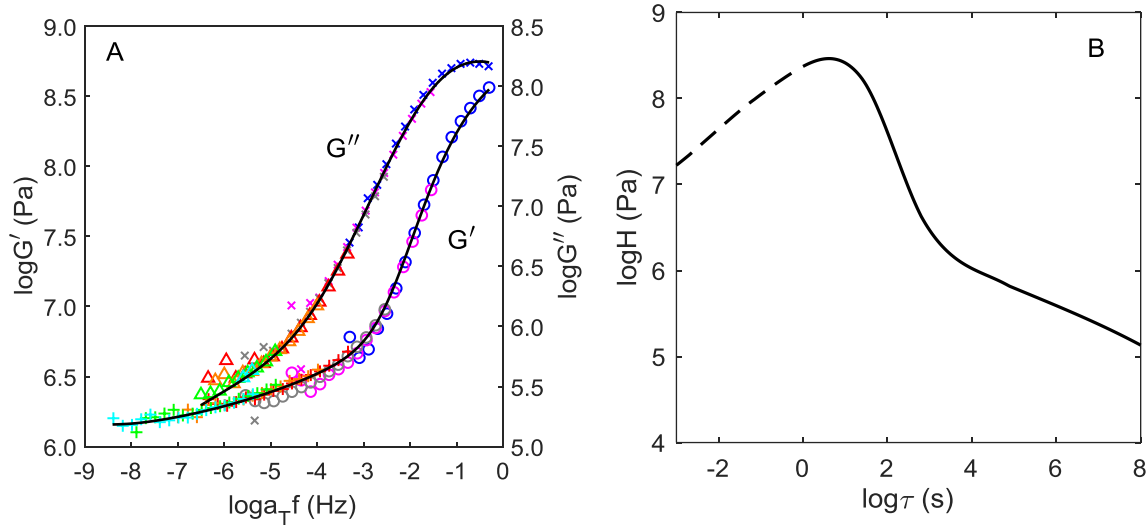


Figure 3.18. (A)  $G'$  and  $G''$  master curves for EPON1007F-DDS. Isotherms before shift are given in Figure A.9. Symbols indicate the isotherms temperature:  $G'$ : 115°C (○), 120.5°C (◐), 125.5°C (○), 130.5°C (+), 135.5°C (+), 145.5°C (+), 155°C (+);  $G''$ : 115°C (×), 120.5°C (×), 125.5°C (×), 130.5°C (△), 135.5°C (△), 145.5°C (△), 155°C (△). Solid line is fit using Equation (3.1) with the relaxation spectrum shown in panel (B).

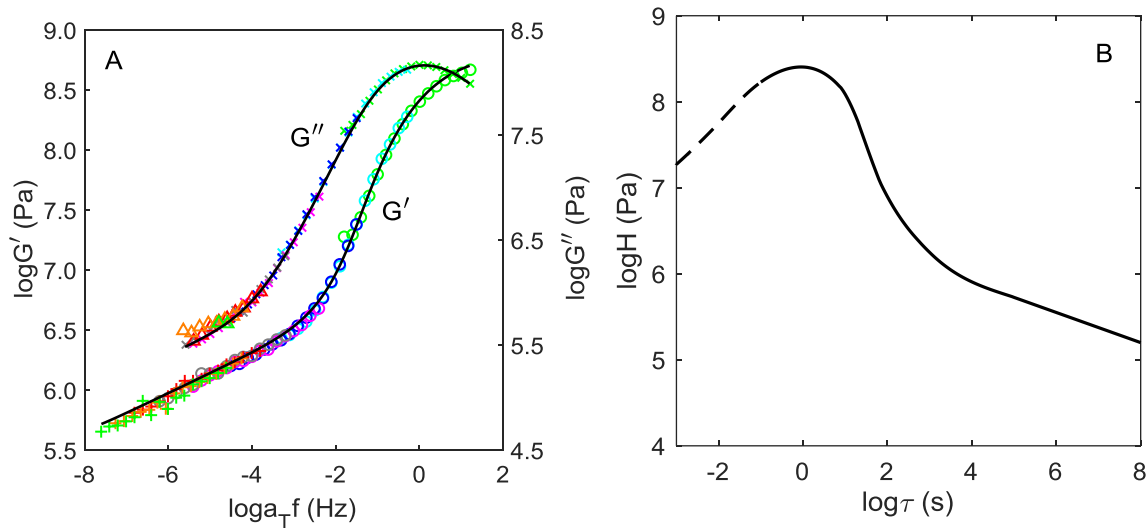


Figure 3.19. (A)  $G'$  and  $G''$  master curves for EPON1009F-DDS. Isotherms before shift are given in Figure A.10. Symbols indicate the isotherms temperature:  $G'$ : 103°C (○), 108°C (◐), 113°C (○), 118°C (◐), 123°C (○), 128°C (+), 133°C (+), 138°C (+);  $G''$ : 103°C (×), 108°C (×), 113°C (×), 118°C (×), 123°C (×), 128°C (△), 133°C (△), 138°C (△). Solid line is fit using Equation (3.1) with the relaxation spectrum shown in panel (B).



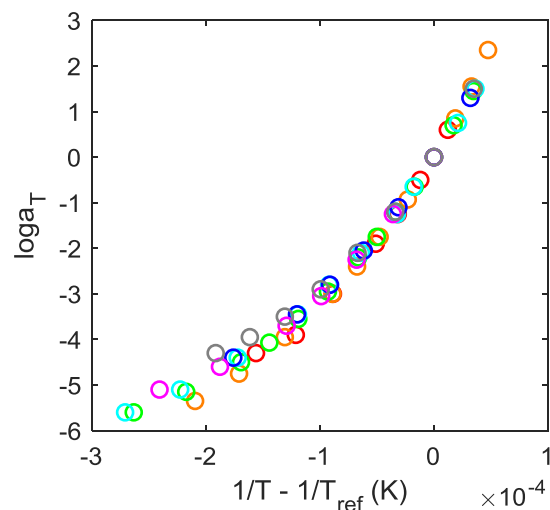


Figure 3.20.  $\log a_T$  vs temperature for the DDS series. The values  $T_{\text{ref}}$  are given in Table 4.2.

Materials are indicated as follows: EPON828-DDS – red, EPON834-DDS – orange, EPON1001F-DDS – green, EPON1002F-DDS – cyan, EPON1004F-DDS – blue, EPON1007F-DDS – magenta, EPON1009F-DDS – grey.

Table 3.2.  $T_{\text{ref}}$  used to construct master curves in Figure 3.13A through Figure 3.19A,  $T_g$  and WLF parameters for the series of DGEBA resins cured with DDS

Material	$T_{\text{ref}}$ °C	$T_\alpha$ (DMA) °C		$T_g$ °C		WLF Parameters	
		Curliss[34]	Enns[38]	Dilat. Curliss[34]	Dilat. Choy[31]	DSC LeMay[39]	$C_1$ $C_2$ , °C
EPON828-DDS	225	214	215		204	212	10.4 57.4
EPON834-DDS	191	181	186				11.8 59.7
EPON1001F-DDS	146	136		127	127	132	11.4 50.3
EPON1002F-DDS	136	127		119		121	11.4 50.2
EPON1004F-DDS	125	118		102	112	113	11.8 48.8
EPON1007F-DDS	115	103		97	101	105	9.9 35.8
EPON1009F-DDS	108	100		95			9.6 35.9

The relaxation spectra for the DGEBA-DDS materials were determined using eqn. (1) to fit the  $G'$  and  $G''$  master curve data shown in Figure 3.13A-Figure 3.19A and are shown in Figure 3.13B-Figure 3.19B. The four most tightly crosslinked materials (i.e. EPON828, EPON834, EPON1001F and EPON1002F resins) show a single, relatively broad  $\alpha$ -peak. In contrast, the looser networks (i.e. EPON1004F, EPON1007F and EPON1009F resins) show a narrower  $\alpha$ -peak along with a wide shoulder at longer relaxation times associated with the  $\alpha^+$ -process.

### 3.4 Discussion

In the Results section the linear viscoelastic behavior of a series of polymeric systems whose common structural unit is the diglycidyl ether of bisphenol-A (DGEBA) repeat unit was reported. Specifically, the dynamic linear viscoelastic properties were measured for a thermoplastic polymer, i.e. phenoxy, and two groups of thermoset polymers – DGEBA diepoxides of varying molecular weight cured with 4,4'-methylenedianiline (MDA) and diamino diphenyl sulfone (DDS). The focus of this research is on the temperature range above  $T_g$ , where the  $\alpha$ - and  $\alpha^+$ -relaxation processes are located; and, the temperature shift factors  $\log a_T$  and the relaxation times spectra  $H(\log \tau)$  were determined. The objective is to determine pattern(s) in how the relaxation spectrum and  $\log a_T$  shift factor change with chemical composition with special emphasis on the effect of crosslink density. In what follows we will first discuss the effects of chemical structure on the relaxation behavior for the DGEBA systems reported in the Results section and then expand the discussion to include other glass forming polymers and small molecules that have been reported in the literature. In many cases the literature does not directly report  $H(\log \tau)$  but rather provides the storage and loss isotherms or master curves. In these cases we analyze the literature data (see Appendix D for details for each material) using the same methodology employed to extract the relaxation spectra for the DGEBA materials as detailed in the previous section. Other mechanical datasets in literature were screened by not included for further spectral analysis due to specific reasons as given in Appendix E.

When analyzing the DGEBA based materials it is natural to include the DGEBA monomer. Using broadband dielectric relaxation spectroscopy, the relaxation response of the DGEBA monomer

above  $T_g$  was studied by Casalini et al.[40] Linear viscoelastic mechanical spectroscopy was employed in the study of the DGEBA systems reported in this paper; however, mechanical data for DGEBA monomer are not available. Similarly, the dielectric spectroscopy data for polymeric DGEBA materials are not useful in the high temperature region above  $T_g$  due to conduction and electrode polarization. Whether mechanical and dielectric spectroscopy data result in the same relaxation spectrum is an important topic.[41] For glycerol large discrepancies between mechanical and dielectric data in the  $\alpha$ -region have been reported;[42] whereas, for several other materials a good agreement between dielectric and mechanical data have been observed.[42-44] Notwithstanding a possible difference between the relaxation spectra determined from linear viscoelastic and dielectric relaxation, we believe that the Casalini et al. dielectric data provides a point of comparison between the relaxation response of the monomer and the associated polymeric materials reported in the Results Section above.

As typical for a large frequency range explored by broadband dielectric spectroscopy the thermorheological complexity of Casalini et al data is apparent, where different isotherms clearly do not superpose when shifted.[11] Thus, storage and loss dielectric susceptibilities for a single isotherm at 288 K as shown in Figure 3.21 were fit using eqn. (1) to extract the relaxation spectrum shown in Figure 3.22. Note that, although a fit for the entire frequency range could have been obtained using this procedure, we have focused on only the  $\alpha$ -relaxation process (i.e., the low frequency peak in Figure 3.21B) consistent with the analysis of the other DGEBA materials. The key feature of the relaxation time spectrum for the DGEBA monomer shown in Figure 3.22 is that it has a clear upper bound, i.e., maximum relaxation time after which the spectrum abruptly ends. For comparison the  $\alpha$ -process observed for the EPON1009F-MDA, shown previously in Figure 3.4B, exhibits a gradual decline with increasing relaxation times. Note that the spectrum for the DGEBA monomer derived from the dielectric spectroscopy data had to be shifted vertically by 9.3 logarithmic decades to align its height with that of the EPON1009F-MDA that was determined from the mechanical spectroscopy data. The spectral comparison in Figure 3.22 shows a clear qualitative difference between small molecular and polymeric glass formers at least for the DGEBA system.

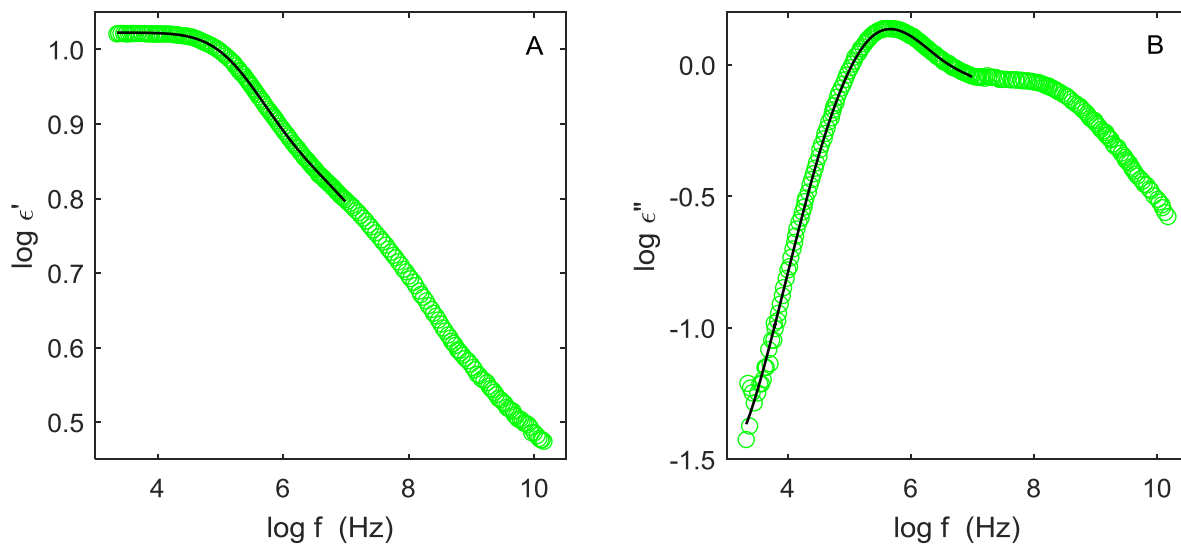


Figure 3.21. Storage (A) and loss (B) dielectric susceptibility for DGEBA monomer at 288 K; data are from Casalini et al.[40] Line is fit using the relaxation spectrum shown in Figure 3.22.

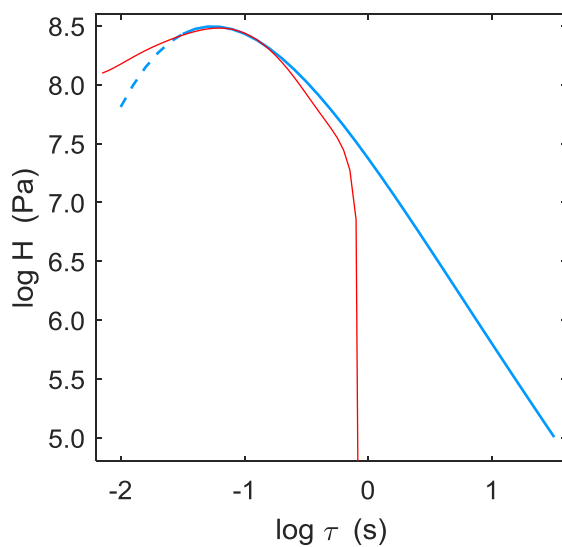


Figure 3.22. Relaxation times spectrum for DGEBA monomer at 288 K – red and the  $\alpha$ -process for the EPON1009F-MDA – blue. The spectrum for DGEBA monomer (obtained from the analysis of the dielectric relaxation data of Casalini et al[40]) has been shifted vertically by 9.3 decades.

The  $\log a_T$  vs temperature data for all of the DGEBA systems are shown in Figure 3.23A, including the phenoxy, EPON-MDA and EPON-DDS reported in this paper, DGEBA-DEA reported by Adolf et al[45] as well as the DGEBA monomer.  $\log a_T$  vs temperature for the DGEBA monomer is from Casalini et al[40] where they estimated the temperature dependence of the  $\alpha$ -process from the position of the maximum loss peak  $\varepsilon''$  despite the fact that the frequency-temperature superposition procedure fails. Examining Figure 3.23, the pattern is striking – all the “loose” materials, including DGEBA monomer, phenoxy, and the  $\alpha$ +process for EPON1009F-MDA follow the upper, less-steep branch; in contrast, the more ‘tight’ materials, including all the DGEBA-DDS materials, DGEBA-DEA, EPON825-MDA, and  $\alpha$ -process for EPON1009F-MDA as shown in Figure 3.23A follow the steeper branch. This conclusion becomes even stronger when the results of Gerard et al[25] are added. Specifically, Gerard et al carried out viscoelastic study of six DGEBA based epoxy systems, of which three were cured with 100% diamines and the other three were cured with combination of 75% monoamines and 25% diamines. The diamines used were 4,4’ diamino diphenyl methane (DDM), hexamethylene diamine (HMDA), and isophorone diamine (IPD) and the monoamines were aniline (AN), hexylamine (HA), and trimethylcyclohexylamine (TMCA). Unfortunately, Gerard et al did not report the original isotherms for their materials or the  $\log a_T$  data; however, they did provide the WLF parameters extracted from the data. When the WLF parameters are used to recreate the  $\log a_T$  behavior as shown in Figure 3.23B, it is apparent that all the diamine cured systems fall on the steep branch and two out of three predominantly monoamine cured systems fall on the less steep branch. Plazek and Choy[32] also studied networks of EPON1001F epoxy cured with varying combinations of monoamine – methyl aniline (MA) and diamine – DDS, for which they reported the WLF parameters. All of Plazek and Choy systems fall onto the steep branch as shown in Fig. 22B; this includes the neat EPON1001F resin, for which they measured viscosity as a function of temperature.

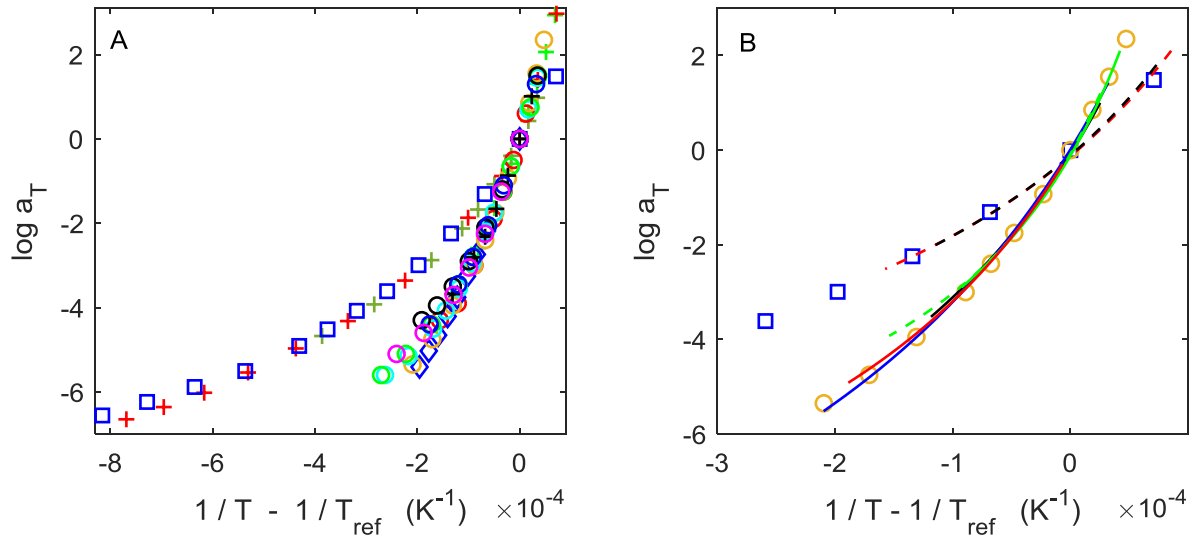


Figure 3.23. (A)  $\log a_T$  vs temperature for DGEBA based systems: DGEBA monomer – blue squares, phenoxy – red pluses, EPON 1009F-MDA ( $\alpha^+$ ) – dark green pluses, EPON 1009F-MDA ( $\alpha$ ) – green pluses, EPON 825-MDA – black pluses, EPON 828-DDS – red circles, EPON 834-DDS – orange circles, EPON 1001F-DDS – green circles, EPON 1002F-DDS – cyan circles, EPON 1004F-DDS – blue circles, EPON 1007F-DDS – magenta circles, EPON 1009F-DDS – black circles, DGEBA-DEA (Adolf et al[45]) – blue diamonds.  $T_{ref}$  is given in Table 4.2. (B) Materials for which only WLF parameters are available: DGEBA-DDM – solid green, DGEBA-25%DDM/75%AN – dashed green, DGEBA-HMDA – solid red, DGEBA-25%HMDA/75%HA – dashed red, DGEBA-IPD – solid black, DGEBA-30%IPD/70%TMCA – dashed black, Gerard et al[25]; EPON1001F-MA/DDS – solid blue (Plazek and Choy[32]). DGEBA monomer – blue squares and EPON 834-DDS – orange circles are shown for reference.

As shown in Figure 3.23, for EPON1009F-MDA the  $\alpha$ -process follows the steeper  $\log a_T$  vs temperature curve vs the  $\alpha^+$ -process that exhibits a gentler temperature dependence. The presence of two branches in the  $\log a_T$  vs temperature response is not unanticipated, since the  $\alpha$  and  $\alpha^+$ -process will have different temperature dependences. For EPON1009F-DDS  $\log a_T$  only exhibited the  $\alpha$ -process, where no  $\alpha^+$ -process could be determined; however, the high temperature isotherms were truncated and quite noisy, where it is possible that better experiments would have revealed an  $\alpha^+$ -process. The collapse of all  $\log a_T$  vs temperature curves for the ‘tighter’ DGEBA thermosets onto a single curve is not unexpected, since it is consistent with the observation of Ferry and coworkers[22] of “universal” WLF behavior for the  $\alpha$ -process. What is unexpected is that there are two distinct branches for all DGEBA based materials – one for the ‘tighter’ networks and a second

for the ‘looser’ materials, including the DGEBA monomer, phenoxy and the imperfect networks studied by Gerard et al.[25] There is an abrupt jump between the two branches of the  $\log a_T$  vs temperature response as the crosslink density is changed. It would seem more natural if a continuum of behaviors covering the entire space between the upper and the lower branches in Figure 3.23 were observed as the crosslink density increased. We have no explanation for the abrupt change in the  $\log a_T$  temperature dependence of with crosslink density.

The next question is how the relaxation spectrum changes with chemical composition for the DGEBA materials. To compare across materials the spectrum obtained for each material is shifted along the horizontal (i.e., relaxation time) axis such that the positions of the  $\alpha$  peaks approximately coincide. The spectra are also shifted vertically to enable comparison of the spectral shapes for different materials. The values of the horizontal and vertical shifts for all materials presented here are given in Appendix D. In Figure 3.24 the spectra for the DGEBA-MDA materials reported in this study are shown, including the spectra for phenoxy and the DGEBA monomer. The long time spectral tail is present in the lightly crosslinked EPON1009F-MDA system, which corresponds to the  $\alpha^+$ -process, and the un-crosslinked phenoxy. At the same time, what can be called the  $\alpha$  proper process for these systems is distinct and the shape of this process is, in the first approximation, the same (and is also similar to the spectrum of the DGEBA monomer at least near the spectral peak). In contrast, the spectrum for the tightly crosslinked EPON825-MDA material exhibits a single broad peak. However, the possibility that the observed shape of the EPON825-MDA spectrum is a result of an overlap between (i) the  $\alpha$  proper process that is the same as for EPON1009F-MDA and (ii) a hypothetical  $\alpha^+$ -process, which in case of EPON825-MDA is located closer to the  $\alpha$ -process, cannot be ruled out.

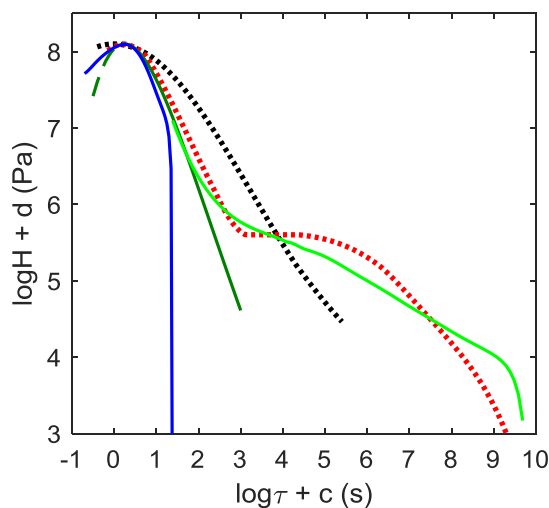


Figure 3.24. Relaxation times spectra for DGEBA-MDA systems: DGEBA monomer – blue solid line, phenoxy – red dotted line; EPON 1009F-MDA ( $\alpha$ ) – dark green solid line; EPON 1009F-MDA ( $\alpha^+$ ) – light green solid line; EPON 825-MDA – black dotted line.

The relaxation spectra for the series of DGEBA-DDS materials are shown in Figure 3.25, including the spectra for phenoxy and the EPON825-MDA that are shown for comparison. Qualitatively we can draw the same conclusions as from the DGEBA-MDA systems shown in Figure 3.24. The spectra of the tightly crosslinked materials, i.e. EPON828-DDS, EPON834-DDS, EPON1001F-DDS and EPON825-MDA, exhibit a single broad peak, where the shape of this peak is nearly the same within the uncertainty of the data. As the degree of crosslinking decreases: first, a long time shoulder emerges, i.e. the cyan curve in Figure 3.25 for the EPON1002F-DDS: and then, a separation grows between the short time  $\alpha$ -proper process and the long time  $\alpha^+$ -process. Finally, the spectra of the two loosest networks, EPON1007F-DDS (magenta) and EPON1009F-DDS (grey), begin to resemble the spectrum of phenoxy (red dotted). Here again it is not possible to rule out that for the tighter networks the  $\alpha^+$ -process is present, but has moved under the  $\alpha$  proper process and broadened its long relaxation time tail.



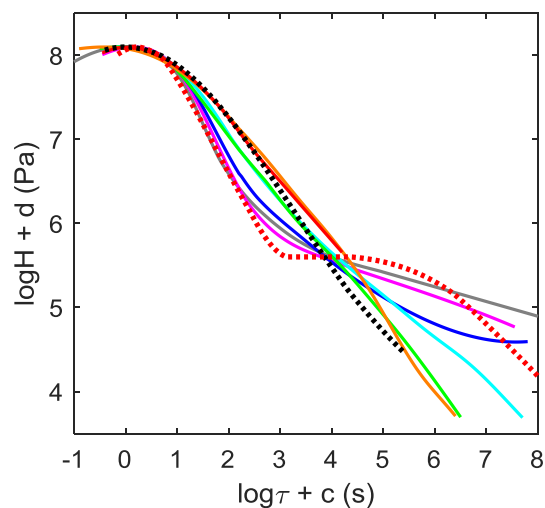


Figure 3.25. Relaxation times spectra for DGEBA based polymers: phenoxy – red dotted line, EPON 825-MDA – black dotted line; solid lines: EPON 828-DDS – solid red line; EPON 834-DDS – solid orange line; EPON 1001F-DDS – solid green line; EPON 1002F-DDS – solid cyan line; EPON 1004F-DDS – solid blue line; EPON 1007F-DDS –solid magenta line; and EPON 1009F-DDS – solid grey line.

The patterns observed in the relaxation spectra for the DGEBA based systems of varying molecular architecture can also be seen for other polymeric materials. Literature materials, for which sufficient information was provided to extract the relaxation spectrum, are (i) linear PB,[46] PPO;[47] (ii) three-armed PS-3Arm;[48] and (iii) network systems: PMMA crosslinked with 5% EGDMA[49] and highly branched dendrimer of DPPI-G5.[13] Details of the analysis of master curves used for determination of the relaxation spectrum for these systems using Equation (3.1) are given in Appendix D. The resulting spectra are shown in Figure 3.26, where the spectra for phenoxy and the EPON825-MDA are also shown for comparison. The spectra of the network materials PMMA-EGDMA and DPPI-G5 exhibit single broad peak, where the shape of this peak is nearly the same as for EPON825-MDA. In contrast, the spectra of the linear polymers consist of two distinct components – the short time  $\alpha$ -proper process and the long time  $\alpha$ +-process. The  $\alpha$ -process appears to be nearly universal across systems (as a reminder, the curves in Figure 3.26 have been shifted horizontally and vertically so that their respective  $\alpha$  peaks coincide). The  $\alpha$ +-process is material specific and dependent on molecular weight.

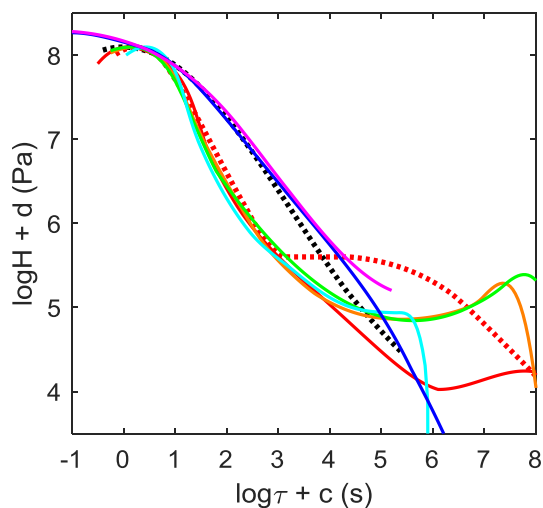


Figure 3.26. Relaxation times spectra for: phenoxy – red dotted line; EPON 825-MDA – black dotted line; PS-3Armed – solid red line; PBd1 – solid orange line; PBd2 – solid green line; PPO – solid cyan line; DPPI-G5 – solid blue line; and PMMA-EGDMA – solid magenta line.

To effect of molecular weight on the shape of the spectrum was studied by Fuchs et al,[50] where they obtained the relaxation spectra for a series of PMMA systems of various tacticity and molecular weight. Unfortunately, the linear viscoelastic experiments of Fuchs et al were carried out so far above  $T_g$  that they only observed the beginning of the  $\alpha$ -process, which precludes direct comparison of their spectra with the ones shown in Figure 3.26, where the alignment of the spectra for different systems in Figure 3.26 is on the basis of the  $\alpha$ -peak. Nevertheless the spectrum of the  $\alpha^+$ -process is well resolved for the Fuchs et al PMMA materials, where the shape of  $\alpha^+$ -process for PMMA is similar (i.e., it has a nearly flat portion spanning several decades in time followed by a small peak prior to the abrupt end corresponding to terminal relaxation) to that of PB ( $M_w$  40 and 80 kg/mol) and PPO ( $M_w$  12 kg/mol) shown in Figure 3.26. The terminal relaxation, i.e. the steep end of the  $\alpha^+$ -spectrum, in PMMA shifts by four orders-of-magnitude toward longer times when the PMMA molecular weight ( $M_w$ ) changes from 45 kg/mol (PMMA45 in Fuchs et al) to 390 kg/mol (PMMA450 in Fuchs et al).

The effect of molecular weight on the shape of the relaxation spectrum is clearly apparent when oligomers are considered. The relaxation spectra for three literature systems are shown in Figure 3.27 – oligomeric styrene (OS) with 10 repeat units, oligomeric  $\alpha$ -methyl styrene (O $\alpha$ MS) with 6

repeat units, and oligomeric isobutylene (OIB) with 11 repeat units, where the details of how these spectra were obtained from the corresponding master curves from respectively Ref.[51], Ref.[52], and Ref.[53] given in Appendix D. The spectrum for DGEBA monomer, the  $\alpha$ -component of the spectrum for EPON1009F-MDA and the spectrum for EPON825-MDA are also shown for comparison. Examining Figure 3.27, the spectra of oligomers only contain a single peak; although, just like in case of tightly crosslinked systems described above, the possibility that the observed peak is a result of merging of two closely spaced peaks cannot be ruled out: specifically, an even narrower  $\alpha$ -peak proper that merges with a wedge-like  $\alpha$ +-peak. The long time slopes of the spectra for oligomers are steeper than those of the tightly crosslinked EPON825-MDA, but generally are less steep than that of the  $\alpha$ -process for EPON1009F-MDA. Note: there is an apparent shoulder on the OIB spectrum (cyan curve in Figure 3.27); however, the uncertainty of the data does not allow robust determination if it is real or an artifact.

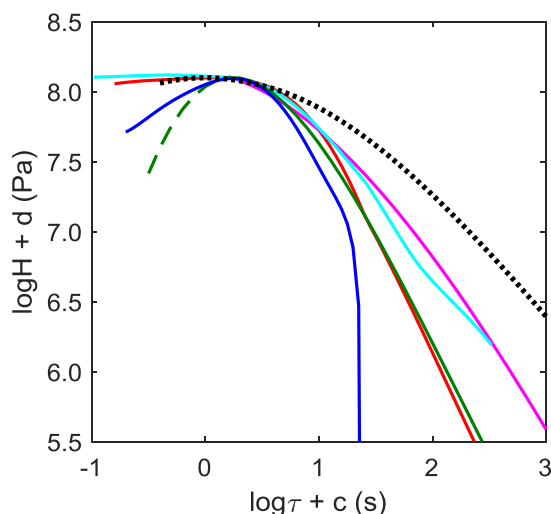


Figure 3.27. Relaxation times spectra for: EPON 825-MDA – black dotted line; solid lines: DGEBA monomer – blue, EPON 1009F-MDA ( $\alpha$ ) – dark green, OS – red, OIB – cyan, O $\alpha$ MS – magenta.

Finally, the relaxation spectra for some molecular liquids, including sucrose benzoate (SB)[54] and m-Toluidine (mTd)[54, 55] are shown in Figure 3.28, where the spectrum for DGEBA monomer and the  $\alpha$ -component of the spectrum for EPON1009F-MDA are included for comparison. The details of the extraction of the relaxation times spectrum from viscoelastic data

are provided in Appendix D. The individual spectra were shifted horizontally to account for difference in  $T_g$  and vertically to account for difference in height of the  $\alpha$ -peak. The spectra of molecular liquids shown in Figure 3.28 look remarkably similar; moreover, it is possible that even the small difference between SB, mTd and DGEBA monomer is due to experimental scatter and/or mismatch between dielectric (DGEBA monomer) and mechanical relaxation (SB and mTd) relaxation response. Clearly, more materials need to be investigated before a conclusion about universality of the shape of the  $\alpha$ -process can be drawn.

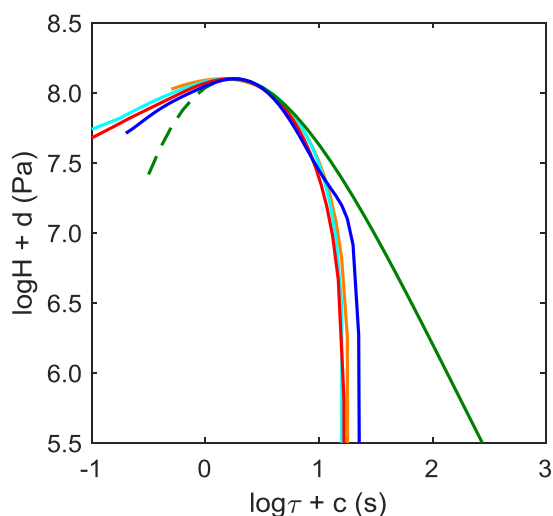


Figure 3.28. Relaxation times spectra for: EPON 1009F-MDA ( $\alpha$ ) – dark green, DGEBA monomer – blue, m-Toluidine1 – red, m-Toluidine2 – cyan, SB – orange.

In summary, the key features of how the relaxation spectra in the  $\alpha$  and  $\alpha+$  regions change with molecular architecture revealed in this communication are:

1. Molecular glass formers exhibit an abrupt end to the  $\alpha$  relaxation spectrum at long times and no discernable presence of any  $\alpha+$ -process. This is a significant result with respect to developing a fundamental understanding of the  $\alpha$ -process that is the physics controlling formation of the glass. The results shown in Figure 3.28 include linear viscoelastic mechanical and dielectric relaxation data – both of which clearly show a sharp end of the  $\alpha$ -process.

2. Linear polymers and loosely crosslinked network polymers exhibit an  $\alpha$ -process in the relaxation spectrum that is similar to that shown by molecular glass formers, but where there is no abrupt end at longer relaxation times, i.e. the  $\alpha$ -process appears broader for linear polymers vs molecular glass formers. In addition, if the molecular weight is high enough a shoulder appears on the relaxation spectrum at longer relaxation times associated with  $\alpha$ +-process. The location and shape of the  $\alpha$ +-process depends upon the molecular architecture and molecular weight of the polymer.
3. In the  $\alpha$  region of the relaxation spectrum oligomers exhibit a single process that is broader than the  $\alpha$ -process proper observed for linear polymers; oligomers do not exhibit any discernable  $\alpha$ +-process.
4. More tightly crosslinked networks including both the DGEBA systems reported in this paper as well as other network polymers reported in the literature exhibit only a single spectral peak in the  $\alpha$  and  $\alpha$ + regions, where that peak is much broader than the  $\alpha$  proper peak for linear polymers. And, no distinct  $\alpha$ + process is observed, although it is possible that the  $\alpha$ + process has been subsumed into the long relaxation time region of the  $\alpha$  process resulting in a single broader peak.
5. The  $\alpha$ -peaks proper for the loosely crosslinked networks and linear polymers have nearly universal spectral shape (when shifted to account for differences in  $T_g$  and intensity); the spectral shape of the  $\alpha$ + process for these materials depends upon the molecular weight and architecture.
6. For the DEGBA network polymers reported in this study the more tightly crosslinked networks have a similar spectral shape (when the  $\alpha$ -peak is shifted to account for differences in  $T_g$  and intensity). What is perhaps surprising is the noticeable change in the spectral shape between EPON1001F-DDS ( $\bar{M}_c=1072$  g/mole via titration, see SI) and EPON1002F-DDS ( $\bar{M}_c=1356$  g/mole via titration, see SI) – how could such a minimal change in  $\bar{M}_c$  have such a large effect on the spectral shape.

7. The  $\log a_T$  vs temperature curves for the DGEBA based systems shown in Figure 3.23 have two branches: (i) a steep temperature dependence for the EPON825-MDA, all of the EPON-DDS network polymers, the diamine cured network polymers reported by Gerard et al and for the EPON1009F-MDA  $\alpha$ -process, and (ii) a weaker temperature dependence for the DGEBA monomer, phenoxy linear polymer, the 75% monoamine – 25% diamine cured network polymers reported by Gerard et al and for the EPON1009F-MDA  $\alpha$ +-process. The scatter between materials on each of the two  $\log a_T$  vs temperature curves is minimal. What is surprising is that only these two distinct  $\log a_T$  vs temperature dependencies are apparently possible for all DGEBA based systems; it would seem natural to expect a broad variety of  $\log a_T$  vs temperature curves manifested with changing molecular architecture.

Some of the features mentioned above can be surmised from what have been reported elsewhere, including the abrupt end of the spectrum at long times for small molecular weight glass formers, the emergence of an  $\alpha$ +-process for linear polymers at long relaxation times for linear polymers of sufficient molecular weight, and the absence of a distinct  $\alpha$ +-process for oligomers.[13, 16, 56] In this study we have added network polymers to determine how this aspect of polymer architecture affects the  $\alpha$  and  $\alpha$ + components of the relaxation spectrum at least for the DGEBA class of linear and network polymers. It would be of considerable interest to have a similar set of monomer, linear and network polymers for another type of repeat unit to assess if the finding of this study are observed for polymers with different chemistries.

### 3.5 References

1. Doolittle, A.K., *Studies in Newtonian Flow. II. The Dependence of the Viscosity of Liquids on Free-Space*. Journal of Applied Physics, 1951. **22**(12): p. 1471-1475.
2. Turnbull, D. and M.H. Cohen, *Free-Volume Model of the Amorphous Phase: Glass Transition*. Journal of Chemical Physics, 1961. **34**(1): p. 120-125.
3. Cohen, M.H. and G.S. Grest, *Liquid-glass transition, a free-volume approach*. Physical Review B, 1979. **20**(3): p. 1077-1098.

4. Adam, G. and J.H. Gibbs, *On the Temperature Dependence of Cooperative Relaxation Properties in Glass-Forming liquids*. Journal of Chemical Physics, 1965. **43**(1): p. 139-146.
5. Caruthers, J.M. and G.A. Medvedev, *Quantitative model of super-Arrhenian behavior in glass forming materials*. Physical Review Materials, 2018. **2**(5): p. 055604.
6. Medvedev, G.A. and J.M. Caruthers, *A Quantitative Model of Super-Arrhenian Behavior in Glass-Forming Polymers*. Macromolecules, 2019. **52**(4): p. 1424-1439.
7. Roland, C.M., et al., *Supercooled dynamics of glass-forming liquids and polymers under hydrostatic pressure*. Reports on Progress in Physics, 2005. **68**: p. 1405-1478.
8. Ngai, K.L. and C.T. White, *Frequency dependence of dielectric loss in condensed matter*. Physical Review B, 1979. **20**(6): p. 2475-2486.
9. Chamberlin, R.V., et al., *Signature of ergodicity in the dynamic response of amorphous systems*. Physical Review B, 1992. **46**(9): p. 5787-5790.
10. Ni, Y., et al., *Rethinking the Analysis of the Linear Viscoelastic Behavior of an Epoxy Polymer near and above the Glass Transition*. Macromolecules, 2020.
11. Schonhals, A. and F. Kremer, *Analysis of Dielectric Spectra*, in *Broadband Dielectric Spectroscopy*, F. Kremer and A. Schonhals, Editors. 2003, Springer-Verlag: Berlin, Heidelberg. p. 57-97.
12. Gabriel, J., F. Pabst, and T. Blochowicz, *Debye Process and  $\beta$ -Relaxation in 1-Propanol Probed by Dielectric Spectroscopy and Depolarized Dynamic Light Scattering*. The Journal of Physical Chemistry B, 2017. **121**(37): p. 8847-8853.
13. Hofmann, M., et al., *Field-Cycling Relaxometry as a Molecular Rheology Technique: Common Analysis of NMR, Shear Modulus and Dielectric Loss Data of Polymers vs Dendrimers*. Macromolecules, 2015. **48**(20): p. 7521-7534.
14. Kimmich, R. and E. Anoardo, *Field-cycling NMR relaxometry*. Progress in Nuclear Magnetic Resonance Spectroscopy, 2004. **44**: p. 257-320.
15. Kariyo, S., et al., *From Simple Liquid to Polymer Melt. Glassy and Polymer Dynamics Studied by Fast Field Cycling NMR Relaxometry: Rouse Regime*. Macromolecules, 2008. **41**(14): p. 5322-5332.
16. Herrmann, A., et al., *Universal Polymer Dynamics Revealed by Field Cycling  $^1\text{H}$  NMR*. Macromolecules, 2009. **42**(14): p. 5236-5243.
17. Hofmann, M., et al., *Field-Cycling NMR Relaxometry Probing the Microscopic Dynamics in Polymer Melts*. Macromolecules, 2014. **47**(22): p. 7917-7929.
18. Doi, M. and S.F. Edwards, *The Theory of Polymer Dynamics*. 1988: Clarendon Press.
19. Vogel, H., *Das Temperaaturabhängigkeitsgesetz der Viskosität Flüssigkeiten*. Physikalische Zeitschrift, 1921. **22**: p. 645-646.

20. Fulcher, G.S., *Analysis of Recent Measurements of the Viscosity of Glasses*. Journal of the American Ceramic Society, 1925. **8**(6): p. 339-355.
21. Tammann, G., *Glasses as supercooled liquids*. Journal of the Society of Glass Technology, 1925. **9**: p. 166-185.
22. Williams, M.L., R.F. Landel, and J.D. Ferry, *The Temperature Dependence of Relaxation Mechanisms in Amorphous Polymers and Other Glass-forming Liquids*. Journal of the American Chemical Society, 1955. **77**(14): p. 3701-3707.
23. Ferry, J.D., *Viscoelastic Properties of Polymers*. 3<sup>rd</sup> ed. 1980, New York: John Wiley and Sons. 641.
24. Vleeshouwers, S., A.M. Jamieson, and R. Simha, *Effect of physical aging on tensile stress relaxation and tensile creep of cured EPON 828/epoxy adhesives in the linear viscoelastic region*. Polymer Engineering & Science, 1989. **29**(10): p. 662-670.
25. Gerard, J.F., et al., *Viscoelastic response of model epoxy networks in the glass transition region*. Polymer Engineering & Science, 1991. **31**(8): p. 615-621.
26. Mikolajczak, G., J.Y. Cavaille, and G.P. Johari, *Dynamic mechanical behaviour and its dependence on preparation method of structural epoxide resin*. Polymer, 1987. **28**(12): p. 2023-2031.
27. Lionetto, F. and A. Maffezzoli, *Relaxations during the postcure of unsaturated polyester networks by ultrasonic wave propagation, dynamic mechanical analysis, and dielectric analysis*. Journal of Polymer Science Part B: Polymer Physics, 2005. **43**(5): p. 596-602.
28. Alves, N.M., et al., *Viscoelastic Behavior of Poly(methyl methacrylate) Networks with Different Cross-Linking Degrees*. Macromolecules, 2004. **37**(10): p. 3735-3744.
29. Carsí, M., et al., *Effect of slight crosslinking on the mechanical relaxation behavior of poly(2-ethoxyethyl methacrylate) chains*. European Polymer Journal, 2013. **49**(6): p. 1495-1502.
30. Zajac, M., et al., *Relaxation behavior of polyurethane networks with different composition and crosslinking density*. Polymer, 2017. **111**: p. 83-90.
31. Plazek, D.J. and I.C. Choy, *The physical properties of bisphenol-a-based epoxy resins during and after curing. II. Creep behavior above and below the glass transition temperature*. Journal of Polymer Science Part B: Polymer Physics, 1989. **27**(2): p. 307-324.
32. Plazek, D.J. and I.-C. Chay, *The evolution of the viscoelastic retardation spectrum during the development of an epoxy resin network*. Journal of Polymer Science Part B: Polymer Physics, 1991. **29**(1): p. 17-29.
33. *D1652-97 Standard Test Methods for Epoxy Content of Epoxy Resins*. 1997, ASTM International: West Conshohocken, PA.



34. Curliss, D.B., *Linear and Nonlinear Viscoelastic Behavior of a Series of DGEBA Epoxy Resins*. 1987, Purdue University: West Lafayette, IN. p. 416.
35. Lunkenheimer, P. and A. Loidl, *Glassy Dynamics Beyond the  $\alpha$ -Relaxation*, in *Broadband Dielectric Spectroscopy*, F. Kremer and A. Schonhals, Editors. 2003, Springer-Verlag: Berlin, Heidelberg. p. 131-165.
36. Rouse Jr., P.E., *A Theory of the Linear Viscoelastic Properties of Dilute Solutions of Coiling Polymers*. The Journal of Chemical Physics, 1953. **21**(7): p. 1272-1280.
37. Treloar, L.R.G., *The Physics of Rubber Elasticity*. 1975: Oxford University Press, USA.
38. Enns, J.B., *The Cure of Thermosetting Epoxy/Amine Systems*. 1982, Princeton University: Princeton, NJ.
39. LeMay, J.D., *The Influence Of Molecular Structure On The Mechanical And Fracture Behavior Of Highly Crosslinked Epoxy Networks (thermoset)*. 1985, University of Akron: Akron, OH. p. 462.
40. Casalini, R., et al., *Influence of the glass transition on the secondary relaxation of an epoxy resin*. Physical Review B, 1997. **56**(6): p. 3016-3021.
41. Pakula, T., *Dielectric and Mechanical Spectroscopy – a Comparison*, in *Broadband Dielectric Spectroscopy*. 2003, Springer-Verlag: Berlin, Heidelberg. p. 597-623.
42. Jensen, M.H., et al., *Slow rheological mode in glycerol and glycerol–water mixtures*. Physical Chemistry Chemical Physics, 2018. **20**(3): p. 1716-1723.
43. Adrjanowicz, K., et al., *Communication: Slow supramolecular mode in amine and thiol derivatives of 2-ethyl-1-hexanol revealed by combined dielectric and shear-mechanical studies*. The Journal of Chemical Physics, 2015. **143**(18): p. 181102.
44. Jakobsen, B., K. Niss, and N.B. Olsen, *Dielectric and shear mechanical alpha and beta relaxations in seven glass-forming liquids*. The Journal of Chemical Physics, 2005. **123**(23): p. 234511.
45. Adolf, D.B., R.S. Chambers, and J.M. Caruthers, *Extensive validation of a thermodynamically consistent, nonlinear viscoelastic model for glassy polymers*. Polymer, 2004. **45**(13): p. 4599-4621.
46. Robertson, C.G. and C.M. Rademacher, *Coupling Model Interpretation of Thermorheological Complexity in Polybutadienes with Varied Microstructure*. Macromolecules, 2004. **37**(26): p. 10009-10017.
47. Nicolai, T. and G. Floudas, *Dynamics of Linear and Star Poly(oxypropylene) Studied by Dielectric Spectroscopy and Rheology*. Macromolecules, 1998. **31**(8): p. 2578-2585.
48. Guo, J., L. Grassia, and S.L. Simon, *Bulk and shear rheology of a symmetric three-arm star polystyrene*. Journal of Polymer Science Part B: Polymer Physics, 2012. **50**(17): p. 1233-1244.

49. Alves, N.M., et al., *Departure from the Vogel behaviour in the glass transition - thermally stimulated recovery, creep and dynamic mechanical analysis studies*. Polymer, 2004. **45**(3): p. 1007-1017.
50. Fuchs, K., C. Friedrich, and J. Weese, *Viscoelastic Properties of Narrow-Distribution Poly(methyl methacrylates)*. Macromolecules, 1996. **29**(18): p. 5893-5901.
51. Inoue, T., et al., *Viscoelasticity of low molecular weight polystyrene. Separation of rubbery and glassy components*. Journal of Polymer Science Part B: Polymer Physics, 1999. **37**(4): p. 389-397.
52. Zheng, W., G.B. McKenna, and S.L. Simon, *The viscoelastic behavior of polymer/oligomer blends*. Polymer, 2010. **51**(21): p. 4899-4906.
53. Jakobsen, B., et al., *Beta relaxation in the shear mechanics of viscous liquids: Phenomenology and network modeling of the alpha-beta merging region*. Journal of Non-Crystalline Solids, 2011. **357**(2): p. 267-273.
54. Hutcheson, S.A. and G.B. McKenna, *The measurement of mechanical properties of glycerol, m-toluidine, and sucrose benzoate under consideration of corrected rheometer compliance: An in-depth study and review*. Journal of Chemical Physics, 2008. **129**: p. 074502.
55. Maggi, C., et al., *Supercooled Liquid Dynamics Studied via Shear-Mechanical Spectroscopy*. The Journal of Physical Chemistry B, 2008. **112**(51): p. 16320-16325.
56. Hofmann, M., et al., *Glassy, Rouse, and Entanglement Dynamics As Revealed by Field Cycling 1H NMR Relaxometry*. Macromolecules, 2012. **45**(5): p. 2390-2401.

#### **4. EFFECT OF DEFORMATION HISTORY ON STRESS-STRAIN BEHAVIORS OF GLASSY POLYMERS FROM A MOBILITY PERSPECTIVE**

In previous chapters, it has been demonstrated how mobility is affected by temperature where mobility is evaluated by linear deformation experiments. Critically, a linear/small deformation experiment serves only as a reporter on the state of the material without changing it. When deformation becomes nonlinear/large, the state of material changes and so does the mobility. Most directly this effect of active deformation on mobility was observed in the photobleaching experiments of Ediger and co-workers.[1] In these experiments an optically active probe molecules were dispersed in the glassy polymer matrix and the rate of rotational diffusion of the probes served as a reporter on the mobility of the matrix. Ediger and co-workers demonstrated that the rate of rotational diffusion accelerated by three orders-of-magnitude upon application of a load to a specimen, where the specimen was undergoing a nonlinear creep deformation. In addition to optical experiments of Ediger, the effect of large deformation on mobility is inferred from the phenomenon of yield. Specifically, it is believed that yield in constant strain rate experiment is a viscoelastic behavior where the characteristic relaxation time is made dramatically shorter by deformation (as compared to that for an undeformed material).[2-4] Several constitutive models have been proposed to describe experimentally observed response of polymer glasses to large deformations, where the underlying idea is that mobility, i.e. rate of relaxation, is affected by deformation. There are two main classes of such models: in the first class the characteristic relaxation time depends on the *current deformation*, e.g. current stress, strain, strain rate, etc.; in the second class the characteristic relaxation time depends on the entire *deformation history*. The dependence of mobility on the deformation history in the second class of constitutive models is implemented as follows: (i) some internal (also called structural) variable is postulated to control mobility, (ii) a constitutive equation describing how this internal variable depends on the deformation history is postulated or derived, and (iii) an equation describing how the relaxation time depends on this the internal variable is postulated. Examples of internal variables found in the literature include free volume[5, 6], configurational entropy[7, 8] and configurational internal energy[9, 10] as well as unspecified “structural variable”[11, 12]. The first class of constitutive

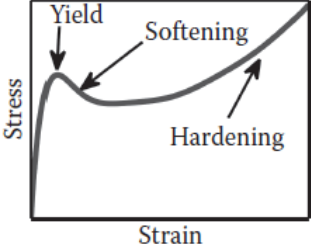
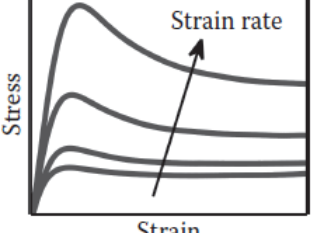
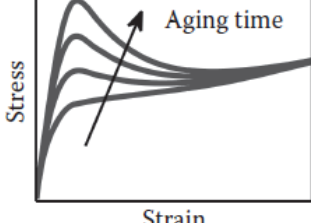
models comprises phenomenological models. In contrast, a successful model of the second class would have a fundamental significance, because its success implies that a particular internal variable truly captures the underlying physics of glass. Thus, testing and validation of constitutive models for glassy polymers is important from both practical and fundamental standpoints.

By definition, a constitutive model must describe material response to arbitrary thermal and deformation history. The simplest history is just an isothermal aging at a sub- $T_g$  temperature i.e. no deformation. Next is a single-step deformation either at constant applied stress (i.e. creep) or at constant strain rate. The majority of experiments in the literature are single-step experiments. In turn, most of the constitutive models for polymer glasses only attempt to predict the single-step experiments. The models of Boyce and co-workers[13], Buckley and co-workers[14, 15], the Eindhoven model for glassy polymers[16-18], the thermo-viscoelastic model of Caruthers and co-workers[9, 19], and the visco-plastic model of Anand and co-workers [20, 21] successfully describe single-step experiments, although to do so most of these models require large number of fitting parameters. Medvedev and Caruthers argued[22] that single-step experiments are not sufficiently discriminating and multi-step experiments must be included in model validation. An important example of a two-step experiment is loading followed by unloading. If a specimen had been aged for a certain amount of time prior to deformation experiment, what is the state of the material after the loading-unloading cycle? Two contradictory scenarios have been reported: in the works of Sternstein and co-workers[23] they found that material behaved as if it was closer to equilibrated state – the accelerated aging scenario; on the other hand, several authors[24, 25] observed that the material behaved as if the aging that occurred prior to deformation experiment had been erased – the rejuvenation scenario. When three-step experiments are considered, for example loading-unloading-reloading, the key question is if the stress-strain response during reloading is the same as during the original loading. According to Medvedev and Caruthers analysis,[22] when two, three, etc.-step experiments are considered most of the known constitutive models fail to predict the experimental data. Of particular significance are the four-step experiments of Dreistadt et al,[26] where they carried out (1) constant strain rate loading, (2) constant strain rate *partial* unloading to a given stress, (3) creep under this stress, and (4) constant strain rate loading. They studied the effect of the stress value in the step 3 on the shape of the stress-strain curve obtained in the final loading, i.e. step 4. Unexpectedly, Dreistadt et al found that

the magnitude of the overshoot in the step 4 loading *increased* with the creep stress. Medvedev and Caruthers demonstrated[22] that none of the existing constitutive models predicts this result; in fact, they predict the opposite outcome – that increase in creep stress will result in smaller overshoot. Moreover, the results of this four-step experiment of Dreistadt et al appear to call into question the central assumption of all existing constitutive models – that the deformation effect on mobility is the sole explanation of observed response of glassy polymers to deformation. Considering how consequential the four-step experiments of Dreistadt et al appear to be, in this chapter we: (i) in the theoretical part, carefully analyze how specific assumptions of ‘the mobility is the driver’ picture lead to contradictions with the experiments and (ii) in the experimental part, attempt to reproduce Dreistadt et al protocol. We study a different material – thermoset Epon1009F-MDA epoxy (vs thermoplastic polycarbonate in Dreistadt et al) and different geometry – extension (vs compression in Dreistadt et al).

#### 4.1 Signatures of Stress-Strain Behaviors Explained by Mobility Change

Table 4.1. Features of a single-step nonlinear stress-strain behavior of a glassy polymer

	<p>Five stages where <math>d\sigma/d\varepsilon</math> changes sign:</p> <ol style="list-style-type: none"> <li>linear portion, where the slope is elastic modulus,</li> <li>yield (<math>d\sigma/d\varepsilon = 0</math>), featured with a stress overshoot peak,</li> <li>post-yield softening (<math>d\sigma/d\varepsilon &lt; 0</math>),</li> <li>flow (<math>d\sigma/d\varepsilon = 0</math>),</li> <li>post-yield hardening (<math>d\sigma/d\varepsilon &gt; 0</math>).</li> </ol>
	<p>At a faster strain rate,</p> <ol style="list-style-type: none"> <li>magnitude of stress overshoot at yield increases,</li> <li>magnitude of stress in flow region increases.</li> </ol>
	<p>If the material is more aged before experiment,</p> <ol style="list-style-type: none"> <li>magnitude of stress overshoot at yield increases,</li> <li>magnitude of stress in flow region does not significantly increase.</li> </ol>

Before digging into multi-step experiment with complicated deformation history, the result of one-step loading experiment at a constant strain rate is schematically plotted in Table 4.1, where five stages are observed.

From the perspective of mobility, yield is the point where mobility increases to such an extent that the material starts to exit glassy state (and to enter liquid/equilibrium state) on the microscopic level.[27] If the material is aged prior to the experiment, it has lower mobility at  $t = 0$  and requires more external mechanical input to reach yield, which is why the stress overshoot at yield increases with aging time.

The flow region is a steady state ( $d\sigma/d\varepsilon = 0$ ) where the stress no longer increases with strain. Once the flow region has been reached, the material is microscopically similar to an equilibrium liquid (or that of a super-cooled liquid, or a freshly quenched glass). Since flow state is considered as an equilibrium state, the mobility is only dependent on current thermal and mechanical state. In the case of constant strain experiment, mobility depends on current temperature and strain rate, regardless of how the liquid state is arrived at (i.e., thermal and deformation history). That is to say previous aging effect has been removed in the flow region. The stress in flow and the subsequent hardening stages will be the same for differently aged specimens as long as they are under the same temperature and strain rate.

When strain rate is different, the mobility at steady-state flow region will be different. Qualitatively, mobility is higher when the strain rate is faster.

Post-yield hardening is a feature of polymers and is explained by a different assumption consisting molecular chains. It is not a common feature for all glass-forming materials. Therefore, the feature of post-yield hardening will not be used to examine constitutive models for glassy materials.

## **4.2 Constitutive Models Describing Mobility**

In constitutive models, mobility is quantified as a characteristic relaxation time  $\log\tau$ , or the shift factor  $\log a = \log(\tau/\tau_{\text{ref}})$  which is the relaxation time with respect to a reference time scale. In this section, a list of constitutive models will be examined by qualitatively comparing the model

prediction to experimental behaviors. Granted that a constitutive model should capture a totality of thermo-mechanical signatures, the focus is on the model prediction of stress-strain behaviors since they are informative with many discriminative features as shown in Table 4.1. As will be discussed below, stress-strain behaviors are also discriminative that models lacking an appropriate assumption will fail to capture the experimental behavior. In this sense, major constitutive models will be categorized into three types: (i) the very basic Maxwell model where relaxation time  $\tau$  is independent on deformation, (ii)  $\tau$  is dependent on current stress or current strain, and (iii)  $\tau$  is dependent on current deformation as well as deformation history. For each category, examples of constitutive models often seen in literature will be given, along with their key equation that addresses the  $\log\tau$  and/or  $\log\alpha$  mobility term.

#### 4.2.1 Maxwell Model

The simplest model to describe a viscoelastic solid is a Maxwell element where a purely viscous dashpot and a purely elastic spring are connected in series. The relaxation time of the Maxwell element is defined as  $\tau = \eta/G$ , where  $\eta$  and  $G$  are viscosity of the dashpot and shear modulus of the spring. According to the definition,  $\tau$  is dependent only on temperature. Under isothermal conditions, it is a constant which does not change during the mechanical experiment. The constitutive equation is given in Equation (4.1):

$$\frac{d\varepsilon}{dt} = \frac{\sigma}{G\tau} + \frac{1}{G} \frac{d\sigma}{dt} = \dot{\varepsilon}_0 \quad (4.1)$$

By solving the equation, predicted stress-strain curve is given in Figure x, where strain rate  $\dot{\varepsilon}$  is known by experimental setting, shear modulus  $G$  and relaxation time  $\tau$  are evaluated in linear mechanical experiments.

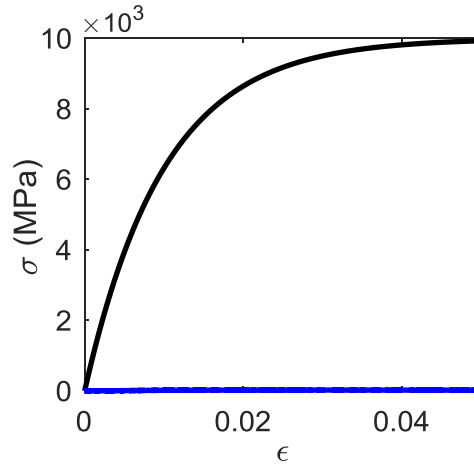


Figure 4.1. Predicted stress-strain behavior by Maxwell model (black line) compared to experimental data (blue line) obtained for a crosslinked DGEBA material at  $T_g - 16^\circ\text{C}$ .

As shown in Figure 4.1, the basic Maxwell element can only predict linear-range stress-strain curve. When strain is in non-linear range, the predicted stress is over 3 orders of magnitude higher than the actually measured stress. Apparently, it is inappropriate to assume  $\tau$  is independent of deformation.

#### 4.2.2 Nonlinear, “Material Clock” Models

With larger deformation, more mechanical work is input to the system and mobility will increase. Relaxation time should decrease with deformation. This is intuitively correct by examining the steady-state solution  $\sigma = \dot{\epsilon}G\tau$ . The stress values in non-linear range will be closer to the actual data if  $\tau$  decreases with deformation. As to which deformation-related variable is directly related to  $\tau$ , there are three choices: stress  $\sigma$ , strain  $\epsilon$ , and strain rate  $\dot{\epsilon}$ . In the case of constant strain rate experiment,  $\tau(\dot{\epsilon})$  is still a constant throughout the experiment, which will fail in the same way as Maxwell model. The other two categories of constitutive models will be examined organized by a material clock model concept. “Clock” is the word to emphasize the mobility as the key variable that relates all thermal-mechanical behaviors.[22] The idea of a material clock model is that all material responses are various manifestations of the same underlying glassy behavior, while the differences in their experimental behaviors with respect to the lab time scale (or the lab clock) are



due to the differences between clocks. The material clock will slow down during vitrification, and will be accelerated under large deformation. The material clock model assumption might be inadequate, but it is consistent with timescale-dependent or mobility-dependent nature of glasses, which is a concise way to introduce the variable that directly controls mobility.

### ***“Stress Clock” Models***

This type of model says relaxation time decreases with the increase of stress. With appropriate parameter and functional form, the non-linear portion of stress-strain curve up to yield are successfully captured. The values are also consistent with experimental measurements. However, at yield where  $d\sigma/d\epsilon=0$ , the stress reaches steady state and stops changing. After yield  $\tau$  will not change. The predicted stress-strain curve does not have post-yield softening region, as shown in Figure 4.2.

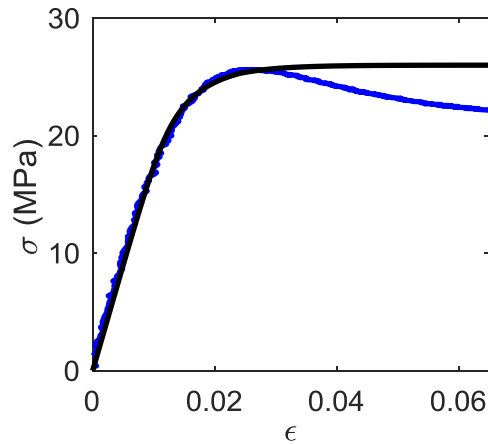


Figure 4.2. Predicted stress-strain behavior by a one-dimensional stress clock model (black line) compared to experimental data (blue line) obtained for a crosslinked DGEBA material at  $T_g - 16^\circ\text{C}$ .

Plasticity-based models are essentially stress clock models. Eyring proposed the first plasticity model where mobility was quantified as the dashpot viscosity which is proportional to relaxation time ( $\tau = \eta/G$ ). The functional form is given by Equation (4.2).

$$\frac{1}{\tau} \sim f(T) \sinh \frac{\sigma \lambda}{kT} \quad (4.2)$$

Due to failure in predicting post-yield softening and other features (e.g., physical aging), later basic plasticity models add extra terms to the Eyring viscosity for each non-predicted features. Typical plastic models are listed in Table 4.2.

Table 4.2. Plasticity-based constitutive models for polymers in glassy state

Constitutive Model	Key Function(s) Describing Mobility	Effect of Deformation on Mobility
Haward, Thackray, 1968 [28]	Modified Eyring viscosity, $\frac{1}{\eta} \sim \sinh \frac{\sigma_s(1+\varepsilon_p)V^*}{k_B\theta}$ At large stress ( $\sigma_s$ ), $\frac{1}{\eta} \sim \frac{1}{2} \exp\left(\frac{\sigma_s(1+\varepsilon_p)V^*}{k_B\theta}\right)$	Mobility ( $1/\eta$ ) increases with stress ( $\sigma_s$ ).
Boyce, Park, Argon, 1988 [13]	Eyring viscosity $\times$ post-yield softening factor, $\eta(\theta, \sigma_s^d, D) = \eta(\theta, \sigma_s^d) \exp(-D)$ $\dot{D} = h \dot{\varepsilon}_p (D_\infty - D), D(t=0) = D_0$	Mobility ( $1/\eta$ ) increases with stress ( $\sigma_s$ ) and plastic strain rate ( $\dot{\varepsilon}_p$ ).
Buckley et al., 2004 [14, 15]	Eyring viscosity $\times$ Buckley Fictive temperature $\theta_f = \theta_{f0} + \Delta\theta_f \left[ 1 - \exp\left(-\frac{\bar{\varepsilon}_p}{\varepsilon_{p0}}\right) \right]$ $\bar{\varepsilon}_p = \int_0^t \sqrt{\frac{2}{3}} (\mathbf{D}_p(s) : \mathbf{D}_p(s)) ds$	Mobility ( $1/\eta$ ) increases with stress ( $\sigma_s$ ). Mobility (-loga) also increases with plastic strain ( $\varepsilon_p$ ) through fictive temperature (loga $\sim$ -( $\theta - \theta_f$ )).
Eindhoven model for glassy polymer, 2005 [17]	Eyring viscosity $\times$ aging factor, $a(\theta, \sigma_s^d, \bar{\gamma}_p) = \exp\left(\frac{\Delta U}{k_B\theta}\right) \exp\left(\mu \frac{pV^*}{k_B\theta}\right)$ $\times \frac{\bar{\sigma}_s V^*}{k_B\theta} \left[ \sinh\left(\frac{\bar{\sigma}_s V^*}{k_B\theta}\right) \right]^{-1} \exp(S_{age} R(\bar{\gamma}_p))$	Mobility ( $1/a$ ) increases with stress ( $\sigma_s$ ), decreases with plastic strain ( $\gamma_p$ ).

With more complicated functions and more form factors, the equations listed in Table 4.2 are capable of fitting experimental curves. Anand et al. model (2009)[20] is more complicated where a set of parameters  $\{c_i, \mu_{cv,i}, \mu_{i0}, h_0, s_{cv}, b, \phi_{cv}, s_{00}, g_0, \phi_0, s_{i0}\}$  are separately determined to address different experimental features. In all plasticity-based models, each form factor to describe a

separate feature is associated with an activation energy, which is not consistent with the non-equilibrium nature of glassy state. Activation energy is associated with Arrhenian equation which is used to describe thermally-activated transitions between two thermodynamically equilibrium states. In glassy state, it is not physical to assume that the thermal-mechanical signatures are triggered events separately added up to a basic plastic foundation. All predicted features should manifest from the same underlying physics.

### ***“Strain Clock” Models***

The other option is that  $\tau$  decreases with the increase of strain. With this assumption, the predicted stress-strain curve up to yield is consistent with experimental observations, as seen in Figure 4.3.

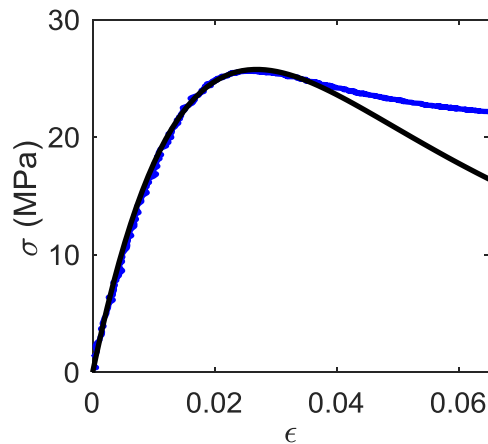


Figure 4.3. Predicted stress-strain behavior by a one-dimensional strain clock model (black line) compared to experimental data (blue line) obtained for a crosslinked DGEBA material at  $T_g - 16^\circ\text{C}$ .

However, in post-yield region, since strain is increasing during the entire experiment,  $\tau$  will always decrease and will not reach a steady-state flow region. The consequence is that the predicted stress will always decrease until it reaches zero, which is inconsistent with experimental observations. An example of strain clock model in literature is given in Table 4.3.

Table 4.3. “Strain clock” constitutive models for polymers in glassy state

Constitutive Model	Key Function(s) Describing Mobility	Effect of Deformation on Mobility
Popelar, Liechti, 2003 [29]	$\log a = \frac{b}{2.303} \left[ \frac{1}{f} - \frac{1}{f_0} \right] + \frac{b_s}{2.303} \left[ \frac{1}{f_s + \bar{\epsilon}_{eff}} - \frac{1}{f_s} \right]$ $\bar{\epsilon}_{eff} = \sqrt{\frac{2}{3} (\boldsymbol{\epsilon}^d : \boldsymbol{\epsilon}^d)}$	Mobility (-loga) increases with strain ( $\epsilon_{eff}$ ).

### 4.2.3 “Internal Variable History Clock” Models

The failure of predicting all features on a stress-strain curve means there is still something missing in the underlying structure of constitutive models. One signature about glass has been overlooked that properties of a glass depend on how the glassy state is arrived at. For constitutive models, mobility terms should not only be dependent on current state, but also on deformation history. A structural variable  $S$  is used to address the dependence of deformation history, despite the disagreement of what  $S$  is. Practitioners in this field have proposed different internal variables, such as free volume, configurational entropy, configurational energy, etc, as listed in Table 4.4.

Table 4.4. “Internal variable history clock” constitutive models for polymers in glassy state

Constitutive Model	Key Function(s) Describing Mobility	Effect of Deformation on Mobility
Knauss, Emri, 1987 [30]	<p>Generalized Doolittle free volume,</p> $\log a = \frac{b}{2.303} \left[ \frac{1}{f} - \frac{1}{f_0} \right] = \frac{b_s}{2.303} \left[ \frac{1}{f_0 + \Delta f_\theta + \Delta f_\sigma} - \frac{1}{f_0} \right]$ $\Delta f_\theta = A \int_{-\infty}^t \alpha(t^* - s^*) \frac{d\theta}{ds} ds$ $\Delta f_\sigma = B \int_{-\infty}^t \beta(t^* - s^*) \frac{d}{ds} tr(\sigma(s)) ds$	Dilatational volume ( $tr(\boldsymbol{\sigma})$ )
Shay, Caruthers, 1990 [19]	$\log a = \frac{B}{2.303} \left[ \frac{1}{TS} - \frac{1}{T_0 S_0} \right]$	Adam-Gibbs configurational entropy $S$
Caruthers et al., 2004 [9]	$e(t) = \Psi(t) + \theta \eta(t)$	Helmholtz free energy $\psi$
Medvedev, Caruthers, 2013 [31]	$\log \hat{a}(\theta, V, \hat{\mathbf{x}}) = c_1 \left( \frac{e_{c,ref}^\infty}{e_c^\infty(\theta, V) + \hat{e}_c(\hat{\mathbf{x}})} - 1 \right)$	Internal energy $e(\theta, V)$ with local fluctuation $e(\mathbf{x})$

Not knowing what exactly  $S$  is, the functional form of  $S$  is given by Equation (4.3) and (4.4), where the first term on RHS of Equation (4.3) accounts for thermal history and the second term for deformation history. Note that Equation (4.3) and (4.4) are only a one-dimensional approximation for constant strain rate experiment in order to check if the functional form is correct. The actual constitutive equation is more complex.

$$\frac{dS}{dt} = -\frac{S - S_f}{\tau(S)} + C|\dot{\epsilon}| \quad (4.3)$$

$$S(t=0) = S_i$$

$$\log \frac{\tau}{\tau_{ref}} = \frac{B}{S - S_{ref}} \quad (4.4)$$

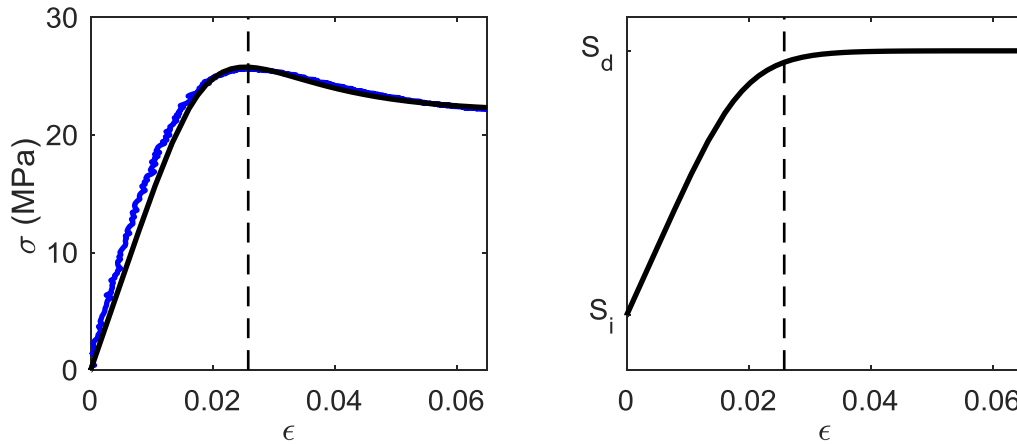


Figure 4.4. Left: Predicted stress-strain behavior by a one-dimensional internal variable history clock model (black line) compared to experimental data (blue line) obtained for a crosslinked DGEBA material at  $T_g - 16^\circ\text{C}$ . Right: Evolution of the internal variable  $S$  mobility with larger strain. The dashed line in both panels indicates the strain at yield.

Figure 4.4 gives the predicted stress-strain curves and corresponding evolution of the intermediate variable  $S$ . The general trend of  $S$  mobility is increasing with deformation, with a delay compared to the change of stress. Such a delay in  $S$  gives rise to the post-yield softening. Specifically, when stress is maximized ( $d\sigma/dt = 0$ ),  $S$  is still increasing and  $\log\tau$  will decrease. Based on Equation

(4.1), the steady-state stress  $\sigma = \dot{\epsilon}G\tau$  will also decrease, until  $S$  is in steady state. In flow region both  $S$  and  $\sigma$  are in steady state and remain constant.

Equation (4.3) and (4.4) are not a true constitutive model since (i) the  $S$  values are not assigned to any thermodynamic properties, and (ii) these two equations do not address tensorial stress and strain. However, the predicted stress-strain curve is qualitatively consistent with experimental data, meaning the equation at least has a correct functional form associated with current deformation and deformation history.

The next step is to examine if internal variable history clock model can capture the changes in stress-strain behaviors affected by (i) strain rate, which represents determines the current deformation state, (ii) physical aging at the same temperature prior to mechanical test, which is the simplest form of thermal history, and (iii) previous loading steps in a multi-step mechanical experiment. A qualitative comparison between experimental data and internal variable history clock model predictions will be given in the rest of this section.

### ***Effect of Strain Rate***

As described in Table 4.1, a higher strain rate will cause an increase in stress overshoot at yield and the stress in flow region. This experimental feature can be explained in terms of steady-state mobility  $S_d$  which is given by Equation (4.5).

$$S_d = S_f + C|\dot{\epsilon}|\tau_d \quad (4.5)$$

where  $S_f$  means the final mobility without deformation. With the presence of deformation,  $S_d$  is much larger than  $S_f$ , consistent with the observation that mobility can be increased by three orders of magnitude under large deformation. The effect of strain rate on mobility is that it increases the steady-state mobility  $S_d$ , as shown in Figure 4.5. A larger  $S_d$  also results in more delay in the increase of  $S$  mobility, i.e.,  $\Delta S = S_d - S_i$  is larger, which is the direct reason for a larger overshoot. The predicted stress-strain curve is given in Figure 4.5 and is consistent with experimental observations.

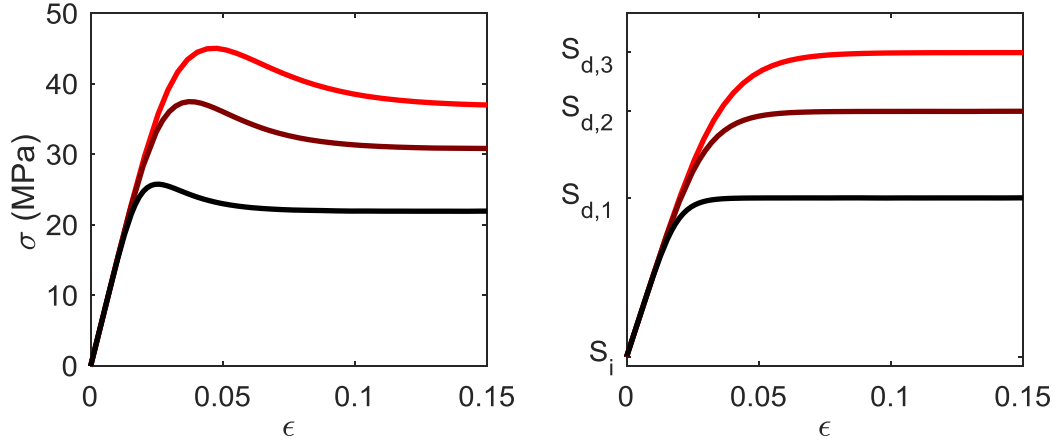


Figure 4.5. Left: Predicted stress-strain behavior by a one-dimensional internal variable history clock model at the following strain rates:  $1.1 \times 10^{-4}/s$  (black),  $5.5 \times 10^{-4}/s$  (brown),  $1.1 \times 10^{-3}/s$  (red). Right: Corresponding internal variable  $S$  mobility change with strain at the same strain rates.

### ***Effect of Physical Aging***

In Table 4.1 typical aging effect has been illustrated. From the mobility perspective, pre-test aging will decrease initial mobility but has no effect of steady-state mobility. This is also supported by Equation (4.6) where the  $S$  mobility change with time is given by the first term.

$$\frac{dS}{dt} = -\frac{S - S_f}{\tau(S)} \quad (4.6)$$

Solution to Equation (4.6) is plotted in Figure 4.6, where  $S$  mobility exponentially decreases with time.

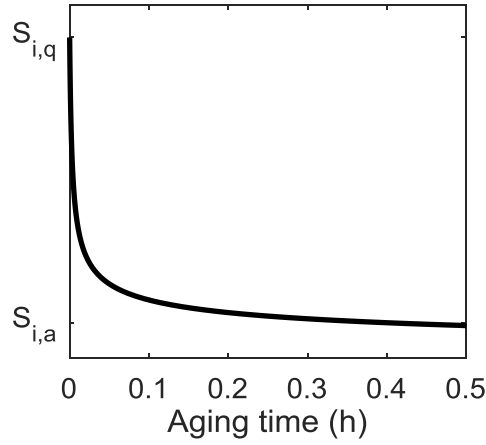


Figure 4.6. Solution to Equation (4.6) which indicates how internal variable  $S$  mobility decreases with longer aging time.

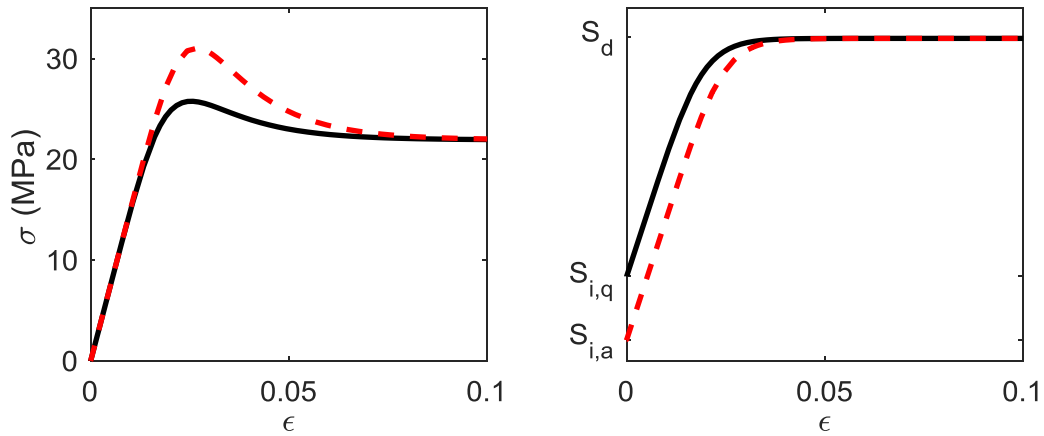


Figure 4.7. Left: Predicted stress-strain behavior by a one-dimensional internal variable history clock model for quenched (black) and 30-min aged (red dashed) materials. Right: Corresponding internal variable  $S$  mobility change with strain.

When deformation is applied to two specimens that have been aged differently, the initial mobility  $S_i$  will be different. The change in mobility with strain during the experiment is given in Figure 4.6, where the  $S_d$  obtained in steady state is the same for these two specimens since the strain rate is the same. That is to say the thermal history has been erased when the specimen is in flow region. Such an erase of thermal and deformation history can also be achieved by heating the specimen up



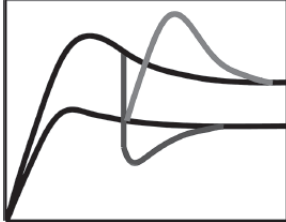
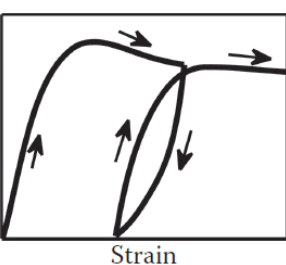
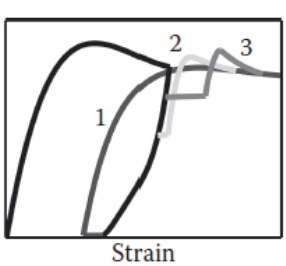
to above- $T_g$  terminal region. The stress-strain predictions for a quenched and an aged material are given in Figure 4.7 and are consistent with experimental results.

Now with all the features listed in Table 4.1 have been captured by the internal variable history clock models which correctly predicts stress-strain behaviors with different aging and strain rate, more complicated experiment will be introduced to further test the model.

### 4.3 Internal Variable History Clock Model Predictions for Multi-Step Stress-Strain Behaviors

In addition to the basic one-step stress-strain behavior, a constitutive model should also be capable of predicting thermo-mechanical behaviors with deformation histories at least qualitatively. Within the topic of strain-controlled experiments, relevant datasets are described in Table 4.5.

Table 4.5. Features of multi-step stress-strain behaviors of glassy polymers

	<p>2-step switch-of-strain-rate experiment:</p> <ol style="list-style-type: none"> <li>The strain rate is initially low and increased to a high value in the post-yield region. A stress overshoot in the second step is observed.</li> <li>If strain rate is initially high and decreased to a low value, then there will be an undershoot in the second step.</li> </ol>
	<p>3-step loading-unloading-reloading experiment:</p> <ol style="list-style-type: none"> <li>Step #1: loading at a constant strain rate <math>\dot{\epsilon}_0</math>, where an overshoot at yield is observed,</li> <li>Step #2: unloading to zero stress at <math>-\dot{\epsilon}_0</math>,</li> <li>Step #3: reloading at the same initial strain rate <math>\dot{\epsilon}_0</math>.</li> </ol> <p>Comparing Step #3 to Step #1, the modulus (initial slope) is approximately the same, while the stress overshoot at yield in the reloading is smaller.</p>
	<p>4-step loading-unloading-creep-reloading experiment:</p> <ol style="list-style-type: none"> <li>Step #1: loading at a constant strain rate <math>\dot{\epsilon}_0</math> up to post-yield region,</li> <li>Step #2: unloading to a given stress <math>\sigma_3</math> at <math>-\dot{\epsilon}_0</math></li> <li>Step #3: creep at <math>\sigma_3</math> for a period of time <math>t_3</math>,</li> <li>Step #4: reloading at the same initial strain rate <math>\dot{\epsilon}_0</math>.</li> </ol> <p>The overshoot in initial loading (step #1) and reloading (step #4) steps indicates that the material is more aged when creep stress <math>\sigma_3</math> and/or creep time <math>t_3</math> increases.</p>

### 4.3.1 Two-Step Switch of Strain Rate Behaviors

The experiments were performed for PMMA at  $T_g - 15.8^\circ\text{C}$ , where the strain rate switched from  $8.3 \times 10^{-6}/\text{s}$  to  $8.3 \times 10^{-4}/\text{s}$  (or reversely).[32] Experimental results are plotted in Figure 4.8. A change in mobility is indirectly reflected by the amount of overshoot (or undershoot) of the second step. With longer deformation history, i.e., longer duration of the first slow-rate step, the magnitude of overshoot in the subsequent fast-rate step will increase and then remains the same. In the case of fast-to-slow switch, the amount of undershoot will increase with more deformation history and then remains the same.

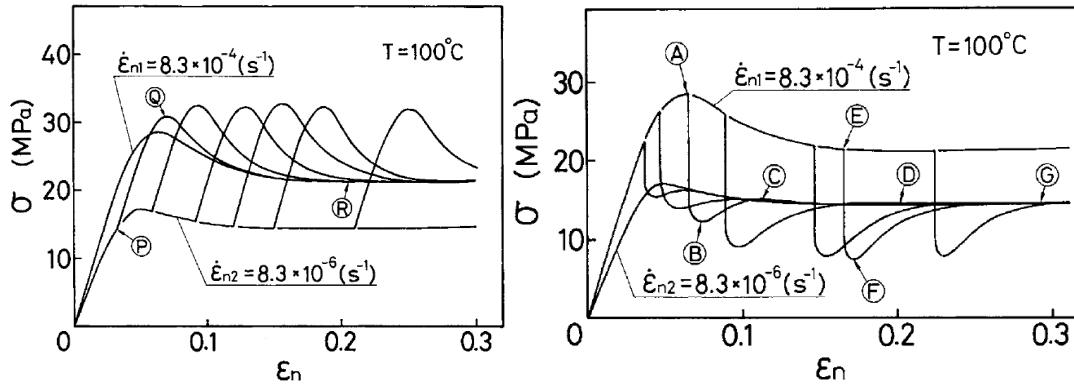


Figure 4.8. Left: Stress-strain behavior of PMMA at  $T_g - 15.8^\circ\text{C}$  at a slow strain rate ( $8.3 \times 10^{-6}/\text{s}$ ) jumping to a fast strain rate ( $8.3 \times 10^{-4}/\text{s}$ ). Right: Stress-strain behaviors during a fast-to-slow strain rate switch experiment. [32]

Model descriptions of stress-strain behaviors and corresponding mobility changing with strain are qualitatively consistent with the experimental results, as shown in Figure 4.9. Again, the delayed increase (or decrease) in mobility compared to stress gives rise to the overshoot (or undershoot). The “saturation” of the overshoot (or undershoot) with longer deformation history can also be explained with the same mobility assumption. If the switch happens after the material is already in flow region where  $S_d$  will not change with larger strain, the amount of overshoot (or undershoot) will remain the same since  $\Delta S = S_{d2} - S_{d1}$  will be the same.

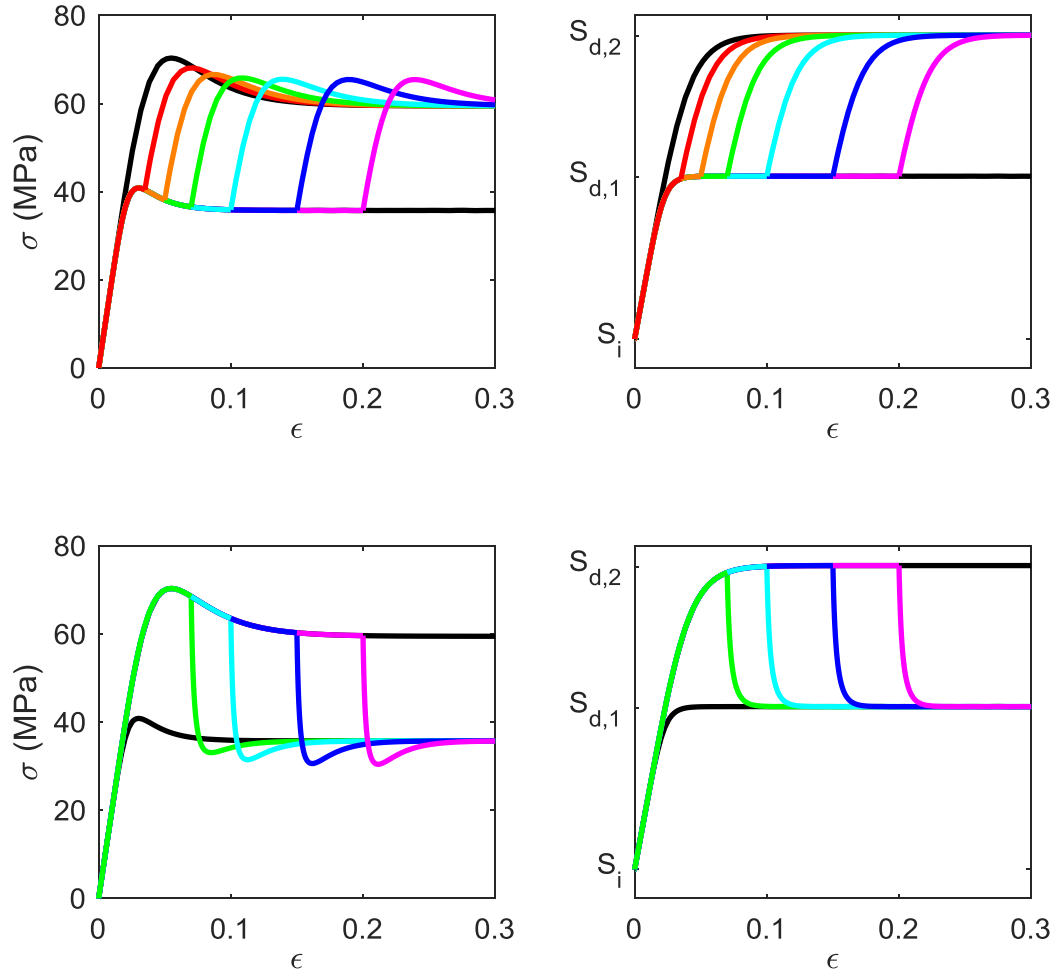


Figure 4.9. Left: Predicted stress-strain behaviors by a one-dimensional internal variable history clock model for slow-to-fast (Upperleft) and fast-to-slow (Lowerleft) strain rate switch experiment. Right: Corresponding internal variable  $S$  mobility change with strain.

With no additional mechanism, the internal variable history clock is also qualitatively capable of predicting the 2-step switch-of-strain-rate experimental behaviors. The predicted overshoot in Figure 4.9 after the low-to-fast strain switch is smaller than the overshoot in monotonic loading. This problem could be solved by optimizing model parameters for this particular dataset.

### 4.3.2 Three-Step Loading-Unloading-Reloading Behaviors

This type of experiment is more commonly used to test the fatigue property of materials during cyclic loading-unloading conditions. A representative dataset is given in Figure 4.10 for bisphenol A polycarbonate at  $T_g - 123\text{ }^\circ\text{C}$  using strain rate =  $10^{-3}/\text{s}$  in both initial loading and reloading steps. [26]

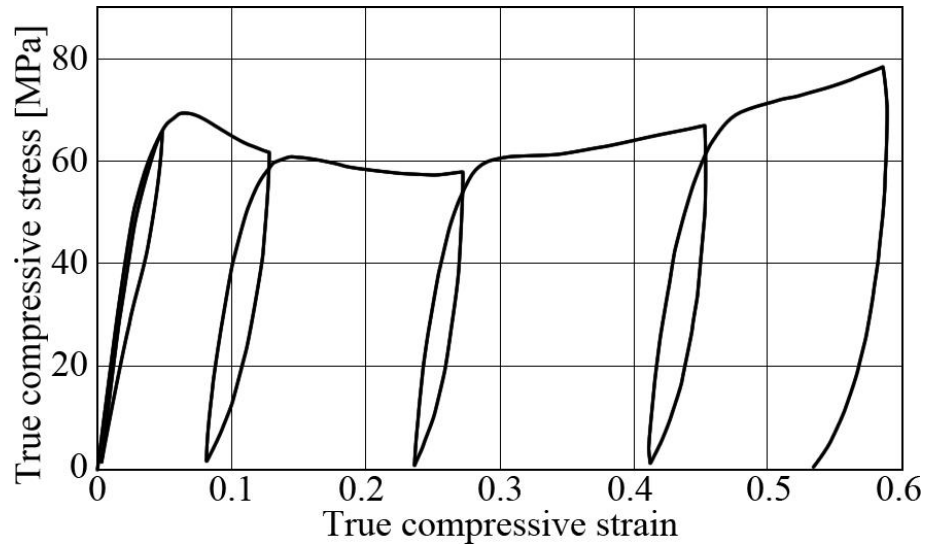


Figure 4.10. Stress-strain behaviors of polycarbonate at  $T_g - 123\text{ }^\circ\text{C}$  during 2 cycles of loading at  $10^{-3}/\text{s}$ . [26]

A much smaller overshoot is observed in the reloading step. With the knowledge that a glassy material deformed up to flow region has a high mobility similar to a super-cooled liquid or a freshly quenched glass, the smaller overshoot is expected since the thermal history has been erased. Such deformation-induced removal of thermal history is called “rejuvenation” and it requires large deformation past yield.

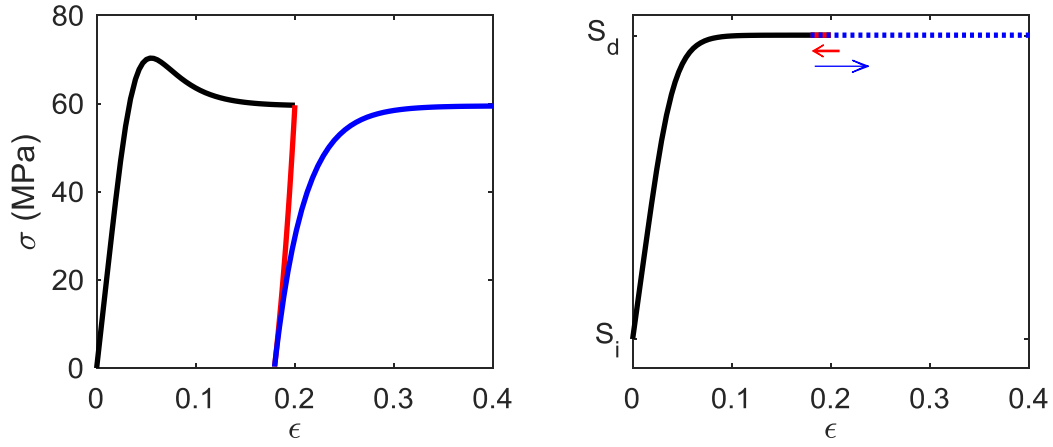


Figure 4.11. Left: Predicted stress-strain behaviors for loading-unloading-reloading experiment. Right: Corresponding internal variable  $S$  mobility change with strain.

As shown in Figure 4.11, the predicted stress-strain behaviors are consistent with observations. Change of mobility is also demonstrated where no decrease of  $S$  is observed during unloading step as  $S$  is already in steady state, where the value of  $S$  is dependent only on the magnitude of strain rate (Equation 4.5).

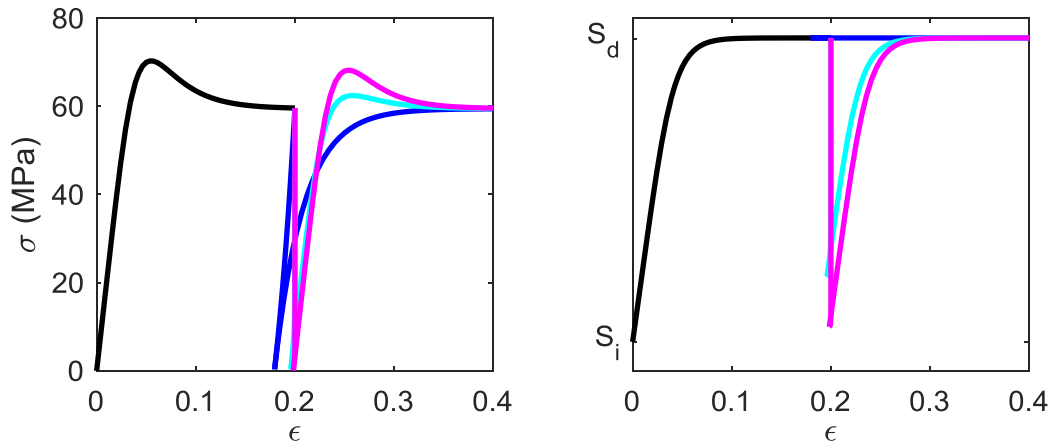


Figure 4.12. Left: Predicted stress-strain behaviors for loading-unloading-reloading experiment with different unloading rates as follows:  $10^{-3}$ /s (blue),  $10^{-4}$ /s (cyan),  $10^{-5}$ /s (magenta). Right: Corresponding internal variable  $S$  mobility change with strain.

If the unloading strain rate is lower,  $S$  will decrease and cause a slight overshoot in the reloading step, as plotted in Figure 4.11. The overshoot becomes larger as the unloading strain rate decreases. When strain rate is sufficiently small, deformation will have almost no effect on mobility (i.e.,  $dS/dt$  will be dominantly affected by the first term on RHS of Equation (4.3), which is the physical aging term). Experiment with slow unloading strain rate has not been performed by any research group, but can be anticipated to have similar results as a combination of unloading and physical aging. Longer aging time is equivalent to lower average unloading strain rate. The results of the equivalent loading-unloading-aging-reloading experiment have been performed for an amorphous polymer tBA-co-XLS at  $T_g - 16^\circ\text{C}$  where the aging time between two loading cycles varied from 1 min to 14 days.[33] The experimental results are shown in Figure 4.13. Comparing Figure 4.12 to Figure 4.13, model prediction is consistent with literature data.

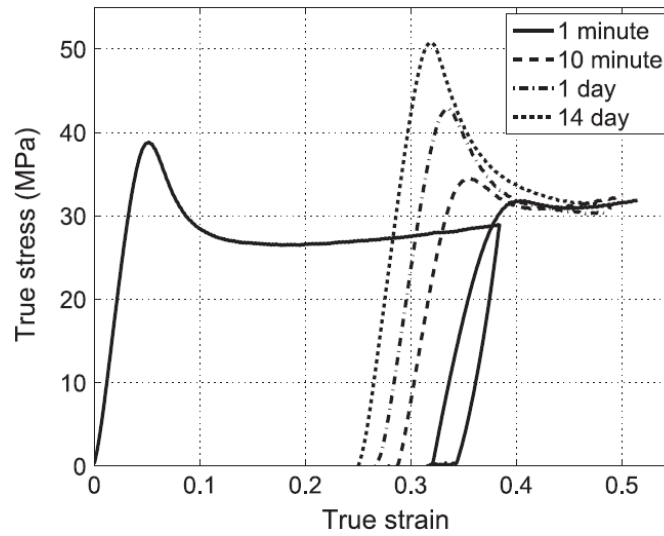


Figure 4.13. Stress-strain behaviors of a tBA-co-XLS polymer at  $T_g - 16^\circ\text{C}$  during 2 cycles of loading with different intermediate aging times. The polymer is tert-butyl acrylate (tBA), poly(ethylene glycol) dimethacrylate (PEGDMA) and di(ethylene glycol) dimethacrylate (DEGDMA) random copolymer network, with 10 wt% PEGDMA-DEGDMA (XLS) crosslink density. [33]

#### 4.3.3 Four-Step Loading-Unloading-Creep-Reloading Behaviors

The experiment shown in Figure 4.13 can also be considered as a 4-step loading-unloading-creep-reloading experiment where the creep is at zero stress. A more complete dataset of such 4-step

experiment has been reported by Dreistadt et al. for a bisphenol A polycarbonate at  $T_g - 123\text{ }^\circ\text{C}$ . [26] They studied the effect of creep duration and creep stress. Experimental setting has been described in Table 4.5. Predicted stress-strain behaviors by internal variable history clock model will be examined by experimental features with a focus on how the overshoot in reloading step influenced by previous deformation.

### *Effect of Creep Duration at a Low Creep Stress*

When the specimen is unloaded from a post-yield region to a near-zero stress, the subsequent reloading will have almost no overshoot, as plotted in Figure 4.14. Effect of creep duration on reloading overshoot can be neglected as the experiment was performed at  $T_g - 123\text{ }^\circ\text{C}$  where aging effect is not apparent.

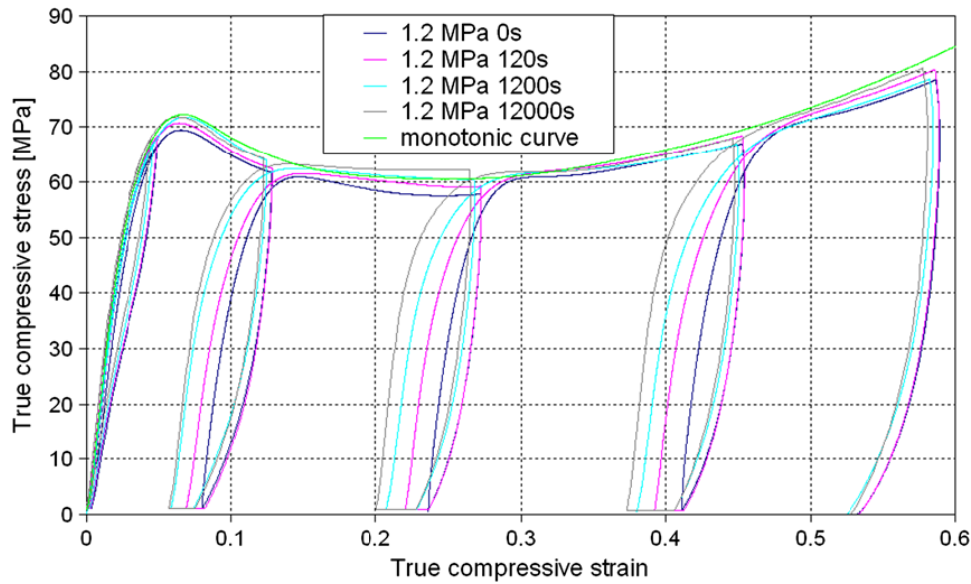


Figure 4.14. Stress-strain behaviors of polycarbonate at  $T_g - 123\text{ }^\circ\text{C}$  during a 4-step loading-unloading-creep-reloading experiment where the creep stress is 1.2 MPa.

The features are successfully captured by internal variable history clock model. Predicted stress-strain and mobility-strain behaviors are given in Figure 4.15.

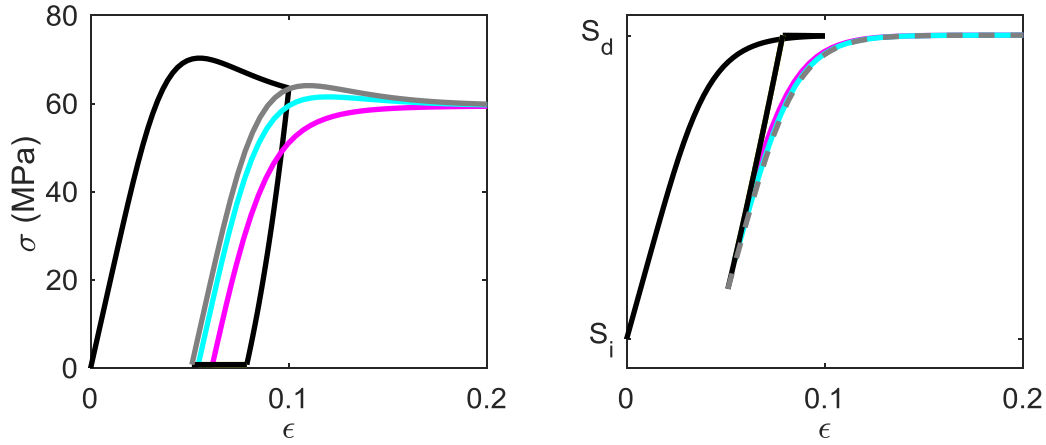


Figure 4.15. Left: Predicted loading-unloading-creep-reloading stress-strain behaviors where the creep stress is 0.15 MPa. Right: Corresponding  $S$  mobility change with strain.

The mobility change is similar to that of the 3-step experiment described in 4.3.2. To be specific, the mobility increases to a steady-state value  $S_d$ , and is almost the same during unloading since the unloading strain rate is of the same magnitude as the initial loading strain rate. During the creep step, the mobility decreases towards a new steady-state value which is very close to  $S_i$  since the creep stress is almost zero. However, within the relatively short period of creep, the new steady-state will not be reached before reloading is applied where mobility increases again. Longer time of creep will allow more decrease in mobility, and thus the amount of overshoot will increase with longer creep duration. However the overshoot in reloading is much smaller than that in initial loading. The predicted results are consistent with rejuvenation idea with a slight increase of overshoot in reloading for longer creep duration. Figure 4.15 gives the predicted mobility decrease with physical aging when there is no deformation. The purpose of this plot is to confirm that with the set of model parameters, no apparent aging effect will be predicted as is the case of actual experimental setting.

#### ***Effect of Creep Duration at a High Creep Stress***

If the second unloading step is terminated at a high stress level and the creep is performed at a higher stress, experimental observations will be different as shown in Figure 4.16.



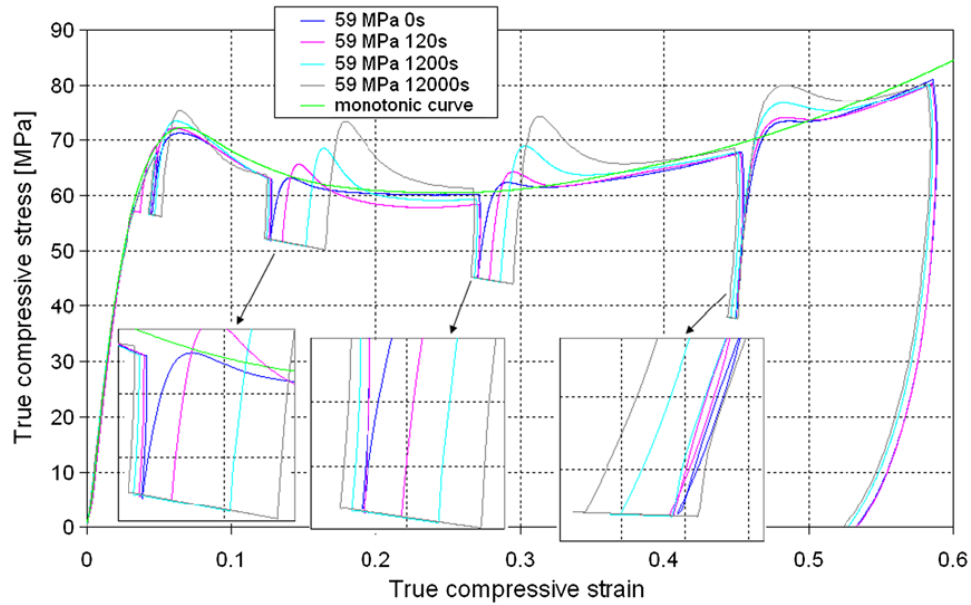


Figure 4.16. Stress-strain behaviors of polycarbonate at  $T_g - 123$  °C during a 4-step loading-unloading-creep-reloading experiment where the creep stress is 59 MPa.

The overshoot in reloading increases with creep duration if the creep is at a high stress. At the longest creep time, the reloading overshoot is almost the same as the initial loading overshoot, indicating a significant decrease of mobility after creep and is almost the same as  $S_i$ . Another feature is that there is no saturation in the overshoot with larger deformation, unlike in 4.3.1 where the overshoot increases and then remains the same.

Using the same internal variable history clock model, the predicted stress-strain curve is given in Figure 4.17, which is not consistent with experimental data. The predicted overshoot in reloading increases and then remains the same when mobility in the creep step reaches its steady state. As the creep stress is large, the corresponding steady-state mobility is also closer to  $S_d$  and much higher than  $S_i$ . Therefore the difference between mobility for reloading is much smaller than that for initial loading. The reloading overshoot is again much smaller than initial overshoot and a qualitative “rejuvenation” result is predicted. However, the experimental data shows an “accelerated aging” trend, and no saturation of overshoot (i.e., no steady state of mobility during creep step). Failure of predicting or explaining the experimental results from a mobility perspective motivates further exploring stress-strain behaviors using the same 4-step setting.

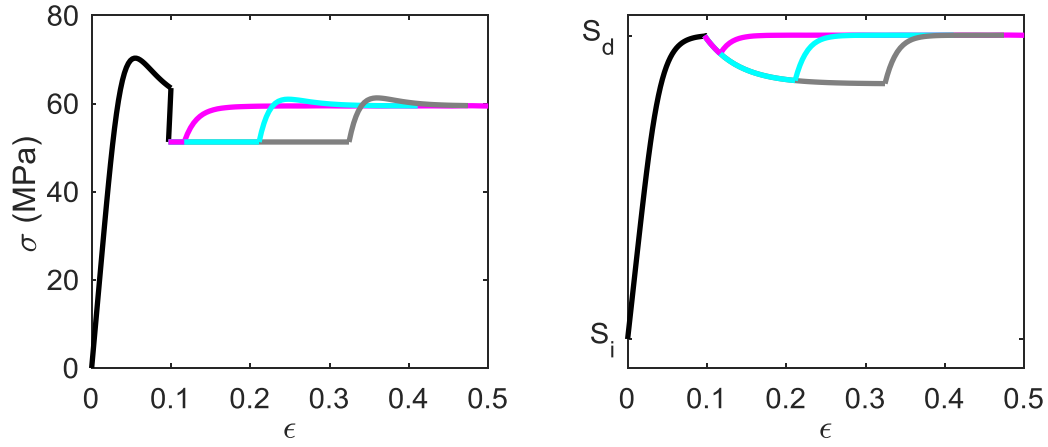


Figure 4.17. Left: Predicted loading-unloading-creep-reloading stress-strain behaviors where the creep stress is 51.28 MPa. Right: Corresponding  $S$  mobility change with strain.

### *Effect of Creep Stress*

The last set of data is to compare the effect of creep stress on the amount of overshoot, where an increase of overshoot with larger creep stress is experimentally observed, as shown in Figure 4.18.

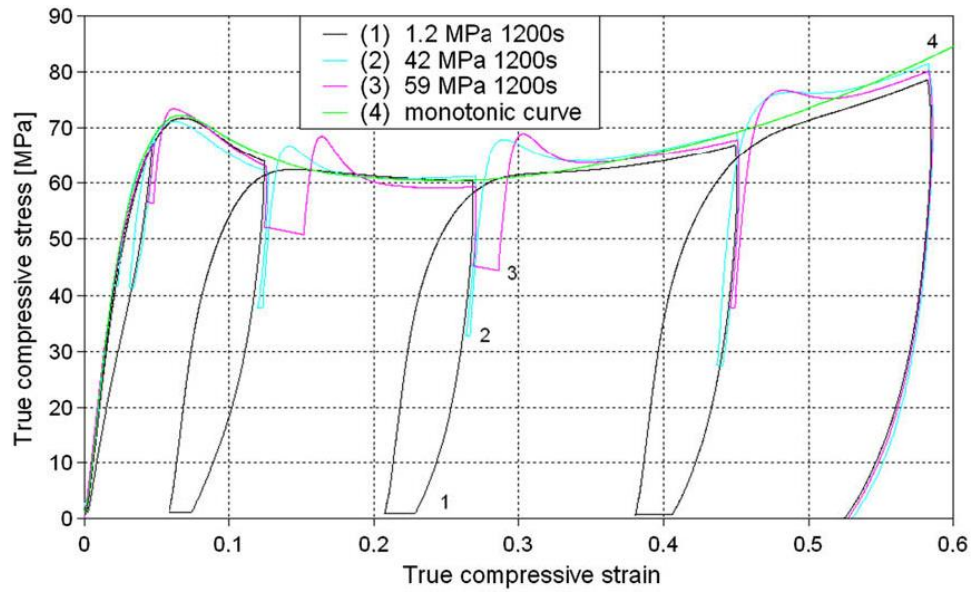


Figure 4.18. Stress-strain behaviors of polycarbonate at  $T_g - 123^\circ\text{C}$  during a 4-step loading-unloading-creep-reloading experiment where the creep stresses are 1.2, 42 and 59 MPa.

Based on Figure 4.18, the increase of reloading overshoot with creep stress seems non-stopping. This trend is counterintuitive, since a single-step stress-strain behavior can also be considered as a loading-creep-reloading combination where the creep starts somewhere in the flow region where stress is a constant. According to the ever-increasing trend of overshoot, there should be an enormous overshoot after creep, or a discontinuity on a single-step stress-strain curve, which is never observed.

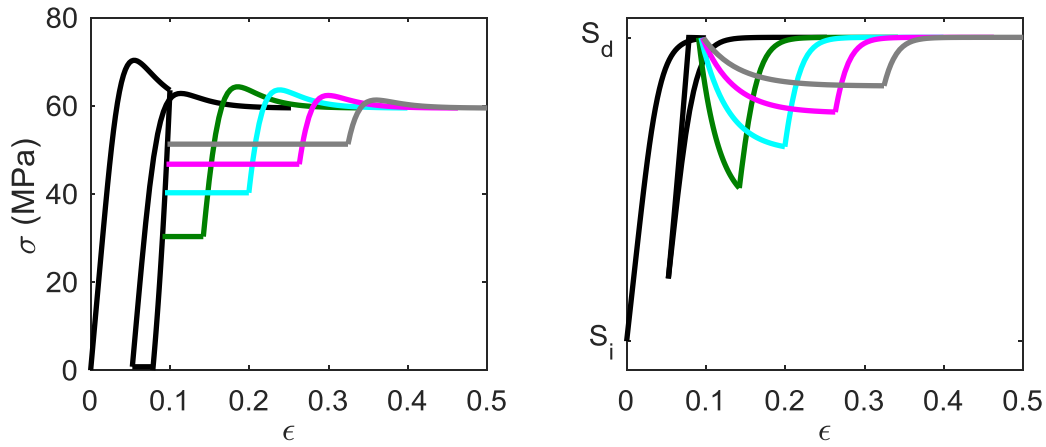


Figure 4.19. Left: Predicted loading-unloading-creep-reloading stress-strain behaviors where the creep stress is varied: 0.15 MPa (black), 30.31 MPa (dark green), 40.25 MPa (cyan), 46.73 MPa (magenta), and 51.28 MPa (grey). Right: Corresponding S mobility change with strain.

Despite the unreasonable increasing trend of reloading overshoot, prediction of stress-strain behaviors by internal variable history clock model has been plotted in Figure x where the overshoot first increase and then decrease with the increase of creep stress. Corresponding mobility change with strain is plotted in Figure 4.19. Since creep duration is the same, it is easier to reach a second steady state when creep stress is higher, and the new steady-state mobility also increases with stress. Therefore in the subsequent reloading step, less overshoot will be observed as the increase of mobility during step #4 is smaller for higher creep stress. The prediction shows contradictory trend to the experimental data. But the predicted trend will not cause a discontinuity.

Since this is the only dataset in literature of such 4-step experiment, it is worth further exploring whether the literature data is incomplete where conditions of higher creep stresses are not studied,

or the mobility-based explanation and models are inadequate to capture stress-strain behaviors of complicated deformation histories.

## 4.4 Experimental

No constitutive model can predict Dreistadt's 4-step experimental results which have been described in 4.3.3. As a matter of fact, the experimental findings are contradictory from the assumptions built in all internal variable history clock models. The experimental results at long creep duration and high creep stress are consistent with "accelerated aging" assumption which says a material is more aged (i.e., closer to the equilibrium state) after large deformation, while mobility-based constitutive models will all predict reversely saying a material is less aged (i.e., more like a quenched glass) if deformed to flow region. These results are almost counter-intuitive because higher stress and longer creep time means more mechanical work has been input to the system, and the molecular mobility should increase which will manifest as smaller or no overshoot after creep. We would like to repeat the same 4-step experiment and to explore more on the effect of complex deformation history, in order to find out the inadequacy of the current understanding about the effect of deformation history.

### 4.4.1 Machining of Dogbone Specimen

Although Dreistadt did the 4-step experiment with a polycarbonate sample at  $T_g - 123\text{ }^{\circ}\text{C}$  in compression, with the available instrument and material, the 4-step experiment was repeated for a crosslinked DGEBA material (EPON 1009F-MDA) at  $85\text{ }^{\circ}\text{C}$  ( $T_g - 13\text{ }^{\circ}\text{C}$ ) in extension. Protocols of chemical synthesis were given in 2.2.1.

A  $4\text{ in} \times 6\text{ in} \times 0.079\text{ in}$  sheet of EPON 1009F-MDA sample was made in the same way as described in 2.2 and machined in to dogbone shape by a technician. Each dogbone specimen has a parallel gauge section of  $0.236\text{ in wide} \times 3.94\text{ in long}$ , and a fillet radius of  $\frac{1}{4}\text{ in}$ . The procedure as shown in Figure 4.20 takes three steps: (i) The sheets were cut into strip pieces of  $0.709\text{ in} \times 6\text{ in}$ ; (ii) A stack of 5 – 10 strip specimens were clamped at two ends and fastened onto mill platform, on top of which covered by a pre-machined aluminum of the target dogbone shape; (iii) A rotating  $\frac{1}{4}$  jig was pushed towards the sample stack from one side, while the other side of the stack was

held by a stopper. By repeating step (iii) for several times, the designed shape was obtained for the target side, and the other side would be cut in the same way.



Figure 4.20. Machining of a stack of dogbone specimens

#### **4.4.2 Experimental Settings**

As shown in Figure 4.21, the specimen was mounted inside a thermal chamber connected to the Instron 5567 frame with a 1kN load cell. A camera to measure strain by tracking white dots on the specimen was positioned outside the thermal chamber. A mirror was put inside the chamber to check the side view of the specimen in order to avoid buckling during clamping or heating. Extension of crosshead connected to the upper grip was applied by Bluehill software with a Test Profiler procedure. Force and travelled distance of the crosshead were recorded by Bluehill software, while actual strain was measured using the camera.

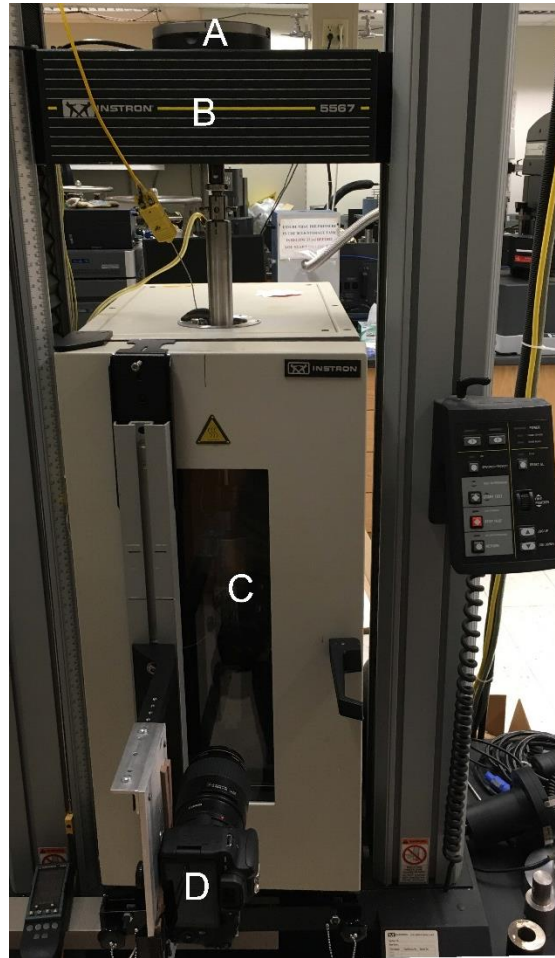


Figure 4.21. Instrument setup for the 4-step experiment consisting: (A) 1kN load cell, (B) crosshead that moves up and down with the upper grip, (C) thermal chamber, and (D) camera to track dots on the specimen for strain measurement.

The experimental inputs were given in Figure 4.22. The pre-test annealing was carried out in a separate vacuum oven under 140 °C and -80 kPa vacuum. During annealing, the specimen was placed on a flat and non-stick surface for 10 mins to remove residual stress and strain. The specimen was then quenched to R.T. while the shape was kept flat and straight. Width and thickness were measured by a caliber. The specimen was mounted onto Instron for tensile test inside the thermal chamber. The chamber was pre-heated to 85 °C, while a drop of ~15 °C was observed when mounting the specimen. The next step was to ensure temperature stability before mechanical test.

The mechanical inputs were designed to be similar as Dreistadt's experiment, consisting loading, unloading, creep and reloading. Creep stress and duration can be altered in Test Profiler, while the amount of stress overshoot in subsequent reloading indicate mobility change.

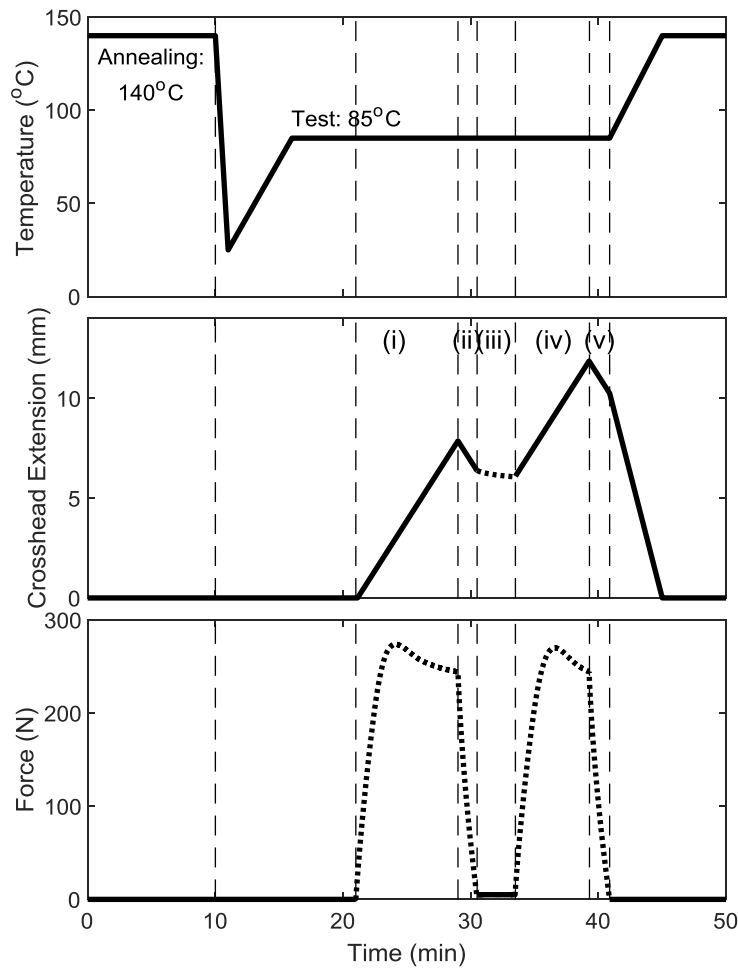


Figure 4.22. Thermal history and mechanical inputs for each cycle of 5-step tensile test. During the test, temperature is kept at 85 °C ( $T_g - 13$  °C) while the mechanical stimuli at each step are illustrated as solid lines: (i) loading at 1 mm/min crosshead extension, (ii) unloading at -1 mm/min, (iii) creep at a constant force, (iv) reloading at 1 mm/min, and (v) unloading at -1 mm/min. Mechanical responses are schematically plotted as dotted lines. Residual extension after each test is removed by annealing the specimen at 140 °C ( $T_g + 38$  °C).

The specific mechanical input during each step is: (i) a constant crosshead speed of 1 mm/min, corresponding to a nominal strain rate of  $1.67 \times 10^{-4}$  /s, for 6min or 8min which are both in post-yield flow region, (ii) partially unloading at -1 mm/min until force reaches the target creep force, F, (iii) creep for a certain amount of time, (iv) reloading at 1 mm/min, and (v) completely unloading to zero force. By varying creep force and creep time in step (iii), the overshoot during reloading, i.e., step (iv) will be examined and compared to literature data.

#### 4.4.3 Temperature Measurement

Temperature of the thermal chamber was input by a Eurotherm 2408 controller. Actual temperatures were measured by three thermocouples placed near upper and lower grips and the center of specimen, as shown in Figure 4.23. Temperatures were recorded using LabVIEW interface.

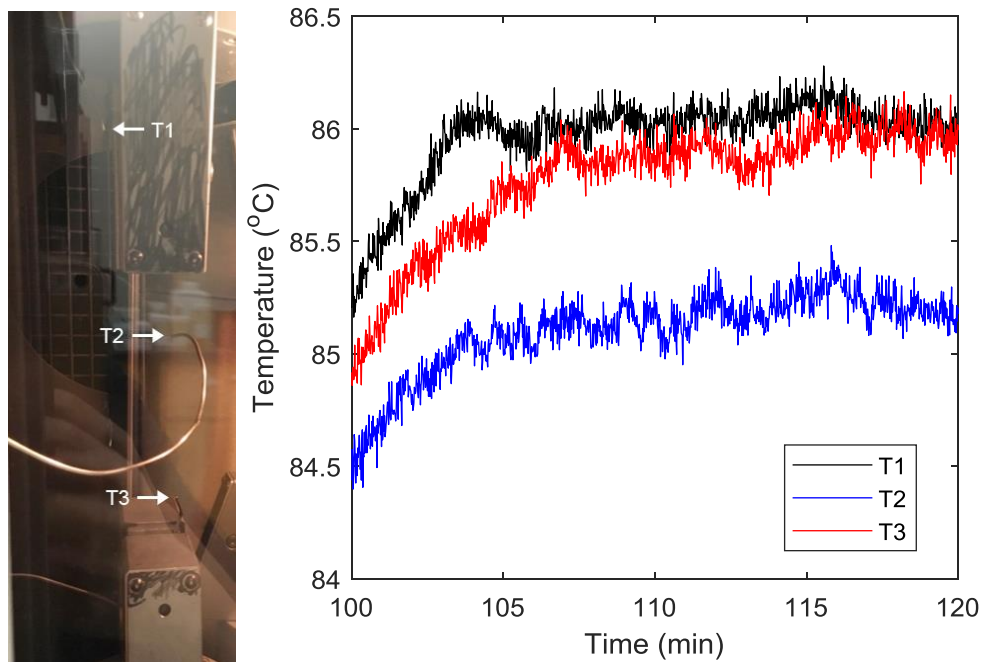


Figure 4.23. Temperature gradient inside the thermal chamber near grips and specimen.

After the specimen was mounted onto Instron, temperature inside the thermal chamber would re-stabilize at 85 °C within 10 min. When the temperature was set to be 85 °C, the measured



temperature near specimen (T2) was 85.0 °C – 85.3 °C, while temperatures near upper and lower grips (T1 and T3) were both ~1°C higher than the setting. The temperature at each place was stabilized within 0.5 °C fluctuation, while an increase of 0.8 °C was found from center part of the specimen to the gripping region.

#### 4.4.4 Strain Measurement

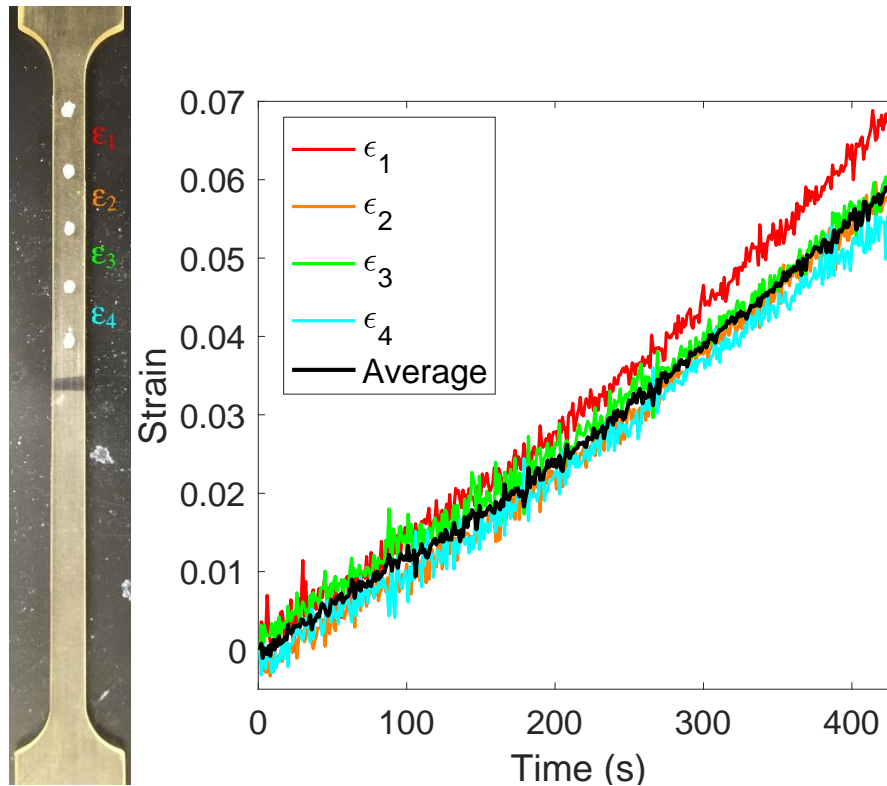


Figure 4.24. Strain obtained by camera tracking five white dots located on the upper half of a strip EPON 1009f-MDA specimen during uniaxial tension at 85 °C ( $T_g - 17$  °C) at a constant overhead speed of 1 mm/min. The red line represents the strain defined by two dots nearest upper grip, while the cyan line is by two dots in the center part. The black line represents average strain of two segments in the middle as plotted in orange and green lines.

A nominal constant crosshead speed was input to Bluehill software which controls the displacement of the upper grip. The actual strain was measured separately using a Canon SL2 camera with a EF 100mm macro lens to track white dots on the specimen from the front view. Only one camera was used because (i) out-of-plane deformation could be neglected, (ii) practically

the thermal chamber possessed only one window through which a camera could see dots. Position and angle of the camera were (i) optimized so that all dots were within the picture frame throughout the experiment, (ii) fixed with screws and metal brackets, and (iii) calibrated before each test by taking a picture of a grid pattern. During the test, the camera took one photo every second. Photos were then analyzed by Matlab image processing toolbox. The Matlab code mainly consists three parts: (i) white dots are filtered out based on the histogram of the greyscale image, (ii) centroid of each white dot is calculated in terms of pixels, and (iii) strain between two adjacent dots is calculated based on the distance between two centroids.

The nominal crosshead speed was 1 mm/min for all tests, corresponding to a nominal strain rate of  $1.67 \times 10^{-4}$  /s. Original length was measured as the distance between upper and lower grips to be 100 mm, and was kept the same for all tests by returning the upper grip to the initial position using the Bluehill software. Actual strain rates measured by camera varied from  $1.2 \times 10^{-4}$  /s to  $1.3 \times 10^{-4}$  /s during 50 – 100 s, while during 300 – 350 s strain rates ranged from  $1.5 \times 10^{-4}$  /s to  $2.3 \times 10^{-4}$  /s as listed in Table 4.6.

Strain was found to be higher at positions nearer upper grip. Such a distribution was also observed in all other tests for both strip and dogbone specimens. There were two possibilities causing such a strain gradient: (i) the temperature gradient that air surrounding the grips were 1 °C higher than around center part of specimen, i.e., the material was softer near the upper grip; (ii) concentration of stress near upper grip.

As shown in Figure 4.24, an increase in averaged strain rate by 25% was observed from  $1.2 \times 10^{-4}$  /s ( $t = 50 - 100$  s) to  $1.5 \times 10^{-4}$  /s ( $t = 300 - 350$  s). Such an increase by 25% – 50% in actual strain rate was also observed for all other tests regardless of specimen. The increase of strain rate happened at around  $t = 200$  s during initial loading. In reloading there was also an increase in strain rate by 5% – 10%. One possible reason for such an increase is that the stress was not uniformly distributed, and the distribution was changing with elongation. That is to say the material was not homogeneous probably due to poor mixing when the material was synthesized, while at  $T_g - 17$  °C and large deformation, the effect was pronounced.

It is ideal to keep the strain rate the same during the entire experiment. However, the current equipment does not allow input of actual strain rate into its feedback loop for more precise control of strain rate. To minimize the effect of mismatching in nominal strain rate and actual strain rate, the dataset whose actual strain rate was closer to nominal strain rate was selected for further study.

#### 4.4.5 Run-to-Run Deviation of Bar and Dogbone-Shaped Specimens

Based on previous experiences, dogbone specimen allows much larger tensile strain before the specimen breaks. However, run-to-run error using the same specimen of dogbone shape was found to be larger than that of a bar-shaped specimen. Comparison of stress-strain behaviors using dogbone and bar specimens is shown in Figure x, where two repeats for each specimen are plotted.

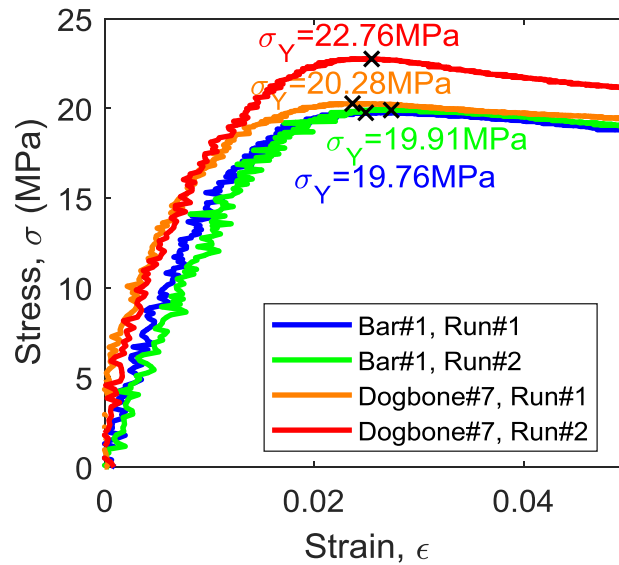


Figure 4.25. Stress-Strain behaviors of EPON 1009f-MDA strip bar and dogbone-shape specimens at 85 °C ( $T_g - 17$  °C) during uniaxial tension. Two repeats for each specimen are plotted. Crosshead speed input for all test is 1 mm/min, corresponding to a nominal strain rate of  $1.67 \times 10^{-4}$  /s. Actual strain rates are given in Table 4.6. Black cross symbols indicate the maximum stress (yield stress  $\sigma_Y$ ) during initial loading.

As shown in Figure 4.25, two stress-strain curves for the bar specimen overlap with each other, while a large run-to-run difference in stress is observed for the dogbone specimen. The stress difference is most apparent at yield and does not disappear in post-yield region. This typical run-

to-run difference is also observed for other tests on dogbone specimens. In Table 4.6, yield stress is reported for the same specimen, while the deviation indicates how large the run-to-run error is.

Table 4.6 Run-to-run variation of actual strain rate and yield stress for all specimens

Specimen	Number of Tests	Strain Rate, $\dot{\epsilon}_l$ (/s) *		Yield Stress, $\sigma_Y$ (MPa) **	
		Mean	Deviation	Mean	Deviation
Bar #1	4	1.6e-4	1.0e-5	19.79	0.57
Dogbone #1	1	1.6e-4	-	17.27	-
Dogbone #2	1	1.5e-4	-	19.57	-
Dogbone #3	2	1.9e-4	7.1e-6	24.14	1.34
Dogbone #4	3	2.3e-4	5.8e-6	24.00	1.53
Dogbone #5	4	2.1e-4	5.0e-6	22.63	1.03
Dogbone #6	6	2.0e-4	8.2e-6	20.25	1.67
Dogbone #7	7	1.8e-4	1.2e-5	20.65	1.28

\* Strain rate is calculated via linear regression of average strain rate of 300 – 350 s measured by camera tracking dots on the specimen.

\*\* Yield stress is the maximum stress during initial loading.

In general, the yield stress measured for the EPON1009F-MDA specimen is  $\sigma_Y = 21.2 \pm 2.08$  MPa, typical of a polymer at  $T_g - 17$  °C.

Run-to-run deviation of yield stress for a bar specimen is 0.57 MPa, while for dogbone specimens the deviations are larger than 1 MPa as listed in Table 4.6. A larger scattering / less repeatability in stress-strain behavior is observed for dogbone specimens compared to bar, which may result from the non-uniform strain field along the dogbone curvature region. Specifically, when a dogbone specimen is stretched, elementary strain vectors in the curved part will change both direction and magnitude, causing a redistribution of strain field of the entire specimen. For strip specimen, only magnitude will change since all elementary strain vectors are aligned along the longitudinal direction, and there is no rearrangement in strain field unless defects are formed. Hence response of a dogbone specimen is less repeatable.

Comparing the shape of specimens, strip specimen has a more uniform strain field and smaller run-to-run error, i.e., results are more repeatable. However when strain approached 0.08, observable notches developed at the edge of bar specimen which caused a drop in yield stress to 16 MPa measured in subsequent tests. Dogbone specimens, on the other hand, were intact up to 0.12 strain. Although they are more sensitive to changes in settling, gripping, defects introduced

during synthesizing and manufacturing, dogbone specimens are the only choice for large strain measurements.

To minimize the effect of run-to-run variation and to better compare stress-strain behaviors affected by deformation history, rescaling of stress will be used to solve the dogbone shape problem.

Nondimensionalized stress is obtained via dividing stress values by the yield stress during initial loading step, which assumes the shape effect of dogbone only influences stress values and the influence is linearly dependent on stress. Such an assumption is empirical but serves the practical purpose of qualitative comparing effects of deformation history. Scaled stress – strain behaviors ( $\sigma/\sigma_Y$  vs.  $\epsilon$ ) will be reported and the amount of stress overshoot will be quantified as  $\sigma_{\max}/\sigma_Y$ .

## **4.5 Results**

With run-to-run deviation issue resolved in 4.4.5, effect of deformation history is studied following the protocol illustrated in Figure 4.22. The scaled stress-strain behaviors for a crosslinked DGEBA-MDA epoxy at  $T_g - 17^\circ\text{C}$  in tensile tests are compared especially focusing on reloading overshoot magnitude.

### **4.5.1 Effect of Physical Aging with No Deformation**

A big difference between current work and Dreistadt's experimental settings is the temperature. Dreistadt's experiment was reported at  $T_g - 123^\circ\text{C}$  where aging would happen at an extremely slow rate that can be neglected. The current test is performed at  $T_g - 17^\circ\text{C}$  where allowable strain is large but aging effect is pronounced and might preclude the comparison of deformation history effect.

Before studying complex deformation history, the effect of physical aging on mobility will be tested first. Mobility is quantified as the scaled yield stress overshoot where the yield stress of the quenched specimen is set as a reference. Bar specimen is used for the study of aging effect because bar specimen shows small run-to-run deviation (Table 4.6) and because the aging test does not

require large strain. Figure 4.26 shows the results of four cycles of two-step loading-unloading experiment, while the time of aging varies from 30min to 0min as determined according to Struik's protocol.

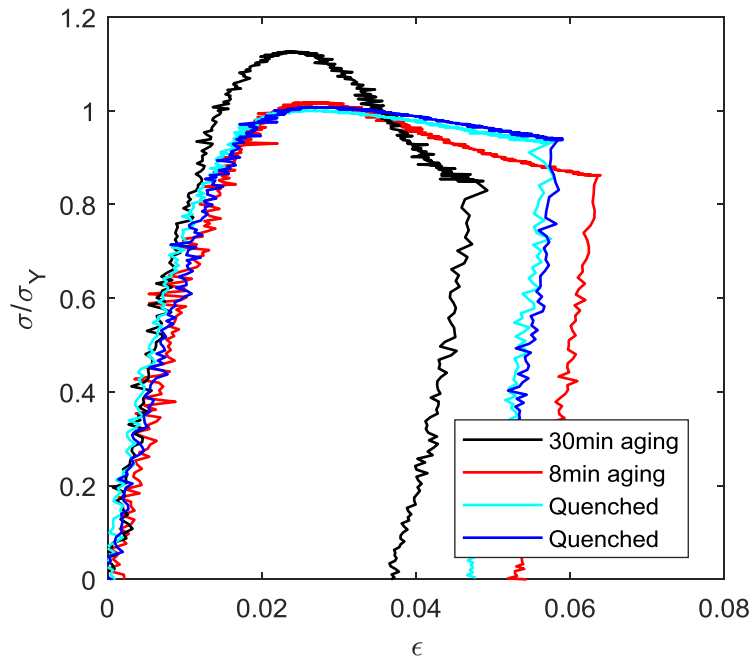


Figure 4.26. Scaled stress-strain behaviors of EPON 1009f-MDA bar specimen #1 at 85 °C ( $T_g - 17$  °C) during loading-unloading tensile tests. Before the test, specimen was aged inside Instron thermal chamber at 85 °C ( $T_g - 17$  °C) for a certain amount of time as labeled in figure. Thermal history for each test cycle is plotted in Figure 4.22.

Table 4.7 Actual strain rate and unscaled yield stress for each test included in Figure 4.26

Specimen	Test Sequence	Aging Time (min)	Strain Rate, $\dot{\epsilon}_t$ (/s) *	Yield Stress, $\sigma_Y$ (MPa)	Scaled Yield Stress, $\sigma_Y/\sigma_{Y,q}$
Bar #1	Test #4	30	1.1e-4	22.24	1.13
Bar #1	Test #3	8	1.7e-4	20.12	1.02
Bar #1	Test #5	0	1.6e-4	19.76	1.00
Bar #1	Test #6	0	1.5e-4	19.91	1.01

\* Strain rate is calculated via linear regression of average strain rate of 300 – 350 s measured by camera tracking dots on the specimen.

Due to a difference in the actual strain rate, stress-strain curves do not overlap in the flow region. The actual strain rate calculated from actual strain between 300 – 350s is reported in Table 4.7 for

each run. The aging responses are typical of a glassy polymer at  $T_g - 17\text{ }^\circ\text{C}$ , where 30 min aging significantly decreases mobility and induced a large overshoot. 8 min aging has a slight effect compared to the quenched case. Post-yield behaviors of the two quenched runs are reproducible. Necking near upper grip was observed after yield for the 30min run, causing (i) a decrease in actual strain rate, and (ii) a sharper decrease of stress in post-yield softening region. Necking was eliminated during above- $T_g$  annealing before the next test and is believed having no effect for subsequent tests.

In Table 4.7, stress overshoot is quantified as the ratio of yield stress divided by the yield stress of the quenched specimen ( $\sigma_Y/\sigma_{Y,q}$ ). An increase of stress overshoot indicated lower mobility. The quantified overshoot is plotted against aging time in Figure 4.31.

#### 4.5.2 Effect of Creep Duration at a Small Creep Stress

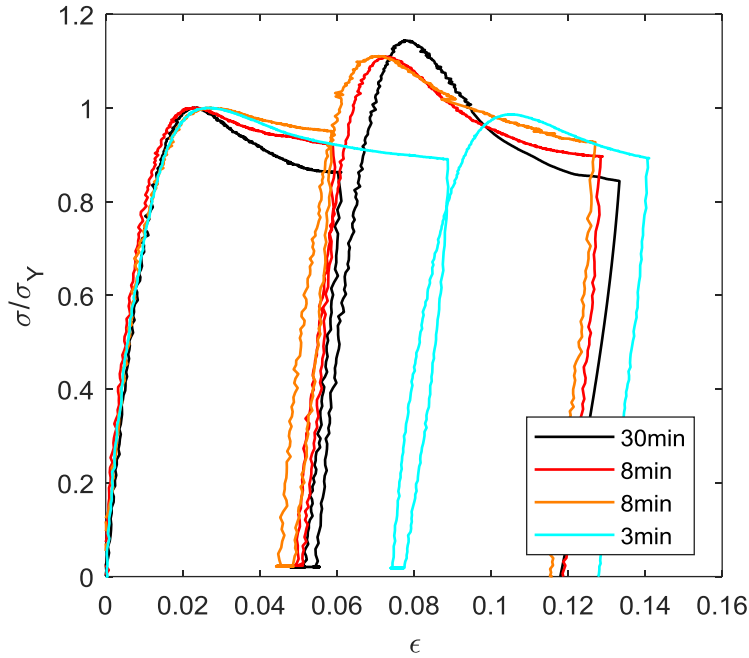


Figure 4.27. Scaled stress-strain behaviors of EPON 1009f-MDA dogbone specimens at  $85\text{ }^\circ\text{C}$  ( $T_g - 17\text{ }^\circ\text{C}$ ) during 4-step tensile experiments following the protocol in Figure 4.22. The creep time in step (iii) is given in figure legend. The creep force is 5N, corresponding to a nominal creep stress of 0.4 MPa.

With the correlation established between aging time at  $T_g - 17\text{ }^\circ\text{C}$  and the amount of overshoot, effect of deformation history will be studied. In the first case where creep stress is small, Dreistadt et al. reported no overshoot in reloading after a creep at 1.2 MPa (2% of yield stress) regardless of creep time ( $t_1 = 2\text{min}, 20\text{min}, 200\text{min}$ ). The internal variable history clock model is able to predict this result. Repeat of this experiment at  $T_g - 17\text{ }^\circ\text{C}$  showed a different result as plotted in Figure 4.27.

As shown in Figure 4.27, a second overshoot was observed in the reloading step after creep at 0.4 MPa (2% of yield stress), which is different from Dreistadt's results. The reason for this difference is due to the difference in test temperature. In current work at  $T_g - 17\text{ }^\circ\text{C}$ , significant amount of physical aging can happen during the course of experiment. In Dreistadt's experimental condition, aging has no measurable effect since the temperature is  $120\text{ }^\circ\text{C}$  below  $T_g$ .

Non-scaled yield stresses in initial loading and reloading steps are given in Table 4.8, where the scaled maximum stress in reloading ( $\sigma_{\max, \text{re}}/\sigma_Y$ ) is also listed as a quantification of the reloading overshoot.

Table 4.8 Actual strain rate and unscaled yield stress for each test included in Figure 4.27

Specimen	Test Sequence	Creep Time (min)	Strain Rate, $\dot{\epsilon}_t$ (/s) *	Yield Stress, $\sigma_Y$ (MPa)	Reloading max. Stress, $\sigma_{\max, \text{re}}$ (MPa)	Overshoot Magnitude, $\sigma_{\max, \text{re}}/\sigma_Y$
Dogbone#7	Test#9	30	1.9e-4	21.79	24.92	1.14
Dogbone#7	Test#8	8	1.9e-4	18.75	20.80	1.11
Dogbone#7	Test#7	8	1.8e-4	20.25	22.49	1.11
Dogbone#5	Test#2	3	2.1e-4	22.08	21.78	0.99

\* Strain rate is calculated via linear regression of average strain rate of 300 – 350 s measured by camera tracking dots on the specimen.

According to Table 4.8, magnitude of the reloading overshoot increases with creep time of the previous step. Comparing the magnitude of overshoot induced by aging vs. low-stress creep, i.e., the last column in Table 4.7 and Table 4.8, the scaled stress overshoot increases with time with or without the presence of stress. Especially at the longest aging or creep time (30min), the stress overshoot after creep (1.14) is almost the same as that after aging (1.13). That is to say the



reloading overshoot shown up in Figure 4.27 is mostly due to physical aging at  $T_g - 17^\circ\text{C}$  instead of deformation history.

The same aging effect on a reloading stress-strain behavior is also observed for an amorphous copolymer network tBA-co-XLS at  $T_g - 16^\circ\text{C}$  in compression as shown in Figure 4.13.

### 4.5.3 Effect of Creep Duration at a Large Creep Stress

At large creep stress, Dreistadt's results are showing accelerated aging trend, which cannot be explained by internal variable history clock model. A repeat of this set of experiment is necessary to figure out what is missing in the basic assumptions of the model. At high creep stress, it is hopeful that deformation history can outweigh the effect of thermal history. In Figure x, stress-strain behaviors of the 4-step experiment with a creep stress  $\sim 15\text{ MPa}$  ( $\sim 75\%$  of yield stress) are plotted for different creep times. Note that the apparent difference in creep stress is a result of rescaling by different yield stress.

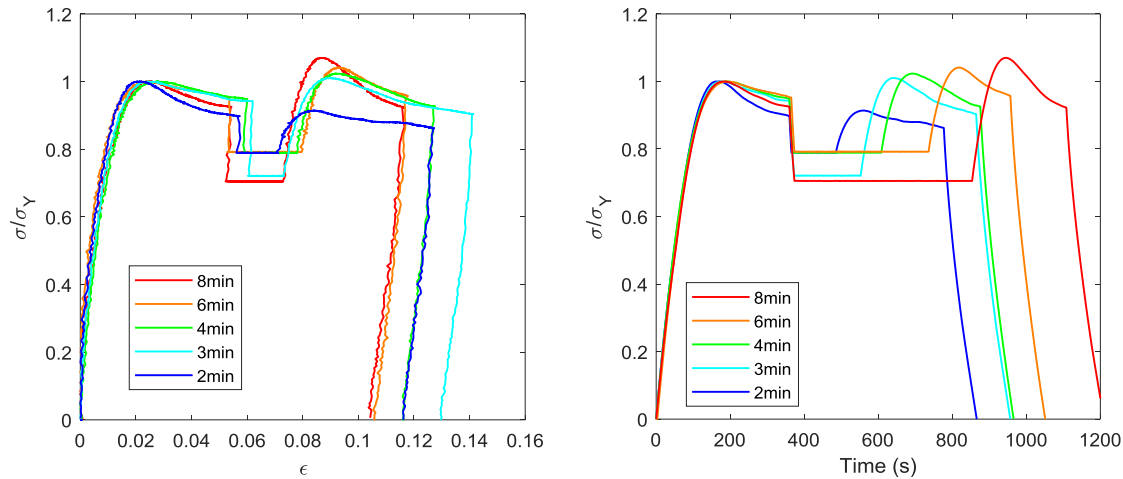


Figure 4.28. Scaled stress-strain (left) and stress-time (right) behaviors of EPON 1009f-MDA dogbone specimens at  $85^\circ\text{C}$  ( $T_g - 17^\circ\text{C}$ ) during 4-step tensile experiments following the protocol in Figure 4.22. The creep time in step (iii) is given in figure legend. The creep force is  $180\text{N}$ , corresponding to a nominal creep stress of  $15\text{ MPa}$ .

Unfortunately, aging effect still dominates when creep stress is at  $\sim 15\text{ MPa}$ . The overshoot magnitude in reloading step increases systematically with creep time as shown in Figure 4.31. In

Table 4.9, the quantified stress overshoot in reloading ( $\sigma_{\max, \text{re}}/\sigma_Y$ ) is reported, which is not significantly larger than that induced by physical aging.

Table 4.9 Actual strain rate and unscaled yield stress for each test included in Figure 4.28

Specimen	Test Sequence	Creep Time (min)	Strain Rate, $\dot{\epsilon}_l$ (/s) *	Yield Stress, $\sigma_Y$ (MPa)	Reloading max. Stress, $\sigma_{\max, \text{re}}$ (MPa)	Overshoot Magnitude, $\sigma_{\max, \text{re}}/\sigma_Y$
Dogbone#7	Test#6	8	1.6e-4	22.76	24.36	1.07
Dogbone#7	Test#2	6	1.7e-4	20.28	21.11	1.04
Dogbone#7	Test#3	4	1.9e-4	20.35	20.82	1.02
Dogbone#6	Test#5	3	2.0e-4	20.49	20.70	1.01
Dogbone#7	Test#1	2	1.8e-4	20.35	18.60	0.91

\* Strain rate is calculated via linear regression of average strain rate of 300 – 350 s measured by camera tracking dots on the specimen.

#### 4.5.4 Effect of Creep Stress

Dreistadt's results of different creep stress also showed accelerated aging effect which is counter-intuitive as explained in 4.3.3. Although in current study, the reloading overshoot is predominately due to physical aging, the comparison between different creep stresses with the same creep duration (or aging time) could possibly eliminate the effect of aging (which is purely dependent on time under the isothermal condition).

In Figure 4.29 the stress-strain curves are directly compared where creep duration is 8min. The overall behavior is opposite to Dreistadt's results. In Figure 4.29, the overshoot decreases when creep stress increases from 5N to 180N. Nevertheless, it is hard to tell if the overshoot is truly decreasing with higher stress level (which supports rejuvenation assumption) or within scattering. The quantified stress overshoot is given in Table 4.10.

Stress-strain behaviors where the creep step lasts for 3 min are plotted in Figure 4.30. No conclusion can be made based on this set of results since the run-to-run scattering is as large as the effect of deformation history. Two repeats with a creep force of 50 N (corresponding to a nominal stress of 4.2 MPa) indicate the scattering of stress-strain behaviors in post-yield regions and reloading steps. As give in Table 4.10, the differences in reloading overshoot magnitude ( $\sigma_{\max, \text{re}}/\sigma_Y$ ) induced by different creep stresses after a 3-min creep are no more than run-to-run scattering.

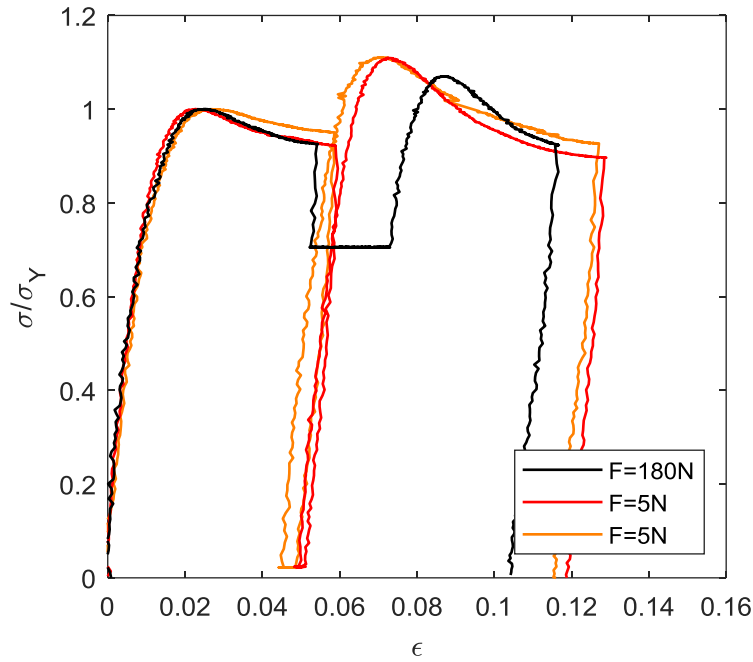


Figure 4.29. Scaled stress-strain behaviors of EPON 1009f-MDA dogbone specimens at 85 °C ( $T_g - 17$  °C) during 4-step tensile experiments following the protocol in Figure 4.22. The creep force in step (iii) is given in figure legend. The creep time is 8 min.

Table 4.10 Actual strain rate and unscaled yield stress for each test included in Figure 4.29 and Figure 4.30

Specimen	Test Sequence	Creep Time (min)	Creep Force (N)	Strain Rate, $\dot{\epsilon}_t$ (/s) *	Yield Stress, $\sigma_Y$ (MPa)	Reloading max. Stress, $\sigma_{\max, re}$ (MPa)	Overshoot Magnitude, $\sigma_{\max, re}/\sigma_Y$
Dogbone#7	Test#6	8	180	1.6e-4	22.76	24.36	1.07
Dogbone#7	Test#8	8	5	1.9e-4	18.75	20.80	1.11
Dogbone#7	Test#7	8	5	1.8e-4	20.25	22.49	1.11
Dogbone#6	Test#5	3	180	2.0e-4	20.49	20.70	1.01
Dogbone#1	Test#3	3	50	1.6e-4	17.27	17.01	0.98
Dogbone#3	Test#1	3	50	1.8e-4	23.20	20.81	0.90
Dogbone#5	Test#2	3	5	2.1e-4	22.08	21.78	0.99

\* Strain rate is calculated via linear regression of average strain rate of 300 – 350 s measured by camera tracking dots on the specimen.

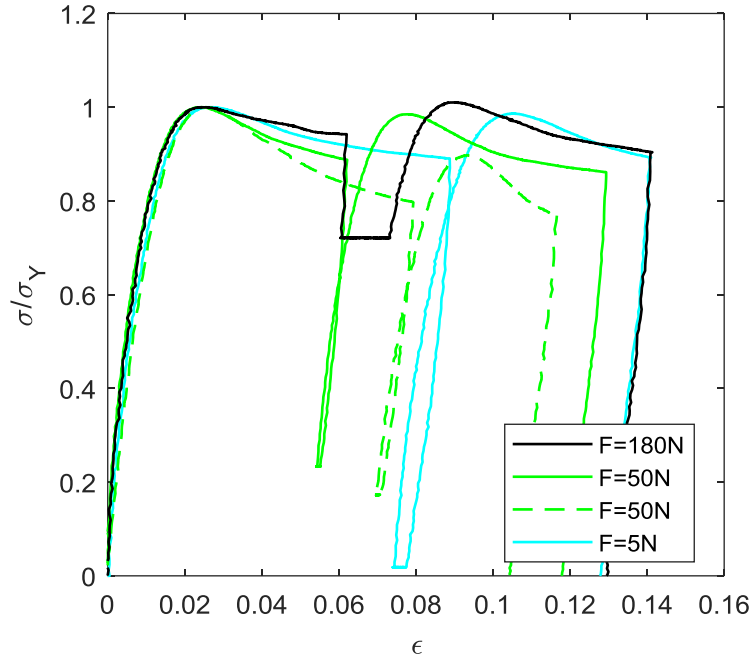


Figure 4.30. Scaled stress-strain behaviors of EPON 1009f-MDA dogbone specimens at 85 °C ( $T_g - 17$  °C) during 4-step tensile experiments following the protocol in Figure 4.22. The creep force in step (iii) is given in figure legend. The creep time is 3 min.

#### 4.5.5 Summary

In summary, current experimental results are (i) dominated by physical aging effect while the difference of reloading overshoot caused by deformation history is within run-to-run scattering, (ii) showing no rejuvenation or accelerated aging preference.

Including Dreistadt's, four literature datasets have been compared to the current work from the perspective of stress overshoot vs. creep or aging time, as shown in Figure 4.31.

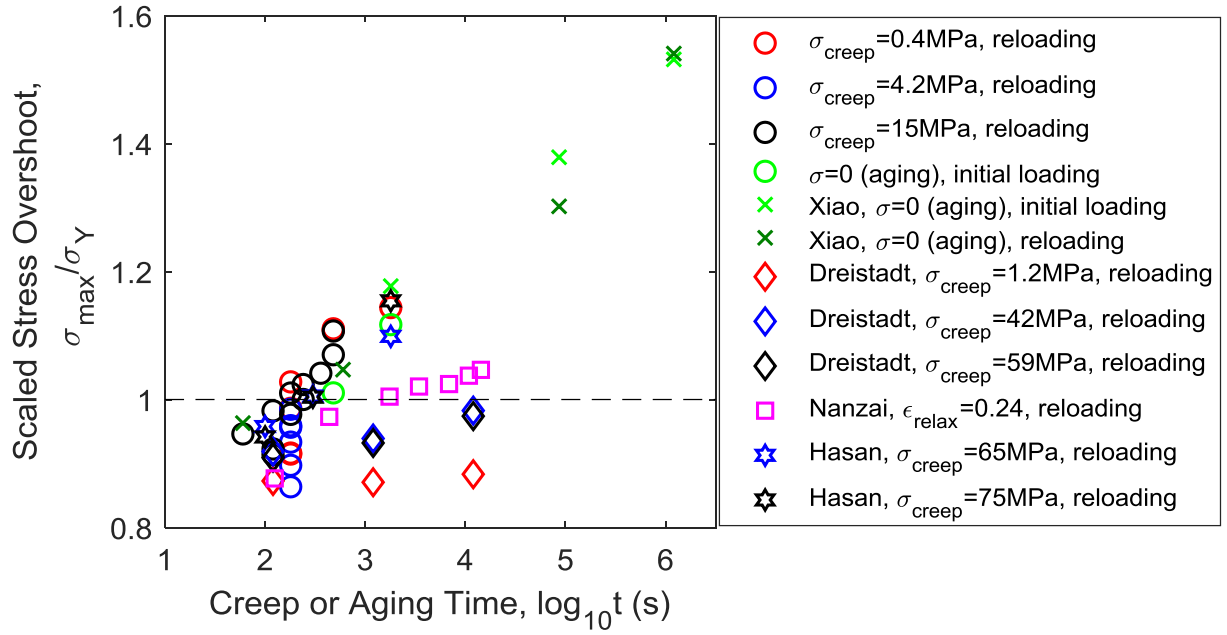


Figure 4.31. Stress overshoot during a second loading after creep or aging step compared across different datasets. Materials are all in glassy state but tested at different temperatures.

Data reported in Figure 4.31 are digitized from original literatures, where the test temperatures are different. Aging effect is most pronounced for current study ( $T_g - 17^\circ \text{C}$ ) and Xiao ( $T_g - 16^\circ \text{C}$ ), where the amount of stress overshoot has a strong aging time dependence. Hasan's results for PMMA at  $29^\circ \text{C}$  (whose  $T_g$  is not reported) are close to aging effect. Assuming PMMA has a  $T_g$  of  $105^\circ \text{C}$ , Hasan's datasets were performed at  $T_g - 76^\circ \text{C}$ , where the overshoot should mostly be due to deformation history. Hasan's results are similar to that of Dreistadt's where overshoot increases with creep time under a large creep stress. Again accelerated aging effects were observed. Nanzai performed the experiments at  $T_g - 36^\circ \text{C}$  where the increase of overshoot with longer deformation history is also observed. However Nanzai and Hasan's datasets would be more complete if smaller deformation input was used so that the effect of deformation history and thermal history can be de-convoluted.

Limitation of current study is the stiffness of the epoxy material below  $T_g - 30^\circ \text{C}$ . The current material is only capable of a large deformation ( $>10\%$  strain) at temperatures near  $T_g$ , where aging effect dominates. A more ductile copolymer-based polymer will be used in future which allows

study of stress-strain behaviors during 4-step experiment at temperatures lower than  $T_g - 30\text{ }^{\circ}\text{C}$ , where the effect deformation history on mobility change is more pronounced.

#### 4.6 Reference

1. Lee, H.-N., et al., *Dye reorientation as a probe of stress-induced mobility in polymer glasses*. The Journal of chemical physics, 2008. **128**(13): p. 134902.
2. Hasan, O. and M.C. Boyce, *Energy storage during inelastic deformation of glassy polymers*. Polymer, 1993. **34**(24): p. 5085-5092.
3. Capaldi, F.M., M.C. Boyce, and G.C. Rutledge, *Enhanced Mobility Accompanies the Active Deformation of a Glassy Amorphous Polymer*. Physical Review Letters, 2002. **89**(17): p. 175505.
4. Lee, E.-W., G.A. Medvedev, and J.M. Caruthers, *Deformation induced evolution of mobility in PMMA*. Journal of Polymer Science Part B: Polymer Physics, 2010. **48**(22): p. 2399-2401.
5. Turnbull, D. and M.H. Cohen, *Free-volume model of the amorphous phase: glass transition*. The Journal of chemical physics, 1961. **34**(1): p. 120-125.
6. Cohen, M.H. and G. Grest, *Liquid-glass transition, a free-volume approach*. Physical Review B, 1979. **20**(3): p. 1077.
7. Gibbs, J.H. and E.A. DiMarzio, *Nature of the glass transition and the glassy state*. The Journal of Chemical Physics, 1958. **28**(3): p. 373-383.
8. Di Marzio, E.A., *The entropy theory of glass formation after 40 years*. Computational materials science, 1995. **4**(4): p. 317-324.
9. Caruthers, J.M., et al., *A thermodynamically consistent, nonlinear viscoelastic approach for modeling glassy polymers*. Polymer, 2004. **45**(13): p. 4577-4597.
10. Adolf, D.B., R.S. Chambers, and M.A. Neidigk, *A simplified potential energy clock model for glassy polymers*. Polymer, 2009. **50**(17): p. 4257-4269.
11. Chen, K. and K.S. Schweizer, *Theory of aging, rejuvenation, and the nonequilibrium steady state in deformed polymer glasses*. Physical Review E, 2010. **82**(4): p. 041804.
12. Narayanaswamy, O., *A model of structural relaxation in glass*. Journal of the American Ceramic Society, 1971. **54**(10): p. 491-498.
13. Boyce, M.C., D.M. Parks, and A.S. Argon, *Large inelastic deformation of glassy polymers. Part I: rate dependent constitutive model*. Mechanics of materials, 1988. **7**(1): p. 15-33.
14. Buckley, C., et al., *Deformation of thermosetting resins at impact rates of strain. Part 2: constitutive model with rejuvenation*. Journal of the Mechanics and Physics of Solids, 2004. **52**(10): p. 2355-2377.

15. Wu, J. and C. Buckley, *Plastic deformation of glassy polystyrene: A unified model of yield and the role of chain length*. Journal of Polymer Science Part B: Polymer Physics, 2004. **42**(11): p. 2027-2040.
16. Tervoort, T., E. Klompen, and L. Govaert, *A multi-mode approach to finite, three-dimensional, nonlinear viscoelastic behavior of polymer glasses*. Journal of Rheology, 1996. **40**(5): p. 779-797.
17. Klompen, E., et al., *Modeling of the postyield response of glassy polymers: influence of thermomechanical history*. Macromolecules, 2005. **38**(16): p. 6997-7008.
18. Van Breemen, L., et al., *Extending the EGP constitutive model for polymer glasses to multiple relaxation times*. Journal of the Mechanics and Physics of Solids, 2011. **59**(10): p. 2191-2207.
19. Shay Jr, R. and J. Caruthers, *A predictive model for the effects of thermal history on the mechanical behavior of amorphous polymers*. Polymer Engineering & Science, 1990. **30**(20): p. 1266-1280.
20. Anand, L., et al., *A thermo-mechanically coupled theory for large deformations of amorphous polymers. Part I: Formulation*. International Journal of Plasticity, 2009. **25**(8): p. 1474-1494.
21. Anand, L. and N. Ames, *On modeling the micro-indentation response of an amorphous polymer*. International journal of plasticity, 2006. **22**(6): p. 1123-1170.
22. Medvedev, G.A. and J.M. Caruthers, *A comparison of constitutive descriptions of the thermo-mechanical behavior of polymeric glasses*, in *Polymer Glasses*. 2016, CRC Press. p. 467-552.
23. FA, M., C. FC, and S. SS, *Mechanically Enhanced Aging of Glassy Polymers*. 1976.
24. Struik, L.C.E., *Physical aging in amorphous polymers and other materials*. 1977.
25. McKenna, G.B., *Mechanical rejuvenation in polymer glasses: fact or fallacy?* Journal of Physics: Condensed Matter, 2003. **15**(11): p. S737.
26. Dreistadt, C., et al., *Experimental study of the polycarbonate behaviour during complex loadings and comparison with the Boyce, Parks and Argon model predictions*. Materials & Design, 2009. **30**(8): p. 3126-3140.
27. Bending, B. and M. Ediger, *Comparison of mechanical and molecular measures of mobility during constant strain rate deformation of a PMMA glass*. Journal of Polymer Science Part B: Polymer Physics, 2016. **54**(19): p. 1957-1967.
28. Haward, R. and G. Thackray, *The use of a mathematical model to describe isothermal stress-strain curves in glassy thermoplastics*. Proceedings of the Royal Society of London. Series A. Mathematical and Physical Sciences, 1968. **302**(1471): p. 453-472.
29. Popelar, C. and K.M. Liechti, *A distortion-modified free volume theory for nonlinear viscoelastic behavior*. Mechanics of Time-Dependent Materials, 2003. **7**(2): p. 89-141.

30. Knauss, W.G. and I. Emri, *Volume change and the nonlinearly thermo-viscoelastic constitution of polymers*. Polymer Engineering & Science, 1987. **27**(1): p. 86-100.
31. Medvedev, G.A., J.W. Kim, and J.M. Caruthers, *Prediction of the relationship between the rate of deformation and the rate of stress relaxation in glassy polymers*. Polymer, 2013. **54**(24): p. 6599-6607.
32. Nanzai, Y., *Transition mechanism from elastic deformation to plastic flow in poly (methyl methacrylate)*. Polymer Engineering & Science, 1990. **30**(2): p. 96-107.
33. Xiao, R. and T.D. Nguyen, *An effective temperature theory for the nonequilibrium behavior of amorphous polymers*. Journal of the Mechanics and Physics of Solids, 2015. **82**: p. 62-81.



## 5. CONCLUSION

The first objective of this research was to explore the linear viscoelastic behaviors of crosslinked DGEBA epoxies. Dynamic mechanical data of EPON1009F-MDA over a wide range of temperatures revealed the thermorheological complexity with lack of superposition of isotherms below  $T_g$ . A new approach to analyze the experimental responses was introduced based on relaxation spectrum of non-uniform spectral spacing. This new method accommodates two difficulties in analyzing linear viscoelastic data of glass-formers: (i) thermorheological complexity that has been observed for all materials in glassy state especially when the frequency window is wide, and (ii) unrealistic change in the strength of a single dipole moment if dielectric responses were analyzed in conventional methods. Using the new method, density of relaxation processes was determined for EPON1009F-MDA and showed a distribution over relaxation time, where peaks and shoulders were associated to features of glassy polymers such as  $\alpha$  relaxation, excess wing, etc. Temperature dependence of  $\log \tau$  mobility was determined where two different patterns were observed at temperatures near and above  $T_g$ : (i) the  $\alpha$  region where lines representing relaxation processes were tightly bunched and approximately parallel, and (ii) the  $\alpha+$  region where relaxation processes were sparse and non-uniform. A transition across temperature was also observed in the relaxation map that the temperature dependence changed from WLF-like behavior above  $T_g$  to Arrhenian behavior below  $T_g$ .

Study on the  $\alpha+$  region was focused on comparing the linear viscoelastic behaviors between different glass-forming materials. Dynamic mechanical data for a series of crosslinked DGEBA materials with different crosslink densities, and a linear polymer named phenoxy with the same chemical structure were analyzed. Digitized dielectric data of DGEBA resin (the monomer) was added to the dataset for comparison. Their temperature dependence of  $\log a$  mobility in  $\alpha$  and  $\alpha+$  regions were collapsed to two lines which was consistent with the “universal WLF-type behavior” assumption proposed for  $\alpha$  relaxation. With more literature datasets analyzed, two distinct branches for all DGEBA materials were observed: (i) one with steeper temperature dependence for “tighter” networks like EPON825-MDA, (ii) the other with mild  $\log a$  vs. temperature behavior for “loose” species including phenoxy, DGEBA monomer, loose and imperfect networks.

Examining relaxation spectrum in  $\alpha+$  region of various types of glass-forming materials, the key features are: (i) molecular glass formers showed a clear and sharp end of  $\alpha$  process at high temperature side and no  $\alpha+$  process, (ii) for oligomers there was no discernable  $\alpha+$  process, but a broader  $\alpha$  peak compared to that of molecular glasses, (iii) tight networks exhibited no separate  $\alpha+$  process while the dispersion of  $\alpha$  peak was wider than oligomers, and (iv) linear and lightly-crosslinked polymers showed a narrow  $\alpha$  peak and  $\alpha+$  shoulder where the height and span of  $\alpha+$  shoulder was related to molecular weight and molecular structure.

The second objective of this research was to discriminate constitutive models for glassy polymers with critical non-linear viscoelastic datasets. Specifically, a four-step constant strain rate experiment was performed to examine the effect of deformation history on the magnitude of yield overshoot during the first and second stretching, where the yield was a probe of mobility. Dogbone specimen of EPON1009F-MDA was tested at  $T_g - 13$  °C under various mechanical conditions. However, at this temperature the effect of physical aging was predominate, while the effect of deformation was minimal. Neither rejuvenation nor accelerated aging assumption was supported.

Further study on linear viscoelasticity would require deciphering sub- $T_g$  relaxation behaviors measured by multiple techniques. The current difficulty is that in  $\beta$  and  $\gamma$  region the relaxation processes are convoluted and relaxation spectrum might not be determined as robustly as in  $\alpha$  region. Screening of glass-formers with different chemical structure would assist the choice of a particular material that may practically solve this problem.

Continuation of study on the effect of deformation history would require a more ductile specimen, such as an ethylene-butene copolymer, so that the 4-step experiment could be performed at lower temperatures below  $T_g$  where the effect of physical aging would be minor.

## APPENDIX A. DIELECTRIC ANALYSIS FOR EPON 1009F-MDA

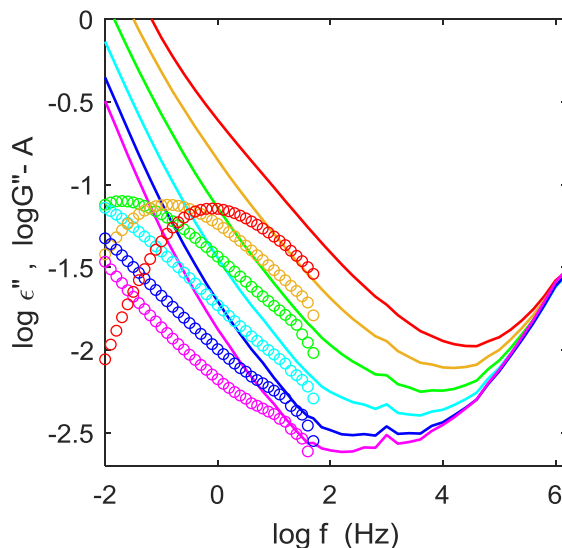


Figure A.1 Dynamic mechanical loss modulus isotherms shifted by constant amount  $A=9.35$  for the following temperatures: 102.5°C – red circles, 100°C – orange circles, 97.5°C – green circles, 95°C – cyan circles, 92.5°C – blue circles, 90°C – magenta circles; loss dielectric susceptibility isotherms: solid lines in corresponding colors.

The dielectric spectroscopy experiments were performed at the same temperatures as the dynamic mechanical experiment. The measured loss components for both sets of data are shown in Figure A.1 as function of frequency, where the  $\log G''$  isotherms have been shifted vertically downward by the same constant value of 9.35. The value 9.35 was chosen because it results in the smooth merging of the lowest temperature dielectric and mechanical isotherms (both shown in magenta color). The dielectric loss contains spurious contributions due to conductivity and electrode polarization effects, which become more pronounced at lower frequencies and higher temperatures. These effects dominate the measured dielectric response at temperatures above 105°C (not shown in Figure A.1). It is possible to subtract the conductivity and electrode polarization contributions for the dielectric loss isotherms given in Figure A.1 such that the remainders will coincide with the (shifted) mechanical loss isotherms; however, this procedure does not result in independent data and hence does not provide additional constraints for extraction of the relaxation spectrum. The latter statement is only true for the frequency window up to  $10^{1.7}$  Hz considered in this

communication. When higher frequencies (up to  $10^{6.2}$  Hz) are included, the dielectric data allow for expanding the relaxation time spectrum by 4 orders-of-magnitude. This becomes of particular value at lower temperatures where the aforementioned effects of conductivity and electrode polarization are not present. The analysis of the sub-Tg dielectric response for the Epon1009F-MDA system will be reported in a future publication.

Using the Cole-Davidson function, the storage dielectric susceptibility is given by

$$\varepsilon'(\omega) = \varepsilon_{\infty} + \Delta\varepsilon \left[ \cos(\phi) \right]^{\beta} \cos(\phi\beta), \quad \tan(\phi) = \omega\tau_{CD} \quad (\text{A-1})$$

where  $0 < \beta < 1$  is the shape parameter and  $\tau_{CD}$  is the Cole-Davidson time. In case of a thermorheologically simple material obeying Equation (A-1) only  $\tau_{CD}$  would change with temperature, while  $\Delta\varepsilon$  and  $\beta$  would be constant. In the static limit (i.e. at  $\omega \rightarrow 0$ ) of Equation (A-1),  $\varepsilon_0 = \varepsilon'(\omega \rightarrow 0) = \varepsilon_{\infty} + \Delta\varepsilon$  regardless of the value of the shape parameter. Therefore to accommodate the apparent temperature dependence of  $\varepsilon_0$  seen in Figure 2.10 one has to postulate that  $\Delta\varepsilon = \Delta\varepsilon(T)$ .

Similarly, the discrete spectral representation is given by

$$\varepsilon'(\omega) = \varepsilon_{\infty} + \bar{\varepsilon} \sum_{i=1}^n \frac{1}{1 + \omega^2 \tau_i^2} \quad (\text{A-2})$$

where the static limit is  $\varepsilon_0 = \varepsilon_{\infty} + n\bar{\varepsilon}$ . Unlike in the previous case using the Cole-Davidson function, the increase in  $\varepsilon_0$  with decreasing temperature can be obtained straightforwardly by adding new processes such that  $\varepsilon_0 = \varepsilon_{\infty} + n'\bar{\varepsilon}$  where  $n' > n$ . A similar conclusion would occur if other empirical functions like KWW, Cole-Cole, Havriliak-Negami, etc. are used to fit the dielectric susceptibility. We believe that the postulated emergence of new relaxation processes is not merely a convenient way of fitting the data, but a better representation of physical reality.

## APPENDIX B. EQUATION (2-5) FITTING PARAMETERS FOR ALL ISOTHERMS

Table A.1 Optimized Equation (2-5) fitting parameters for EPON1009F-MDA isotherms shown in Figure 2.6.

	$\bar{\rho} \cdot 10^{-5}$	$A \cdot 10^3$	$k_{\alpha}$	$x_{\alpha}$	$k_s$	$x_s$	$B \cdot 10^3$	$k_{nt}$	$x_{nt}$
90°C	3.4	2.7	0.55	5.3	2.8	4.5			
92.5°C	3.5	3.0	0.52	5.0	2.9	4.0			
95°C	2.4	3.0	0.46	4.2	2.6	3.4	6.3*	0.8*	4.1*
97.5°C	2.1	3.2	0.43	3.3	2.2	2.5	5.3	0.8*	3.1*
100°C	2.1	3.0*	0.46*	2.4	1.9	1.7	4.8	0.8*	2.1*
102.5°C	2.0	3.0*	0.46*	1.5	2.0	0.8	4.2	0.9*	1.1*
105°C	2.0	3.0*	0.46*	0.8	2.2	0.2	4.8	0.8*	0.2*
107.5°C	0.9				1.9	-0.6	5.2	0.74	0.25
110°C	0.8				1.8	-1.3	5.6	0.77	-0.2
112.5°C	0.9				1.8	-1.9	4.9	0.74	-0.7
115°C	0.9				1.6	-2.4	5.4	0.67	-1.4
120°C	0.9				1.6	-3.4	4.6	0.70	-1.8
125°C	1.0				1.9	-4.1	5.2	0.70	-2.7
130°C	1.0				2.1	-4.7	5.0	0.74	-2.9
140°C	1.0				2.2	-5.5	5.1	0.75	-3.6
160°C	1.0				2.2*	-6.5*	5.2	0.79	-4.5
180°C	1.0				2.2*	-7.2*	5.4	0.80	-5.3

Empty cells correspond to cases where the relevant portion of the density function Equation (2-5) does not affect the fit to the data within the experimental window and hence where the values of the fitting parameters could not be established. Stars indicate the cases where the corresponding parameters, although having some discernable effect on the fit, cannot be robustly determined from the optimization.

## APPENDIX C. MOLECULAR WEIGHT DISTRIBUTION FOR EPON RESINS

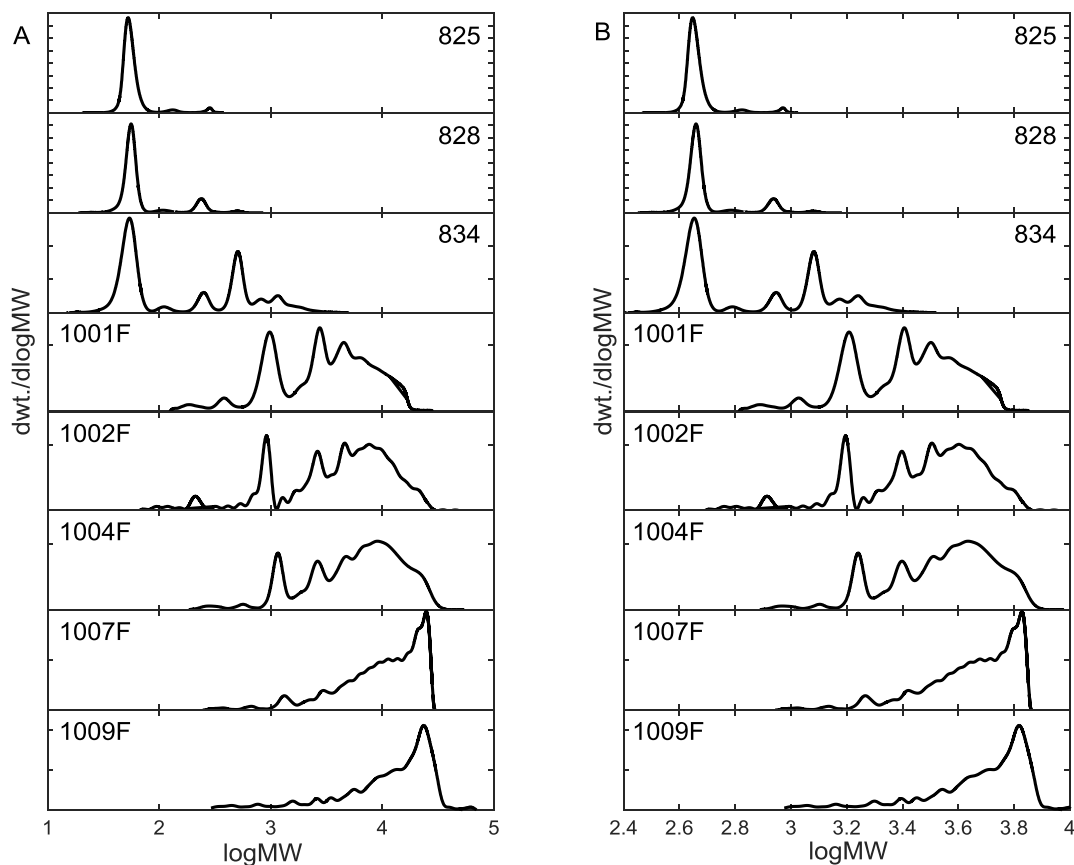


Figure A.2 GPC trace of various Epon resins. (A) The molecular weight axis was determined using monodisperse polystyrene standards and (B) the corrected molecular weight axis using the correlation shown in Figure A.3 (see text).

The molecular weight (MW) distribution of the DGEBA diepoxide resins was determined by GPC using the methods described in the Experimental Section in the main paper and are shown in Figure A.2A. Epon828 is an industrial product that primarily is monomer with small amount of dimers and a larger amount of trimers. Epon825 is purified Epon825 where most of the dimers and trimers have been removed. The widths of the peaks shown in Figure A.2A are due to dispersion in the GPC trace and not due to a distribution of molecular weights around the monomer/dimer/etc. weights. The MW axis was determined using polystyrene standards and thus is not directly related

to the DGEBA resins. Specifically, the first peak is associated with the DGEBA diepoxide monomer with a MW of 340 g/mole as determined from the chemical structure and is consistent with two times the epoxide equivalent weight from titration; in contrast, the first GPC peak occurs at a  $\log(\text{MW})$  of  $10^{1.73} = 53.7$  g/mole. Thus, the GPC trace in Figure A.2A gives a qualitative picture of the molecular weight distribution, but not the exact values of the molecular weight of the individual components.

In order to account for the difference between polystyrene and DGEBA in the GPC calibration, the peaks shown in Figure A.2A were identified as monomers, dimers, trimers, etc. with the molecular weights determined from their chemical structure and compared with the molecular weights from the GPC using the polystyrene standards.

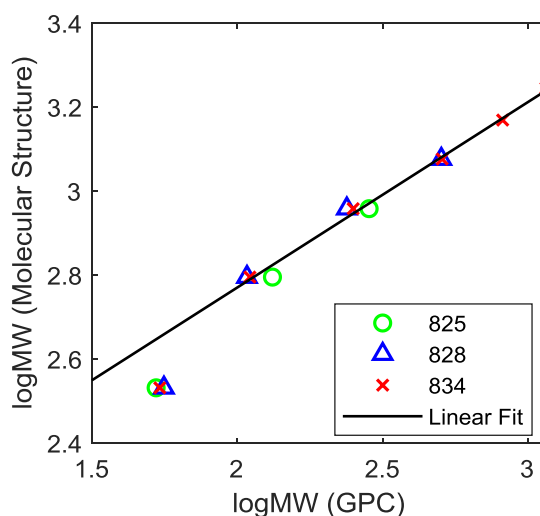


Figure A.3 Correlation between the actual molecular weight of monomer through 6-mer of DGEBA vs. the molecular weight shown in Figure A.2A determined via GPC using polystyrene standards.

As shown in Figure A.3 there is a linear relationship between the two molecular weights, where the deviation for the monomer ( $\text{MW} = 340.4$  g/mole) is expected because of the relatively rigid molecular structure of the monomer as compared to the higher molecular weight DGEBA diepoxides. Using the linear line in Figure A.3, the x-axis in Figure A.2A was corrected in Figure A.2B, where the monomer location in Figure A.2B is off because of the deviation of the monomer

from the linear line in Figure A.3. Due to the construction of Figure A.2B the molecular weights are exact for dimers through hexamers. Examining the Epon1009F trace, the main peak is located at  $\log(\text{MW}) = 3.8$ , which corresponds to  $\text{MW} = 6310 \text{ g/mole}$ . This should be compared with the number average molecular weight determined by titration (i.e. an epoxide equivalent of 2737 g/mole) of 5474 g/mole, which is very reasonable considering the tail towards lower molecular weights shown in Figure A.2B. We believe that this calibration procedure provides a good estimate of the molecular weight distribution for the DGEBA series of diepoxides.

Epon834 is a qualitatively different material than the Epon825 and Epon828 that includes (i) a large amount of monomer with a MW of 340 g/mole and (ii) a distribution of molecular weights with a central peak associated with a tetramer with MW of 1738 g/mole, but also includes trimers, pentamers and higher oligomers. The epoxide equivalent weight of Epon834 is 245 g/mole which corresponds to a MW of 490 g/mole, although there is no molecule with this specific MW.

Table A.2 Average molecular weight and epoxy equivalent weight of DGEBA resins

DGEBA	Mn (g/mol)	Mw (g/mol)	EEW (g/mol)
Epon825	454	474	171
Epon828	468	523	189
Epon834	507	873	245
Epon1001F	1781	2862	536
Epon1002F	1598	3298	678
Epon1004F	2296	3792	842
Epon1007F	2999	4713	1862
Epon1009F	2621	5061	2737

The distribution fundamentally changes for the Epon1001F through Epon1009F series, where no monomer is present. For Epon100F, Epon1002F and Epon1004F the distributions look quite similar, where the size of the peak centered at approximately  $10^{3.6} \text{ g/mole}$  on the GPC decreases in magnitude, which is the reason why the epoxide equivalent weight increases from 536 to 678 to 842 g/mole. There is a change in the basic shape of the MWD for the Epon1007F and Epon1009F, where the distribution has a maximum at the highest molecular weight with a tail to smaller molecular weights and no material with the peak at  $10^{3.2} \text{ g/mole}$  as seen in the Epon1001F, Epon1002F and Epon1004F material. Number- and weight- averaged molecular weight for each



EPON resin are calculated based on GPC traces in Figure A.2B, and compared to their epoxy equivalent weight (EEW) as in Table A.2.

The epoxide equivalent weight determined by titration provides an important characterization of the diepoxide resins that is necessary to determine the amount of diamine needed to fully cure the epoxy resin. However, the MWD determined by GPC shows a much more complete picture of the diepoxide resins. Moreover, it is important to measure this distribution to ensure that material with the same name but from different batches are the same. For another epoxide system we purchased material over a period of several years with the same name; however, the physical properties of the materials had small, but noticeable, changes, where we discovered that the MWD was different for the different batch of the ‘same’ material, although they had the same epoxide equivalent weight. *Caveat emptor.*

## APPENDIX D. VISCOELASTIC RELAXATION DATA

Mechanical datasets reported for other glass-forming materials will now be analyzed. For each dataset considered the data from figures in the literature were digitized and then analyzed in the same way as used for the phenoxy and Epon825-MDA systems discussed in the main text. When the isotherms were reported, the individual isotherms were digitized, and then the master curve was constructed (using the  $\log a_T$  shifts from the original source, if they were provided, or by manually shifting) – this method produces more accurate master curves because the isotherms are typically shown with higher resolution than the master curve. However, in some papers only the master curve and  $\log a_T$  shift factors are reported, in which case only the master curve is digitized. Spectra were determined for a number of glass forming polymers, oligomers and small molecules.

### D1. DGEBA Epoxy Resins Crosslinked with 4,4'-Diaminodiphenyl Sulfone (DDS)

Seven DGEBA diepoxide resins of different molecular weights were cured with DDS. The molecular weight between crosslinks,  $M_c$ , is reported in Table A.3.  $M_c$  was determined using (i) two times the epoxide equivalent and (ii) from the tensile modulus at high temperatures using the standard theory of rubber elasticity that was measured using strip specimens on a Rheometrics RMS-800/RDS-II spectrometer.[2] There is good agreement between  $M_c$  determined from the epoxide equivalent and that determined via rubber elasticity.

Table A.3 Characteristics of various DGEBA resins cured with DDS polymers.

DGEBA	$M_c$ (g/mol) from Epoxide Equivalent	$M_c$ (g/mol) from rubber elasticity
Epon828	362	346
Epon834	391	441
Epon1001F	850	986
Epon1002F	1007	1262
Epon1004F	1553	1586
Epon1007F	2673	3612
Epon1009F	5224	5983

The  $G'$  and  $G''$  isotherms for each of the resins systems are given in Figure A.4 through Figure A.10 including the temperature dependence of the  $\log a_T$  shift function to construct the  $G'$  and  $G''$  master curves in the main text. The original data was published in Ref. [2] in terms of radians/sec, which has been converted to Hz in order to be consistent with the other materials reported in the paper. The spectra for these seven systems were shown in the main text.

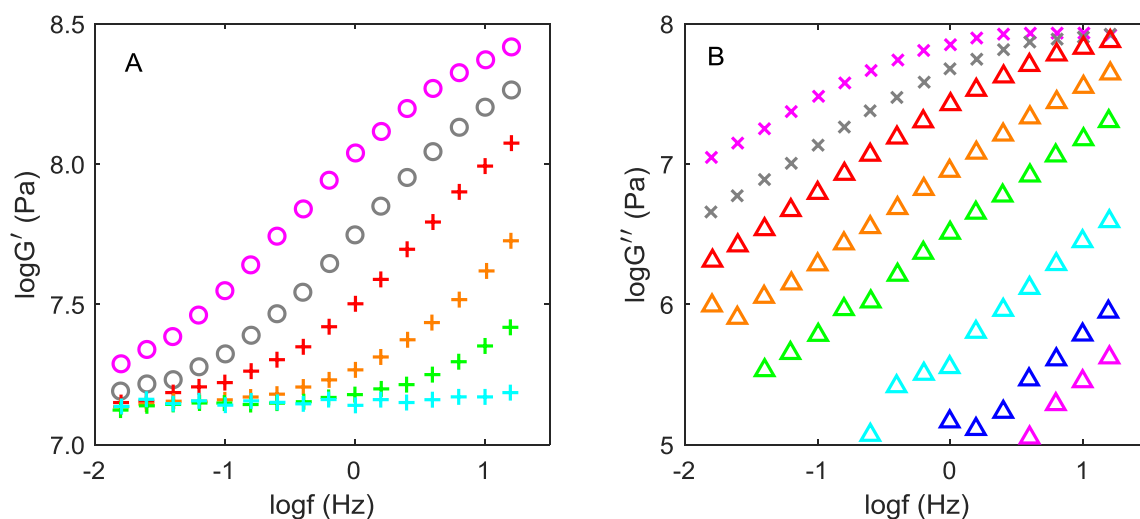


Figure A.4  $G'$  (A) and  $G''$  (B) isotherms for Epon828-DDS from 222oC to 267oC with the  $\log a_T$  shift function used to construct the master curves shown in Fig. 12A in the main text. Symbols indicate the isotherms temperature:  $G'$ : 222°C (○), 225°C (○), 228°C (+), 233°C (+), 238°C (+), 248°C (+);  $G''$ : 222°C (×), 225°C (×), 228°C (△), 233°C (△), 238°C (△), 248°C (△), 257°C (△), 267°C (△).

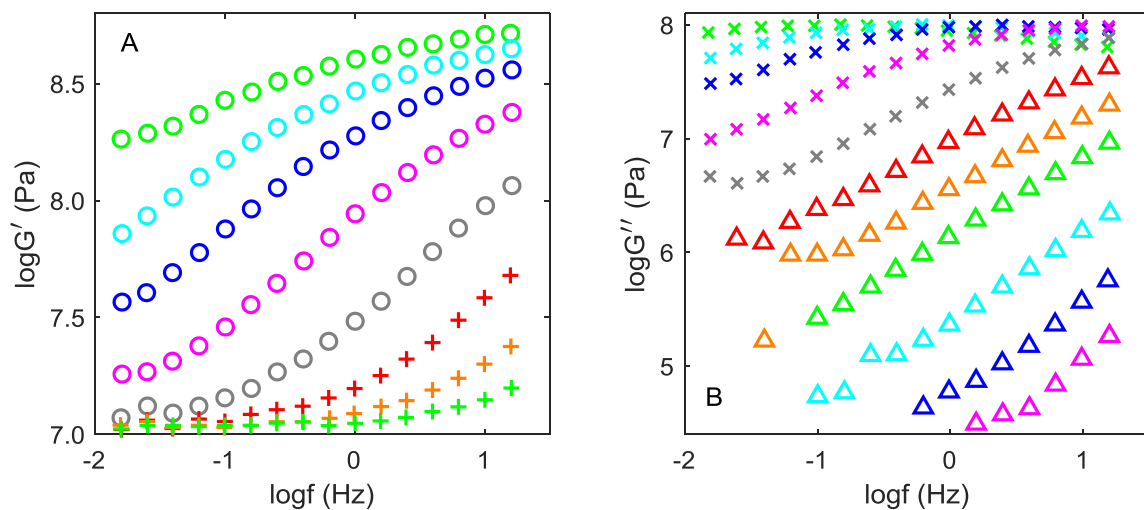


Figure A.5  $G'$  (A) and  $G''$  (B) isotherms for Epon834-DDS from 171°C to 241°C with the  $\log a_T$  shift function used to construct the master curves shown in Fig. 15 in the main text. Symbols indicate the isotherms temperature:  $G'$ : 181°C (○), 184°C (○), 187°C (○), 191°C (○), 196°C (○), 201°C (+), 206°C (+), 211°C (+);  $G''$ : 181°C (×), 184°C (×), 187°C (×), 191°C (×), 196°C (×), 201°C (△), 206°C (△), 211°C (△), 221°C (△), 231°C (△), 241°C (△).

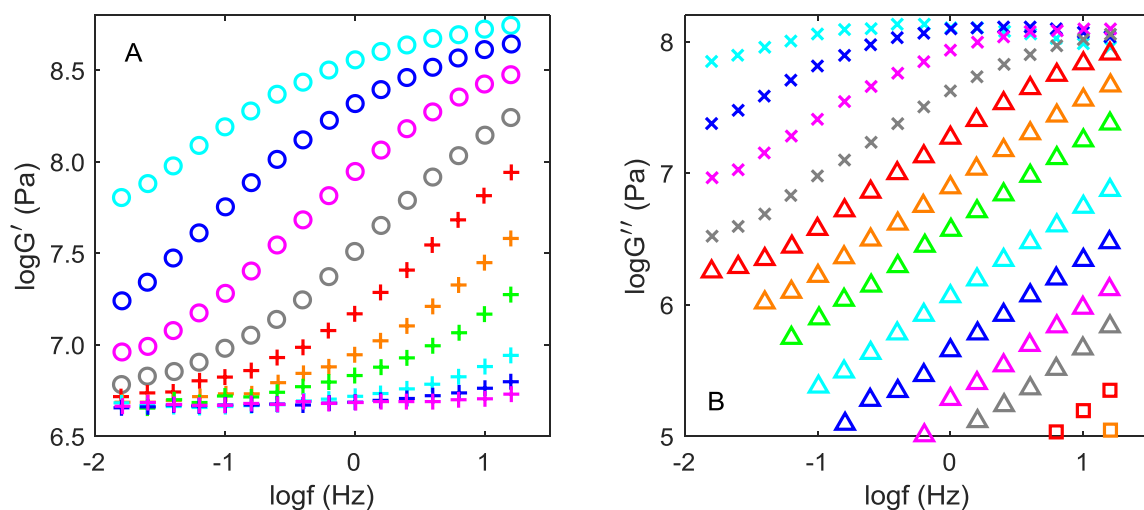


Figure A.6  $G'$  (A) and  $G''$  (B) isotherms for Epon1001F-DDS from 127°C to 198°C with the  $\log a_T$  shift function used to construct the master curves shown in Fig. 15 in the main text. Symbols indicate the isotherms temperature:  $G'$ : 140°C (○), 143°C (○), 146°C (○), 149°C (○), 152°C (+), 155°C (+), 158°C (+), 163°C (+), 168°C (+), 173°C (+);  $G''$ : 140°C (×), 143°C (×), 146°C (×), 149°C (×), 152°C (△), 155°C (△), 158°C (△), 163°C (△), 168°C (△), 173°C (△), 178°C (△), 188°C (□), 198°C (□).

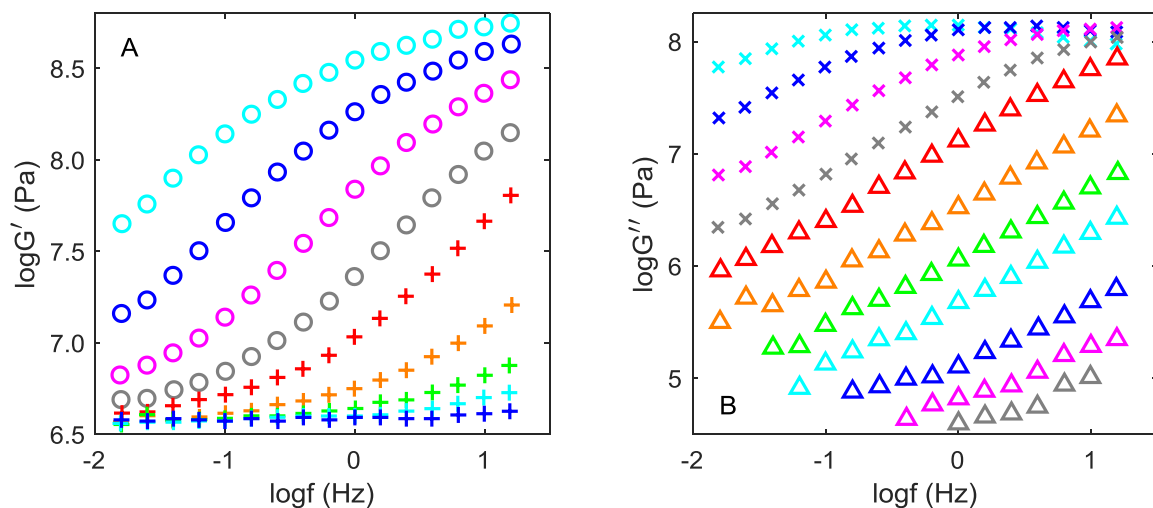


Figure A.7  $G'$  (A) and  $G''$  (B) isotherms for Epon1002F-DDS from 117°C to 187°C with the  $\log a_T$  shift function used to construct the master curves shown in Fig. 15 in the main text. Symbols indicate the isotherms temperature:  $G'$ : 130°C (○), 132.5°C (○), 136°C (○), 139°C (○), 141°C (+), 147°C (+), 152°C (+), 157°C (+), 167°C (+);  $G''$ : 130°C (×), 132.5°C (×), 136°C (×), 139°C (×), 141°C (△), 147°C (△), 152°C (△), 157°C (△), 167°C (△), 177°C (△), 187°C (△).

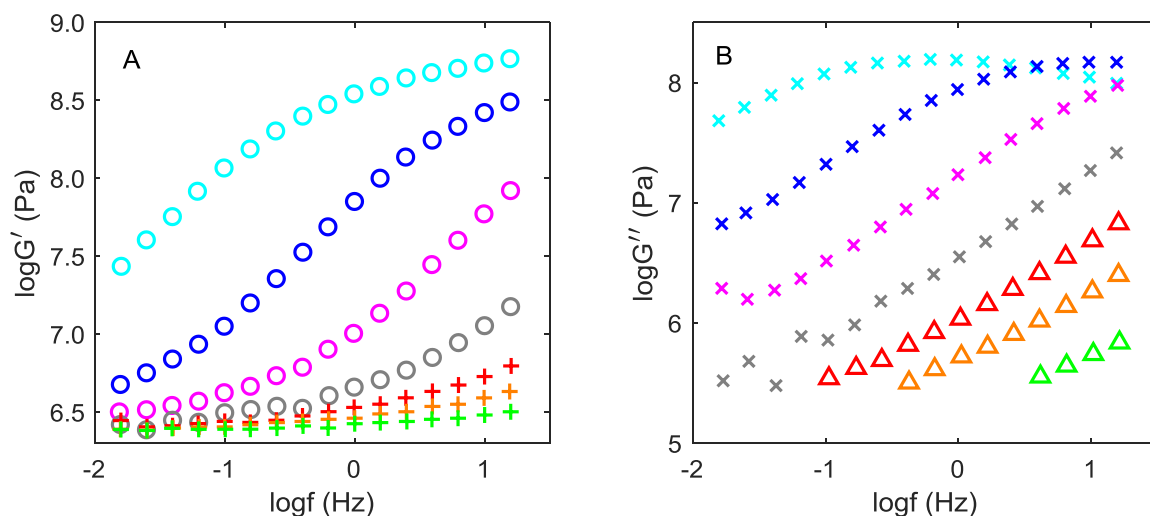


Figure A.8  $G'$  (A) and  $G''$  (B) isotherms for Epon1004F-DDS from 100°C to 155°C with the  $\log a_T$  shift function used to construct the master curves shown in Fig. 15 in the main text. Symbols indicate the isotherms temperature:  $G'$ : 120°C (○), 125°C (○), 130°C (○), 135°C (○), 140°C (+), 145°C (+), 155°C (+);  $G''$ : 120°C (×), 125°C (×), 130°C (×), 135°C (×), 140°C (△), 145°C (△), 155°C (△).

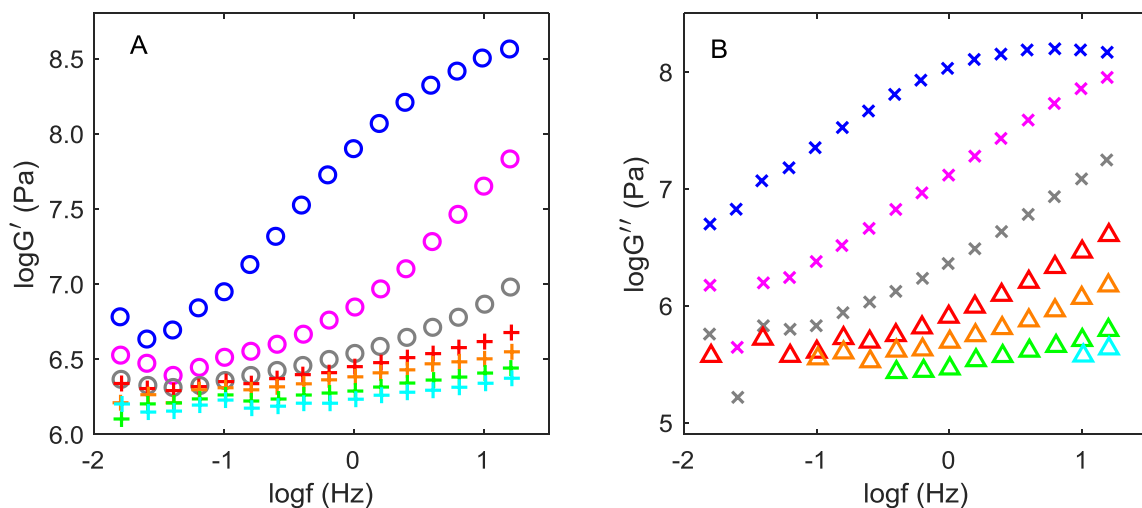


Figure A.9  $G'$  (A) and  $G''$  (B) isotherms for Epon1007F-DDS from 90°C to 155°C with the  $\log a_T$  shift function used to construct the master curves shown in Fig. 15 in the main text.

Symbols indicate the isotherms temperature:  $G'$ : 115°C (○), 120.5°C (○), 125.5°C (○), 130.5°C (+), 135.5°C (+), 145.5°C (+), 155°C (+);  $G''$ : 115°C (×), 120.5°C (×), 125.5°C (×), 130.5°C (△), 135.5°C (△), 145.5°C (△), 155°C (△).

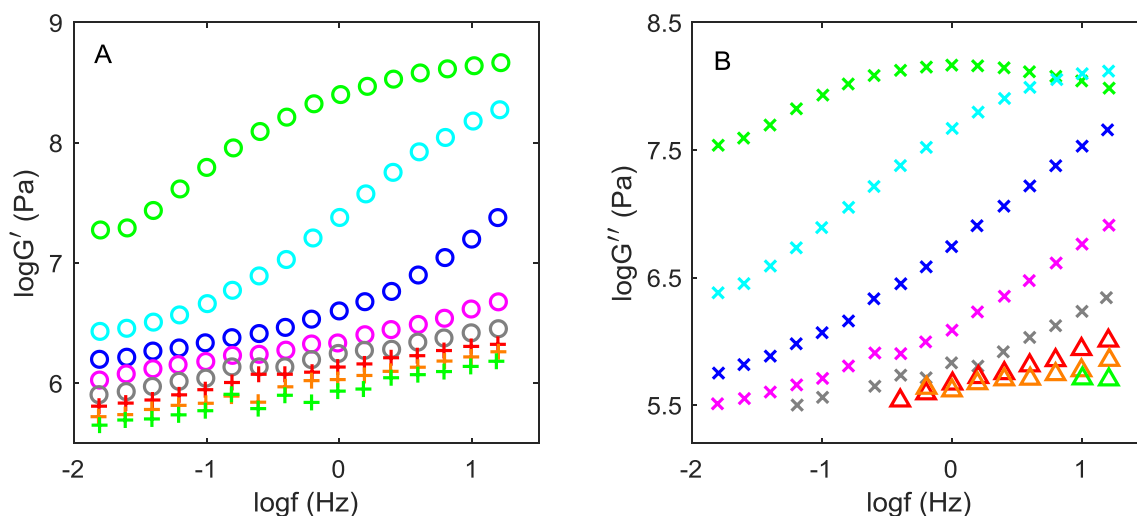


Figure A.10  $G'$  (A) and  $G''$  (B) isotherms for Epon1009F-DDS from 94°C to 138°C with the  $\log a_T$  shift function used to construct the master curves shown in Fig. 15 in the main text.

Symbols indicate the isotherms temperature:  $G'$ : 103°C (○), 108°C (○), 113°C (○), 118°C (○), 123°C (○), 128°C (+), 133°C (+), 138°C (+);  $G''$ : 103°C (×), 108°C (×), 113°C (×), 118°C (×), 123°C (×), 128°C (△), 133°C (△), 138°C (△).

## D2. Crosslinked Poly(methyl methacrylate), P(MMA-EGDMA)

Dynamic linear viscoelastic tensile data was reported for a crosslinked PMMA ( $T_g = 121.4\text{ }^\circ\text{C}$ ) where methyl methacrylate was polymerized with 5 wt.% of an ethylene glycol dimethacrylate (EGDMA) crosslinking agent. Assuming EGDMA was reacted the molecular weight between crosslinks was 1900 g/mol corresponding to approximately 19 repeat units. The number of units between of MMA-mers between crosslinks is the same as that of Epon1009F-MDA system, which has approximately 19 DGEBA units between crosslinks; however, the size of a DGEBA unit is much larger than the MMA repeat unit.

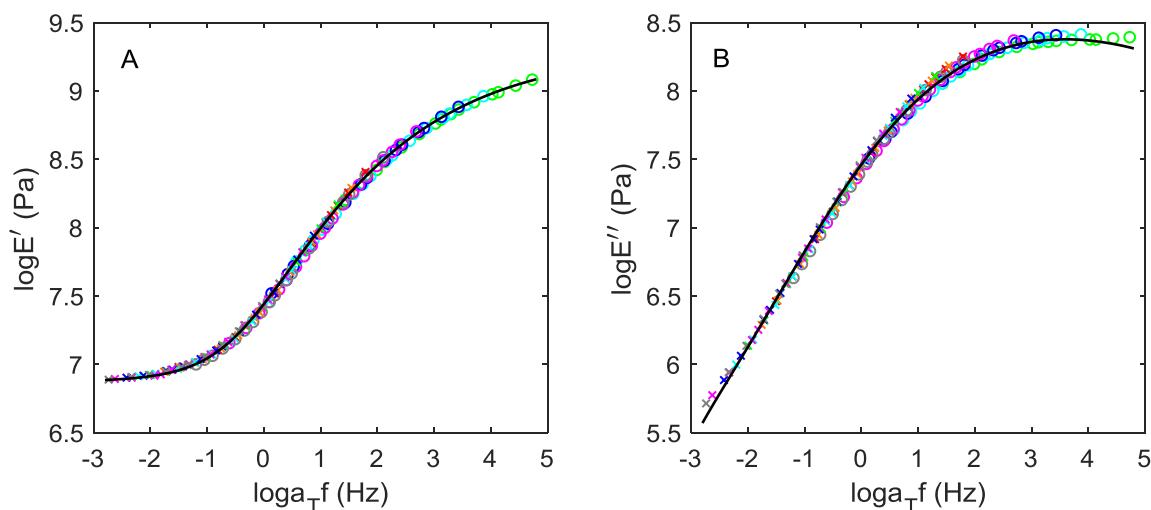


Figure A.11 Master curves of  $E'$  (A) and  $E''$  (B) shifted to  $T_{\text{ref}} = 147.5\text{ }^\circ\text{C}$  ( $T_g + 26.1\text{ }^\circ\text{C}$ ) for methyl methacrylate crosslinked with 5 wt% ethylene glycol dimethacrylate, P(MMA-EGDMA) at the following temperatures:  $118.7\text{ }^\circ\text{C}$  (○),  $122.5\text{ }^\circ\text{C}$  (○),  $126.1\text{ }^\circ\text{C}$  (○),  $129.6\text{ }^\circ\text{C}$  (○),  $133\text{ }^\circ\text{C}$  (○),  $134.8\text{ }^\circ\text{C}$  (○),  $138.3\text{ }^\circ\text{C}$  (○),  $141.6\text{ }^\circ\text{C}$  (×),  $144.1\text{ }^\circ\text{C}$  (×),  $147.5\text{ }^\circ\text{C}$  (×),  $149.3\text{ }^\circ\text{C}$  (×),  $150.8\text{ }^\circ\text{C}$  (×),  $152.6\text{ }^\circ\text{C}$  (×),  $156.4\text{ }^\circ\text{C}$  (×). Isotherms of  $E'$ ,  $\tan\delta$  and  $\log a_T$  with respect to  $T_{\text{ref}} = 147.5\text{ }^\circ\text{C}$  were digitized, while  $E''$  were calculated based on  $E'$  and  $\tan\delta$ . Solid lines are the predictions using the relaxation spectrum shown in Figure A.12.

The reported  $E'$  and  $\tan\delta$  isotherms[3] were digitized and  $E''$  was calculated, where the  $E'$  and  $E''$  isotherms are reported in Figure A.11 along with the digitized  $\log a_T$  shift function. Master curves of  $E'$  and  $E''$  were constructed in Figure A.11 with a reference temperature  $T_{\text{ref}} = 147.5\text{ }^\circ\text{C}$  ( $T_g + 26.1\text{ }^\circ\text{C}$ ). The  $\log a_T$  horizontal shift factors were reported and was fit by WLF equation with

C1=-7.6 and C2=59.1°C. in the original paper.[3] Superposition is good for the high temperature isotherms, but lack of superposition occurs in the  $T_g$  region. The relaxation spectrum was computed from the  $E'$  and  $E''$  response as shown in Figure A.12.

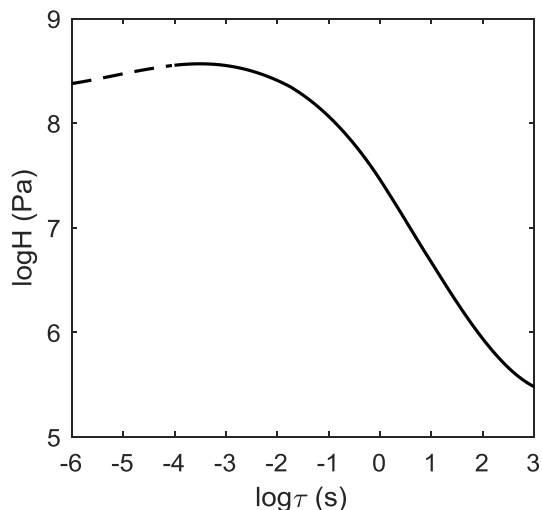


Figure A.12 The relaxation spectrum determined from superposed  $E'$  and  $E''$  master curves shown in Figure A.11.

### D3. Polybutadiene, PBd

The linear viscoelastic behavior of two linear polybutadienes (PBd-1 and PBd-2) with different amounts of cis/trans content (see Table A.4) have been reported,[4] where the molecular weight and fraction of 1,2-addition units were tuned so that the entanglement plateaus have similar frequency range.

The digitized  $G'$  and  $G''$  isotherms for PBd-1 were shifted using the  $\log a_T$  shift function reported in the original paper[4] to match  $G''$  peak at all temperatures except for  $T = 278\text{K}$ . Shift factor at 278 K was chosen to superpose high-frequency part of  $G''$  isotherm. Shift factors at 262 – 268 K were the same as reported in the original paper [4] which were fit by VFT equation with  $A_\alpha = 1.023 \times 10^{-18}$  s,  $B_\alpha = 1601\text{K}$ . The resulting master curves are shown in Figure A.13. Good superposition was achieved both at low and high temperatures, i.e. in the  $\alpha$  and terminal regions, but the material exhibits thermo-rheological complexity between  $\alpha$  and terminal regions. The low-



frequency data at 278 K are scattered, because the data were plotted on a linear scale and cannot be accurately retrieved by digitization. The relaxation spectrum was determined from the approximate master curves in Figure A.13 using the methodology given in SI.2 and is shown in Figure A.14.

Table A.4 Characteristics of two polybutadiene samples.

	$M_w$ (kg/mol)	$M_w/M_n$	1,2 (mol %)	<i>Trans</i> -1,4 (mol %)	<i>Cis</i> -1,4 (mol %)	$T_g$ (°C)
PBd-1	80.1	1.03	94	6% in total of <i>trans/cis</i> -1,4		-4
PBd-2	38.7	1.04	7	56	37	-82

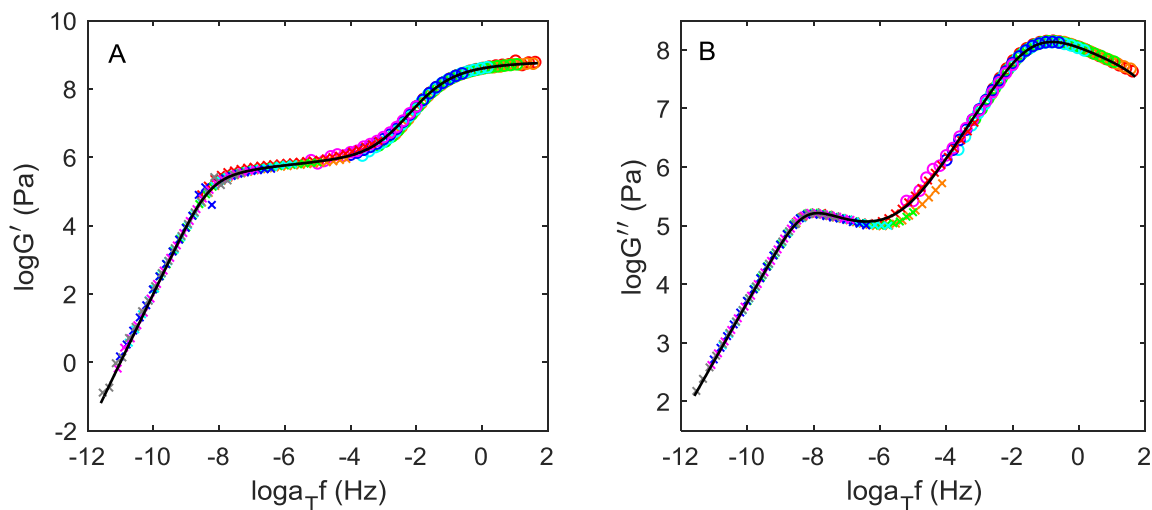


Figure A.13 Approximate master curves of  $G'$  (A) and  $G''$  (B) shifted to  $T_{\text{ref}} = 225.6$  K ( $T_g - 43.4$ K) for PBd-1 consisting isotherms at the following temperatures: 262K (○), 263K (○), 264K (○), 266K (○), 268K (○), 278K (○), 285K (×), 293K (×), 303K (×), 313K (×), 323K (×), 333K (×), 343K (×). Shift factors were reported in the original paper.[4] Lines are predicted relaxation behaviors using spectrum shown in Figure A.14.

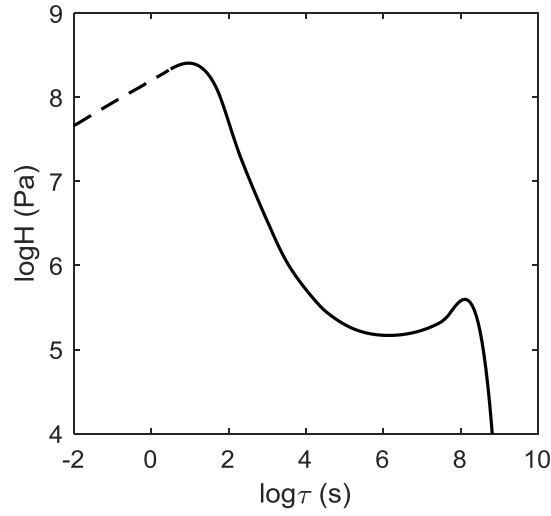


Figure A.14 Relaxation spectrum for PBd-1 determined based on the approximate  $G'$  and  $G''$  master curves shown in Figure A.13.

The other specimen “PBd-2” with a lower molecular weight and lower percentage of 1,2-structures are also investigated. Digitized  $G'$  and  $G''$  isotherms for PBd-2 were shifted using the shift factors given in the original reference.[4] The values of  $\log a_T$  were chosen to match  $G''$  peaks in  $\alpha$  and plateau regions at all temperatures except  $T=187\text{K}$ . Shift factors used from 176K to 180K were the same as those reported in the original paper[4] and could be fit by VFT equation with  $A_\alpha = 3.311 \times 10^{-16} \text{ s}$  and  $B_\alpha = 1374\text{K}$ . Resulting master curves are shown in Figure A.15. Similar to PBd-1, good superposition was found for PBd-2 within  $\alpha$  and terminal regions, but isotherms between  $\alpha$  and terminal regions are showing lack of superposition. Low-frequency data at 187 K are scattered as they were plotted in linear scale and could not be accurately digitized. The relaxation spectrum is shown in Figure A.16.

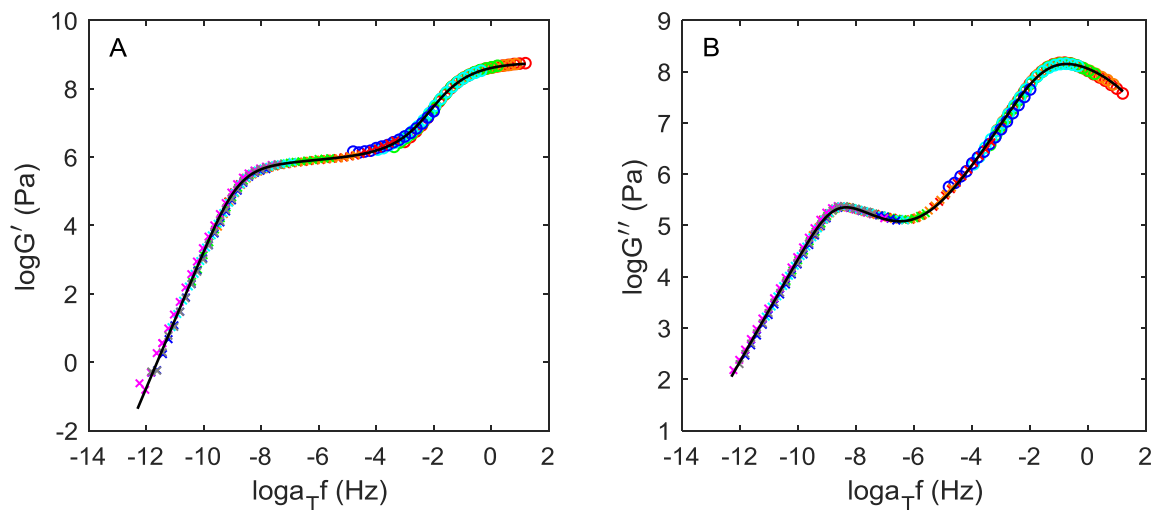


Figure A.15 Approximate master curves of  $G'$  (A) and  $G''$  (B) shifted to  $T_{ref} = 138.1$  K ( $T_g = 42.9$  K) for PBd-2 consisting isotherms at the following temperatures: 176K (○), 177K (○), 178K (○), 180K (○), 187K (○), 197K (×), 208K (×), 218K (×), 228K (×), 233K (×), 238K (×), 248K (×). Lines are predicted relaxation behaviors using spectrum shown in Figure A.16.

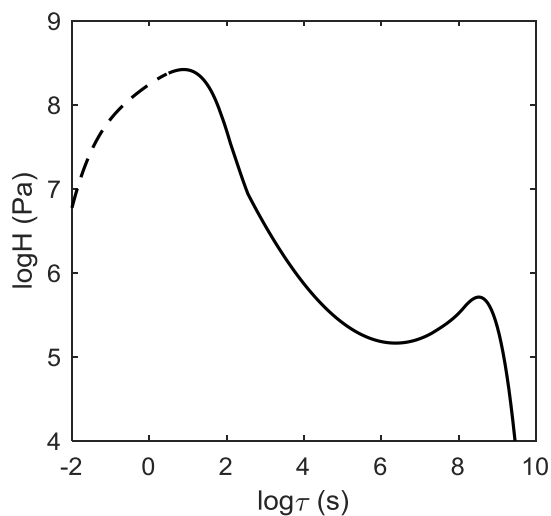


Figure A.16 Relaxation spectrum of PBd-2 determined based on the approximate  $G'$  and  $G''$  master curves shown in Figure A.15.

#### D4. Poly(propylene oxide), PPO

The dynamic mechanical and dielectric responses for linear and star-shaped poly(propylene oxide) of different molecular weights were reported.[5] The data was fit by the linear sum of four KWW stretched exponential functions that were identified as the terminal, segmental, slow  $\beta$  and fast  $\beta$  relaxation processes, where a decoupling between segmental and terminal relaxation processes were reported on dielectric spectroscopic data. The relaxation times in the four empirical KWW functions had the same VTF[5] temperature dependence for both shear and dielectric responses of all investigated materials. The only full linear viscoelastic dataset reported was the  $G'$  and  $G''$  master curves for a linear PPO of  $M_n = 11\text{kg/mol}$ ,  $T_g = 205\text{K}$  that was determined by time-temperature superposition of isotherms from 200 and 340 K with respect to  $T_{\text{ref}} = 218\text{K}$ . In Figure A.17 digitized master curves are shown as well as the fit using the spectrum. The relaxation spectrum was determined from the master curves in Figure A.17 using the methodology given in SI.2 and is shown in Figure A.18.

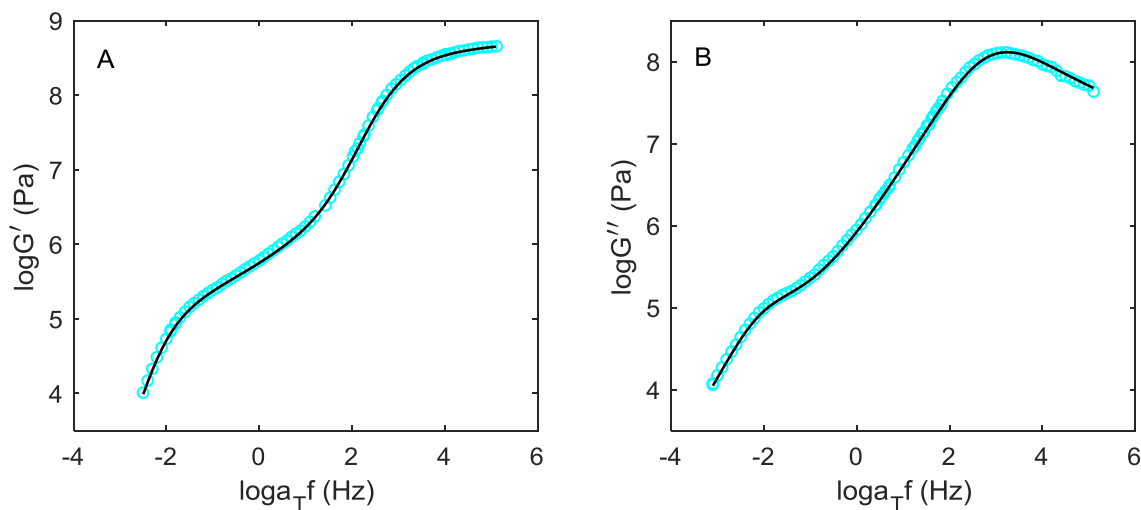


Figure A.17 Digitized master curve of  $G'$  (A) and  $G''$  (B) for poly(propylene oxide) of  $M_n = 11\text{ kg/mol}$  with respect to  $T_{\text{ref}} = 218\text{K}$ . [5] Lines are predicted relaxation behaviors using spectrum shown in Figure A.18.

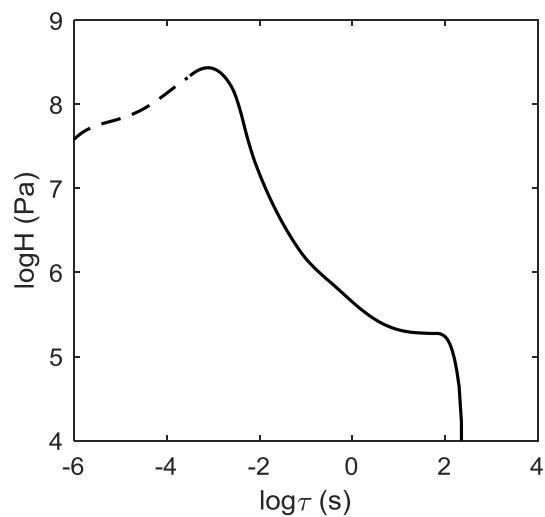


Figure A.18 Relaxation spectrum for PPO determined from master curves given in Figure A.17.

#### D5. Oligomer of $\alpha$ -methyl styrene, O $\alpha$ MS

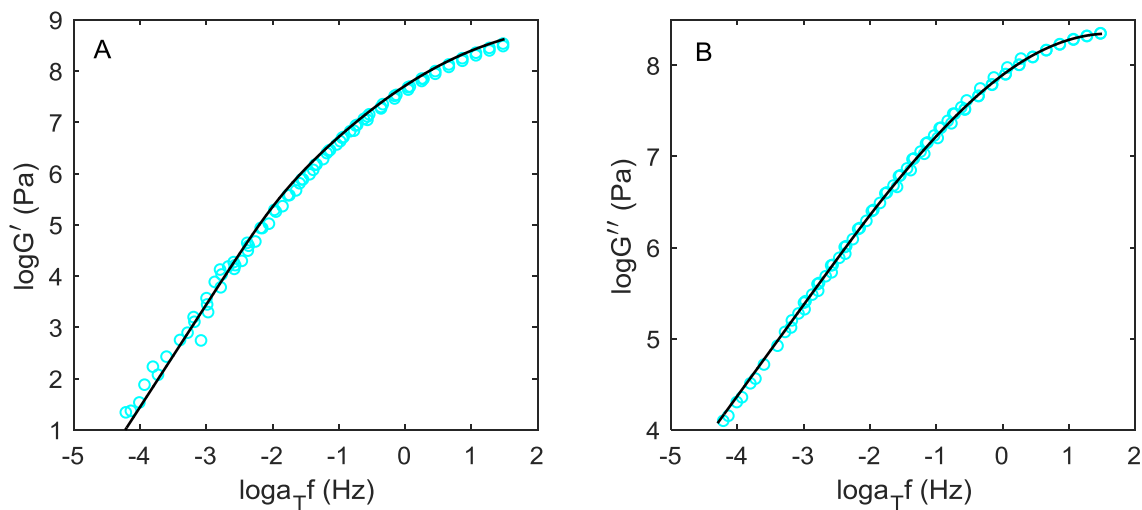


Figure A.19 Master curve of  $G'$  (A) and  $G''$  (B) for poly( $\alpha$ -methyl styrene) of  $M_n = 769$  g/mol with respect to  $T_{ref} = 47$  °C. Lines are predicted relaxation behaviors using spectrum shown in Figure A.20. Data are provided by Dr. S. Simon.

$G'$  and  $G''$  master curves of  $\alpha$ -methyl styrene hexamer (O $\alpha$ MS) of  $T_g = 37^\circ\text{C}$  were reported [6] and plotted in Figure A.19, where the  $G'$  data covered a remarkably large vertical range of 8 decades in Pa. Data were provided by Zheng et al.[6] In both  $G'$  and  $G''$  curves, typical terminal flow behaviors are observed below  $10^{-2}$  Hz with asymptotic slopes being  $\log G'/\log f = 2$  and  $\log G''/\log f = 1$ . Relaxation spectrum was constructed based on master curves and reported in Figure A.20.

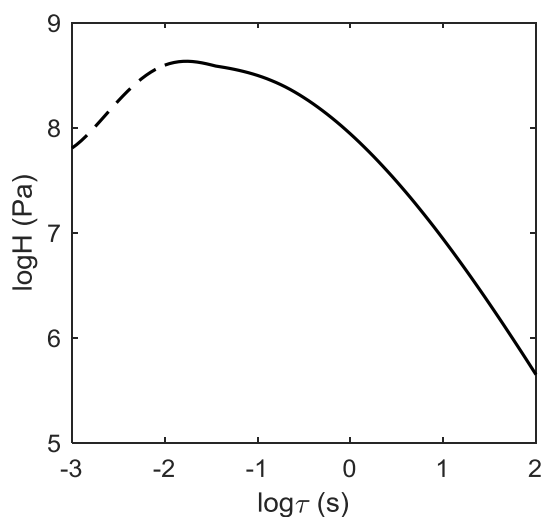


Figure A.20 Relaxation spectrum for O $\alpha$ MS determined from master curves given in Figure A.19.

## D6. Oligomer of isobutylene, OIB

$G'$  and  $G''$  isotherms at 216K for an oligomeric isobutylene with 11 repeat units are downloaded from an online database which had also been reported by Jakobsen et al.[7] In the original dataset, frequency-dependent responses were given from 198 K ( $T_g+3\text{K}$ ) to 234 K ( $T_g+39\text{K}$ ) measured using a piezoelectric shear gauge that converts capacitance to modulus and thus possessing a much wider frequency range compared to torsional pendulum instruments. The frequency range was over 6 orders of magnitude, which allowed  $\alpha$  process to be observed at each tested temperature. The  $G''$  peak associated with  $\alpha$  relaxation was clearly changing with temperature, indicating thermorheological complexity. The isotherms at 216K was chosen for analysis as it exhibits richest viscoelastic behaviors in transition zone. Isotherms at higher temperatures had shorter frequency

range since they stopped at  $G' = 10^5$  Pa. Isotherms at lower temperatures had less data on the left side of the  $\alpha$  peak in  $G''$ , i.e., less data above  $T_g$ . As plotted in Figure A.21, asymptotic Rouse behaviors are observed at the lowest frequency ( $f < 10^{-1}$  Hz). Based on the isotherm at 216K, relaxation spectrum was determined and plotted in Figure A.22.

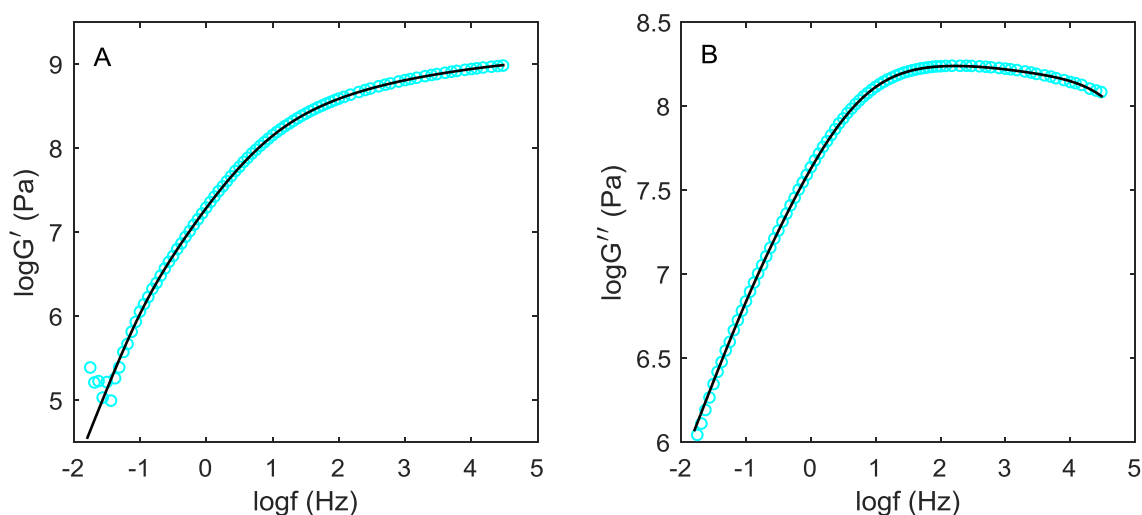


Figure A.21  $G'$  (A) and  $G''$  (B) isotherms at 216K for isobutylene oligomer,  $M_w = 680$  g/mol,  $M_w/M_n=1.06$ ,  $T_g = 195$  K. Lines are predicted relaxation behaviors using spectrum shown in Figure A.22. Data are downloaded from a “Glass and Time” online database (<http://glass.ruc.dk/data>).

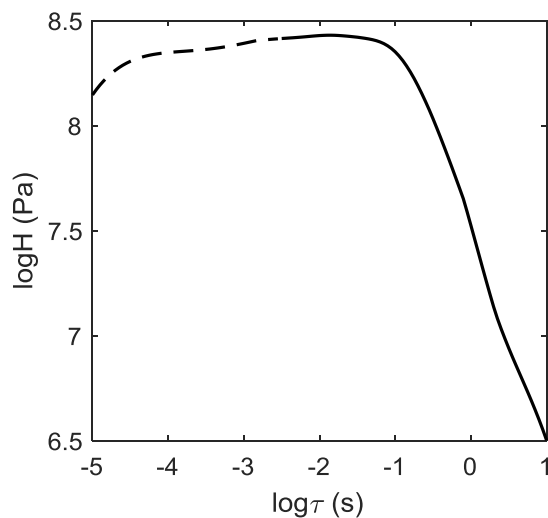


Figure A.22 Relaxation spectrum for OIB determined from isotherms given in Figure A.21.

## D7. Oligomer of styrene, OS

$G'$  and  $G''$  master curves for a styrene oligomer of 9 repeating units ( $M_w = 1050$  g/mol,  $M_w/M_n=1.13$ ,  $T_g = 8.8$  °C) were digitized from Inoue et al.[8] Master curves were plotted in Figure A.23 and were constructed from isotherms measured from 5 °C ( $T_g-4$ °C) to 30 °C ( $T_g+21$ °C) shifted to  $T_{ref} = 25$  °C ( $T_g+16$ °C).  $G'$  data near  $10^2$  Hz were obscured in the original figure and hence not possible to digitize. Relaxation spectrum was determined and given in Figure A.24, while the predicted  $G'$  and  $G''$  behaviors were plotted in Figure A.23.

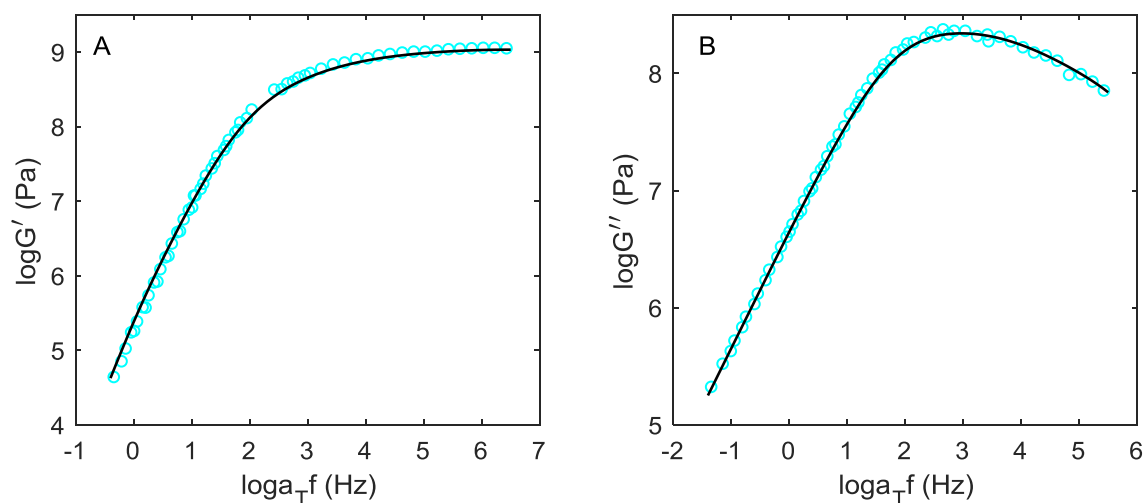


Figure A.23 Digitized  $G'$  (A) and  $G''$  (B) master curves [8] for styrene oligomer,  $M_w = 1050$  g/mol,  $M_w/M_n=1.13$ ,  $T_g = 8.8$  °C. Data were measured from 5 °C to 30 °C and shifted to  $T_{ref}=25$ °C. Solid lines are predicted relaxation behaviors using spectrum shown in Figure A.24.



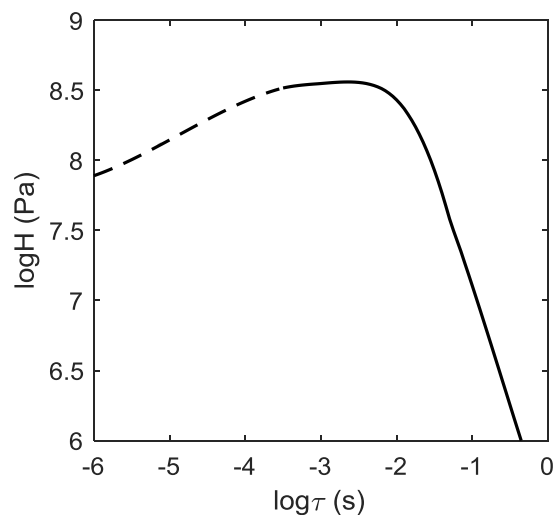


Figure A.24 Relaxation spectrum for OS determined from master curves given in Figure A.23.

#### D8. Three-Armed Star Polystyrene, 3AS-PS

$G'$  and  $G''$  behaviors of a three-armed, star-shape polystyrene were reported by Guo et al.[9] Each PS branch has a molecular weight of  $M_w = 117.5$  kg/mol and distribution of  $M_w/M_n = 1.07$ .  $T_g$  of the three-armed PS is  $98.2^\circ\text{C}$ ,  $1^\circ\text{C}$  lower than  $T_g$  of a linear PS of  $M_w = 221$  kg/mol. Isotherms and shift factors were digitized and used to construct the master curves plotted in Figure A.25. ( $T_{\text{ref}} = 93.8^\circ\text{C}$ ) The shift factors were fit by WLF equation with  $C_1 = 18.2$  and  $C_2 = 42.8\text{K}$ . [9] Relaxation spectrum was determined based on master curves and plotted in Figure A.26. The fit to master curves using the spectrum is good as shown in Figure A.25. A peak at  $\tau = 10^{10}\text{s} - 10^{12}\text{s}$  in the spectrum is consistent with the presence of a plateau around  $f = 10^{-10}\text{Hz} - 10^{-12}\text{Hz}$  in the master curve. This small relaxation peak at a high temperature is possibly associated with entanglement of the long-branching chains.

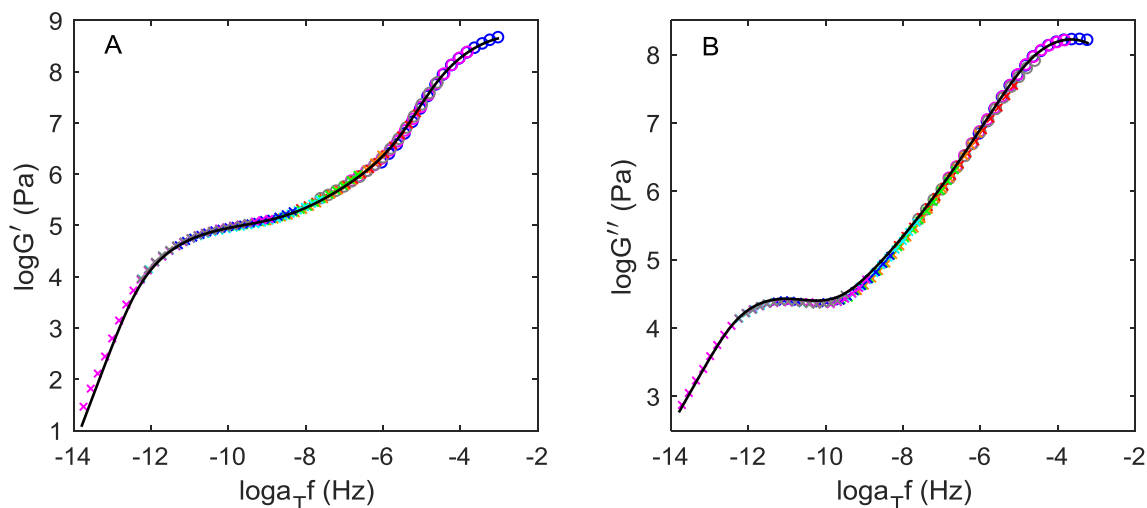


Figure A.25 Approximate master curves of  $G'$  (A) and  $G''$  (B) shifted to  $T_{\text{ref}} = 93.8^\circ\text{C}$  ( $T_g - 4.4^\circ\text{C}$ ) for 3-armed PS consisting isotherms of the following temperatures:  $110^\circ\text{C}$  ( $\circ$ ),  $113.5^\circ\text{C}$  ( $\circ$ ),  $117^\circ\text{C}$  ( $\circ$ ),  $120^\circ\text{C}$  ( $\times$ ),  $125^\circ\text{C}$  ( $\times$ ),  $130^\circ\text{C}$  ( $\times$ ),  $140^\circ\text{C}$  ( $\times$ ),  $150^\circ\text{C}$  ( $\times$ ),  $160^\circ\text{C}$  ( $\times$ ),  $170^\circ\text{C}$  ( $\times$ ). Shift factors were digitized. Lines are predicted relaxation behaviors using spectrum shown in Figure A.26.

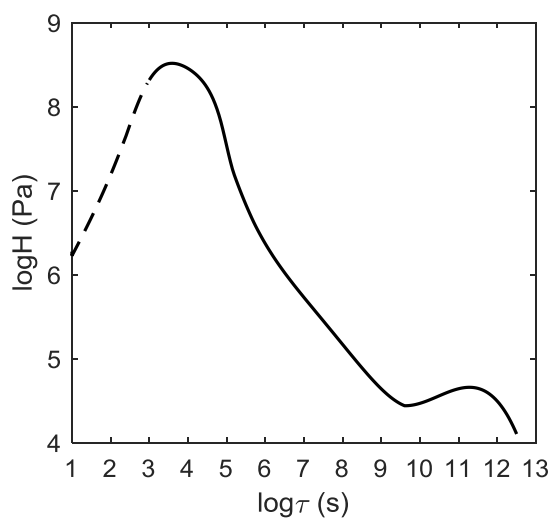


Figure A.26 Relaxation spectrum for 3-armed PS determined based on the approximate  $G'$  and  $G''$  master curves shown in Figure A.25.

## D9. Dendrimers of Poly(propyleneimine), D-PPI

The frequency-dependent dynamic shear responses for 2<sup>nd</sup> to 5<sup>th</sup> generation dendrimers of polypropyleneimine (D-PPI) and linear polypropyleneglycol (PPG) polymers of different MWs were measured by Hofmann et al[10] and compared to dielectric and FC NMR spectroscopy data.  $G'$  and  $G''$  master curves for PPI and PPG of different MWs were compared on the same figure by horizontal shifting to align their glassy-state  $G'_{\max}$ . Master curves included a wide frequency range above  $T_g$  where typical behaviors in glassy, transition and terminal zones were observed. All materials in their terminal zones (i.e., at low-frequency end) show asymptotic behaviors where  $\log G'/\log f=2$  and  $\log G''/\log f=1$ . As MW increases, linear PPGs show wider plateau regions where  $G' \sim G'_{\max}/1000$  between transition and terminal zones; whereas for dendrimers D-PPI as the number of generation increases, a dispersion of  $\alpha$  peak in transition zone emerges where  $G' > G'_{\max}/1000$ . Specifically, in transition zone  $G'$  and  $G''$  curves of all linear PPGs and the 2<sup>nd</sup>-generation D-PPI were overlapping with a slope of  $\log G'/\log f=0.6$  and  $\log G''/\log f=0.6$ , while curves of 3<sup>rd</sup>, 4<sup>th</sup> and 5<sup>th</sup> generation D-PPI were exhibiting  $\log G'/\log f=0.7$  and  $\log G''/\log f=0.7$ , i.e.,  $G'$  and  $G''$  were decreasing with frequency (or temperature) more slowly.

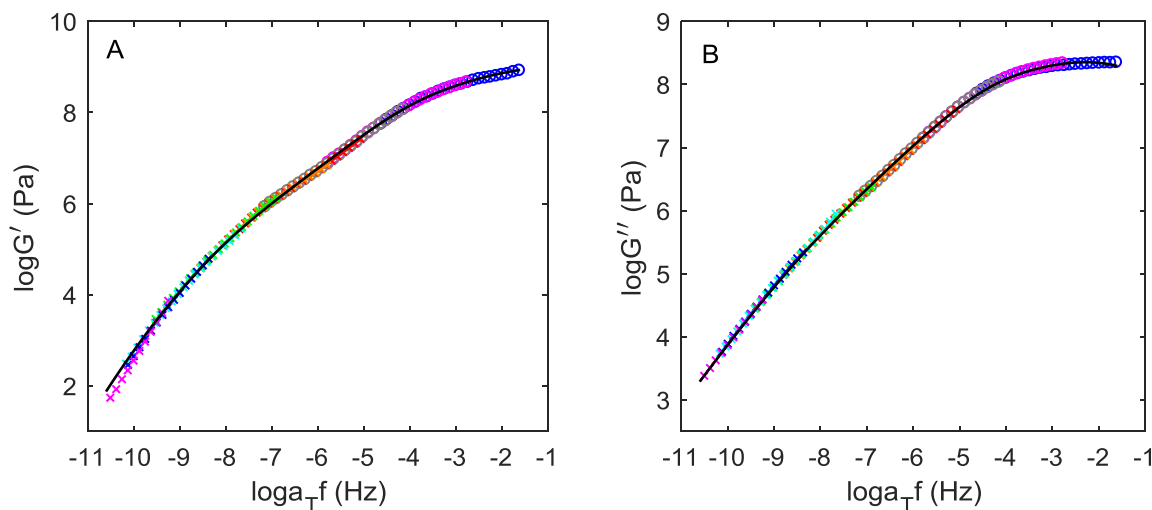


Figure A.27 Approximate master curves of  $G'$  (A) and  $G''$  (B) shifted to  $T_{\text{ref}} = 205\text{K}$  ( $T_g+5\text{K}$ ) for D-PPI consisting isotherms at the following temperatures: 215K (○), 220K (◐), 227.5K (○), 235K (×), 242.5K (×), 250K (×), 265K (×), 280K (×), 300K (×). Shift factors were digitized. Lines are predicted relaxation behaviors using spectrum shown in Figure A.28.

Digitized isotherms from 205 K ( $T_g+5K$ ) to 300 K ( $T_g+100K$ ) for the 5<sup>th</sup>-generation D-PPI were shifted using the digitized  $\log a_T$  shift factors. Resulting master curves are shown in Figure A.27 with respect to  $T_{ref} = 205K$ . Relaxation spectrum calculated based on the master curves is given in Figure A.28.

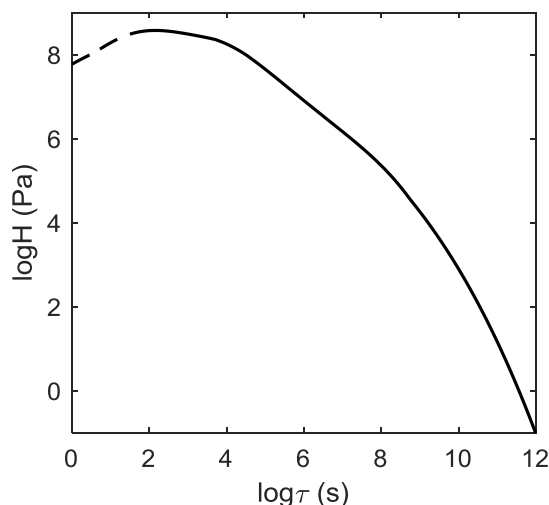


Figure A.28 Relaxation spectrum for D-PPI determined based on the approximate  $G'$  and  $G''$  master curves shown in Figure A.27.

#### D10. *m*-Toluidine

Two sets of  $G'$  and  $G''$  behaviors of a molecular glass former *m*-toluidine were measured by two research groups using different techniques.[11, 12] The first set of  $G'$  and  $G''$  isotherms were downloaded from an online database “Glass and Time: Data repository”, <http://glass.ruc.dk/data> measured using a piezoelectric shear-modulus gauge capable of probing dynamic shear moduli over a wide frequency range ( $10^{-3} - 10^4$  Hz). Responses in  $\alpha$  relaxation region were compared across test temperatures from 186 K ( $T_g-1K$ ) to 198 K ( $T_g+11K$ ). Shift factors were calculated by matching  $G''$  peaks. Despite a change in height of  $G'$  glass plateau and  $G''$  peak values, superposition was applied to construct approximate master curves as shown in Figure A.29.  $G'$  below  $10^6$  Pa exhibit scattering and inconsistencies among isotherms. The spectrum shown in Figure A.30 was obtained based on approximate master curves.

A second dataset[12] of  $G'$  and  $G''$  isotherms of m-toluidine from 186K ( $T_g-1K$ ) to 192K ( $T_g+5K$ ) were digitized along with  $\log a_T$  shift factors and used to create the master curves shown in Figure A.31, based on which the relaxation spectrum was calculated given in Figure A.32.

In both datasets a clear terminal relaxation with asymptotic behaviors is found in all isotherms. Both relaxation spectra exhibit a narrow dispersion of  $\alpha$  peak at the long-time side, i.e., no  $\alpha+$  region.

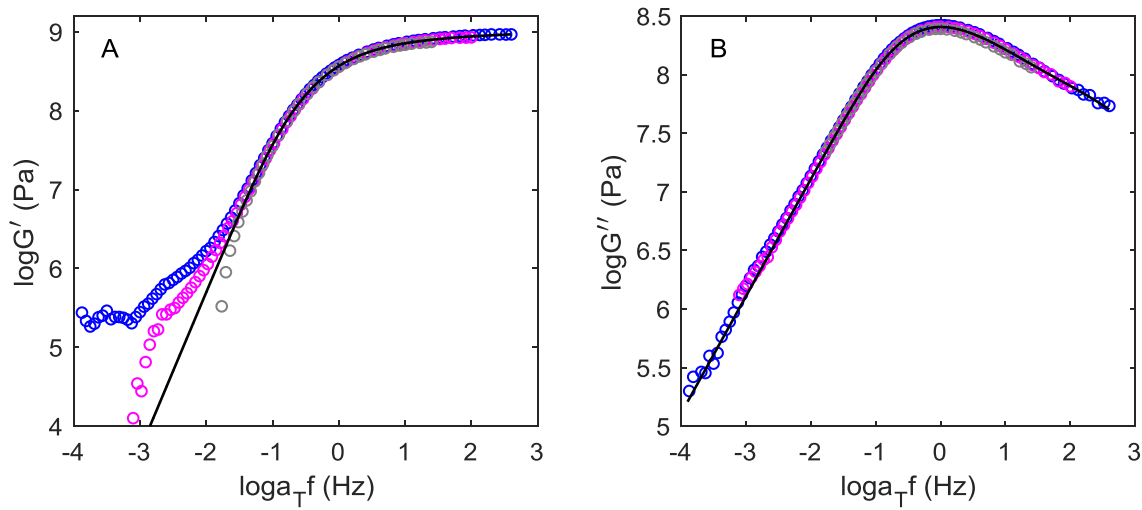


Figure A.29 Approximate master curves of  $G'$  (A) and  $G''$  (B) shifted to  $T_{ref} = T_g = 187K$  for m-toluidine consisting isotherms at the following temperatures: 194K ( $\circ$ ), 196K ( $\circ$ ), 198K ( $\circ$ ).

Data were reported by Maggi et al[11] and downloaded from a “Glass and Time” online database”. Shift factors were obtained by matching  $G''$  peak. Lines are predicted relaxation behaviors using spectrum shown in Figure A.30.

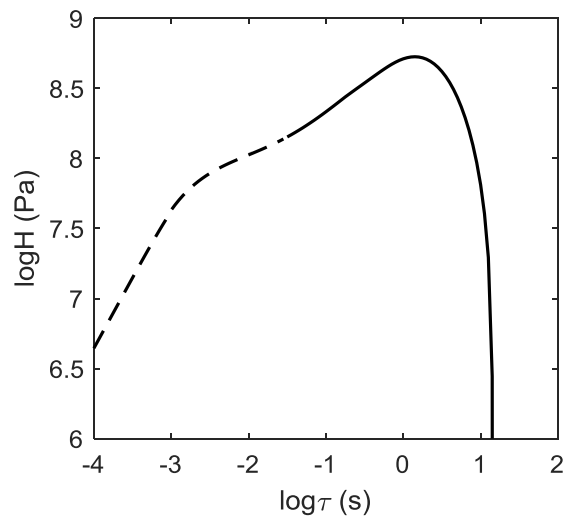


Figure A.30 Relaxation spectrum for m-toluidine determined based on the approximate  $G'$  and  $G''$  master curves shown in Figure A.29.

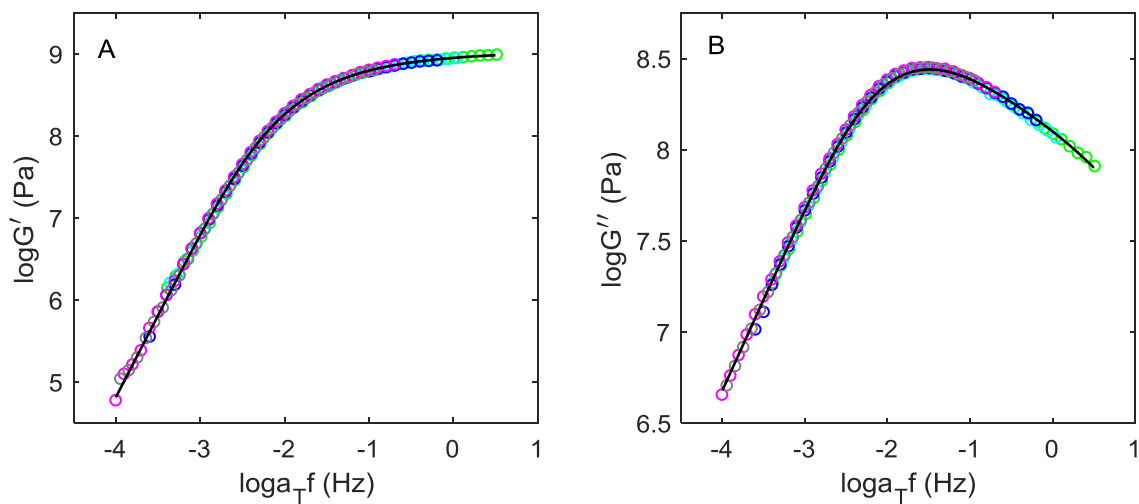


Figure A.31 Approximate master curves of  $G'$  (A) and  $G''$  (B) shifted to  $T_{\text{ref}} = T_g = 187\text{K}$  for m-toluidine consisting of isotherms at the following temperatures: 188K (●), 189K (●), 190K (●), 191K (●), 192K (●). Shift factors were digitized from Ref. [12]. Lines are predicted relaxation behaviors using spectrum shown in Figure A.32.

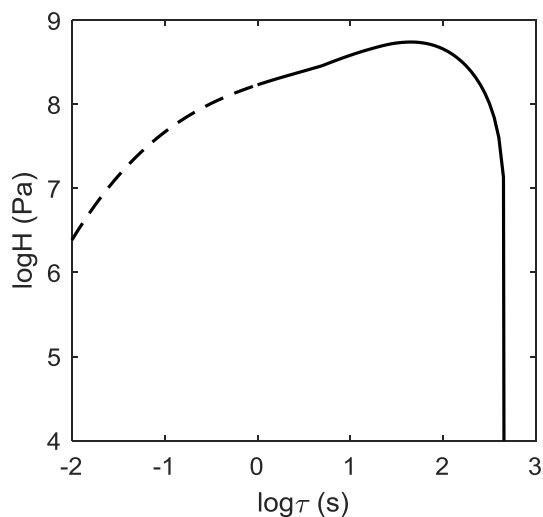


Figure A.32 Relaxation spectrum for m-toluidine determined based on the approximate  $G'$  and  $G''$  master curves shown in Figure A.31.

#### D11. Sucrose Benzoate

Shear moduli isotherms for sucrose benzoate from 335K ( $T_g-2K$ ) to 347K ( $T_g+10K$ ) reported by Hutcheson and McKenna[12] were digitized along with  $\log a_T$  shift factors and used to construct the master curves plotted in Figure A.33. The DSC  $T_g$  was 337K determined by a 10 K/min heating scan after dehydration in a vacuum oven at 140 °C. Relaxation spectrum determined based on master curves is shown in Figure A.34. The spectrum exhibits an abrupt end (i.e. narrow transition zone) and no  $\alpha+$  process.

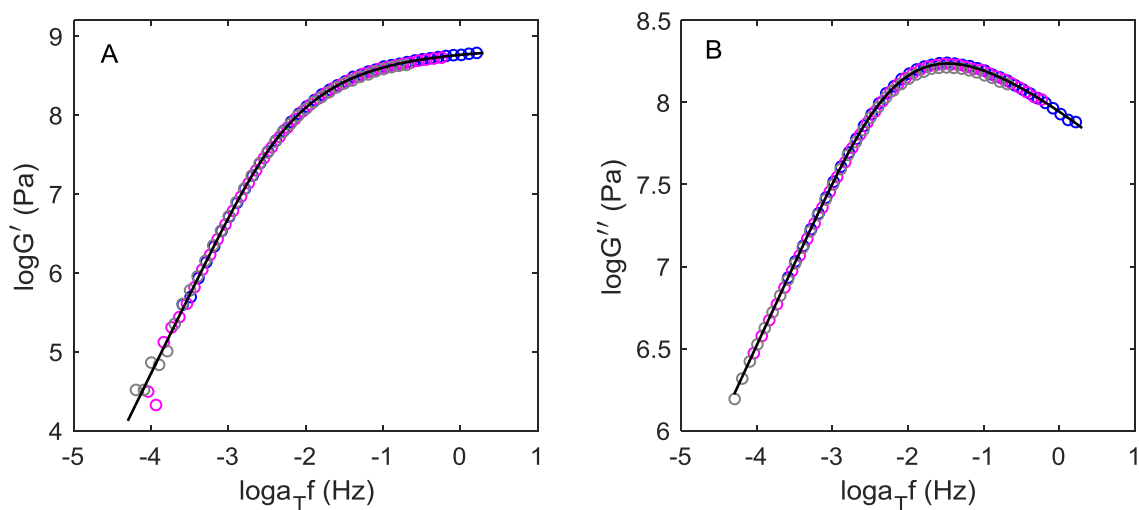


Figure A.33 Approximate master curves of  $G'$  (A) and  $G''$  (B) shifted to  $T_{\text{ref}} = T_g = 337\text{K}$  for sucrose benzoate consisting isotherms at the following temperatures: 343K ( $\circ$ ), 345K ( $\circ$ ), 347K ( $\circ$ ). Shift factors were digitized from Ref. [12]. Lines are predicted relaxation behaviors using spectrum shown in Figure A.34.

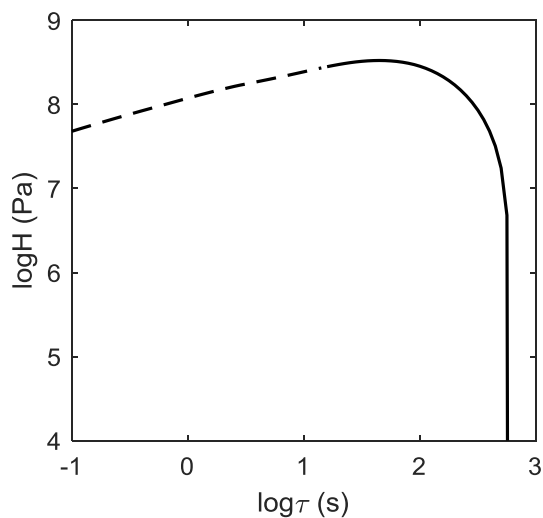


Figure A.34 Relaxation spectrum for sucrose benzoate determined based on the approximate  $G'$  and  $G''$  master curves shown in Figure A.33.



## D12. References

1. Ferry, J.D., *Viscoelastic Properties of Polymers*. 3<sup>rd</sup> ed. 1980, New York: John Wiley and Sons. 641.
2. Curliss, D.B., *Linear and Nonlinear Viscoelastic Behavior of a Series of DGEBA Epoxy Resins*. 1987, Purdue University: West Lafayette, IN. p. 416.
3. Alves, N.M., et al., *Viscoelastic Behavior of Poly(methyl methacrylate) Networks with Different Cross-Linking Degrees*. *Macromolecules*, 2004. **37**(10): p. 3735-3744.
4. Robertson, C.G. and C.M. Rademacher, *Coupling Model Interpretation of Thermorheological Complexity in Polybutadienes with Varied Microstructure*. *Macromolecules*, 2004. **37**(26): p. 10009-10017.
5. Nicolai, T. and G. Floudas, *Dynamics of Linear and Star Poly(oxypropylene) Studied by Dielectric Spectroscopy and Rheology*. *Macromolecules*, 1998. **31**(8): p. 2578-2585.
6. Zheng, W., G.B. McKenna, and S.L. Simon, *The viscoelastic behavior of polymer/oligomer blends*. *Polymer*, 2010. **51**(21): p. 4899-4906.
7. Jakobsen, B., et al., *Beta relaxation in the shear mechanics of viscous liquids: Phenomenology and network modeling of the alpha-beta merging region*. *Journal of Non-Crystalline Solids*, 2011. **357**(2): p. 267-273.
8. Inoue, T., et al., *Viscoelasticity of low molecular weight polystyrene. Separation of rubbery and glassy components*. *Journal of Polymer Science Part B: Polymer Physics*, 1999. **37**(4): p. 389-397.
9. Guo, J., L. Grassia, and S.L. Simon, *Bulk and shear rheology of a symmetric three-arm star polystyrene*. *Journal of Polymer Science Part B: Polymer Physics*, 2012. **50**(17): p. 1233-1244.
10. Hofmann, M., et al., *Field-Cycling Relaxometry as a Molecular Rheology Technique: Common Analysis of NMR, Shear Modulus and Dielectric Loss Data of Polymers vs Dendrimers*. *Macromolecules*, 2015. **48**(20): p. 7521-7534.
11. Maggi, C., et al., *Supercooled Liquid Dynamics Studied via Shear-Mechanical Spectroscopy*. *The Journal of Physical Chemistry B*, 2008. **112**(51): p. 16320-16325.
12. Hutcheson, S.A. and G.B. McKenna, *The measurement of mechanical properties of glycerol, m-toluidine, and sucrose benzoate under consideration of corrected rheometer compliance: An in-depth study and review*. *Journal of Chemical Physics*, 2008. **129**: p. 074502.

## APPENDIX E. OTHER MECHANICAL DATASETS OF GLASS-FORMING MATERIALS INVESTIGATED

Table A.5 Other mechanical datasets available for amorphous polymers but not included in Chapter 3.

Polymer	Data source limitation	Ref.
PMMA	For samples of various MW and tacticity, reported $G'$ , $G''$ data are in entanglement plateau and flow region only.	[1]
PMMA	Data in terminal flow region only.	[2]
PEMA	Symbols on the master curves covered. Figure of poor quality. Cannot digitize accurately.	[3]
PVAc	Data in the glassy region only.	[4]
PVAc	$J(t)$ isotherms and $L$ spectrum reported. Dynamic data re-calculated from spectrum but not directly measured.	[5]
PVAc	Reported $G$ of arbitrary unit. Unable to retrieve raw $G^*$ data.	[6]
PPS	Symbols on the master curves covered. Cannot digitize accurately. Data may be trimmed to construct a smooth master curve.	[7, 8]
Polyhexene-1	$G'$ , $G''$ data in $\alpha$ region are of poor quality. Cannot determine the location of main $\alpha$ peak.	[9]
PBd	Cannot digitize accurately.	[10]
PBd	Data in terminal region only. Cannot determine the location of main $\alpha$ peak.	[11]
PBd	Figure of poor quality. Cannot digitize accurately.	[12]
PS	Data in plateau and terminal flow regions only. Cannot determine the location of main $\alpha$ peak.	[13]
PS	Data and spectrum in plateau and terminal flow regions only.	[14-16]
PS	Data in terminal flow region only.	[17,18]
PS	$G''/G''_{max}$ are reported. No $G'$ data.	[19]
PIB	Creep $J(t)$ isotherms in terminal zone only. $J'$ , $J''$ are measured with Bohlin VOR rheometer but test results are given as lines without data points.	[20]
PIB	Data in plateau and terminal flow regions only.	[21]
PIB	Figure of poor print quality. Cannot digitize accurately.	[22]
PIB	Data in terminal flow region only. No loss component.	[23]
PIB	Data obtained in temperature scans.	[24]
PIP	$E''/E''_{max}$ master curves are reported. No $E'$ data.	[25]
PIP	$G'$ , $G''$ data in plateau and terminal flow regions only.	[26]
PIP	Symbols on the master curves covered. Cannot digitize accurately.	[27]
aPP	Reported $G''$ master curve as an insert that only contains data in $\alpha$ region. Cannot digitize accurately.	[28, 29]
aPP	Data in plateau and terminal flow regions only.	[30]
PVC	Data and spectrum of large uncertainty due to lack of constrain. Each isotherm contains 2 – 4 data points / decade of frequency.	[31]
PVC	Test results are given as lines without data points. Cannot digitize.	[32]
PVC	Samples are gels containing <10% polymer.	[33]
PDMS	Data in plateau and terminal flow regions only.	[16, 34, 35]

PDMS	Data in plateau and terminal flow regions only.	[30]
PDMS	Data in plateau and terminal flow regions only.	[35]
PMPS	G'' data in the T <sub>g</sub> region only. No G' data.	[36]
PC	Data obtained in transient experiments (torsional creep and stress relaxation) for BPA-PC.	[37]
PC	Data obtained in temperature scans at 3 fixed frequencies for BPA-PC.	[38, 39]
PC	Data in plateau and terminal flow regions only.	[40, 41]
PC	Samples are blends. Data obtained in temperature scans.	[42, 43]
PC	Symbols on the master curves covered. Cannot digitize accurately. Each isotherm contains 5 data points only.	[44]
Phenoxy, PC, PAr, PSF	E', E'' master curves in $\alpha$ region only. G', G'' master curves in plateau and terminal flow regions only. Cannot digitize accurately.	[45]
PSF	Cannot determine the location of main $\alpha$ peak. Symbols on the master curves too large. Cannot digitize accurately.	[46, 47]
PSF	Data obtained in temperature scans.	[48]
PA	Polyamide samples of single and bimodal (i.e. two peaks) MW distribution. G(t) isotherms and spectra are reported, but H values are 3 orders of magnitude lower than G(t).	[49]
SAN	Data mostly in plateau and terminal flow regions except for 5 data points in $\alpha$ region. Cannot determine the location of main $\alpha$ peak.	[50]
PET	Data obtained in temperature scans at 6 fixed frequencies.	[51]
PET, PEI, PHMT, PNMT	PET annealed at 70, 80, 120C, PEI, PHMT, PNMT: only E'' isotherms reported; PET annealed at 200C: both E', E'' isotherms reported but the specimen has a high crystallinity (55.8%)	[52]
PET	Master curves are scattering. Figure of poor print quality.	[53]
PET	Data obtained in temperature scans.	[54]
Methyl-PEEK	Data in plateau and terminal flow regions only.	[55]
EPON/DDS	Data obtained in transient experiments (creep) for crosslinked EPON resins.	[56, 57]
Butyl rubber	Symbols on the master curves covered. Cannot digitize accurately.	[58]
SBS	D', D'' in rubbery plateau and terminal flow regions only.	[59]
EPDM	Noncrystalline rubber networks of ethylene, propylene and a diene monomer. Data in plateau and terminal flow regions only.	[60]
EPDM, PBd	Data in plateau and terminal flow regions only.	[61]
PU	Data in terminal and a small part of transition regions. Cannot determine the location of main $\alpha$ peak.	[62]
PU	Linear and network PU. Data may be trimmed to construct a smooth master curve.	[63]
PU	Symbols on the master curves covered. Cannot digitize accurately. Cannot determine the location of main $\alpha$ peak.	[64]
PS solution	NBS nonlinear test fluid #1. Data obtained in transient experiments.	[65]

## Reference

1. Fuchs, K., C. Friedrich, and J. Weese, *Viscoelastic properties of narrow-distribution poly (methyl methacrylates)*. *Macromolecules*, 1996. **29**(18): p. 5893-5901.
2. Kopesky, E.T., et al., *Thermomechanical properties of poly (methyl methacrylate) s containing tethered and untethered polyhedral oligomeric silsesquioxanes*. *Macromolecules*, 2004. **37**(24): p. 8992-9004.
3. Wind, M., et al., *Structural Reasons for Restricted Backbone Motion in Poly (n - alkyl methacrylates): Degree of Polymerization, Tacticity and Side - Chain Length*. *Macromolecular Chemistry and Physics*, 2005. **206**(1): p. 142-156.
4. Kovacs, A., R.A. Stratton, and J.D. Ferry, *Dynamic mechanical properties of polyvinyl acetate in shear in the glass transition temperature range*. *The Journal of Physical Chemistry*, 1963. **67**(1): p. 152-161.
5. Plazek, D.J., *The temperature dependence of the viscoelastic behavior of poly (vinyl acetate)*. *Polymer Journal*, 1980. **12**(1): p. 43-53.
6. Wu, X. and Z. Zhu, *Dynamic crossover of  $\alpha'$  relaxation in poly (vinyl acetate) above glass transition via mechanical spectroscopy*. *The Journal of Physical Chemistry B*, 2009. **113**(32): p. 11147-11152.
7. Nicol, E., D. Durand, and T. Nicolai, *Dynamics of end-linked poly (propylene sulfide)*. *Macromolecules*, 2001. **34**(1): p. 59-65.
8. Nicol, E., T. Nicolai, and D. Durand, *Dynamics of poly (propylene sulfide) studied by dynamic mechanical measurements and dielectric spectroscopy*. *Macromolecules*, 1999. **32**(22): p. 7530-7536.
9. Kurath, S.F., E. Passaglia, and R. Pariser, *Dynamic Mechanical Properties of Polyhexene - I*. *Journal of Applied Physics*, 1957. **28**(4): p. 499-502.
10. Zorn, R., et al., *Rheological investigation of polybutadienes having different microstructures over a large temperature range*. *Macromolecules*, 1995. **28**(25): p. 8552-8562.
11. Baurngaertel, M., et al., *The relaxation time spectrum of nearly monodisperse polybutadiene melts*. *Rheologica Acta*, 1992. **31**(1): p. 75-82.
12. Colby, R.H., L.J. Fetters, and W.W. Graessley, *The melt viscosity-molecular weight relationship for linear polymers*. *Macromolecules*, 1987. **20**(9): p. 2226-2237.
13. Majeste, J.-C., et al., *Viscoelasticity of low molecular weight polymers and the transition to the entangled regime*. *Rheologica acta*, 1998. **37**(5): p. 486-499.
14. Baumgaertel, M., A. Schausberger, and H. Winter, *The relaxation of polymers with linear flexible chains of uniform length*. *Rheologica Acta*, 1990. **29**(5): p. 400-408.
15. Schausberger, A., G. Schindlauer, and H. Janeschitz-Kriegl, *Linear elastico-viscous properties of molten standard polystyrenes*. *Rheologica acta*, 1985. **24**(3): p. 220-227.

16. Holly, E.E., et al., *Fourier transform mechanical spectroscopy of viscoelastic materials with transient structure*. Journal of non-newtonian fluid mechanics, 1988. **27**(1): p. 17-26.
17. Lipatov, Y.S., et al., *Viscoelastic properties of polystyrene–polycarbonate blends in melt*. Journal of Applied Polymer Science, 1981. **26**(2): p. 499-508.
18. Huang, C.-L., et al., *Effect of tacticity on viscoelastic properties of polystyrene*. Macromolecules, 2011. **44**(15): p. 6155-6161.
19. Santangelo, P. and C. Roland, *Molecular weight dependence of fragility in polystyrene*. Macromolecules, 1998. **31**(14): p. 4581-4585.
20. Plazek, D., et al., *Viscoelastic properties of polymers. 4. Thermorheological complexity of the softening dispersion in polyisobutylene*. Macromolecules, 1995. **28**(19): p. 6432-6436.
21. Pechhold, W., et al., *Mechanical and dielectric investigations of relaxations in polymers*. Die Makromolekulare Chemie: Macromolecular Chemistry and Physics, 1979. **3**(S19791): p. 247-275.
22. Fetters, L.J., W. Graessley, and A. Kiss, *Viscoelastic properties of polyisobutylene melts*. Macromolecules, 1991. **24**(11): p. 3136-3141.
23. Simmons, J., *A servo-controlled rheometer for measurement of the dynamic modulus of viscoelastic liquids*. Journal of Scientific Instruments, 1966. **43**(12): p. 887.
24. Wu, J., et al., *Confinement effect of polystyrene on the relaxation behavior of polyisobutylene*. Journal of Polymer Science Part B: Polymer Physics, 2010. **48**(20): p. 2165-2172.
25. Roland, C. and K. Ngai, *Segmental relaxation and molecular structure in polybutadienes and polyisoprene*. Macromolecules, 1991. **24**(19): p. 5315-5319.
26. Gotro, J. and W.W. Graessley, *Model hydrocarbon polymers: rheological properties of linear polyisoprenes and hydrogenated polyisoprenes*. Macromolecules, 1984. **17**(12): p. 2767-2775.
27. Santangelo, P. and C. Roland, *Temperature dependence of mechanical and dielectric relaxation in cis-1, 4-polyisoprene*. Macromolecules, 1998. **31**(11): p. 3715-3719.
28. Santangelo, P., K. Ngai, and C. Roland, *Temperature Dependence of Relaxation in Polypropylene and Poly (ethylene-co-propylene)*. Macromolecules, 1996. **29**(10): p. 3651-3653.
29. Roland, C., et al., *Temperature dependence of segmental and terminal relaxation in atactic polypropylene melts*. Macromolecules, 2001. **34**(18): p. 6159-6160.
30. Pearson, D.S., et al., *Rheological properties of poly (1, 3-dimethyl-1-butenylene) and model atactic polypropylene*. Macromolecules, 1988. **21**(2): p. 478-484.
31. Becker, G.W., *Mechanische Relaxationserscheinungen in nicht weichgemachten hochpolymeren Kunststoffen*. Kolloid-Zeitschrift, 1955. **140**(1): p. 1-32.
32. Sommer, W., *Elastisches Verhalten von Polyvinylchlorid bei statischer und dynamischer Beanspruchung*. Kolloid-Zeitschrift, 1959. **167**(2): p. 97-131.

33. Morton, S.D. and J.D. Ferry, *DYNAMIC MECHANICAL PROPERTIES OF POLYVINYL CHLORIDE GELS*. The Journal of Physical Chemistry, 1962. **66**(9): p. 1639-1645.
34. Warren, T.C., J.L. Schrag, and J.D. Ferry, *Infinite-Dilution Viscoelastic Properties of Poly (dimethylsiloxane)*. Macromolecules, 1973. **6**(3): p. 467-468.
35. Barlow, A., G. Harrison, and J. Lamb, *Viscoelastic relaxation of polydimethylsiloxane liquids*. Proceedings of the Royal Society of London. Series A. Mathematical and Physical Sciences, 1964. **282**(1389): p. 228-251.
36. Roland, C., et al., *Relaxation dynamics in poly (methylphenylsiloxane), 1, 1-bis (p-methoxyphenyl) cyclohexane, and their mixtures*. Macromolecules, 1993. **26**(23): p. 6164-6170.
37. Mercier, J., et al., *Viscoelastic behavior of the polycarbonate of bisphenol A*. Journal of Applied Polymer Science, 1965. **9**(2): p. 447-459.
38. Jho, J.Y. and A.F. Yee, *Secondary relaxation motion in bisphenol A polycarbonate*. Macromolecules, 1991. **24**(8): p. 1905-1913.
39. Yee, A. and S. Smith, *Molecular structure effects on the dynamic mechanical spectra of polycarbonates*. Macromolecules, 1981. **14**(1): p. 54-64.
40. Aloisio, C. and V. Boehm, *Oscillatory Rheology: Polycarbonate*, in *Rheology*. 1980, Springer. p. 513-518.
41. Boehm, V.W., *A dynamic mechanical characterization of polycarbonate*. 1978, Georgia Institute of Technology.
42. Wyzgoski, M.G. and G.S.-Y. Yeh, *Relation between Free Volume and the Low-Temperature "Beta" Transition in Glassy Polycarbonate*. Polymer Journal, 1973. **4**(1): p. 29-34.
43. Makaruk, L. and H. Polanska, *The effect of physical crosslinking on dynamic mechanical properties of polycarbonate low molecular weight additive systems*. Polymer Bulletin, 1981. **4**(1-2): p. 127-132.
44. Wimberger-Friedl, R. and J. De Bruin, *The time-dependent stress-optical behavior of polycarbonate in the glass transition region*. Rheologica acta, 1991. **30**(5): p. 419-429.
45. Alegria, A., E. Macho, and J. Colmenero, *Dynamic mechanical study of four amorphous polymers around and above the glass transition: breakdown of the time-temperature superposition principle in the frame of the coupling model*. Macromolecules, 1991. **24**(18): p. 5196-5202.
46. Torres Arellano, A.K. and G.B. McKenna, *Extremely fragile glass - formers? Calorimetric and rheological determinations*. Journal of Polymer Science Part B: Polymer Physics, 2015. **53**(18): p. 1261-1272.
47. Arellano, A.K.T., *Dynamics of glass forming materials*. 2015.
48. Aitken, C., J. McHattie, and D.R. Paul, *Dynamic mechanical behavior of polysulfones*. Macromolecules, 1992. **25**(11): p. 2910-2922.

49. Emri, I. and B.S. von Bernstorff, *The effect of molecular mass distribution on time-dependent behavior of polyamides*. 2006.
50. Pathak, J.A., et al., *Rheology of miscible blends: SAN and PMMA*. *Macromolecules*, 1998. **31**(25): p. 8988-8997.
51. Woodward, A. and J. Sauer, *The dynamic mechanical properties of high polymers at low temperatures*, in *Fortschritte Der Hochpolymeren-Forschung*. 1958, Springer. p. 114-158.
52. Tajiri, K., et al., *Linear viscoelastic properties of polyethylene terephthalate and its related polymers*. *Journal of Macromolecular Science, Part B: Physics*, 1970. **4**(1): p. 1-38.
53. Fujino, K., et al., *Experimental Study of the Viscoelastic Properties of Textile Fibers Part II: The Influence of Physical Treatments upon the Dynamic Properties of Some Fiber-Forming Polymers*. *Textile Research Journal*, 1956. **26**(11): p. 852-871.
54. Illers, K. and H. Breuer, *Molecular motions in polyethylene terephthalate*. *Journal of Colloid science*, 1963. **18**(1): p. 1-31.
55. Wang, F., J. Roovers, and P.M. Toporowski, *Synthesis and molecular characterization of narrow molecular weight distribution fractions of methyl-substituted poly (aryl ether ether ketone)*. *Macromolecules*, 1993. **26**(15): p. 3826-3832.
56. Plazek, D. and I. Choy, *The physical properties of bisphenol - a - based epoxy resins during and after curing. II. Creep behavior above and below the glass transition temperature*. *Journal of Polymer Science Part B: Polymer Physics*, 1989. **27**(2): p. 307-324.
57. Plazek, D.J. and I.C. Chay, *The evolution of the viscoelastic retardation spectrum during the development of an epoxy resin network*. *Journal of Polymer Science Part B: Polymer Physics*, 1991. **29**(1): p. 17-29.
58. Sanders, J.F. and J.D. Ferry, *Dynamic mechanical properties of cross-linked rubbers. VII. Butyl rubber networks*. *Macromolecules*, 1974. **7**(5): p. 681-684.
59. Cohen, R. and N. Tschoegl, *Dynamic Mechanical Properties of Block Copolymer Blends—A Study of the Effects of Terminal Chains in Elastomeric Materials: 2. Forced Oscillation Measurements*. *International Journal of Polymeric Materials and Polymeric Biomaterials*, 1973. **2**(3): p. 205-223.
60. Scholtens, B.J., *Linear thermoviscoelasticity and characterization of noncrystalline EPDM rubber networks*. *Journal of Polymer Science: Polymer Physics Edition*, 1984. **22**(3): p. 317-344.
61. Prabhu, R., *A critical analysis of the viscoelastic mechanical response of elastomers*. 2012, Purdue University.
62. Landel, R.F., *Mechanical properties of a polyurethane elastomer in the rubber-to-glass transition zone*. *Journal of Colloid Science*, 1957. **12**(3): p. 308-320.
63. Prochazka, F., D. Durand, and T. Nicolai, *Dynamic mechanical properties of linear and cross-linked polyurethane*. *Journal of Rheology*, 1999. **43**(6): p. 1511-1524.

64. Havranek, A., et al., *Viscoelastic behaviour of model polyurethane networks in the main transition zone*. Colloid and Polymer Science, 1987. **265**(1): p. 8-18.
65. Plazek, D.J., *II. Viscoelastic and Steady-State Rheological Response*, in *Methods in Experimental Physics*. 1980, Elsevier. p. 1-58.